Mon. Not. R. Astron. Soc. **000**, 1–30 (2015) Printed 11 August 2015 (MN LATEX style file v2.2)

arXiv:1508.02369v1 [astro-ph.GA] 10 Aug 2015

# An ATCA Survey of Sagittarius B2 at 7 mm: Chemical Complexity Meets Broadband Interferometry

Joanna F. Corby[1] *, Paul A. Jones[2], Maria R. Cunningham[2],
Karl M. Menten[3], Arnaud Belloche[3], Frederic R. Schwab[4], Andrew J. Walsh[5],
Egon Balnozan[2], Leonardo Bronfman[6], Nadia Lo[6], Anthony J. Remijan[4]
[1] *Department of Astronomy, University of Virginia, Charlottesville, VA 22903*
[2] *School of Physics, University of New South Wales, NSW 2052, Australia*
[3] *Max-Planck-Institut für Radioastronomie, D-53121 Bonn, Germany*
[4] *National Radio Astronomy Observatory, Charlottesville, VA 22903, USA*
[5] *Department of Physics and Astronomy, Curtin University, WA 6102, Australia*
[6] *Departamento de Astronomía, Universidad de Chile, Santiago, Chile*

Accepted 2015 July 3. Received 2015 June 16; in original form 2015 March 24

## ABSTRACT

We present a 30 - 50 GHz survey of Sagittarius B2(N) conducted with the Australia Telescope Compact Array (ATCA) with 5 - 10 arcsec resolution. This work releases the survey data and demonstrates the utility of scripts that perform automated spectral line fitting on broadband line data. We describe the line-fitting procedure, evaluate the performance of the method, and provide access to all data and scripts. The scripts are used to characterize the spectra at the positions of three HII regions, each with recombination line emission and molecular line absorption. Towards the most line-dense of the three regions characterised in this work, we detect ∼500 spectral line components of which ∼90% are confidently assigned to H and He recombination lines and to 53 molecular species and their isotopologues.

The data reveal extremely subthermally excited molecular gas absorbing against the continuum background at two primary velocity components. Based on the line radiation over the full spectra, the molecular abundances and line excitation in the absorbing components appear to vary substantially towards the different positions, possibly indicating that the two gas clouds are located proximate to the star forming cores instead of within the envelope of Sgr B2. Furthermore, the spatial distributions of species including CS, OCS, SiO, and HNCO indicate that the absorbing gas components likely have high UV-flux.

Finally, the data contain line-of-sight absorption by ∼15 molecules observed in translucent gas in the Galactic Center, bar, and intervening spiral arm clouds, revealing the complex chemistry and clumpy structure of this gas. Formamide ($NH_2CHO$) is detected for the first time in a translucent cloud.

**Key words:** astrochemistry – ISM: HII REGIONS – ISM: MOLECULES – RADIO LINES:ISM – STARS: FORMATION – TECHNIQUES: INTERFEROMETRIC – ISM:INDIVIDUAL (SAGITTARIUS B2)

## 1 INTRODUCTION

The complex high mass star forming region Sagittarius B2 (Sgr B2) is a uniquely interesting source for studying star formation and molecular chemistry. Sgr B2 is an exceptionally massive cloud complex at $\sim 3\times10^6$ $M_\odot$ (de Vicente, Martin-Pintado & Wilson 1996), an order of magnitude higher than most star-forming Giant Molecular Clouds, and is in the Central Molecular Zone of the Galactic Center, where widescale shocks and supersonic turbulence are observed to be nearly ubiquitous (Martín-Pintado et al. 2001; Martín et al. 2008). Furthermore, the region has an exceptionally high X-ray flux (Terrier et al. 2010), cosmic ray ionization rate (van der Tak et al. 2006), and magnetic field strength (Crutcher et al. 1996), making it an exceptional case of star formation that is perhaps more similar to the central regions of starburst galaxies than it is to most star forming regions in the Galaxy. In fact, the

---

* jfc2113@gmail.com

star formation rate in Sgr B2 qualifies the region as a mini-starburst (Belloche et al. 2013).

Sgr B2 has a complex physical structure with more than 50 known extended, compact, ultra-compact, and hypercompact HII regions embedded in an extended envelope of molecular, atomic, and ionized gas (Gaume et al. 1995; Goicoechea, Rodríguez-Fernández & Cernicharo 2003; Jones et al. 2008). Most of the star forming activity in the region is concentrated in the North, Main, and South cores. The three cores of star formation have a $v_{LSR}$ of ∼55 - 70 $\mathrm{km\,s^{-1}}$, and the star formation is thought to be triggered by the collision of a cloud of gas at ∼80 - 90 $\mathrm{km\,s^{-1}}$ with the main body of Sgr B2 at ∼40 $\mathrm{km\,s^{-1}}$ (Hasegawa et al. 1994; Sato et al. 2000). Possible ejecta from Sgr B2 have been identified via line-of-sight molecular absorption at 0 - 20 $\mathrm{km\,s^{-1}}$, although recent observations indicate that this may correspond to a more extended feature across the Galactic Center (Wirström et al. 2010; Jones et al. 2012; Royster & Yusef-Zadeh 2014). Additional foreground components of molecular gas associated with the Galactic Center and spiral arms are similarly observed in line-of-sight absorption towards Sgr B2 (Greaves & Nyman 1996; Gerin et. al 2010 and references therein).

Towards the North core of Sgr B2 (Sgr B2(N)), the focus of this study, continuum emission is produced by a complex of HII regions, as observed and discussed in Gaume et al. (1995). Two ∼10 arcsec (= 0.4 pc) concentric shell-shaped regions – K5 and K6 – are thought to be expanding ionization fronts (Figure 1). To the NW of these, the more compact region K4 is thought to be a similar system at an earlier stage of development. Three sub-arcsecond cores of continuum emission – K1, K2, and K3 – are located to the SW of K5 and K6. Finally, a cometary HII region, L, is located ∼35 arcsec NE of the North core.

Molecular gas is observed in the foreground of the HII regions and in extended material surrounding the cores (Hüttemeister et al. 1995; Jones et al. 2008). Additionally, the Large Molecule Heimat (LMH) is a ∼5 arcsec region surrounding K2 that is continuum-free at radio wavelengths, but bright in submillimeter continuum (Miao et al. 1995; Qin et al. 2011). The LMH is a hot core that is home to the most diverse molecular chemistry observed in the ISM, and a significant fraction of the molecular lines detected towards the LMH remain unidentified (Belloche et al. 2013). In addition to the LMH, Sgr B2(N) has a second hot core named "h" (Belloche et al. 2013). The "h" region is located on the K5 shell and was first identified as a quasi-thermal methanol core (Mehringer & Menten 1997). Like the LMH, "h" produces submillimeter continuum emission (Qin et al. 2011) and line emission by many complex organic species, including the first branched alkyl species detected in the ISM (Hollis et al. 2003; Belloche et al. 2013, 2014).

Sgr B2 has been targeted by spectral line surveys from centimeter to sub-millimeter wavelengths (Turner 1989; Nummelin et al. 1998; Neill et al. 2012; Belloche et al. 2013; Neill et al. 2014), however, most surveys have been conducted with single dish telescopes at frequencies > 80 GHz. At these frequencies, there is significant line confusion (a single feature can be assigned to multiple possible known or yet unknown carriers) and line blending (a single feature consists of multiple transitions of known molecules), as the data are line confusion limited rather than noise limited. On the other hand, data are noise-limited at centimeter wavelengths, with significantly less line confusion and blending, enabling more confident line identifications and measurements of spectral line parameters (i.e. shape, velocity, width, and flux) (McGuire et al. 2012).

In Sgr B2 and other sources with chemical variation on size scales smaller than the beam of a single dish telescope, interferometric observations are critically important for understanding the chemical environments. Observing the same portion of the spectrum with both an interferometer and a single dish telescope provides sensitivity to weak lines in extended gas (single dish) and resolves fine spatial variations to distinguish chemically distinct regions (interferometer). In molecule-rich sources, interferometric observations can also help to mitigate line confusion and blending, as lines from different molecules can peak at distinct positions. This further enables interferometric observations to be useful for demonstrating that multiple lines originate from a common molecular carrier, particularly for weak features (sub-100 mK) produced by species with low abundance, low dipole moments, or high partition functions.

To date, only a few molecular lines mapped with the spatial resolution required to distinguish the distinct chemical environments in Sgr B2(N) have been published (Liu & Snyder 1999; Hollis et al. 2003; Belloche et al. 2008). With the arrival of broadband radio interferometers including the Australia Telescope Compact Array (ATCA) with the CABB backend, the Karl G. Jansky Very Large Array (VLA), and the Atacama Large Milimeter Array (ALMA), interferometric line surveys are now efficient, providing access to the spatial distributions of hundreds of molecular lines within a reasonable observing time. With the new wealth of information available, however, come new challenges in data analysis that require automated methods. To date, these are not adequately developed, and large scale efforts to provide improved visualization and analysis tools for rich spectral line data cubes are underway (Teuben et al. 2013).

In this work, we describe a 30 - 50 GHz spectral line survey conducted with the ATCA. The survey provides detailed information on chemical differentiation in Sgr B2(N), the most extensive catalog of radio recombination lines collected with an interferometer, and novel information on the structure and molecular content of clouds observed in the line-of-sight to Sgr B2. The survey serves as a pathfinder for a planned science verification project with ALMA Band 1 (35-50 GHz), presently being developed, and showcases methods that will be useful for this and other future projects. We describe the observations (§2), present an automated line fitting and identification routine (§3), and apply the algorithms to selected regions of the Sgr B2(N) complex (§4). In §5, we characterise the molecular gas and highlight the distributions of a few molecular species showing distinct morphologies. We focus specifically on line identifications and parameter fitting towards K6, K4, and L, and do not provide full line identifications towards the LMH and h. The primary aim of this work is not to perform a complete spectral line analysis but rather to test the functionality of the fitting routine on regions that show line absorption and emission at multiple velocity components. The type of data analysis routines described will be essential for characterizing and analyzing the spectra of complex molecular line sources at higher frequencies. Furthermore, we release all data and routines to the community to facilitate more complete analyses on the many projects that the data set enables.

## 2 OBSERVATIONS

### 2.1 Telescope Configurations

The observations were conducted with the Australia Telecope Compact Array (ATCA) with the Compact Array Broadband Backend (CABB) (Wilson et al. 2011) in broadband mode (CFB 1M-0.5k), providing two simultaneous spectra with 2048 channels of

1MHz width. Eleven different tunings with a separation of 1.85 GHz were required to cover the full 30 - 50 GHz range available with the 7 mm receiver (Table 1). The 1 MHz channels provide a velocity resolution of 10 - 6 $\mathrm{km\,s^{-1}}$ from 30 - 50 GHz. Even given the broad linewidths in Sgr B2, the spectral resolution is suboptimal, so that lines may not be Nyquist sampled. However, the broadband mode of the CABB was selected as it makes a line survey over the whole 7 mm band feasible within a relatively short observing time.

The observations were made in three ∼8 hour sessions in 2011 October and 2013 April, with hybrid arrays H75 and H214, respectively, as shown in Table 1. In each session, two pairs of tunings were observed, and the 43.70 GHz tuning was repeated in each configuration. The H214 hybrid array enables good (u,v)-coverage of Sgr B2(N), providing sufficient resolution to separate the LMH from the shell-shaped HII regions without losing significant surface-brightness sensitivity. The H75 array is more compact than ideal but this is somewhat countered by using this array for the highest frequency tunings. Resulting angular resolutions, ranging from 3.4 to 13 arcsec are provided in Table 2.

The telescope was pointed towards Sgr B2(N) at $\alpha = 17^h47^m20\overset{s}{.}4$, $\delta = -28^\circ22'12''$ (J2000). We observed a cycle of one minute on the complex-gain calibrator (1714-336), ten minutes on source, one minute on the gain calibrator with one pair of tunings (A1 and A2 in Table 1) and then repeated the calibrator-source-calibrator cycle with the second pair of tunings (B1 and B2). The telescope pointing was updated approximately every hour towards the gain calibrator. Uranus and 3C 279 were observed as the primary flux and bandpass calibrators respectively.

### 2.2 Data Reduction

The raw data were reduced into calibrated data cubes using mostly standard techniques of bandpass, absolute flux, and complex gain calibration in the MIRIAD package (Sault, Teuben & Wright 1995). To produce continuum-free line data, the continuum was subtracted in the (u,v)-domain and the fitted continuum was output into separate files. A single continuum image was generated from each of the three observing sessions and deconvolved with the CLEAN algorithm. The CLEAN model was input to determine a phase-only self-calibration solution, which was then applied to the line data and the continuum data. A final continuum image was generated using the CLEAN algorithm from the 7.5 GHz bandwidth data obtained in each observing session.

As this is among the first spectral line surveys completed with a broadband interferometer, we highlight our method for baseline subtraction and challenges for bandpass stability. We performed baseline subtraction using the MIRIAD task UVLIN, generating a linear fit to the baseline of each 2 GHz tuning in the (u,v)-domain. The continuum images were generated from the continuum solutions output by UVLIN. Because Sgr B2 has a very high line density and because it is difficult to define line-free channels in the (u,v)-domain, we only excluded channels covering strongly masing lines from the fit. As very strong lines covered a small fraction of the bandwidth of each image, this had a very small effect on the continuum subtraction, resulting in a ∼1 mJy/beam offset that is <0.1% of the continuum level. Such a small effect might be deemed negligible in most data sets, however given the sensitivity of this data, it is non-negligible.

A larger effect was noticed in the form of a baseline wiggle in the images with a maximum amplitude of <1.5% of the continuum strength. This resulted from a limited bandpass stability due to the very large bandwidth in each tuning. The bandpass shape is quite complex, and while the selected bandpass calibrator was very strong (∼25 Jy), the strong continuum of Sgr B2 (∼1 Jy) made it difficult to model the continuum to the dynamic range (about 3 orders of magnitude) required. Furthermore, the continuum positions of Sgr B2(N) and (M) are the positions that contain most of the molecular line features, so that the residual continuum preferentially affected areas that are important for the line study.

To correct for these effects, we applied a continuum correction to the data in the image domain. Lines were masked at the $3\sigma$ level, and each 2 GHz cube was fitted with a high order polynomial to make a baselevel offset spectrum which was subtracted from the data cube. We note further processing of the baseline applied to the published spectra in §3.1.

We note that the CABB flagged a consistent set of channels in each observation. In the publically released images, in which the first and last 50 channels of each 2 GHz wide module are cut, the zero-indexed channels affected include channels 0, 1, 78, 106, 206, 462, 590, 718, 974, 1102, 1126, 1230, 1358, 1486, 1742, 1870, and 1947. All data cubes and continuum images are available at the CDS database(Genova et al. 1995) via anonymous ftp to cdsarc.u-strasbg.fr (130.79.128.5) or via http://cdsarc.u-strasbg.fr/viz-bin/qcat?J/MNRAS/. The continuum-subtracted data cubes provided do not have a primary beam correction applied. Models for the ATCA primary beam can be computed from information provided on the ATCA documentation, or by correspondence with the authors.

## 3 AUTOMATED SPECTRAL LINE FITTING AND LINE IDENTIFICATION

### 3.1 Sources and Spectrum Extraction

The ATCA line survey contains of order a thousand spectral lines with significant spatial and kinematic structure. In order to handle the wealth of information in the dataset, we extracted mean spectra from elliptical regions placed over physically distinct regions of Sgr B2(N), transforming a 3-d problem into a set of 1-d problems. We extracted spectra over the entire 29.8 - 50.2 GHz bandwidth from a radio continuum peak along the K6 shell-shaped HII region, the cometary HII region L located 35 arcsec NE of Sgr B2(N), and the LMH hot core. In the higher spatial resolution section of the spectrum (from 29.8 - 44.6 GHz due to the observed configurations), we additionally extracted mean spectra towards K4 and "h". Figure 1 shows the elliptical regions from which the spectra were extracted and Table 3 reports their positions. Note that we did not vary the size of the elliptical regions in different images depending on the beam size. The elliptical regions are typically larger than the beam sizes in the high spatial resolution data (from 29.8 - 44.6 GHz), but smaller than the beam sizes in the low spatial resolution data observed with the compact array configuration (from 44.6 - 50.2 GHz). The spectra are sensitive to the spatial resolution; for example, low spatial resolution data towards the K6 elliptical region includes flux originating on the K5 shell and in the LMH as the regions are poorly resolved. In the case of the spatially isolated source L, the elliptical region from which the spectrum was extracted is similar to the source size of L and well matched to the ∼5 arcsec beam size of the high spatial resolution data (Gaume et al. 1995). In the low spatial resolution data, the flux is spread over the larger beam, which has the effect of decreasing the flux in the low spatial resolution section of the spectrum.

After extracting spectra, we interpolated over bad spectrometer channels listed in §2.2 using linear interpolation, and performed additional baseline smoothing by applying a Hodrick-Prescott filter to remove a low frequency baseline wiggle (Hodrick & Prescott 1997). Figure 2 shows the baseline with and without the Hodrick-Prescott filter applied. A Hodrick-Prescott filter is a commonly used tool for removing long-term growth trends from economics data and is similar in function to a high-pass filter. It is simple to implement and proved a useful means of removing residual baseline without degraded results at the band edges. We used a modified version of the HP filter, as described in Schlickt (2008), that can use datasets with segments of missing data. This was useful in order to extrapolate over spectral lines, particularly over broad spectral lines, such as the absorption feature of $CH_2CN$ at 40230-40270 MHz. Applying the filter achieved a 10 - 25% reduction in the root mean squared (rms) noise in the spectra extracted from different images.

We then converted from units of Jy beam$^{-1}$ to mean flux density per square arcsec (or equivalently, specific flux density) in order to inspect images with distinct beam sizes on the same scale. Finally, we performed a primary beam correction to the extracted spectra. We applied the beam correction to the extracted data instead of simply extracting the spectra from beam-corrected images for the following reason. For each image, the standard technique in MIRIAD applies a single primary beam (PB) correction based on the central frequency tuning of the image, and does not include frequency dependence within the image. However, over the 2 GHz bandwidth of each image, frequency-dependence is significant, especially towards L. To compute appropriate frequency-dependent beam corrections, we compared the spectra extracted from the regions in the non-PB corrected cubes to the spectra extracted from the same regions in PB corrected cubes. We fit a fifth order polynomial to the ratio of PB corrected to non-PB corrected data across the 20 GHz of bandwidth. This fit provides the PB corrections. They are substantial (up to a factor of 2.6) for L but are very small ($<$1.04) for K4, K6, "h", and the LMH.

The half power beam widths at all frequency tunings and the rms noise levels in the final extracted spectra are reported in Table 2. The supplemental material to this work provides the extracted, HP-filtered, and PB-corrected spectra towards all 5 regions, and the line fitting and identification PYTHON code described in §3.2. This material is additionally available at https://github.com/jfc2113/MicrowaveLineFitter.

### 3.2 Line Fitting Methodology

The line fitting routines operate on the extracted 1-d spectra in order to fit Gaussians and perform line identification by the following procedure:

(i) Identify "detected" features as those with a single-channel flux $I_{chan} > 3.5\sigma_{\rm region}$, where $\sigma_{\rm region}$ is the rms noise of line-free sections of a region's extracted spectrum. The value of $\sigma_{\rm region}$ is determined independently for each frequency tuning. With a threshold of $3.5\sigma_{\rm region}$, one channel in 2149 should be a false detection assuming perfect baseline subtraction and constant noise within an image. The fitter selects channels that meet this criteria and 5 channels on either side.

(ii) Compensate for the poor spectral resolution by using Fourier domain zero padding to interpolate data in the channels selected in step (i). This generates interpolated data with 0.33 MHz channels within segments of the spectrum that contain lines. While the number of independent data points remains the same, this triples the number of points used to constrain the fits, improving the fits significantly. This is essential for the ATCA data because in many cases, only 2-3 original channels sample the lines, and a Gaussian fit to so few channels can return a wildly unreasonable fit. For example, if a line profile is sampled by 2 channels and surrounded by a zero-value baseline, one can imagine many different Gaussian profiles capable of fitting the data perfectly with highly varying heights in particular.

(iii) Fit one or more Gaussians to each feature iteratively. The spectral line fitter first determines an unconstrained best-fit Gaussian to a spectral line using a least squares routine. The best-fit parameters are then used as input guesses for the least squares fitter to re-fit a single Gaussian to the channels within 0.8 × FWHM of the line center. A cutoff of 0.8 × FWHM is selected in order to minimize the effects of the baseline uncertainty, which preferentially affects line wings. If a 1-component Gaussian shape is appropriate, this includes 94% of the power of the line.

(iv) Evaluate the 1-component fit against a set of criteria designed to determine whether a multi-component fit is required. The criteria were determined empirically for this dataset and are described in Appendix A. If the segment of data meets the criteria, a 2-component fit is determined and evaluated. In the event that neither a 1-component nor a 2-component fit is deemed sufficient, the fitter grabs a slightly different segment to fit and retries both a 1- and 2-component fit. If the result remains insufficient, the reported fit is marked as poor, pointing out where further attention is required.

(v) The best 1- or 2-component Gaussian fit is then subtracted from the raw (as opposed to the interpolated) data. If the residual spectrum contains channels with $I_{\rm chan} > 3.5\sigma_{\rm region}$, the residual spectrum re-cycles through steps (ii)-(v). Non-Gaussian line shapes (i.e. lines with wing broadening) are fit in this process, so that the iterative solutions do not provide a full characterisation of the line shape, but do adequately account for the total flux of the line. The treatment of line wings is discussed further in Appendix A.

(vi) Identify lines by comparing the Gaussian fit parameters to spectral line catalogue data.[1] Because the code is optimized to this dataset, the line-ID component is not very sophisticated, with the primarily kinematics-based rather than chemistry-based consistency checks.

Because a large number of steps were required to obtain the resulting fits, we do not adopt the errors to individual fits. Instead, we utilize the power of broadband line surveys to derive upper limits to the errors empirically from the variation in line parameters amongst a large number of fits (§4.2)

Note that the code does not include a model for the molecular composition and radiative transfer. This enables us to measure properties of the gas purely empirically, which is particularly appropriate at centimeter wavelengths, where a large number of lines from various molecules have been shown to be non-thermally excited (Menten 2004; McGuire et al. 2012; Faure, Remijan & Szalewicz 2014). The code is written modularly, enabling adaptation for different datasets. The PYTHON scripts are further described in Appendix A and available in the online journal and at https://github.com/jfc2113/MicrowaveLineFitter.

---

[1] All line data were accessed through the online ALMA Spectral Line Catalogue - Splatalogue (available at www.splatalogue.net; Remijan & Markwick-Kemper (2007)); original line data were compiled in the Cologne Database for Molecular Spectroscopy (CDMS; Müller et al. 2005); the NASA Jet Propulsion Laboratory catalogue (JPL; Pickett et al. 1998); the National Institute for Standards in Technology (NIST) Recommended Rest Frequencies for Observed Interstellar Molecular Microwave Transitions - 2002 Revision (the Lovas/NIST list; Lovas & Dragoset 2004); and the Spectral Line Atlas of Interstellar Molecules (SLAIM; F. J. Lovas, private communication) and references therein accessible on Splatalogue.

## 4 SPECTRAL LINE RESULTS

The data contain recombination lines and molecular transitions. Most detected molecular transitions are either observed in absorption preferentially along the K5 and K6 shells, L, and K4, or in emission towards the LMH and "h" hot cores (Figure 3). Figure 4 shows a representative segment of spectra from all five regions from which spectra were extracted. Detected absorption lines are primarily from low energy states ($E_L \lesssim 20$K), whereas most emission lines from the LMH and "h" have higher energies ($E_U \gtrsim 80$K). The LMH has the most line-dense spectrum as anticipated, and "h" has the second richest spectrum. The excitation and gas phase molecular abundances of "h" appear significantly more similar to the LMH than other regions in Sgr B2(N), confirming that it is a second hot core in Sgr B2(N) (Belloche et al. 2013).

The spectra towards K6, L, and K4 are similar to one another, predominantly showing emission by recombination lines and absorption by molecules. Of all detected features originating at the positions of K6, L, and K4, ∼90% were confidently assigned to recombination line or molecular carriers. The remaining 10% including unidentified transitions are discussed in Appendix B. Figure 32 illustrates the raw data spectrum extracted towards K6 with the output of the line fitter overlaid and line identifications labeled. Figures in this format containing the full spectra towards K6, L, and K4 are provided in Appendix B. Additionally, tables providing line identifications and Gaussian fit parameters, including velocity center, height, width, and integrated flux towards K6, L, and K4 are available in Appendix C. Table 9 is a sample page of the line parameters towards K6. We do not report errors on individual Gaussian fits in the tables, but discuss errors in §4.2. As mentioned in §3.2, lines with wing broadening are approximated by a primary Gaussian component and additional components with lower amplitude. For clarity, we only list the primary Gaussian component parameters in the tables, however, the reported integrated flux values include wing components. It follows that the reported flux is not always equivalent to what you would obtain from the primary Gaussian component alone.

### 4.1 Recombination Lines

In order to assess the performance of the line fitting and identification routine, the output of the code was evaluated using hydrogen and helium recombination lines towards K6, L, and K4. Recombination lines, particularly at higher principal quantum numbers ($n > 90$), are not well described by simple Gaussian line shapes but exhibit Voigt profiles (von Procházka et al. 2010). The line fitting routine applies only Gaussian shapes, which adequately characterise the bulk motion of ionized gas via the velocity center, particularly because the $\alpha$ and $\beta$ transitions have lower quantum numbers with less collisional broadening. However, towards K6 in particular, most H $\alpha$ lines require primary components and weaker components to recover the flux in the wings.

The hydrogen and helium 51 - 59 $\alpha$, 64 - 75 $\beta$, 72 - 85 $\gamma$, 79 - 93 $\delta$, 85 - 100 $\epsilon$, and 90 - 106 $\zeta$ recombination transitions fall in the observed band, enabling measurements of recombination line strengths, widths, and H II region kinematic centers. Figures 6 and 7 present H and He $\alpha$ and $\beta$ transitions towards K6, and Figures 8 and 9 present H and He $\alpha$ transitions towards L and K4 respectively. Each panel shows the H and He data with a single quantum number, with the Gaussian fits reported in the online journal overlaid. The final panel of each figure shows a composite averaged spectrum overlaid with a fit to the averaged spectrum. The best fits to the averaged spectra are provided in Table 5. Additionally, recombination line kinematic measurements generated from H $\alpha$ - $\gamma$ transitions are provided in Table 6 and a histogram of the line centers is shown in Figure 10.

Towards K6, the automated line fitting routine detected 64 hydrogen recombination transitions including H $\alpha$ - H $\zeta$ and 13 helium transitions including He $\alpha$ - He $\beta$ lines. The ionized gas towards K6 has two primary velocity components, at ∼59 and ∼84 km s$^{-1}$ (Figure 6). The automated line fitter determined that a 2-component fit is required for all H $\alpha$ transitions and for nearly all H $\beta$ and He $\alpha$ transitions. Of the 25 unblended H $\alpha$ - $\gamma$ transitions for which the automated fitting routine used a 2-component fit, it obtained a mean velocity of $58.9 \pm 0.8$ km s$^{-1}$ and width $28.7 \pm 1.1$ km s$^{-1}$ for the low velocity component and a mean velocity of $84.7 \pm 0.8$ km s$^{-1}$ and width $27.2 \pm 1.2$ km s$^{-1}$ for the high velocity component. The best fits to the composite averaged spectra of H $\alpha$ and H $\beta$ transitions are both consistent with these parameters (Table 5). As is evident in Figures 6 and 7, hydrogen recombination transitions at higher spatial resolution, (namely the H(56) - (53)$\alpha$ and H(70) - (66)$\beta$ transitions) have more pronounced double-peaked line shapes than the moderate resolution transitions (H(59) - (57)$\alpha$ and H(75) - (71)$\beta$), which in turn are more double-peaked than the lowest resolution transitions (H(52) - (51)$\alpha$ and H(65) - (64)$\beta$). The line profiles are thus highly sensitive to the spatial resolution.

The double-peaked structure towards K6 was first reported by de Pree et al. (1995) in an image of the H(66)$\alpha$ transition observed by the VLA with 1$''$.4 resolution. This work reported a 2-component recombination line profile located internal to the K6 shell at a position roughly 2.5 arcsec north of our selected K6 region. The components were reported at 50 and 93 km s$^{-1}$, and de Pree et al. (1995) argued that the H(66)$\alpha$ line profile provides a direct detection of the two sides of a shell with an expansion velocity of ∼21 km s$^{-1}$. In the ATCA data, a double-peaked profile with components at ∼50 and 90 km s$^{-1}$ is observed towards the K6-internal position noted in that work. However, the spatial positions of the peak 50 and 90 km s$^{-1}$ recombination line emission are offset, with the 50 kms component centered on the base of the K6 shell within our K6 elliptical region, and the 90 km s$^{-1}$ gas centered ∼4 arcsec to the NW (Figure 11). If the two components are part of the same structure, the data are consistent with the ionization front expanding into a clumpy molecular cloud and preferentially illuminating at the position of a clumps on the front and back sides of the shell.

Towards L, the automated line fitting routine detected 52 hydrogen transitions from H $\alpha$ to H $\zeta$ and 8 He $\alpha$ lines. As is evident in Figure 8, higher specific flux densities are observed in the high resolution data, which covers the H(59) - H(53)$\alpha$ transitions, due to the effect of the varying beam size discussed in §3.1. The automated line fitting routine typically fit each recombination line with a single Gaussian. Of 26 unblended 1-component H $\alpha$ - $\gamma$ lines detected by the automated fitting routine, the mean center velocity is $76.3 \pm 0.2$ km s$^{-1}$ and width is $26.3 \pm 0.7$ km s$^{-1}$, consistent with the Gaussian fit to the composite average spectrum of H $\alpha$ lines (Table 5). Towards L, de Pree et al. (1995) reported a recombination line velocity of $75.8 \pm 0.3$ km s$^{-1}$ and width $31.7 \pm 0.7$ km s$^{-1}$, so that the line widths in particular somewhat disagree with the ATCA data. This is a result of the differences in spatial resolution. In the ATCA observations, L appears as a single unresolved source; on the other hand, the higher spatial resolution observations in de Pree et al. (1995) treat L and L13.30 located ∼3 arcsec east as separate sources. Towards L13.30, de Pree et al. obtain a velocity of $76.5 \pm 1.2$ km s$^{-1}$ and width $20.6 \pm 2.8$ km s$^{-1}$. Our line parameters are intermediate between those of the two unresolved sources.

Recombination lines are weaker towards K4 compared to K6 and L. As a result, primarily H $\alpha$ - $\gamma$ transitions were detected (24 total) and only 2 He $\alpha$ transitions were detected. As is apparent in Figure 9, the line profiles suggest a wing on the high velocity side of the line center, near 100 km s$^{-1}$. Of the seven H $\alpha$ transitions from 30 - 44.6 GHz, only H(56)$\alpha$ is known to be blended. Of the remaining six H $\alpha$ transitions, four required a 2-component fit to the line emission from 40 - 80 km s$^{-1}$ (Figures 9 and 10). The other two H $\alpha$ transitions (namely H(57) and H(55)$\alpha$) did not meet the criteria for a 2-component fit, but a 2-component fit appears more appropriate and the reported fit is adjusted from the output of the line fitter. The line shape appears to vary substantially, suggesting a complex kinematic structure resulting in a line shape that is sensitive to the beam size and precise placement of the elliptical region. Indeed Figure 11 shows a steep velocity gradient across K4.

Although most of the H $\alpha$ transitions required a 2-component fit (primary) and a weaker component in the high velocity wing (secondary), the composite line profile is adequately fit by 1-component primary Gaussian fit at 65 km s$^{-1}$ and a weaker wing component (secondary) on the high velocity side at 100 km s$^{-1}$, as reported in Table 5. Using fits to H $\beta$ and H $\gamma$ lines determined by the line fitter, we find that a 1-component treatment of the recombination lines towards K4 has a velocity center of $66.2 \pm 0.5$ km s$^{-1}$ and width of $32.1 \pm 1.4$ km s$^{-1}$. The values we determine are in mild disagreement with those reported by de Pree et al. (1995), who report a velocity of $63.9 \pm 0.8$ km s$^{-1}$ and a width $36.0 \pm 1.9$ km s$^{-1}$. This may be because we are looking at different regions of K4. We determined the shape and placement of the elliptical region towards K4 based on the continuum structure as sampled at 40 GHz by the ATCA, which is offset by ∼1 arcsec SE of the continuum peak at 22 GHz observed by de Pree et al. (1995). In the ATCA data, most of the recombination line emission associated with K4 arises 2-3 arcsec southeast of the 22 GHz continuum peak, and higher velocity line emission is observed to the SE (Figure 11). Some of the higher velocity material is included in the elliptical region placed on K4.

### 4.2 Error Estimation

While many sources of error exist, calibration errors (including absolute flux calibration and amplitude error from gain calibration) are small and fairly independent of frequency and position. The main sources of error with which we are concerned include:

(i) Spectral lines that are barely, or in some cases not, Nyquist sampled have poorly constrained Gaussian line parameters. While the precision of line center and width measurements are obviously limited, this introduces a ∼10 - 15% uncertainty to the line height. We adopt a 12.5% error to the line height for unblended lines. It additionally introduces substantial covariance in the fit parameters of 2-component lines that are not well resolved. This applies to the 2-component recombination lines towards K6 and K4 and to molecular lines that are broad due to saturation or blended hyperfine components.

(ii) The baseline uncertainty, typically of order 0.05 mJy arcsec$^{-2}$, can increase the number of false detections and affect the best-fit Gaussian shapes. While we minimized the baseline residual using a Hodrick-Prescott filter, it is impossible to obtain a fully residual-free baseline, and the remaining baseline can affect low signal-to-noise transitions significantly. This contributes uncertainty in line heights and can artificially broaden the best-fit Gaussian. As discussed in §3.2, we minimize the latter effect by fitting only the region within 0.8 × FWHM of line center.

(iii) Frequency-dependent variations in noise level in data from a single spectral tuning can generate false detections. Noise can also contribute significantly to error for low signal-to-noise detections, particularly because the data is not Nyquist sampled.

(iv) The spectrum extracted from a region can contain flux generated at a different spatial position in low spatial resolution data. This applies primarily to the low spatial resolution data (from 44.6 - 50.2 GHz) in the spectrum of K6, which contains flux arising in the LMH and "h". This effect is discussed further in Appendix B.

(v) Towards the three regions that we characterise in this work, we observe molecular gas with two primary kinematic components separated by ∼20 km s$^{-1}$. For a few low signal-to-noise transitions, the data does not significantly disagree with a single Gaussian profile, so the line fitting routine returns a single fit at a velocity that is intermediate between the two velocity components. We indicate fits for which we suspect this has occured with "$BC$" for blended components. In these cases, the Gaussian parameters are unreliable, but the qualitative statement of transition detection stands. As a primary aim of the study is to demonstrate the functionality of the line fitting code, we correct few instances of this. However, researchers interested in the separate contributions from the two gas cloud components should re-fit these with the velocities and widths fixed to the mean values obtained in this work.

Because there are many sources of uncertainty and a large number of lines detected in the survey, the simplest method for evaluating the error is to derive it from the fits themselves. To do so, we assume that line radiation from all thermal molecular line transitions originates at a consistent set of central velocities for each targeted spatial region, setting an upper limit on the typical error of fits. With very few high signal-to-noise exceptions, this assumption is supported by the data, as typical differences from the mean center velocity are significantly smaller than the channel widths of 6 - 10 km s$^{-1}$.

Using molecular line transitions with signal-to-noise ratios (determined as the ratio of the Gaussian fit height to the noise level in the extracted spectrum) in the 25th - 90th percentile range, we determine the standard deviation of the line velocity centers and widths. The 25th - 90th percentile range excludes the strongest lines which typically have wing broadening and the weakest quartile (with a signal-to-noise ratio $\lesssim 5.4$) which is preferentially affected by baseline issues and noise. The distributions of velocity centers and line widths towards all three regions is shown in Figure 12. Using 129 unblended transitions towards K6 that fall in our target signal-to-noise window (including 51 1-component transitions and 39 2-component transitions) we determine the standard deviation of the center velocity to be $\sigma_v = 1.1$ km s$^{-1}$ and the standard deviation of the velocity width to be $\sigma_{\Delta v} = 2.3$ km s$^{-1}$. The standard deviations of both parameters are significantly lower than the channel resolution of 6 - 10 km s$^{-1}$, indicating that the method performs rather well given the limits of the dataset. We adopt $\sigma_v = 1.1$ km s$^{-1}$ and $\sigma_{\Delta v} = 2.3$ km s$^{-1}$ as $1\sigma$ errors on the fit parameters of 1-component lines and spectrally resolved 2-component lines with a signal-to-noise ratio $>5.4$. This includes unblended 1- and 2-component molecular lines and 1-component recombination lines. These values are consistent with the standard deviations of the parameters fit to high signal-to-noise recombination lines towards L (Figure 10 b), further justifying their validity.

For 2-component recombination lines in which the components are not spectrally resolved, we determine $\sigma_v = 3.6$ km s$^{-1}$ and $\sigma_{\Delta v} = 4.9$ km s$^{-1}$ from 17 H$\alpha$ and $\beta$ lines towards K6, and line height errors of each component are estimated at $\sim$25%. Compared to molecular lines, 2-component recombination lines have larger errors because the two velocity components are poorly resolved. As the line widths of the 2-component recombination line components are larger than the velocity separation between the two components $\left(\frac{\Delta v_1 + \Delta v_2}{2} > v_2 - v_1\right)$, the components are unresolved. While a 1-component fit does a poor job of matching these profiles, a 2-component fit contains significant covariance between the six fit parameters. Errors of the velocity center and width are approximately 40% higher for 2-component H$\gamma$ and $\delta$ lines, and the line heights have a $\sim$40% estimated error.

Table 7 summarizes the errors of the fit parameters that are adopted in this work and recommended for further use of the results.

## 5 MOLECULAR COMPOSITION

### 5.1 Molecular Gas Components Associated with Sgr B2

Nearly all of the molecular lines detected towards K6, L, and K4 are in absorption against the free-free continuum emission. The following molecular species were detected towards one or more of these regions. Tentative detections are marked with a "(?)".

**CS Family**: CS, C$^{34}$S, C$^{33}$S, $^{13}$CS, $^{13}$C$^{34}$S, HCS$^+$, H$_2$CS, CCS, CC$^{34}$S, OCS, CCCS

**Silicon Species**: SiO, $^{29}$SiO, $^{30}$SiO, Si$^{18}$O, SiN, SiS, SiC$_2$

**Other Inorganic Molecules**: SO, PN, Na$^{37}$Cl(?)

**Hydrocarbon Chains**: *l*-C$_3$H, *l*-C$_3$H$^+$, C$_4$H

**Ring Species**: *c*-C$_3$H$_2$, *c*-H$^{13}$CCCH, *c*-HCC$^{13}$CH, *c*-H$_2$C$_3$O, *c*-H$_2$COCH$_2$

**Amines**: NH$_3$, NH$_2$D, CH$_3$NH$_2$(?), NH$_2$CN, CH$_3$CONH$_2$, H$_2$NCO$^+$(?)

**Isonitriles**: CH$_3$NC, HCCNC

**Nitriles**: CCCN, HSCN, NaCN/NaNC, CH$_2$CN, CH$_3$CN, CH$_3^{13}$CN, $^{13}$CH$_3$CN, CH$_2$CHCN, CH$_3$CH$_2$CN, HC$_3$N, HCC$^{13}$CN, HC$^{13}$CCN, H$^{13}$CCCN, HC$_5$N, CH$_3$C$_3$N

**Imines**: CH$_2$NH, *E*-CH$_3$CHNH, *Z*-CH$_3$CHNH, HNCHCN

**Aldehydes**: H$_2$CO, H$_2$COH$^+$, CH$_3$CHO, NH$_2$CHO, NH$_2^{13}$CHO, CH$_3$OCHO, *cis*-CH$_2$OHCHO, *t*-CH$_2$CHCHO, CH$_3$CH$_2$CHO

**Alcohols**: CH$_3$OH, $^{13}$CH$_3$OH, *t*-CH$_3$CH$_2$OH, *g'Ga*-(CH$_2$OH)$_2$

**Other Oxynated Species**: HNCO, *t*-HCOOH, H$_2$CCO, CH$_3$OCH$_3$, (CH$_3$)$_2$CO

**Other Organic Species**: CH$_3$SH

The molecular inventory of the gas includes that reported in the more extended envelope of Sgr B2 and in the north cloud, an extended cloud of material that peaks 1 arcmin north of the Sgr B2(N) core (Jones et al. 2008, 2011). In a survey conducted with the Mopra telescope over the same frequency range on a 6 arcmin × 6 arcmin field of view, the species CS, HCS$^+$, CCS, OCS, SiO, SO, HNCO, HOCO$^+$, HC$_3$N, HC$_5$N, CH$_3$OH, CH$_3$CN, CH$_3$CHO, NH$_2$CHO, CH$_2$CN, and CH$_2$NH were detected in extended material around the North and Main cores (Jones et al. 2011). All of these molecules except HOCO$^+$ were detected in the significantly more sensitive ATCA survey, along with an additional $\sim$40 molecular species. We note that the depletion of HOCO$^+$ in the absorbing material is curious and refrain from further interpreting this. In a 3-mm suvey conducted with Mopra over a similar field of view as the 7 mm survey, multiple other species detected here were observed to have an extended distribution, including NH$_2$CN, CH$_3$OCH$_3$, CH$_3$OCHO, *t*-CH$_3$CH$_2$OH, *c*-C$_3$H$_2$, CH$_2$CHCN, CH$_3$CH$_2$CN, H$_2$CO, H$_2$CS, H$_2$COH$^+$, and CH$_3$SH (Jones et al. 2008).

Towards all three regions, molecular lines were primarily detected at two velocity components separated by $\sim$20 km s$^{-1}$. Figure 12 shows a histogram of the 25th - 90th percentile Gaussian fit parameters of identified molecular lines, and Table 8 presents the mean fit parameters, characterising the kinematic structure of molecular gas towards these positions. K6 and K4 have velocity components centered at 64 and 82 km s$^{-1}$ and 62 and 82 km s$^{-1}$ respectively, whereas L has velocity components at 56 and 76 km s$^{-1}$. While we do not include a full characterisation of the spectra towards the LMH and "h", the spectra of these sources show that line emission from the LMH hot core is at $\sim$64 km s$^{-1}$ and emission from "h" is at 73 km s$^{-1}$, in agreement with previous observations (Hollis et al. 2003; Belloche et al. 2013). Towards K6, L, and K4, both primary velocity components have median line widths $>10$ km s$^{-1}$, indicating highly supersonic turbulence.

A larger number of transitions are detected in the low velocity component gas towards all three regions, and the low velocity component has a higher total integrated line intensity in the detected transitions. Towards K6, the total integrated flux absorbed by the 64 km s$^{-1}$ component is a factor of 3.5 times greater than the total flux absorbed by the 82 km s$^{-1}$ component. Towards L and K4, the low and high velocity components typically have more similar line intensities, with total integrated flux ratios of $\frac{\int (T_L)|_{Low}}{\int (T_L)|_{High}} = 1.7$ and 1.1 respectively. A larger number of distinct molecules were detected towards the low velocity component gas in K6 than towards any other position or velocity component.

While nearly all molecular lines appear in absorption, a few species exhibit weakly masing transitions that appear in emission. Previous work has demonstrated that the unusual environment in the Galactic Center produces unique excitation conditions (Menten 2004). For some large molecules, the conditions cause inversion of the energy levels in some low-$J$ lines and anti-inversion in others, leading to weak maser emission in the first scenario and enhanced absorption in the latter (see §1.2. of Menten 2004 and references therein). In the spectra towards K6 and K4, two transitions of CH$_2$NH are detected, including the $1_{11} - 2_{02}$ transition in absorption and the weakly masing $3_{03} - 2_{12}$ transition in emission. Both transitions are detected both in the high and low velocity gas components towards K6, with similar morphologies over the K5 and K6 shells (Steber et al. in prep). The maser emission is detected in the low velocity gas towards K4 as well. Additionally, the $3_{12} - 3_{03}$ transition of *t*-CH$_3$CH$_2$OH is weakly masing in the high velocity gas component (at 82 km s$^{-1}$) towards K6 and K4, and H$_2$COH$^+$ $3_{03}$-$2_{12}$ appears in emission towards K4. Finally, the $1_{01} - 0_{00}$ transition of H$_2$CS may show weak masing at an offset velocity in the low velocity gas in K4 (see Figure 13c), but further investigation would be required to confirm this. No maser emission is detected towards L.

With the exception of ammonia inversion transitions, methanol masing transitions, one transition of $H_2CO$, and three transitions of $c$-$C_3H_2$, all detected molecular transitions have lower state energies below 20 K, with most being below 10 K. For many of the detected molecules, the highest quantum line strength transitions that fall in the 30-50 GHz range are between low energy states; however, a number of stronger lines between higher energy states (40 - 80 K) are missing. The gas is therefore rotationally cold. Given the typical temperatures of molecular gas in the Galactic Center (> 80 K) (Ao et al. 2013, Martín et al. 2008 and references therein) and the observed supersonic turbulence, excitation temperatures of $T_{Ex}$ ∼10 K are highly subthermal. This result agrees with the conclusions of Hüttemeister et al. (1995), which determined that $T_{Ex} < 20$ K $\ll T_{kin}$ in the absorbing gas components, and with multiple recent characterisations of species detected in absorption in Sgr B2(N), which have determined that $T_{Ex} \sim 9$ K (Loomis et al. 2013; Zaleski et al. 2013; McGuire et al. 2013).

Additionally, ammonia inversion transitions with lower state energies ranging from 1200 - 3500 K are detected in both velocity components towards K6, L, and K4. Most of these transitions have been reported toward Sgr B2(N) previously with single dish observations (Hüttemeister et al. 1995; Flower, Pineau des Forets & Walmsley 1995). Although ammonia inversion lines are useful diagnostics of gas temperature (Ho & Townes 1983; Walmsley & Ungerechts 1983) the very high energy transitions do not likely indicate the kinetic temperature of the molecular gas, as the energy states may be populated due to formation pumping (Lis et al. 2012; E. Bergin, private communication). In work on Sgr B2 using Herschel data from the HEXOS program, Lis et al. (2012) proposed that $H_3O^+$ and $NH_3$, which have homologous structures with inversion transitions between metastable energy states, may be excited to very high energy levels by excess energy available from formation in the presence of X-ray radiation. While they favor an X-ray dominated environment for producing observed abundance ratios of $H_3O^+$ and $H_2O$, they do not rule out cosmic ray or shock driven chemistry. Regardless of the exact scenario, the high energy ammonia transitions can only be explained with significant energy available in the gas (via X-rays, CRs, or shocks). As such, the ATCA data are decidedly not probing cold material in the two primary velocity components towards K6, K4, and L, providing additional evidence that the gas is extremely subthermally excited.

The presence of two velocity components at multiple positions across the field, the spatial extent of the absorbing gas over the full continuum structure (Figure 3a), the similar excitation conditions across the spatial field, and the similarity with the molecular inventory observed in more extended material by Jones et al. (2011, 2008) suggests we may be peering through two extended sheets of gas, perhaps with a kinematic gradient across the field. Previous work has suggested that absorbing gas at ∼65 and 82 $\mathrm{km\,s^{-1}}$ is associated with the extended envelope of Sgr B2 (Hüttemeister et al. 1995) and is not internal to the core. If the components are located in the envelope, they would be anywhere from 3 - 10 pc from the cores (Hüttemeister et al. 1995), a distance that is significantly larger than the projected distance between the cores, as L and K6 are separated by ∼ 1.3 pc and K4 and K6 are separated by 0.4 pc in the plane of the sky. In this scenario, the extended molecular gas components need not interact directly with the local structure of the core (including expanding HII regions), and it is unclear whether the higher or lower velocity component is closer to the star forming core.

### 5.1.1 *Normalised Spectral Line Ratios: Determining Chemical or Excitation Differences In Absorbing Gas*

To determine if the system consists of two extended clouds or if each kinematic component towards each region should be treated as a separate cloud (in which case we would be probing 3 spatial regions × 2 velocity components = 6 clouds), we inspect the line radiation in each component. If the gas is located in the envelope with significant distance between the cores and the absorbing gas, we expect the gas phase molecular abundances and excitation to be fairly self-consistent in low velocity gas across the spatial field and in high velocity gas across the field. The low velocity gas could be quite distinct from the high velocity gas however, as they are clearly separate clouds.

If two components of gas have identical gas phase abundances and excitation, then the line optical depth ratios of the two gas components should be equivalent for any two lines, such that

$$\left(\frac{\tau_{C2}}{\tau_{C1}}\right)_A = \left(\frac{\tau_{C2}}{\tau_{C1}}\right)_B \pm \text{Error} \tag{1}$$

for two gas components C1 and C2 and for spectral lines A and B. The optical depth of an absorption line is related to the measured line and continuum brightness levels by

$$\tau = -ln\left(1+\frac{T_L}{T_C-[f(T_{Ex})-f(T_{CMB})]}\right); f(T)=\frac{h\nu/k}{e^{h\nu/kT}-1} \tag{2}$$

$$\tau \approx \frac{-T_L}{T_C-[f(T_{Ex})-f(T_{CMB})]} \tag{3}$$

$$\tau \approx \frac{-T_L}{T_C} \tag{4}$$

Equation 2 provides the general equation for absorption line optical depth, while Equation 3 is appropriate for optically thin lines, and Equation 4 is appropriate for optically thin lines when the continuum temperature dominates the excitation and cosmic microwave background temperatures. Towards K6, due to the strong continuum and low excitation temperature, Equation 4 is appropriate for optically thin lines. It follows that the line-to-continuum ratio can be read as the optical depth towards K6. The continuum is somewhat weaker towards L and K4, and as a result, the excitation temperature may contribute non-trivially to the denominator in Equation 3 resulting in a factor offset compared to Equation 4. While the factor varies with frequency for a frequency-dependent continuum temperature, the change is small with frequency in the range of 30-44 GHz. For optically thin lines in all cases therefore, Equation 1 can be rewritten as

$$\left(\frac{(T_L/T_C)_{C2}}{(T_L/T_C)_{C1}}\right)_A = \left(\frac{(T_L/T_C)_{C2}}{(T_L/T_C)_{C1}}\right)_B \pm \text{Error.} \tag{5}$$

We refer to the quantity on the left as the normalised line ratio (NLR) of spectral line A with respect to C1 and use the line height generated by the automated line fitter for $T_L$. In the range of 29.8 to 44.6 GHz, we determine the continuum levels using the continuum images with central frequencies of 33.4 and 40.8 GHz and 7.5 GHz bandwidths. From the two images, we derived a power-law fit to the continuum strength towards K6 and linear fits to the continuum ratios $\frac{(T_C)}{(T_C)_{K6}}$ for L and K4. We estimate that uncertainty in the continuum ratios contributes 10% error to an NLR.

Figure 13 shows the profiles of selected transitions of $CH_3CHO$, $CH_3CH_2CN$, $CH_2NH$, and $H_2CS$. Inspecting the profiles towards K6 (Figure 13a), it is clear that the low (64 $\mathrm{km\,s^{-1}}$) and high (82 $\mathrm{km\,s^{-1}}$) velocity components do not show identical gas phase abundances and excitation. The line profiles of $CH_3CHO$ and $CH_3CH_2CN$ appear quite similar, with the peak line strengths in the high velocity gas being $\sim 25\%$ that in the low velocity gas. In terms of Equation 5,

$$\mathrm{NLR}_{CH_3CHO} \approx \mathrm{NLR}_{CH_3CH_2CN} \approx 0.25$$

for the high velocity gas with respect to the low velocity gas for the two specific transitions. However, the NLR is clearly much higher, at $\sim$70%, for the transition of $CH_2NH$ and much lower for $H_2CS$. If the line profiles of $CH_3CHO$ and $CH_3CH_2CN$ are typical towards K6, we can therefore say that the high velocity component towards K6 (K6: 82 $\mathrm{km\,s^{-1}}$) is enhanced in $CH_2NH$ $1_{11} - 2_{02}$ and depleted in $H_2CS$ $1_{01} - 0_{00}$ relative to the low velocity gas in K6 (K6: 64 $\mathrm{km\,s^{-1}}$). Towards K6, it follows that significant differences in gas phase abundances and/or excitation exist in the two gas clouds. As the low and high velocity clouds are obviously distinct bodies, this result is not suprising.

More interestingly, the line profiles towards L and K4 look very distinct compared to those in K6. We first compare only the low velocity gas in all three regions. In the $CH_3CHO$ line, the NLRs with respect to K6: 64 $\mathrm{km\,s^{-1}}$are 50% for the low velocity gas in both L and K4 (L: 56 $\mathrm{km\,s^{-1}}$ and K4: 62 $\mathrm{km\,s^{-1}}$, respectively). In the line of $CH_3CH_2CN$, however, absorption by L: 56 $\mathrm{km\,s^{-1}}$ and K4: 62 $\mathrm{km\,s^{-1}}$ is considerably weaker, at $\sim$25 and 30%, respectively. Whereas the low velocity component absorption by $CH_2NH$ is weak in L: 56 $\mathrm{km\,s^{-1}}$ (at $\sim$22% the strength observed in K6), it is very strong in K4. On the other hand, the line of $H_2CS$ is strong in the low velocity gas towards L: 56 $\mathrm{km\,s^{-1}}$ (at $\sim$ 75% the strength observed in K6), and weak in K4: 62 $\mathrm{km\,s^{-1}}$ (at $\sim$25% the strength observed in K6). From these four lines alone, it is very clear that differences in excitation and/or gas phase molecular abundances exist on small angular scales of $<$10 arcsec.

Comparing the high velocity gas in the three regions produces a similar result. With respect to K6: 82 $\mathrm{km\,s^{-1}}$, the high velocity components in L and K4 have 40 and 80% deeper line absorption by $CH_3CHO$. In the $CH_3CH_2CN$ line, K6: 82 $\mathrm{km\,s^{-1}}$ and L: 76 $\mathrm{km\,s^{-1}}$ have similar line strengths, while the high velocity gas in K4 (K4: 82 $\mathrm{km\,s^{-1}}$) shows significant enhancement. L: 76 $\mathrm{km\,s^{-1}}$ and K4: 82 $\mathrm{km\,s^{-1}}$ have lower line strengths of $CH_2NH$ $1_{11}$-$2_{02}$, and while $H_2CS$ is undetected in K6: 82 $\mathrm{km\,s^{-1}}$, it is observed towards L: 76 $\mathrm{km\,s^{-1}}$ and K4: 82 $\mathrm{km\,s^{-1}}$ . This result does not support the hypothesis that the high velocity gas is an extended cloud located in the envelope of Sgr B2.

Utilizing the bandwidth offered by the survey, we compute the NLRs of unblended, confidently assigned absorption lines from multiple distinct molecular families in the segment of the spectrum extracted from high spatial resolution data (from 29.8 - 44.6 GHz). Figure 14 provides NLR values with respect to K6: 64 $\mathrm{km\,s^{-1}}$ for spectral lines in each velocity component of each spatial region, plotted against the line-to-continuum ratios of the lines in K6: 64 $\mathrm{km\,s^{-1}}$. As follows from Equations 2 - 4, the abscissa provides a proxy for the line optical depth in K6: 64 $\mathrm{km\,s^{-1}}$, while the ordinate is proportional to the line optical depth ratio with respect to K6: 64 $\mathrm{km\,s^{-1}}$ in the indicated gas component. The median NLR is shown by the dashed line with $\pm 3\sigma$ errors shaded around the median. The shaded errors are estimated by 12.5% error on each line height added in quadrature with 10% error introduced by uncertainty in the continuum ratios, resulting in a $\sim$20% total $1\sigma$ error. Finally, we note that the apparent slope at the low optical depth side relates to the detection limit in the spectra. Because K6: 64 $\mathrm{km\,s^{-1}}$ has the strongest continuum level, making the spectrum towrads K6 more sensitive to low optical depth lines and also typically has the highest optical depth, lines that are weakly detected towards K6: 64 $\mathrm{km\,s^{-1}}$ are only detected towards other components if they have enhanced line optical depths compared to the median. This does not imply that these points are unreliable, but implies that the lower left corners of the plot cannot be filled in.

We consider the line radiation with respect to the median ratio, as differences in the median NLR (such that median $\neq 1$) do not necessarily indicate differences in the relative chemical abundances or excitation. Instead the median NLR may correspond to the relative optical depth of molecular gas, and it also holds the factor offset introduced by $[f(T_{Ex}) - f(T_{CMB})]$ in Equation 3 towards L and K4. However, statistically significant differences with respect to the median NLR indicate either (1) excitation differences, with distinct excitation of some molecules, or (2) chemical differences, with different relative gas phase molecular abundances present in distinct gas components. If statistically significant scatter is observed in lines of a single molecule (e.g. differences in the NLR of different lines of $CH_3CHO$), excitation differences are implicated. Although low excitation conditions are common in the gas components discussed here, differences in the excitation conditions can impact the excitation of different K-states, and weak masing effects may selectively enhance or deplete the populations of certain states (Menten 2004; Faure, Remijan & Szalewicz 2014). Where line excitation is not implicated, the differences are attributable to chemical abundance differences.

**Trends in Figure 14:** Transitions that appear to vary the most between different panels of Figure 14 include $CH_2NH$ $1_{11} - 2_{02}$, CCS $3_2 - 2_1$, $HCS^+$ J = (1-0), $H_2CS$ $1_{01} - 0_{00}$, and weaker transitions of large aldehyde and O-bearing species. Of these species, $CH_2NH$ is known to be weakly masing at 1 GHz (Godfrey et al. 1973) and is masing in this survey as well; $H_2CS$ has been reported to exhibit non-thermal behavior at cm wavelengths (Sinclair 1973); and transitions of the O-bearing species *t*-$CH_3CH_2OH$ and $H_2COH^+$ exhibit weak masing in this work. While the lines included in Figure 14 appear in absorption and are therefore not themselves masing, the energy state populations may be very sensitive to the physical conditions. Significant effort will be required to determine the excitation conditions responsible for the observed line strengths, providing powerful constraints on the physical conditions in the gas.

While aware of the presence of non-LTE excitation in these lines, we expect that a few of the trends indicate true gas phase relative abundance differences. In this discussion, relative abundance differences are relative to the median abundance ratio of molecules sampled in two components of gas. In most panels, transitions of $CH_3CH_2CN$ appear consistently below the median value, indicating that K6: 64 $\mathrm{km\,s^{-1}}$ likely has a high gas phase abundance of the species compared to other gas components. Similarly, K6: 64 $\mathrm{km\,s^{-1}}$ likely has enhanced relative abundances of most S-bearing species, with only L: 56 $\mathrm{km\,s^{-1}}$ having NLR values that are similar to the median. As many of the O-bearing species have multiple lines with high NLRs, we expect that these do reflect true abundance differences.

We expected to observe similarity between the low velocity gas towards all three regions and the high velocity gas in the regions, with a distinction apparent between the two sets of spectra. Instead a different trend is present. K6: 64 $\mathrm{km\,s^{-1}}$, L: 56 $\mathrm{km\,s^{-1}}$, and L: 76 $\mathrm{km\,s^{-1}}$ exhibit very similar excitation. This can be seen by inspecting transitions of $CH_3CHO$, $NH_2CHO$, and $CH_2CHCN$ in particular. Each of these three molecules has multiple transitions sampled in Figure 14, and for each of these species, the NLR values of all transitions show little variation. On the other hand, K6: 82 $\mathrm{km\,s^{-1}}$, K4: 62 $\mathrm{km\,s^{-1}}$, and K4: 82 $\mathrm{km\,s^{-1}}$ show a different pattern of excitation and are more similar to each other than they are to the first set of components. Evidence for this follows from the significant amount of scatter observed in lines of $CH_3CHO$ (K6: 82 km s$^{-1}$), $NH_2CHO$ (K6: 82 km s$^{-1}$ and K4: 62 km s$^{-1}$), $CH_2CHCN$ (K4: 82 km s$^{-1}$), $CH_3CH_2CN$ (K4: 62 km s$^{-1}$), $HC_5N$ (K4: 62 km s$^{-1}$ and K4: 82 km s$^{-1}$), and *cis*-$CH_2OHCHO$ (K4: 62 km s$^{-1}$).

In the first set of components, all lines of $NH_2CHO$ and $CH_3CHO$, and most transitions of small molecules are consistent with the median NLRs, although $NH_3$ transitions show some variability. Observed lines of the S-bearing molecules SO, $HCS^+$ and $H_2CS$ are comparatively depleted in L: 76 km s$^{-1}$. Lines of $CH_3CH_2CN$ are depleted in both L: 56 km s$^{-1}$ and L: 76 km s$^{-1}$ relative to K6: 64 km s$^{-1}$, and lines of $CH_2CHCN$ may be slightly depleted in L: 76. km s$^{-1}$. On the other hand, multiple lines of O-bearing species, including *c*-$H_2C_3O$ (L: 56 km s$^{-1}$ and L: 76 km s$^{-1}$), $H_2COH^+$ (L: 76 km s$^{-1}$), $CH_3OCHO$ (L: 56 km s$^{-1}$), and *t*-$CH_3CH_2OH$ (L: 56 km s$^{-1}$), are enhanced in both components in L. While further analysis is required, this likely indicates higher gas phase abundances of the specified O-bearing species, particularly where multiple lines consistently demonstrate enhancement (i.e. for *c*-$H_2C_3O$ and *t*-$CH_3CH_2OH$ in L: 56 km s$^{-1}$). Particularly because no maser emission is detected at either component towards L, we do not anticipate that the energy state populations are significantly enhanced or depleted by these processes, further supporting the interpretation of the results as indicating true differences in relative abundances.

In the second set of components, inclduing K6: 82 km s$^{-1}$, K4: 62 km s$^{-1}$, and K4: 82 km s$^{-1}$, we note low line ratios for some S-bearing species including $H_2CS$, CCS (K6: 82 km s$^{-1}$ and K4: 62 km s$^{-1}$), and $HCS^+$ (K6: 82 km s$^{-1}$). Additionally, $CH_3CH_2CN$ lines are lower than the median NLR towards K6: 82 km s$^{-1}$ and SiO isotopologues have somewhat low values. Towards all three regions, multiple O-bearing species exhibit high NLRs. In K6: 82 km s$^{-1}$, $H_2COH^+$, *cis*-$CH_2OHCHO$, *t*-$CH_2CHCHO$, *t*-$CH_3CH_2OH$, and the nitrile species $C_3N$, exhibit enhanced line radiation relative to the median. In K4: 62 km s$^{-1}$, *cis*-$CH_2OHCHO$ and $H_2COH^+$ have high NLRs, and in K4: 82 km s$^{-1}$, lines of $H_2CCO$ and *c*-$H_2C_3O$ have high NLRs. With respect to one another, K6: 82 km s$^{-1}$ and K4: 82 km s$^{-1}$ exhibit similar excitation (evidenced by NLR values for molecules with multiple line transitions), but very different line strengths for some S-bearing species. With respect to one another, they also show differences in the relative abundances of some aldehyde and nitrile species, with NLR values that are consistently offset from the median. They additionally show differences in which weak O-bearing transitions are detected, possibly indicating relative abundance differences. K4: 64 km s$^{-1}$ has a very similar molecular inventory to that of K6: 82 km s$^{-1}$, but the excitation is somewhat distinct. Besides the relative depletion of SiO isotopologues in K6: 82 km s$^{-1}$, the relative abundances are quite consistent with those in K6: 64 km s$^{-1}$, indicating that these two regions have similar chemical conditions.

As is clear from this discussion and in agreement with the above discussion of Figure 13, Figure 14 reveals statistically significant differences from the median values for both velocity components towards all three regions. In fact, by comparing the panels to one another, it is apparent that no two components have consistent line radiation, revealing variability in excitation and relative abundances on small spatial scales. As a result, the gas phase molecular abundances and excitation of the 3 spatial regions × 2 velocity components should be treated separately. This does not imply that each of the 6 clouds is an entirely, localized body, but that sufficient variability is observed so that signals from different positions cannot be combined, particularly for transitions that exhibit greater degrees of variability.

**Implications for the Structure of Sgr B2:** If the structure of Sgr B2 included two clouds in the envelope that are extended over the continuum structure, we would observe that the molecular abundance ratios and excitation should be self consistent in the low velocity material and in the high velocity material. The low velocity material could show a very distinct pattern from the high velocity gas however. If this were the case, the panels corresponding to low velocity material in Figure 14 (panels b and d) should have very few points outside of the shaded $3\sigma$ errors. While the high velocity material (panels a, c, and e) could have points outside of this, the same points should appear outside of the shaded region in all three panels. As is evident from Figures 14 and from the discussion above, this is not observed. The differences in line radiation thus indicate that we cannot adopt the most simple treatment of the molecular material, namely as two extended sheets of gas that are not interacting directly with the structure of the core. Instead, we observe significant variation on size scales of <30 arcsec, indicating that both the low velocity component and the high velocity component are likely located proximate to the star forming core and are not envelope components.

As K6: 64 km s$^{-1}$ and K4: 62 km s$^{-1}$ components, separated by <10 arcsec, show a great deal of differentiation, it does not appear likely that the low velocity gas is located in the extended envelope, removed from the immediate mechanical and radiative environment of the HII regions and embedded sources. The low velocity gas, varying in both excitation and in relative molecular abundance values towards the regions, is instead likely located proximate to the HII regions. The low velocity gas towards K6 and K4 may be part of the same structure, however we argue that the gas is located close to the core and is therefore responding to localised conditions. Other work has provided evidence that the molecular material is indeed part of an extended structure, as material has been observed at a similar velocity in the foreground of Sgr B2(M), ∼50 arcsec south of K6 (Hüttemeister et al. 1995, and references therein). The low velocity cloud may be an extended structure ($\gtrsim$ 1 arcmin) located in the immediate viscinity of the cores, creating locally variable gas phase abundances and excitation due to radiative and/or mechanical interactions with HII regions. While Figure 14 demonstrates similarity in excitation between K6: 64 km s$^{-1}$ and L: 56 km s$^{-1}$, the ATCA data cannot provide direct observational evidence that the L: 56 km s$^{-1}$ gas is part of the same structure as K6: 64 km s$^{-1}$. Other work has provided some evidence that they are, however (see e.g. Sato et al. 2000, and references therein)

While K6: 82 km s$^{-1}$ and K4: 82 km s$^{-1}$ are more similar to one another, differences nontheless persist. The chemistry and excitation may be localised to a lesser degree than the low velocity gas. While this gas does not appear to be located in the extended envelope, it may be located further from the cores than the low velocity gas in Sgr B2(N). As L: 76 km s$^{-1}$ shows a distinct pattern of excitation and gas phase abundance, it is not clear from our observations that it is related to the high velocity gas observed towards K6 and K4. However, the work of Hasegawa et al. (1994) and Sato et al. (2000) provides evidence connecting the gas clouds, indicating that the high velocity material may also be part of an extended structure (> 40 arcsec). It is plausible however that a very clumpy structure in the envelope, as proposed by Goicoechea, Rodríguez-Fernández & Cernicharo (2003), could account for the differences between the high velocity gas in K6 and K4 while allowing the gas to be located in the envelope.

If we adopt this structure, in which the low velocity material is located closest to the HII regions, then the expanding K6 ionization shell would interact mechanically and radiatively with the 64 $\mathrm{km\,s^{-1}}$ molecular gas given the HII region kinematics compiles in Tables 5 and 6, driving shocks into the system and contributing near-UV radiation to generate a PDR. These conditions could produce the more highly varying line ratios for molecules towards K6. Towards L, the low velocity molecular material would not be expected to mechanically interact with the HII regions given the recombination line kinematics measured in §4.1, although it very likely sets the radiative environment.

Furthermore, if the high velocity components are indeed further from the HII regions than the low velocity components, we may be directly observing the colliding molecular clouds that are triggering star formation in Sgr B2, consistent with the scenario first proposed by Hasegawa et al. (1994). In this scenario, an extended high velocity cloud (at $75 < v_{LSR} < 90$ $\mathrm{km\,s^{-1}}$) collides with the body of Sgr B2 (at $40 < v_{LSR} < 50$ $\mathrm{km\,s^{-1}}$), generating star formation in processed material at an intermediate velocity of $55 < v_{LSR} < 70$ $\mathrm{km\,s^{-1}}$. The observed 2-component molecular gas thus may be a direct observation of remaining material in the high velocity cloud continuing to collide with the processed cloud, a process that may trigger yet more star formation. This scenario is consistent with the observation of molecular line material at ∼65 $\mathrm{km\,s^{-1}}$ towards Sgr B2(M) (Hüttemeister et al. 1995). However, significant pieces of evidence for this scenario remain missing. For example, there should be observational signatures of a shock at the interface of the colliding gas clouds at a velocity intermediate to the high and low velocity gas components. While the line profile of $^{28}$SiO is wing-broadened, the optically thin isotopologues of SiO do not show such a signature. Additionally, to elucidate the interaction between the HII region and the low velocity component molecular gas, high spatial and spectral resolution observations of CI, CII, NI, NII, and OI are required to provide information on the PDR at the surface of the HII region. Notably, however, carbon recombination lines are not observed in this material.

The evidence that the low velocity material is closer to the HII regions remains tenuous however, and additional evidence suggests the situation may be yet more complex. Recombination lines towards K6 have 2-component profiles centered at velocities of 60 and 84 $\mathrm{km\,s^{-1}}$, while molecular gas is observed at 64 and 82 $\mathrm{km\,s^{-1}}$. If the K6 shell is an expanding HII region that only interacts mechanically with the low velocity molecular gas, then it is a coincidence that the high velocity molecular gas is at nearly the same velocity as the far side of the expanding shell. Likewise, this scenario requires that the L: 56 $\mathrm{km\,s^{-1}}$ molecular gas component is more closely associated with the HII region (at 77 $\mathrm{km\,s^{-1}}$) than the L: 76 $\mathrm{km\,s^{-1}}$ molecular gas component. The velocity correspondence between the HII region and the L: 76 $\mathrm{km\,s^{-1}}$ molecular gas may be merely coincidental, however, a deeper look at structure is warranted.

### 5.2 Molecular Absorption by Clouds Along the Line-of-Sight to Sgr B2

The line profiles of ∼2 dozen molecular lines show absorption by additional velocity components associated with intervening clouds in the line-of-sight to Sgr B2 (Appendix B). These clouds have velocities of $v < 50\,\mathrm{km\,s^{-1}}$. Line-of-sight absorption by gas that is associated with (i.) spiral arm clouds or (ii.) material internal to the Galactic bar or Galactic Center is extensively reported in the literature (Greaves & Nyman 1996; Wirström et al. 2010; Gerin et al. 2010; Menten et al. 2011). The clouds are typically translucent (with $10^2 < n < 10^4$ $\mathrm{cm^{-3}}$ and $2 < A_V < 5$) and are highly interesting for understanding the environments and chemistry in regions that can only be studied through line-of-sight absorption techniques. To date, authors have reported primarily di- and triatomic molecules in the foreground of Sgr B2 and other Galactic sources. Furthermore, it is typically presumed that the absorbing gas is extended and homogenous over the field of view (Qin et al. 2010). The ATCA survey provides the first sub-10" resolution view of line-of-sight molecular absorption towards any region in the Galaxy.

Molecules detected in line-of-sight absorption components in this survey include CS, SiO, SO, $NH_3$, CCS, $HCS^+$, *c*-$C_3H_2$, *l*-$C_3H$, *l*-$C_3H^+$, $C_4H$, $CH_3OH$, $CH_3CN$, $HC_3N$, $CH_3CHO$, $NH_2CHO$, and *t*-$CH_3CH_2OH$(?), with a tentative detection marked with a (?). Turner, Terzieva & Herbst (1999) reported most of the complex organic molecules detected here in translucent clouds, however this is the first detection of most of the organic species in the line-of-sight to Sgr B2. Further, to our knowledge, this is the first reported detection of $NH_2CHO$ in translucent cloud material. $NH_2CHO$ is of interest as it is difficult to produce via the gas-phase chemical reaction networks believed to dominate translucent cloud chemistry (Turner 2000). The tentatively detected species *t*-$CH_3CH_2OH$ is also previously undetected in translucent material.

Towards K6, components at 6, -30, -73, and -106 $\mathrm{km\,s^{-1}}$ dominate the line-of-sight absorption spectra. Towards L, components at similar velocities of 35, 20, -5, -35, -75, and -106 $\mathrm{km\,s^{-1}}$ are detected. The absorption profiles vary between the two regions, with relative line strengths differing. Towards K4, only a single velocity component at ∼2 $\mathrm{km\,s^{-1}}$ was detected. The 2 $\mathrm{km\,s^{-1}}$ component has a highly enhanced optical depth towards K4 as compared to the 6 $\mathrm{km\,s^{-1}}$ gas towards K6 and the -5 $\mathrm{km\,s^{-1}}$ gas towards L. The data thus:

(i) reveal a greater molecular complexity in the line-of-sight absorbing gas towards Sgr B2(N) than previously known
(ii) indicate that the ∼0 $\mathrm{km\,s^{-1}}$ component observed towards Sgr B2 cannot be treated as homogenous in the plane of the sky over the field of view of a single dish telescope.

Additionally, the ∼2 $\mathrm{km\,s^{-1}}$ component is observed to produce maser emission by the Class I methanol maser at 36 GHz towards K6 and K4 (see Appendix B). Maser emission has not previously been associated with a line-of-sight absorption cloud, indicating that this component is likely quite distinct from other line-of-sight clouds. Previous authors have proposed that the ∼0 $\mathrm{km\,s^{-1}}$ component consists of ejecta of Sgr B2 (Wirström et al. 2010). Recently, however, a molecular gas component at ∼0 $\mathrm{km\,s^{-1}}$ has been observed to be widespread across the Galactic Center (Jones et al. 2012) and diffuse recombination line emission has been observed at a similar velocity throughout the Galactic Center (Royster & Yusef-Zadeh 2014).

### 5.3 Selected Molecular Distributions in Sgr B2

In this and the following subsection (§5.4), we confine our discussion to Sgr B2, ignoring the line-of-sight absorption components. Most transitions detected towards K6, L, and K4 exhibit spatial distributions similar to the absorption line distributions in Figure 3a. However, low energy transitions from a handful of detected molecules show simultaneous absorption towards the continuum and emission from one or both hot cores. Transitions of $NH_3$, $HCS^+$, $CH_3CN$, $CH_2CHCN$, $CH_3CH_2CN$, $HC_3N$, $NH_2CHO$, $CH_3OCHO$, and $CH_3OCH_3$ are prominent in absorption in the foreground of the HII regions and in emission from the LMH and usually "h" (notably, $NH_2CHO$ is not detected in "h"). Additionally, detected transitions of OCS, HNCO, and $NH_2D$ produce strong emission towards the LMH and "h" and very weak absorption against the radio continuum. The data also contain multiple instances in which molecules whose spatial distributions might be expected to be correlated exhibit very distinct morphologies.

The molecules SiO and HNCO are widely regarded as excellent shock tracers and therefore might be expected to exhibit similar spatial distributions. Enhanced gas phase abundances of SiO are achieved by grain sputtering upon passage of a shock (Schilke et al. 1997; Caselli, Hartquist & Havnes 1997; Pineau des Forets et al. 1997), and HNCO is observed to be enhanced in multiple regions that have known shocks (Rodriguez-Fernandez et al. 2010; Minh & Irvine 2006; Martín et al. 2008). The spatial distribution of HNCO has been observed to follow that of SiO in multiple sources via observations with single dish telescopes (Zinchenko, Henkel & Mao 2000). However, Figure 15 shows that the distributions of transitions between low-energy states of SiO and HNCO in the core of Sgr B2(N) are anti-correlated. The HNCO $2_{02}$-$1_{01}$ transition produces very strong line emission in both hot cores, whereas only very weak absorption is detected towards K6 (the absorption contour of HNCO is at 2.5% of the peak emission line strength). On the other hand, for the J = (1-0) transitions of all isotopologues of SiO, the images include absorption against the continuum structure and a negative "bowl" indicating extended emission that could not be recovered with the interferometer. No compact emission by SiO isotopologues is observed towards the "h" hot core. We note the presence of a weak emission feature on the high velocity wing of $^{28}$SiO eminating from the northwest edge of the LMH. Due to the line density towards the LMH and the absence of an emission feature on the low velocity wing, which would be more consistent with the velocity of the LMH, we cannot firmly identify the noted feature as an SiO line.

The distributions indicate chemical differentiation in Sgr B2(N). HNCO is highly abundant in the LMH and "h" hot cores and depleted in the molecular gas observed against the HII regions; on the other hand, even if the noted wing feature is from SiO, the species has a significantly lower column density in the LMH than in the absorbing gas. Any emission generated by SiO in the LMH is entirely overwhelmed by the absorbing gas components, including in the optically thin transitions of the isotopologues. Although the higher energy states ($100\ \mathrm{K} < E_L < 300\ \mathrm{K}$) of SiO should be preferentially populated in the LMH and "h", Neill et al. (2014) reported the non-detection of SiO in HEXOS data sampling SiO transitions with T >160 K. SiO thus appears to be depleted from the gas phase in the LMH and "h" hot cores, but highly abundant in molecular material in the low velocity (50 - 65 $\mathrm{km\,s^{-1}}$) and high velocity (70 - 85 $\mathrm{km\,s^{-1}}$) gas observed in absorption towards the HII regions, and in extended material around the core. A similar distribution of gas phase SiO has been observed in the source G34.26+0.15 (G34.26), which contains a hot core, UC HII regions, collimated outflows, and molecular gas interacting with stellar winds (Hatchell, Fuller & Millar 2001; Watt & Mundy 1999). Towards G34.26, SiO was observed to be widespread and highly abundant in the material interacting with stellar winds; it was not detected in the hot core, however (Hatchell, Fuller & Millar 2001).

The spatial distributions of transitions from species in the CS-family present yet another puzzle; whereas transitions of CS, CCS, CCCS, and $H_2CS$ are detected in the absorbing gas with no apparent emission from the hot cores, line radiation from the J = (3-2) transition of OCS shows a similar behavior to that of HNCO (Figure 16). Very weak line absorption by OCS (with the lowest contour at 4.5% of the peak emission) is detected towards K6 and K4, but nearly all of the OCS radiation is emission produced in the hot cores. OCS, like HNCO, is believed to form on grain mantles and has been linked to shock enhancement (Ren et al. 2011; Garozzo et al. 2010). Distinct from other CS-containing species, $HCS^+$ appears both in absorption against the continuum and in emission from the hot cores.

### 5.4 Physical Environment in the Absorbing Material: An Integrative View

The detection of SiO, CS, and other CS-bearing species and the depletion of HNCO and OCS in the absorbing molecular material provides insight into the physical environment in the absorbing gas. The strong absorption by SiO likely results from the presence of shocks and supersonic turbulence in the gas, although the enhancement of SiO may instead be attributed to the high X-ray flux in this X-ray reflection nebula (Martín-Pintado et al. 2000; Amo-Baladrón et al. 2009). Other CS-bearing species found in the absorbing gas, particularly CCS and CCCS may be formed by chemistry driven by the radical CH (Petrie 1996; Yamada, Osamura & Kaiser 2002; Sakai et al. 2007), and multiple larger radical species are directly detected in the spectra towards K6, L, and K4 (Appendix B). The presence of radicals typically indicates X-ray or UV irradiation typical of XDRs or PDRs (Danks, Federman & Lambert 1984; Boger & Sternberg 2005; Meijerink, Spaans & Israel 2007).

Further, the ratio of HNCO to CS may be an excellent diagnostic of the radiative environment. Using a limited sample of Galactic Center clouds, in which shocks are believed to be ubiquitous, Martín et al. (2008) demonstrated that the HNCO:CS abundance ratio is high ($\sim$70) in non-PDR shocked regions and an order of magnitude lower in PDRs. While both species can be photodissociated, CS is less easily destroyed by UV radiation and can be replenished by a gas phase reaction of $S^+$, an abundant ion in PDRs (Drdla, Knapp & van Dishoeck 1989; Sternberg & Dalgarno 1995; Martín et al. 2008). In the Horsehead Nebula, CS is observed to be nearly equally abundant in the PDR and in the dense UV-shielded core (Goicoechea et al. 2006). On the other hand, HNCO is believed to form efficiently on grain mantles (Hasegawa & Herbst 1993) and after being released into the gas phase, it is easily photodissociated by UV radiation (Martín et al. 2008; Roberge et al. 1991). While theoretical work contends that the HNCO:CS ratio is time-dependent and more indeterminate (Tideswell et al. 2010), the very high ratio of CS:HNCO in the absorbing gas provides evidence that this material has an enhanced UV radiation field. Like HNCO, OCS is believed to form on grains, and the species has been directly observed on ice grain mantles (Gibb et al. 2004; Garozzo et al. 2010; Palumbo et al. 2011; Ren et al. 2011). Gas phase OCS is destroyed by near-UV radiation with an even higher photodissociation rate than HNCO (Roberge et al. 1991; Sternberg & Dalgarno 1995; Sato et al. 1995). The nearly complete depletion OCS from the absorbing gas is further evidence for PDR conditions.

As Sgr B2 is known to have a strong and pervasive X-ray flux, it is possible that X-ray radiation instead of UV radiation could destroy HNCO and OCS in the absorbing material. Due to the extremely high densities of the LMH and "h" hot cores (Belloche et al. 2008, 2014), even X-ray radiation is well shielded. However, HNCO and OCS exhibit widespread distributions to the west of the core (Jones et al. 2008). In this material, we expect that the X-ray field is more typical of the bulk of material in Sgr B2. This expectation is consistent with the prevalence of the X-ray tracer CN in the material to the west of the core (Jones et al. 2008). The widespread distributions thus suggest that X-ray radiation is not responsible for destroying HNCO and OCS; as such, we interpret the ATCA distributions of CS, OCS, and HNCO as suggesting the presence of a strong UV radiation field in the absorbing gas.

Additional support for a strong UV radiation field in the absorbing material follows from the results of §5.1. First, the highly subthermal excitation indicates that the material is sub-critically dense, with densities typical of PDRs. Without an excitation analysis, it is possible to estimate an upper limit of $n \lesssim$ a few $\times\ 10^5\ \mathrm{cm}^{-3}$ using the critical densities of energy states that had undetected transitions in the 30 - 50 GHz range with high quantum line strengths. Hüttemeister et al. (1995) determined an upper limit to the density of the absorbing gas of $n < 10^4\ \mathrm{cm}^{-3}$ based on the fact that the $HC_3N$ J = (3-2) transition is in absorption instead of emission, and independently based on an analysis of the (1,1) through (6,6) $NH_3$ inversion transitions. However, the latter estimate may not hold if the $H_3O^+$ formation pumping excitation mechanism proposed in Lis et al. (2012) proves effective for $NH_3$. Densities of $10^3 < n < 10^5\ \mathrm{cm}^{-3}$ are typical of PDRs (Teilens et al. 1993; Hollenbach & Teilens 1997), and densities of $n \approx$ a few $\times\ 10^5\ \mathrm{cm}^{-3}$ are reasonable in the hot, supremely dense environment at the core of Sgr B2(N). In section §5.1, we determined that both absorbing gas components appear to be local to the star forming cores rather than in the extended envelope material, with the low velocity gas possibly closer to the interface of the HII regions. If the absorbing gas clouds are proximate to the HII regions, it is not only reasonable, but structurally required, that they are or contain PDRs.

Second, the species $l$-$C_3H^+$ is detected in the absorbing material, but not in the hot core. To date, $l$-$C_3H^+$ has only been firmly detected in the Horsehead Nebula, the Orion Bar, and Sgr B2(N), despite a deep search towards multiple hot cores, hot corinos, and dark clouds (Pety et al. 2012; McGuire et al. 2013, 2014). Additionally, the species was not detected in molecule-rich UV-shielded core in the Horsehead Nebula (Pety et al. 2012). The species is clearly associated with UV-irradiated gas, and its detection in the low and high velocity gas towards K6 supports the hypothesis that both gas components are PDR sources.

Finally, a few of the organic species detected in the absorbing clouds were recently reported to be highly abundant in a PDR environment (Gratier et al. 2013; Guzmán et al. 2014). $CH_3CN$, $HC_3N$, $H_2CCO$, and $CH_3CHO$ were observed in the Horsehead PDR with abundances enhanced by a factor of 1 - 30 as compared to abundances in the UV-shielded core in the Horsehead. While the species are known to be abundant in multiple distinct environments, their detection in the absorbing material in Sgr B2(N) is consistent with the absorbing material being a PDR.

The data and discussions in this work thus support a structure in which molecular gas at $50 < v_{LSR} < 70\ \mathrm{km\,s}^{-1}$ is located on the interface of the HII regions at the core of Sgr B2. This gas component is UV-irradiated by the O-stars that power the HII regions, and may mechanically interact with the HII region, particularly towards K6 where the shell-shaped HII region is thought to be expanding. The high velocity cloud ($70 < v_{LSR} < 85\ \mathrm{km\,s}^{-1}$) is also close to the core, although it may not be as deeply embedded as the low velocity material. It may be actively colliding with the low velocity cloud consistent with a cloud-cloud collision scenario (Hasegawa et al. 1994), although additional evidence is required to verify this. Based on the detection of $l$-$C_3H^+$ and the nearly complete depletion of OCS and HNCO, it appears that both absorbing clouds are PDRs. This hypothesis should be further tested via comparison to high spatial and, ideally, high spectral resolution observations of neutral and ionized carbon, sulfur and oxygen.

However, merely calling the gas clouds PDRs is an oversimplification. The clouds contain supersonic turbulence requiring shocks, have a high X-ray flux, and likely have an enhanced cosmic ray flux as compared to most Galactic sources. It is quite possible that a different factor drives the chemistry of different groups of species; for instance, the strong X-ray flux may produce radicals that drive the chemistry of imine molecules (with an X=N–H group), whereas UV radiation may drive the sulfur and carbon-chain chemistry and selectively destroy certain molecules. Meanwhile, shocks may liberate silicon-bearing species and dust mantle species to be processed in the soup of ionic, atomic, and molecular gas.

Regardless of the physical parameters driving the formation of each species, the extracted spectra suggest that a multitude of organic molecules, including nitriles, aldehydes, alcohols, and imines, either form or persist in the presence of UV irradiation, X-ray radiation, and shocks. While we expect that some of the observed species will not prove ubiquitous in more typical Galactic PDRs, all of the detected species can at least survive moderate UV radiation fields and are promising targets for exploring the chemical complexity in PDRs.

## 6 CONCLUSIONS

We completed a 7 mm spectral line survey of Sgr B2(N) with the ATCA. The data provide:

(i) the largest catalog of radio recombination lines observed with an interferometer

(ii) the 30 - 50 GHz spectrum of the most line-rich interstellar source in the Galaxy, namely the LMH hot core

(iii) a comprehensive picture of the chemistry, excitation, and kinematic structure of clouds of molecular gas in Sgr B2

(iv) new insight into the chemistry and structure of "diffuse" clouds observed in the line-of-sight towards Sgr B2.

Continuum images and continuum-subtracted spectral line data cubes are available at at http://cdsarc.u-strasbg.fr/viz-bin/qcat?J/MNRAS/. Spectra extracted from five positions, including the LMH and "h" hot cores and three HII regions are made available in the online journal and at https://github.com/jfc2113/MicrowaveLineFitter. Upon extraction from the data cubes, the spectra have had a primary beam correction and a baseline correction applied (Figure 2).

In this work, we developed and applied PYTHON scripts to fit the line emision and absorption in 1-d spectra extracted from the data cubes at the positions of three HII regions in Sgr B2. The code provides a purely empirical output rather than comparing with a model, as this was deemed most appropriate at centimeter wavelengths where line radiation is often nonthermal. The code then compares with output generated by Splatalogue or another line catalog after minor formatting. The code is described in §3, released in Appendix A, and available at the same locations as the extracted spectra.

The code was applied to spectra extracted from three unique spatial positions, namely K6, L, and K4, characterised by recombination line emission and molecular line absorption at multiple velocity components. The performance of the code was evaluated based on the handling of 65 recombination line profiles and 90 molecular absorption lines, observed against the free-free radio continuum emission. Typical errors on the fits were significantly lower than the channel width in this survey. Approximate errors are summarized in Table 7.

Using the output of the line-fitting script, the molecular inventories of two primary velocity components of absorbing gas were determined and the approximate excitation conditions were characterised, showing that the gas clouds that give rise to the absorption are highly subthermally excited ($T_{Ex} \sim 10$ K $\ll T_{kin}$). Line radiation was then inspected using the relative line strengths in different gas components to determine whether the molecular line radiation is self-consistent at distinct spatial positions (Figure 14). This methodology can determine the chemical similarity between clouds at different spatial positions or velocities under conditions of similar excitation conditions, and the method could be quantified to further establish the degree of similarity. In the era of broadband spectral line observing, the method could be highly useful for quickly determining if observed clouds are chemically distinct and demonstrating relative enhancement of different families of molecules. The application of this method toward a variety of sources is necessary to determine its utility.

We applied the method to the ATCA data in order to test whether the molecular gas radiation is consistent with an extended distribution that is not interacting with the local structure of the core, as would be expected if the absorbing gas is in the envelope. We determined that in both primary velocity components, the three spatial regions show statistically significant differences in their line radiation, indicating differences in either line excitation or gas-phase molecular abundances. Many of the differences appear to be due to relative gas-phase abundance differences. The molecular gas in the low velocity component proved more highly variable, indicating that it may be subjected to more localized conditions and therefore located deeper within the star-forming core. It may be on the interface of the HII regions, potentially interacting mechanically and radiatively with the structure of the HII regions. In agreement with cloud-cloud collision scenarios, the 82 $\mathrm{km\,s^{-1}}$ gas is likely located further from the core. However, required pieces of observational evidence for the proposed structure remain unavailable, particularly high spatial (few arcsec resolution) and spectral (10 - 25 $\mathrm{km\,s^{-1}}$) resolution images of atomic and ionic lines of carbon, oxygen, and sulfur.

Additionally, the chemistry observed in translucent clouds in the line-of-sight to Sgr B2 was briefly discussed. The data contain line-of-sight absorption by transitions of ∼15 different molecules, including transitions from $NH_2CHO$, which was previously not observed in translucent gas. An absorbing component at ∼0 $\mathrm{km\,s^{-1}}$ proved to vary significantly in its optical depth across the spatial field, revealing that it contains significant density structure.

Finally, we discussed the spatial distributions of a few detected molecular species providing evidence for chemical differentiation between species including SiO, HNCO, OCS, CS, CCS, and additional CS-bearing molecules. We explored the implications of the spatial distributions for the physical environments of the molecular gas. The observed distributions and physical structure indicate that both primary absorbing gas components are likely PDR environments, although shocks, high X-ray fluxes, and high cosmic ray fluxes may have equal influence on the observed chemistry. The data reveal that molecules including (1) silicon-bearing species, (2) sulfur-bearing species, (3) carbon chain molecules, (4) multiple classes of oxygenated species including aldhydes and alcohols, (5) nitrogen species of pre-biotic importance including nitriles and imines are abundant in the exotic PDR environments.

This work highlights only a small fraction of the scientific capacity of the dataset presented and provides a tool to enable researchers to accomplish additional projects. Towards the HII regions, follow-up work including multi-transition analyses of molecules are facilitated by the full-spectrum line identifications provided herein. Furthermore, the data complement existing single dish data covering the same frequency range, namely the PRIMOS survey (Neill et al. 2012). Finally, the spectra extracted from the LMH and "h" are very line-dense and they remain uncharacterised. These spectra will provide unprecedented detail on hot core chemistry in Sgr B2(N).

## ACKNOWLEDGMENTS

We thank the anonymous referee for the helpful comments that improved the quality of this work. The Australia Telescope Compact Array is funded by the Commonwealth of Australia for operation as a National Facility managed by CSIRO. J.F.C. gratefully acknowledges funding by the Grote Reber Doctoral Research Program of the National Radio Astronomy Observatory (NRAO) and by the East Asian and Pacific Summer Institute of the National Science Foundation (NSF). The work was supported by the NSF grant OISE-1310963. The NRAO is a facility of the National Science Foundation operated under cooperative agreement by Associated Universities, Inc. NL's postdoctoral fellowship is supported by CONICYT/FONDECYT postdoctorado, under project number 3130540. LB gratefully acknowledges support by CONICYT Grant PFB-06.

## REFERENCES

Amo-Baladrón M. A., Martín-Pintado J., Morris M. R., Muno M. P., Rodríguez-Fernández N. J., 2009, ApJ, 694, 943
Ao Y., Henkel C., Menten K. M., et al. 2013, A&A, 550, A135
Belloche A., Menten K. M., Comito C., Müller H. S. P., Schilke P., Ott J., Thorwirth S., Hieret C., 2008, A&A, 482, 179
Belloche A., Müller H. S. P., Menten K. M., Schilke P., Comito C., 2013, A&A, 559, A47
Belloche A., Garrod R. T., Müller H. S. P., Menten K. M., 2014, Science, 345, 1584
Boger G. I., Sternberg A., 2005, ApJ, 632, 302
Caselli P., Hartquist T. W., Havnes O., 1997, A&A, 322, 296
Crutcher R. M, Roberts D. A, Mehringer D. M, Troland T. H, 1996, ApJ, 462, L79
Danks A. C., Federman S. R., Lambert D. L, 1984, A&A, 130, 62
de Pree C. G., Gaume R. A., Goss W. M., Claussen M. J., 1995, ApJ, 451, 284
de Vicente P., Martin-Pintado J., Wilson T. L., 1996, in Gredel R., ed, ASP Conf Ser. Vol. 102, The Galactic Center. Astron. Soc. Pac., San Francisco, p. 64
Drdla K., Knapp G. R., van Dishoeck E. F., 1989, ApJ, 345, 815
Genova F., Egret D, Bienaymé O., Bonnarel F., Dubois P., Fernique P., Jasniewicz G., Lesteven S.,Monier R., Ochsenbein, F., Wenger M., 2000, A&AS, 143, 1
Faure A., Remijan A. J., Szalewicz K., 2014, ApJ, 783, 72
Flower D. R., Pineau des Forets G., Walmsley C. M., 1995, A&A, 294, 815

Gaume R. A., Claussen M. J., de Pree C. G., Goss W. M., Mehringer D. M., 1995, ApJ, 449, 663

Gerin M., de Luca M., Black J., Goicoechea J. R., Herbst E., Neufeld D. A., Falgarone E., Godard B., Pearson J. C., Lis D. C. et al., A&A, 518, L110

Gibb E. L., Whittet D. C. B., Boogert A. C. A., Tielens A. G. G. M., 2004, ApJS, 151, 35

Garozzo M., Fulvio D., Kanuchova Z., Palumbo M. E., Strazzulla G., 2010, A&A, 509, A67

Godfrey P. D., Brown R. D., Robinson B. J., Sinclair M. W., 1973, ApJ, 13, 119

Goicoechea J. R., Rodríguez-Fernández N. J., Cernicharo J.,2003, Astron. Nachr., 324, 139

Goicoechea J. R, Pety J., Gerin M., Teyssier D., Roueff E., Hily-Blant P., Baek S., 2006, A&A, 456, 565

Gratier P., Pety J., Guzmán V., Gerin M., Goicoechea J. R, Roueff E., Faure A., 2013, A&A, 557, A101

Greaves J. S., Nyman L.-A., A&A, 305, 950

Guzmán V. V., Pety J., Gratier P., Goicoechea J. R., Gerin M., Roueff E., Le Petit F., Le Bourlot J., 2014, Discuss. Faraday Soc., 168, 103

Hasegawa T. I., Herbst E., 1993, MNRAS, 263, 589

Hasegawa T., Sato F., Whiteoak J. B., Miyawaki R., 1994, ApJ, 429, L77

Hatchell J., Fuller G. A., Millar T. J., 2001, A&A, 372, 281

Ho P. T. P., Townes C. H., 1983, ARA&A, 21, 239

Hodrick R. J., Prescott E. C., 1997, J. Money, Credit & Banking, 29, 1

Hollenbach D. J., Tielens A. G. G. M., 1997, ARA&A, 35, 179

Hollis J. M., Pedelty J. A., Boboltz D. A., Liu S.-Y.,Snyder L. E., Palmer P., Lovas F. J., Jewell P. R., ApJ, 596, L235

Huettemeister S., Wilson T. L., Mauersberger R., Lemme C., Dahmen G.,Henkel C., 1995, A&A, 294, 667

Jones P. A., Burton M. G., Cunningham M. R., Menten K. M., Schilke P., Belloche A., Leurini S., Ott J., Walsh A. J., 2008, MNRAS, 386, 117

Jones, P. A., Burton, M. G., Tothill, N. F. H., Cunningham M. R., 2011, MNRAS, 411, 2293

Jones P. A., Burton M. G., Cunningham M. R., Requena-Torres M. A., Menten K. M., Schilke P., Belloche A., Leurini S., Martín-Pintado J., Ott J., Walsh A. J., 2012, MNRAS, 419, 2961

Lis D. C, Schilke P., Bergin E. A., Emprechtinger M., & the HEXOS Team, 2012, Phil. Trans. R. Soc. A, 370, 5162

Liu S.-Y., Snyder L. E., 1999, ApJ, 523, 683

Loomis R. A., Zaleski D. P., Steber A. L., Neill J. L., Muckle, M. T., Harris B. J., Hollis J. M., Jewell P. R., Lattanzi V., Lovas F. J., Martinez Jr. O., McCarthy M. C., Remijan A. J., Pate B. H., Corby J. F., 2013, ApJ, 765, L9

Lovas F. J. & Dragoset R. A., 2004, J. Phys. Chem. Ref. Data, 33, 177

McGuire B. A., Loomis R. A., Charness C. M., Corby J. F., Blake G. A., Hollis J. M., Lovas F. J. and Jewell P. R., Remijan A. J., 2012, ApJ, 758, L33

McGuire B. A., Carroll P. B., Loomis R. A., Blake G. A., Hollis J. M., Lovas F. J., Jewell P. R., Remijan A. J., 2013, ApJ, 774, 56

McGuire B. A., Carroll P. B., Sanders J. L., Weaver S. L. W., Blake G. A., Remijan A. J., 2014, MNRAS, 442, 2901

Martín S., Requena-Torres M. A., Martín-Pintado J., Mauersberger R., 2008, ApJ, 678, 245

Martín-Pintado J., de Vicente P., Rodríguez-Fernández N. J., Fuente A., Planesas P., 2000, A&A, 356, L5

Martín-Pintado J., Rizzo J. R., de Vicente P., Rodríguez-Fernández N. J., Fuente A., 2001, ApJ, 548, L65

Meijerink R., Spaans M., Israel F. P., 2007, A&A, 461, 793

Mehringer D. M., Menten K. M., 1997, ApJ, 474, 346

Menten K. M., 2004, in Pfalzner S., Kramer C., Staubmeier C., Heithausen, A. eds, Proc. 4th Cologne-Bonn-Zermatt-Symp. The Dense Interstellar Medium in Galaxies, p. 69

Menten K. M., Wyrowski F., Belloche A., Güsten R., Dedes L., Müller H. S. P., 2011, A&A, 525, A77

Miao Y., Mehringer D. M., Kuan Y.-J., Snyder L. E., 1995, ApJ, 445, L59

Minh Y. C., Irvine W. M., 2006, NewAst, 11, 594

Müller H. S. P., Schlder F., Stutzki J., Winnewisser G., 2005, J. Mol. Struct. 742, 215

Neill J. L., Muckle M. T., Zaleski D. P., Steber A. L., Pate B. H., Lattanzi V., Spezzano S., McCarthy M. C., Remijan A. J., 2012, ApJ, 755, 153

Neill J. L., Bergin E. A., Lis D. C., Schilke P., Crockett N. R., Favre C., Emprechtinger M., Comito C., Qin S.-L., Anderson D. E., Burkhardt A. M. and Chen J.-H., Harris B. J., Lord S. D., McGuire B. A. and McNeill T. D.,d Monje R. R., Phillips T. G., Steber A. L., Vasyunina T., Yu S., 2014, ApJ, 789, 8

Nummelin A., Bergman P., Hjalmarson Å., Friberg P., Irvine W. M., Millar T. J., Ohishi M., Saito S., 1998, ApJS, 117, 427

Palumbo M. E., Baratta G., Fulvio D., Garozzo M., Ioppolo S., Kanuchova Z., Leto G., Sangiorgio I., Strazzulla G., 2011, in Cernicharo J., Bachiller R., eds, Proc. IAU Symp. 280, The Molecular Universe, 285P

Petrie S., 1996, MNRAS, 281, 666

Pety J., Gratier P., Guzmán V., Roueff E., Gerin M. Goicoechea, J. R., Bardeau S. , Sievers A., Le Petit F., Le Bourlot J., Belloche A., Talbi D., 2012, A&A, 548, A68

Pickett H. M., Poynter R. L., Cohen E. A., Delitsky M. L., Pearson J. C., Mller H. S. P., 1998, J. Quant. Spectrosc. & Rad. Transfer, 60, 883

Pineau des Forets G., Flower D. R., Chieze J.-P., 1997, in Reipurth B., Bertout, C., Proc. IAU Symp. 182, Herbig-Haro Flows and the Birth of Low Mass Stars, p. 199

Qin S. L.,Schilke P., Comito C., Möller T., Rolffs R., Müller H. S. P., Belloche A., Menten K. M., Lis D. C., Phillips T. G. et al., 2010, A&A, 521, L14

Qin S. L., Schilke P., Rollfs R., Comito C., Lis D. C., Zhang Q., 2011, A&A, 530, L9

Remijan A. J., Markwick-Kemper A., ALMA Working Group on Spectral Line Frequencies, 2007, BAAS, 39, 963

Ren J. Z., Liu T., Wu Y., Li L., 2011, MNRAS, 415, L49

Roberge W. G., Jones D., Lepp S., Dalgarno A, 1991, ApJS, 77, 287

Rodríguez-Fernández N. J., Tafalla M., Gueth F., Bachiller R., 2010, A&A, 516, A98

Royster M. J., Yusef-Zadeh F., 2014, in Sjouwerman L., Ott J., Lang C., eds, Proc. IAU Symp. 303, The Galactic Center: Feeding and Feedback in a Normal Galactic Nucleus. p. 92

Sakai N., Ikeda M., Morita M., Sakai T., Takano S., Osamura Y., Yamamoto S., 2007, ApJ, 663, 1174

Sato Y., Matsumi Y, Kawasaki M., Tsukiyama K., Bersohn R., 1995, J. Phys. Chemistry, 99, 16307

Sato F., Hasegawa T., Whiteoak J. B., Miyawaki R., ApJ, 535, 857

Sault R. J., Teuben P. J., Wright M. C. H., 1995, in Shaw R. A., Payne H. I., Hayes J. J. E., eds, ASP Conf. Ser. Vol. 77, Astronomical Data Analysis Softwards and Systems IV. Astron. Soc. Pac., San Francisco, p. 433

Schilke P., Walmsley C. M., Pineau des Forets G.,Flower D. R.,1997, A&A, 321, 293
Schlickt E. 2008, J. Japan Statist. Soc, 38, 285
Sinclair M. W., Fourikis N., Ribes J. C., Robinson B. J., Brown R. D., Godfrey, P. D., 1973, Aus. J. Phys., 26, 85.
Sternberg A., Dalgarno A., 1995, ApJS, 99, 565
Tielens A. G. G. M., Meixner M. M., van der Werf P. P., Bregman J., Tauber J. A., Stutzki J., Rank D., 1993, Science, 262, 86
Terrier R., Ponti G., Blanger G., Decourchelle A., Tatischeff V., Goldwurm A., Trap G., Morris M. R., Warwick, R., 2010, ApJ, 719, 143
Teuben P., Ip C. Y., Mundy L., Varshney A., 2013, in Friedel D., ed, ASP Conf. Ser. Vol. 475., Astronomical Data Analysis Software and Systems XXII. Astron. Soc. Pac., San Francisco, p. 263
Tideswell D. M., Fuller G. A., Millar T. J., Markwick A. J., 2010, A&A, 510, A85
Turner B. E., 1989, ApJS, 70, 539
Turner B. E., 2000, ApJ, 542, 837
Turner B. E., Terzieva R., Herbst E., 1999, ApJ, 618, 699
van der Tak F. F. S, Belloche A., Schilke P., Guesten R., Phillip S., Comito C., Bergman P., Nyman L., 2006, A&A, 454, 99
von Procházka A. A., Remijan A. J., Balser D. S., Ryans R. S. I., Marshall A. H., Schwab F. R., Hollis J. M., Jewell P. R., Lovas F. J., 2010, PASP, 122, 354
Walmsley C. M., Ungerechts H., 1983, A&A, 122, 164
Watt S., Mundy L. G., 1999, ApJS, 125, 143
Wilson W. E., Ferris R. H., Axtens P., Brown A., et al., 2011, MNRAS, 416, 832
Wirström E. S., Bergman P., Black J. H., Hjalmarson Å, Larsson B., Olofsson A. O. H., Encrenaz P. J., Falgarone E., Frisk U., Olberg, M., Sandqvist A., 2010, A&A, 522, A19
Yamada M., Osamura Y., Kaiser R. I., 2002, A&A, 395, 1031
Zaleski D. P., Seifert N. A., Steber A. L., Muckle M. T., Loomis R. A., Corby J. F., Martinez Jr. O., Crabtree K. N., Jewell P. R., Hollis J. M., Lovas F. J., Vasquez D, Nyiramahirwe J., Sciortino N., Johnson, K., McCarthy M. C., Remijan A. J., Pate B. H., 2013, ApJ, 765, L10
Zinchenko I., Henkel C., Mao R. Q., 2000, A&A, 361, 1079

**Table 1.** Log of ATCA observations showing the arrays and CABB tunings.

| UT Date | Array | Freq. A1 (GHz) | Freq. A2 (GHz) | Freq. B1 (GHz) | Freq B2 (GHz) |
|---|---|---|---|---|---|
| 2011 Oct 21 | H75 | 47.40 | 49.25 | 43.70 | 45.55 |
| 2013 Apr 3 | H214 | 30.75 | 32.60 | 34.45 | 36.30 |
| 2013 Apr 4 | H214 | 38.15 | 40.00 | 41.85 | 43.70 |

**Table 2.** Root mean squared ($1\sigma$) noise level in spectra extracted from K6, L, and K4

| Center Freq | Beamsize | $\sigma_{\mathrm{RMS}}$ ($\mu$Jy arcsec$^{-2}$) | | |
|---|---|---|---|---|
| (GHz) | arcsec × arcsec | K6 | L | K4 |
| 30.75 | $6.3 \times 4.7$ | 58 | 64 | 55 |
| 32.60 | $5.9 \times 4.4$ | 54 | 71 | 54 |
| 34.45 | $5.7 \times 4.0$ | 61 | 74 | 51 |
| 36.30 | $5.2 \times 4.0$ | 70 | 80 | 62 |
| 38.15 | $5.1 \times 3.7$ | 72 | 105 | 66 |
| 40.00 | $4.7 \times 3.6$ | 100 | 124 | 81 |
| 41.85 | $4.6 \times 3.6$ | 82 | 131 | 76 |
| 43.70 | $4.4 \times 3.4$ | 132 | 179 | 108 |
| 45.55 | $13.0 \times 8.9$ | 53 | 83 | |
| 47.40 | $11.9 \times 8.7$ | 51 | 88 | |
| 49.25 | $11.2 \times 8.5$ | 70 | 148 | |

**Table 3.** Coordinates of regions from which spectra were extracted.

| Region | Ellipse Shape | | | |
|---|---|---|---|---|
| | RA Center | Dec Center | ΔRA (arcsec) | ΔDec (arcsec) |
| K6 | $17^h47^m20^{\mathrm{s}}.58$ | $-28^\circ22'13''.2$ | 4.9 | 3.3 |
| L | $17^h47^m22^{\mathrm{s}}.68$ | $-28^\circ21'56''.1$ | 6.8 | 4.8 |
| K4 | $17^h47^m20^{\mathrm{s}}.07$ | $-28^\circ22'04''.9$ | 5.9 | 3.8 |
| LMH | $17^h47^m19^{\mathrm{s}}.93$ | $-28^\circ22'18''.2$ | 6.8 | 4.6 |
| “h” | $17^h47^m19^{\mathrm{s}}.87$ | $-28^\circ22'13''.6$ | 4.1 | 3.4 |

**Table 4.** Sample page of table providing line identifications and Gaussian fit parameters towards K6. See Appendix C for full tables towards K6, L, and K4, and for a full description of labeling conventions.

| Line Rest Freq (MHz) | Species | Transition | Fit Velocity ( $\mathrm{km\,s^{-1}}$) | Height (mJy $\mathrm{arcsec^{-2}}$) | Width ( $\mathrm{km\,s^{-1}}$) | $\int I_v dv$ (mJy $\mathrm{arcsec^{-2}}$ × $\mathrm{km\,s^{-1}}$) |
|---|---|---|---|---|---|---|
| 29853.31 | U | —— | 64.0 | 0.20 | 19.7 | 4.3 |
| 29901.40 | $CH_3OCH_3$ | $1_{10}$-$1_{01}$EE/AA/AE/EA | 64.2 | -0.64 | 20.2 | -13.9 |
| 29914.49 | $NH_3$ | (11,11) | 83.4 | -2.51 | 12.5 | -29.5 |
| | | | 64.6 | -4.96 | 15.9 | -83.5 |
| | | | 11.3 | -0.52 | 18.6 | -11.4 |
| 29956.11 | U | —— | 64.0 | -0.23 | 20.1 | -4.9 |
| 29971.48 | Hydrogen | H(75)$\beta$ | 84.6 | 1.20 | 26.2 | 33.6 |
| | | | 61.8 | 1.82 | 32.3 | 62.7 |
| 29979.38 | *t*-$CH_3CH_2OH$ | $3_{12}$-$3_{03}$ | [1]81.2 | 0.41 | 12.5 | 5.5 |
| | | | 62.0 | -0.29 | 11.5 | -3.6 |
| 30001.55 | SO | $1_0$-$0_1$ | 84.4 | -11.73 | 13.5 | -150.3 |
| | | | 64.2 | -27.56 | 15.4 | -451.7 |
| | | | 8.9 | -1.25 | 21.2 | -30.5 |
| | | | -32.4 | -0.27 | 22.9 | -6.5 |
| | | | -106.3 | -0.54 | 10.9 | -6.3 |
| 30180.60 | NaCN/NaNC$^{BC}$ | $2_{12}$-$1_{11}$ | 74.4 | -0.19 | 20.4 | -4.2 |
| 30239.76 | U | —— | 64.0 | -0.22 | 16.1 | -3.8 |
| 30256.04 | U | —— | 64.0 | -0.17 | 28.6 | -5.1 |
| 30500.20 | Hydrogen | H(85)$\gamma$ | 72.9 | 0.90 | 37.3 | 35.6 |
| | | | 51.1 | 0.38 | 18.6 | 7.5 |
| 30513.96 | Hydrogen | H(106)$\zeta$ | 79.1 | 0.29 | 46.4 | 14.4 |
| 30707.38 | Hydrogen | H(93)$\delta$ | 74.3 | 0.43 | 49.7 | 22.7 |
| 30722.67 | U? | —— | 64.0 | 0.22 | 90.9 | 21.3 |
| 31002.30 | $CH_3CH_2CHO$ | $3_{21}$-$2_{12}$ | 65.9 | -0.25 | 33.6 | -8.9 |
| 31106.15 | $CH_3OCH_3$ | $2_{11}$-$2_{02}$EE/AA/AE/EA | 65.1 | -1.06 | 23.2 | -26.1 |
| 31186.68 | Hydrogen | H(74)$\beta$ | 66.8 | 2.23 | 39.9 | 102.6 |
| 31199.39 | Helium | He(74)$\beta$ | 73.5 | 0.22 | 36.9 | 8.7 |
| 31223.31 | Hydrogen | H(59)$\alpha$ | 78.3 | 7.51 | 29.2 | 233.7 |
| | | | 55.7 | 5.95 | 23.1 | 146.5 |
| 31236.04 | Helium | He(59)$\alpha$ | 89.7 | 0.32 | 16.6 | 5.7 |
| | | | 65.3 | 0.71 | 34.8 | 26.2 |
| 31262.33 | NaCN/NaNC | $2_{02}$-$1_{01}$ | 62.0 | -0.66 | 15.8 | -11.1 |
| 31424.94 | $NH_3$ | (12,12) | 84.5 | -2.50 | 13.3 | -35.5 |
| | | | 65.2 | -7.30 | 19.4 | -150.5 |
| | | | 8.2 | -0.56 | 25.6 | -15.4 |
| 31482.38 | Hydrogen | H(99)$\epsilon$ | 75.6 | 0.31 | 45.0 | 14.8 |
| 31583.40 | Hydrogen | H(84)$\gamma$ | 77.7 | 0.84 | 33.4 | 30.0 |
| | | | 51.2 | 0.49 | 23.6 | 12.2 |
| 31698.47 | Hydrogen | H(92)$\delta$ | 68.7 | 0.28 | 33.6 | 10.1 |
| 31727.07 | *cis*-$CH_2OHCHO$ | $5_{23}$-$5_{14}$ | 77.6 | -0.25 | 13.7 | -3.6 |
| | | | 60.9 | -0.26 | 11.7 | -3.2 |
| 31833.03 | *cis*-$CH_2OHCHO$ | $6_{24}$-$6_{15}$ | 61.2 | -0.22 | 20.1 | -4.8 |
| 31911.20 | $CH_3CH_2CHO$ | $3_{21}$-$2_{20}$ | 65.4 | -0.27 | 10.0 | -2.9 |
| 31951.78 | $HC_5N$ | 12-11 | 84.8 | -0.34 | 8.6 | -3.1 |
| | | | 64.2 | -1.78 | 12.6 | -23.9 |
| 32373.67 | NaCN/NaNC | $2_{11}$-$1_{10}$ | 62.8 | -0.29 | 28.1 | -8.6 |
| 32398.56 | $^{13}CH_3OH^{Maser}$ | $4_{-1,4}$-$3_{03}$ | 82.3 | 0.93 | 12.6 | 12.5 |
| | | | 62.8 | 0.40 | 10.7 | 4.6 |
| 32432.32 | Hydrogen | H(98)$\epsilon$ | 74.0 | 0.26 | 44.3 | 12.1 |
| 32468.48 | Hydrogen | H(73)$\beta$ | 78.2 | 1.92 | 32.8 | 66.8 |
| | | | 55.1 | 1.36 | 23.8 | 34.4 |
| 32627.30 | *l*-$C_3H^{Adj}$ | $J=\frac{3}{2}$-$\frac{1}{2}$ $\Omega=\frac{1}{2}$ F=2-1f | 63.7 | -0.50 | 17.2 | -9.2 |
| | | | 14.5 | -0.16 | 12.0 | -2.1 |
| | | | [2]-2.5 | -0.31 | 18.8 | -6.1 |
| 32640.21 | U | —— | [3]64.0 | -0.31 | 26.2 | -8.7 |
| 32627.30 | *l*-$C_3H$ | $J=\frac{3}{2}$-$\frac{1}{2}$ $\Omega=\frac{1}{2}$ F=2-1f | -108.5 | -0.20 | 21.1 | -4.5 |
| 32660.65 | *l*-$C_3H^{Adj}$ | $J=\frac{3}{2}$-$\frac{1}{2}$ $\Omega=\frac{1}{2}$ F=2-1e | 62.6 | -0.66 | 11.7 | -8.3 |
| 32663.38 | *l*-$C_3H^{Adj}$ | $J=\frac{3}{2}$-$\frac{1}{2}$ $\Omega=\frac{1}{2}$ F=1-0e | 61.8 | -0.19 | 10.5 | -2.1 |
| 32660.65 | *l*-$C_3H^{Adj}$ | $J=\frac{3}{2}$-$\frac{1}{2}$ $\Omega=\frac{1}{2}$ F=2-1e | 17.4 | -0.20 | 24.8 | -5.3 |
| | | | [4]-2.1 | -0.33 | 14.7 | -5.2 |

**Table 5.** Best fits to the composite average of recombination line transitions. The errors quoted are from the diagonal terms of the covariance matrix. However, the matrices contain significant covariance terms, causing the error to be highly overestimated. Fits to the composite average of H$\alpha$ and H$\beta$ transitions agree to a precision that is significantly smaller than the covariance matrix output.

| Region | Species | Gaussian Component 1 | | | Gaussian Component 2 | | | Height Ratio |
|---|---|---|---|---|---|---|---|---|
| | | Height (mJy arcsec$^{-2}$) | Velocity ($\mathrm{km\,s^{-1}}$) | Width ($\mathrm{km\,s^{-1}}$) | Height (mJy arcsec$^{-2}$) | Velocity ($\mathrm{km\,s^{-1}}$) | Width ($\mathrm{km\,s^{-1}}$) | $H_1/H_2$ |
| K6 | H$\alpha$ | 7.1±1.0 | 59.3±3.1 | 28.0 ±3.9 | 5.7 ±1.1 | 83.6±3.7 | 27.0±4.4 | 1.37 |
| | H$\beta$ | 1.9 ± 1.2 | 59.7 ± 17 | 30.0 ± 24 | 1.4 ± 1.9 | 84.2 ± 20 | 27.2 ± 21 | 1.25 |
| | He$\alpha$ | 0.67 ± 0.28 | 60.7 ± 10 | 23.5 ± 21 | 0.51 ± 0.35 | 85.6 ± 12 | 19.8 ± 23 | 1.31 |
| L | H$\alpha$ | 7.3 ±0.3 | 76.6 ±0.4 | 24.9 ±1.0 | | | | |
| | H$\beta$ | 2.0 ±0.3 | 76.5 ±1.6 | 25.3±3.8 | | | | |
| | He$\alpha$ | 0.63 ± 0.27 | 76.1 ± 4.8 | 22.4 ± 11 | | | | |
| K4 | H$\alpha$ | 2.5 ± 0.3 | 65.0 ± 2.5 | 28.4 ± 5.8 | 0.35 ± 0.26 | 100.3 ± 17 | 27.8 ± 44 | 7.1 |

**Table 6.** Mean parameters and standard errors of fits to H$\alpha$ - $\gamma$ transitions. Parameters are calculated from 1-component fits towards L, 2-component fits towards K6, and 1-component fits towards K4.

| Region | Number of Fits | Gaussian Component 1 | | Gaussian Component 2 | | Height Ratio |
|---|---|---|---|---|---|---|
| | | Velocity ($\mathrm{km\,s^{-1}}$) | Width ($\mathrm{km\,s^{-1}}$) | Velocity ($\mathrm{km\,s^{-1}}$) | Width ($\mathrm{km\,s^{-1}}$) | $H_1/H_2$ |
| K6 | 25 | 58.9 ± 0.8 | 28.7 ± 1.1 | 84.7 ±0.8 | 27.2±1.2 | 1.36±0.10 |
| L | 26 | 76.3 ± 0.2 | 26.3 ± 0.7 | | | |
| K4 | 14 | 66.2 ± 0.5 | 32.1 ± 1.4 | | | |

**Table 7.** Recommended errors to fits to the ATCA data output by the automated line fitter.

| Line Type | S:N Regime | $\sigma_v$ ($\mathrm{km\,s^{-1}}$) | $\sigma_{\Delta v}$ ($\mathrm{km\,s^{-1}}$) | $\sigma_{Height}$ (%) |
|---|---|---|---|---|
| 2-Component Recombination Lines | | | | |
| Primarily H$\alpha$ & H$\beta$ | S:N >15 | 3.6 | 4.9 | 25 |
| Primarily H$\gamma$, H$\delta$ & He$\alpha$ | $5 <$ S:N $< 15$ | 5.0 | 6.9 | 40 |
| 1-Component Recombination Lines | S:N >5.4 | 1.1 | 2.3 | 12.5 |
| 1- & 2-Component Molecular Lines | S:N >5.4 | 1.1 | 2.3 | 12.5 |

**Table 8.** Kinematic measurements of molecular gas towards K6, L, and K4 from lines in the 25th - 90th percentile signal-to-noise ratio.

| Region | Low Velocity Component | | | High Velocity Component | | | Height Ratio$^*$ |
|---|---|---|---|---|---|---|---|
| | N Fits | Velocity ($\mathrm{km\,s^{-1}}$) | Width ($\mathrm{km\,s^{-1}}$) | N Fits | Velocity ($\mathrm{km\,s^{-1}}$) | Width ($\mathrm{km\,s^{-1}}$) | $H_1/H_2$ |
| K6 | 90 | 63.5 ± 0.1 | 13.1 ± 0.3 | 39 | 81.9 ± 0.2 | 11.0 ± 0.3 | 3.2±0.3 |
| L | 47 | 56.3 ± 0.2 | 14.1 ± 0.4 | 29 | 75.9 ± 0.3 | 12.0 ± 0.6 | 1.6 ± 0.3 |
| K4 | 30 | 61.8 ± 0.5 | 14.9 ± 0.7 | 20 | 82.0 ± 0.5 | 15.3 ± 0.6 | 1.0 ± 0.1 |

$^*$The height ratio is determined from lines that have both a high and low velocity component.

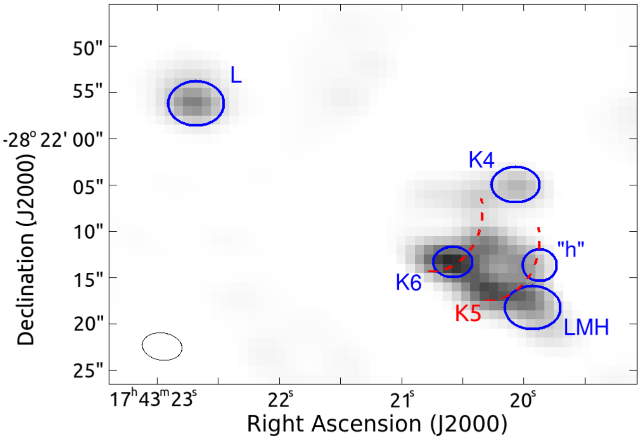

**Figure 1.** Continuum image of Sgr B2(N) and L at 40 GHz showing the elliptical regions from which spectra were extracted. The dashed line arcs point out the K5 and K6 shell-shaped HII regions. The synthesized beam shape is shown in the lower left corner.

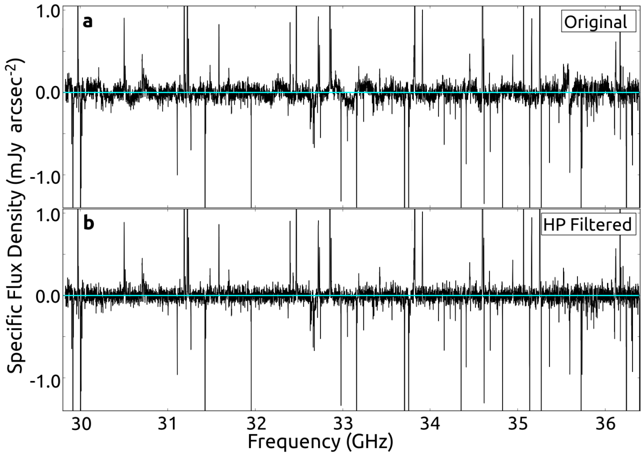

**Figure 2.** A segment of the full spectral coverage towards K6. **a.** shows the spectrum extracted from the data cubes and **b.** is the spectrum after baseline removal using a Hodrick-Prescott filter.

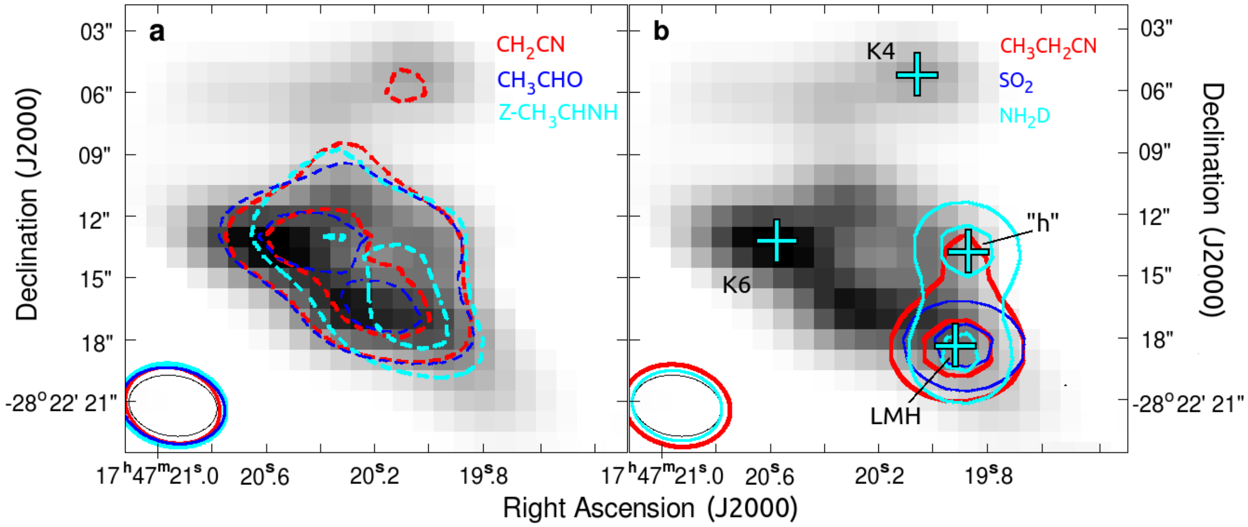

**Figure 3.** 40% and 80% integrated line emission contours over 40 GHz continuum illustrate the two most common distributions of molecular line radiation. **a.** $CH_2CN$ (2 - 1), $CH_3CHO$ ($2_{02}$ - $1_{01}$), and *Z*-$CH_3CHNH$ ($2_{02}$ - $1_{01}$) are observed in absorption (dashed contours) preferentially towards the K5 and K6 shells. **b.** $NH_2D$ ($3_{13}$ - $3_{03}$), $CH_3CH_2CN$ ($4_{31}$ - $3_{30}$), and $SO_2$ ($19_{3,18}$ - $18_{3,15}$) are detected in emission towards the LMH hot core, and $NH_2D$ and $CH_3CH_2CN$ are detected in emission towards "h". The central positions of the elliptical regions from which spectra were extracted are indicated by the crosses. The synthesized beam shapes for the continuum (thin black ellipse) and spectral lines (colored ellipses) are shown in the lower left corner.

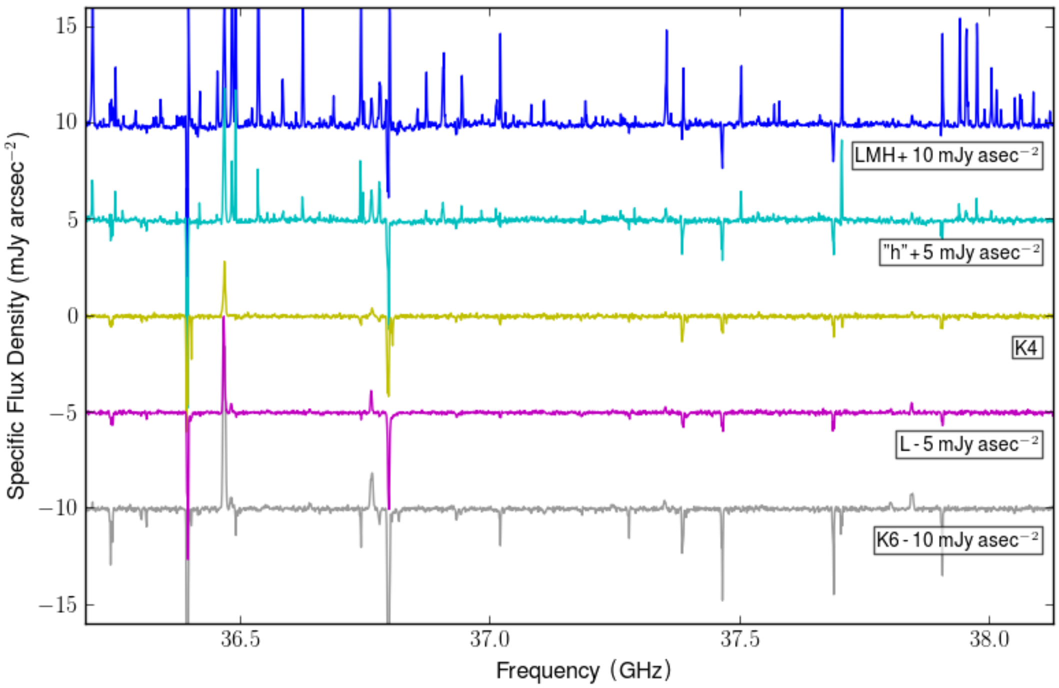

**Figure 4.** A representative segment of spectra extracted from all five regions targeted in this study. Whereas the LMH and "h" have line-dense spectra dominated by molecular line emission, K4, L, and K6 have lower line densities with molecular lines observed in absorption and recombination lines in emission.

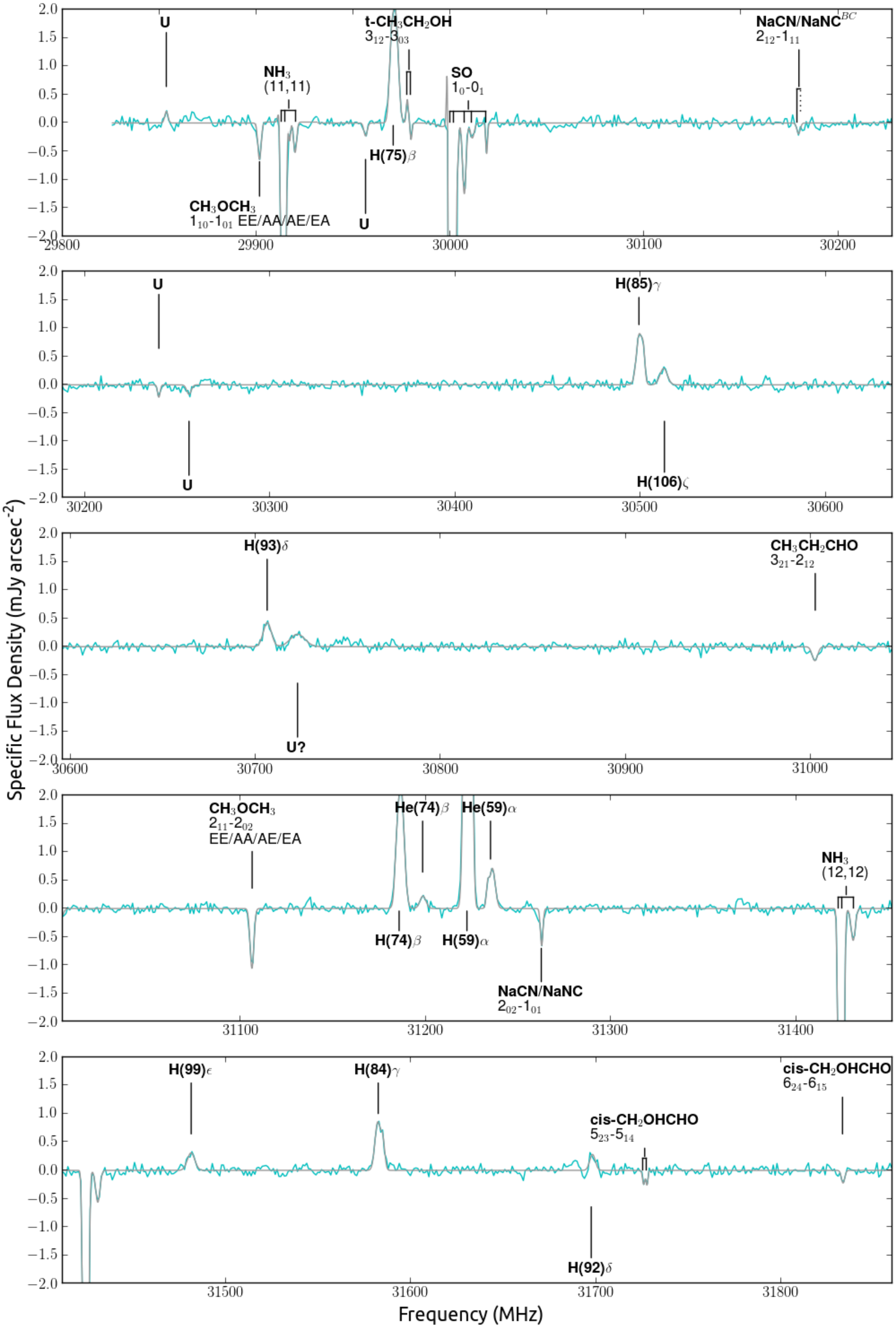

**Figure 5.** A sample page of the full data spectrum extracted towards K6 with line identifications labeled and the output of the automated line-fitter overlaid. See Appendix B for full figures for K6, L, and K4.

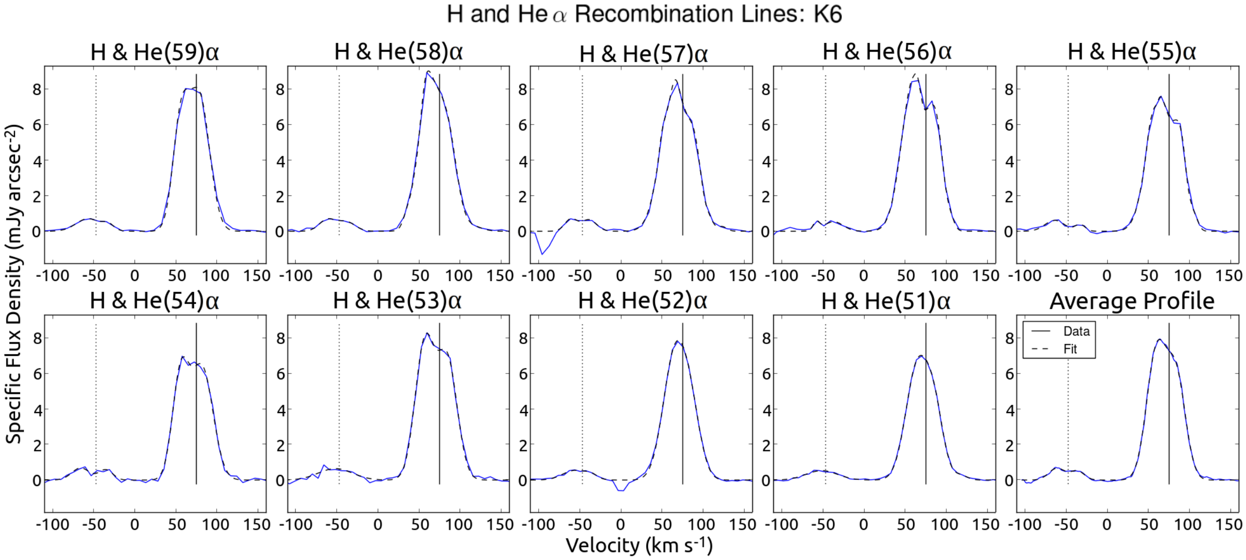

**Figure 6.** Hydrogen and Helium $\alpha$ recombination lines towards K6. Profiles of the H(59) - H(53)$\alpha$ transitions, extracted from high spatial resolution data, show a double peaked profile, whereas the H(52) and H(51)$\alpha$ transitions are well fit by a single component. The averaged profile is best fit by a Gaussian centered at 59 $\mathrm{km\,s^{-1}}$ and a weaker component at 84 $\mathrm{km\,s^{-1}}$. The solid and dashed vertical lines represent the H and He $\alpha$ transitions at 75 $\mathrm{km\,s^{-1}}$ respectively.

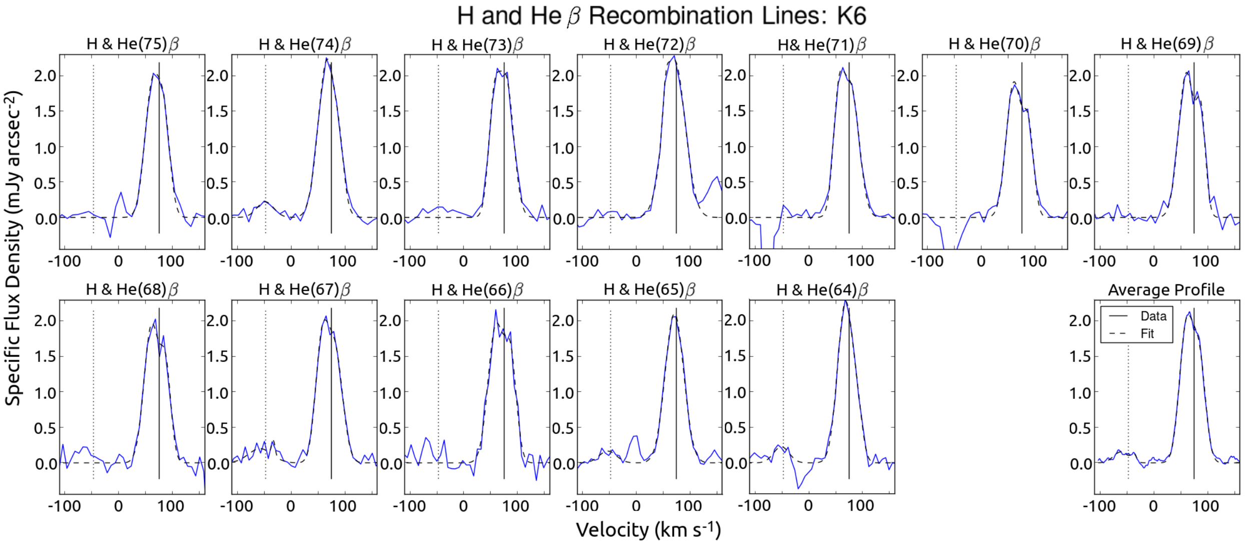

**Figure 7.** Hydrogen and Helium $\beta$ recombination lines towards K6. Profiles of the H(75) - H(66) $\beta$ transitions, extracted from high spatial resolution data, show a double peaked profile, whereas the H(65) and H(64)$\beta$ transitions are well fit by a single component. The averaged profile is best fit by a Gaussian centered at 60 $\mathrm{km\,s^{-1}}$ and a weaker component at 84 $\mathrm{km\,s^{-1}}$. The solid and dashed vertical lines represent the H and He $\beta$ transitions at 75 $\mathrm{km\,s^{-1}}$ respectively.

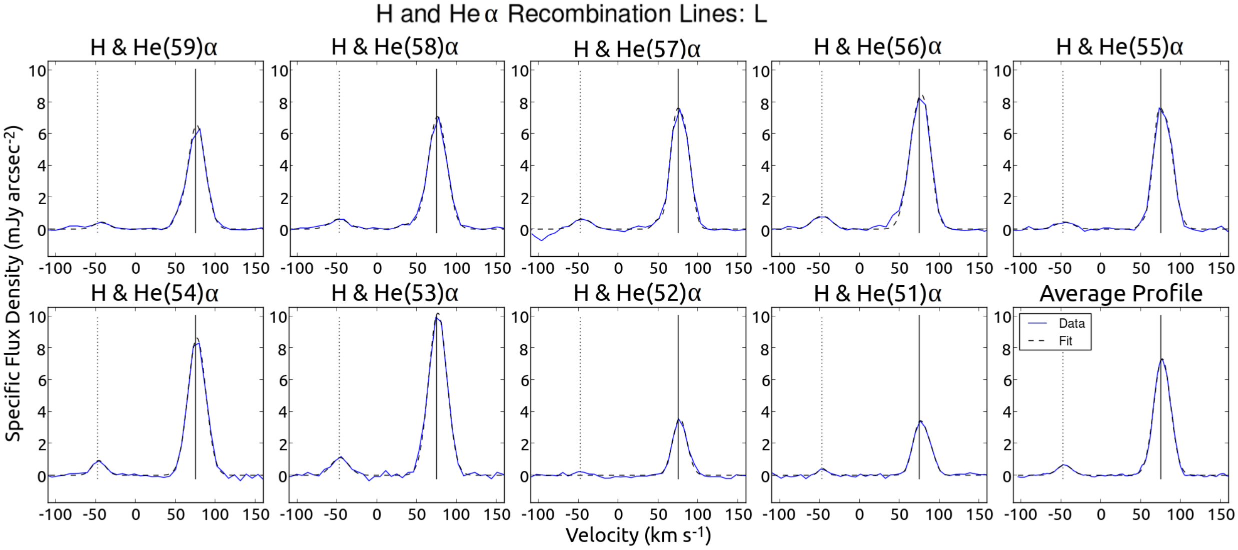

**Figure 8.** Hydrogen and Helium $\alpha$ recombination lines towards L are best fit by a Gaussian at 76.5 $\mathrm{km\,s^{-1}}$. The solid and dashed vertical lines represent the H and He $\beta$ transitions at 75 $\mathrm{km\,s^{-1}}$ respectively.

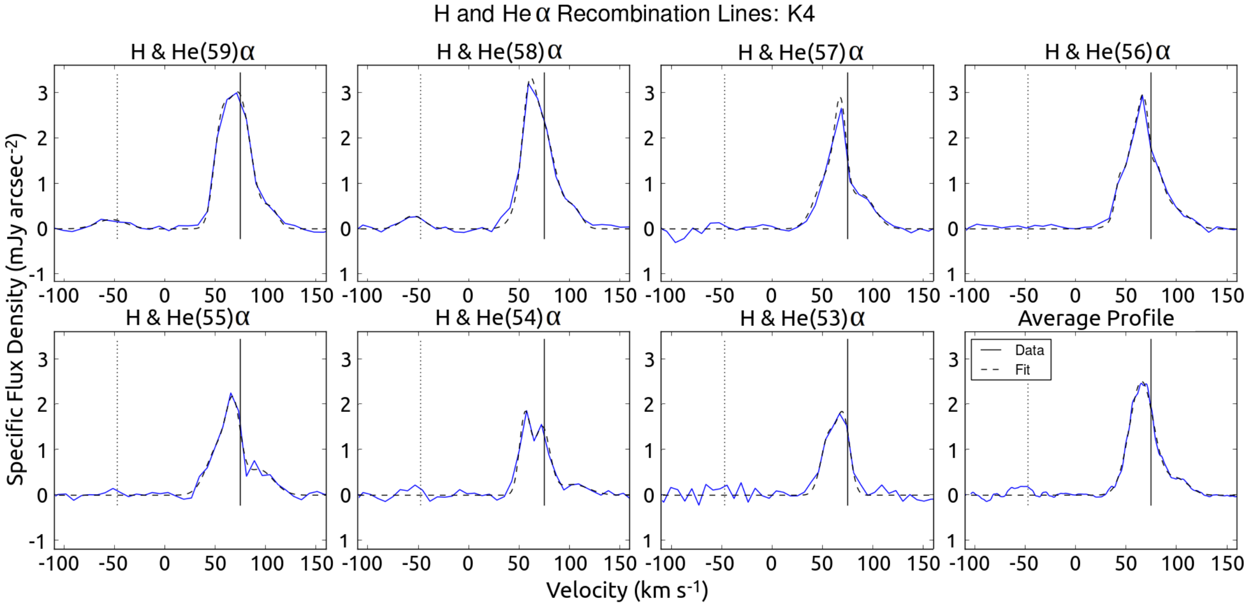

**Figure 9.** Hydrogen and Helium $\alpha$ recombination lines towards K4 show unusual line shapes that are highly sensitive to the spatial resolution of the image from which they were extracted. The lines are typically best fit by two primary components. In addition, a weaker wing component appears at ∼100 $\mathrm{km\,s^{-1}}$. The solid and dashed vertical lines represent the H and He $\beta$ transitions at 75 $\mathrm{km\,s^{-1}}$ respectively.

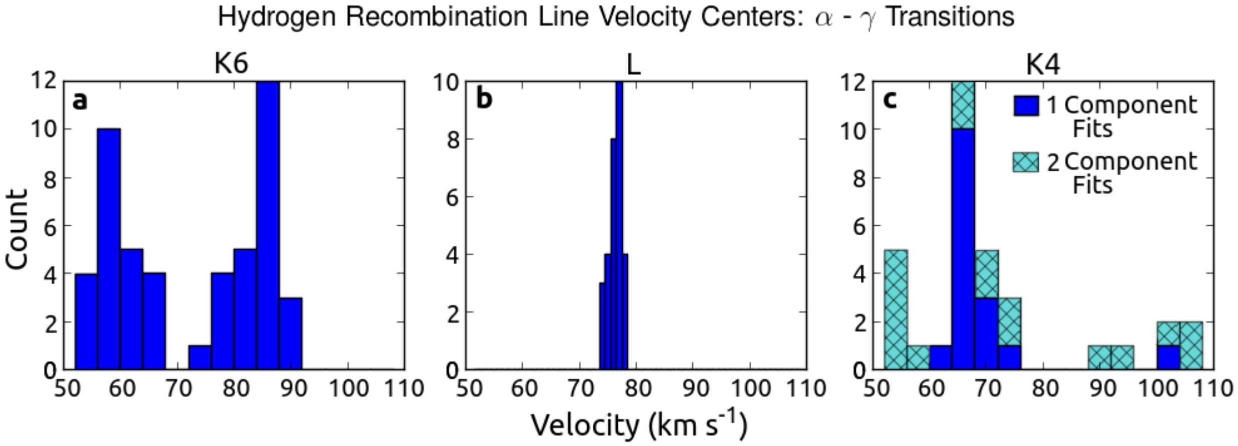

**Figure 10.** Velocity center of H $\alpha$ - $\gamma$ transitions fit towards L, K6, and K4. **a.** includes transitions towards K6 that were fit with 2 Gaussian components; **b.** includes unblended transitions towards L; **c.** includes all transitions towards K4. Components with $v\ > 80\ \mathrm{km\,s^{-1}}$ towards K4 are fitting a high velocity wing that is not a primary components of the line profile.

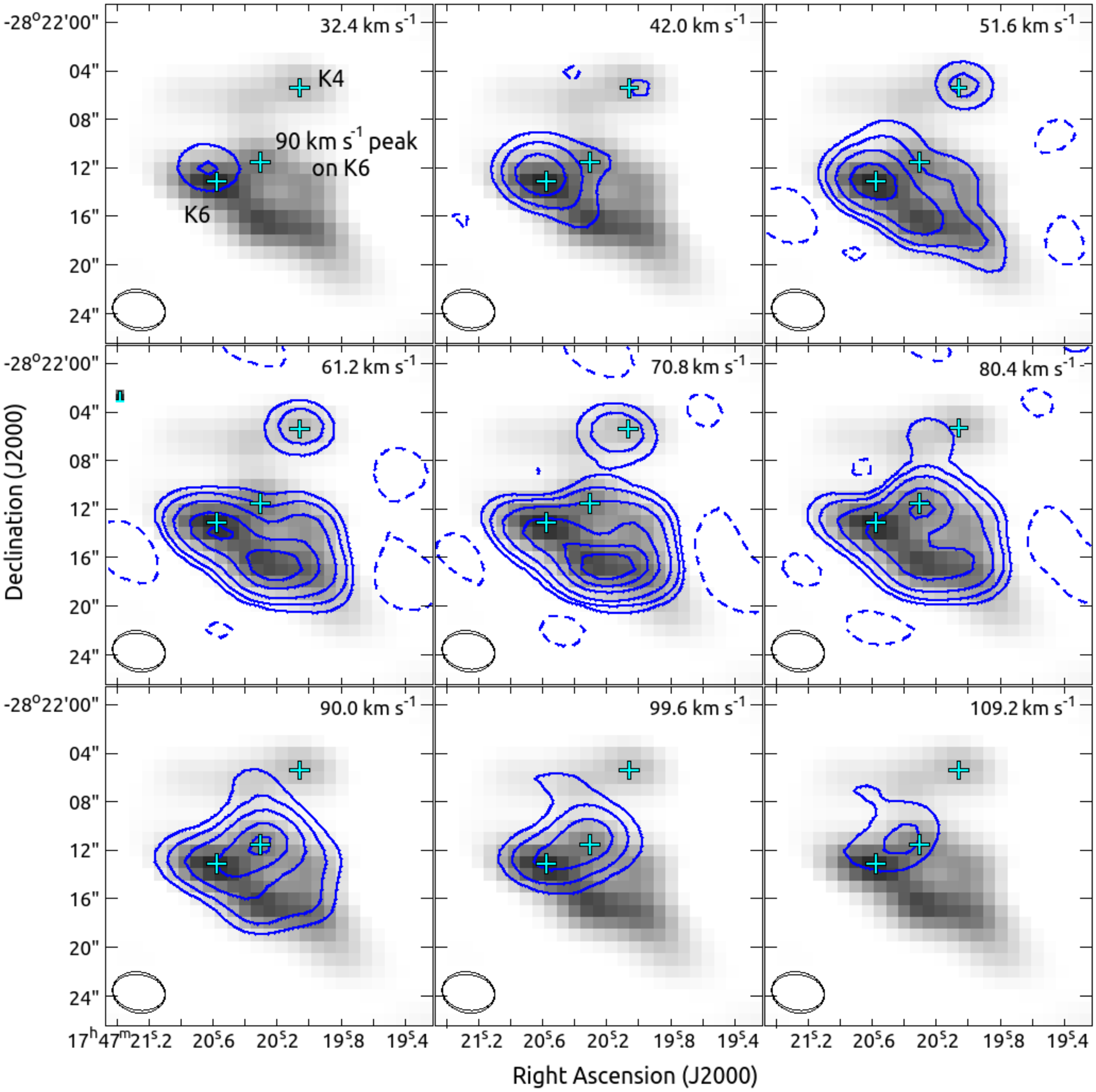

**Figure 11.** Channel maps of the H(53)$\alpha$ transition at 42951 MHz shown in contours over the 40 GHz continuum in greyscale. The synthesized beams for the continuum and line images are shown in the lower left corner. The figure shows a strong velocity gradient from the NW to the SE of K4. The crosses mark the center positions of the regions selected for K4 and K6 (at the base of the K6 shell) and indicate the peak position of the 90 km s$^{-1}$ gas. Notice the offset positions of high and low velocity gas on the K6 shell and the velocity gradient observed at K4.

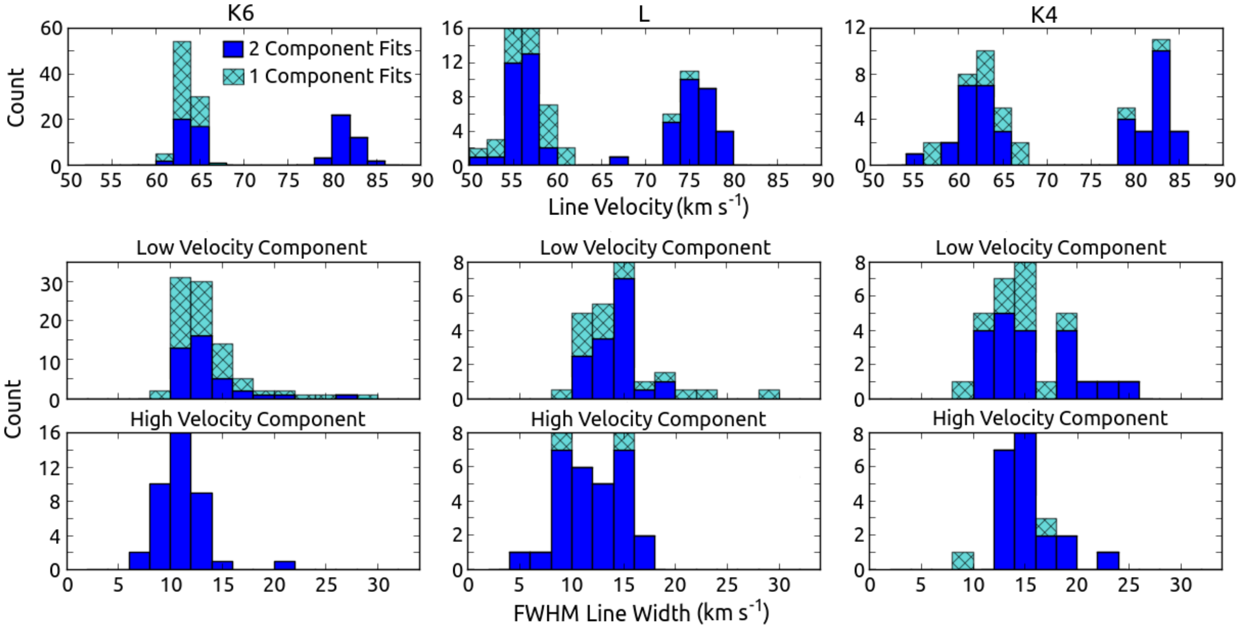

**Figure 12.** Kinematic parameters of molecular line fits output by the automated line fitter. 1-component fits shown include fits with a signal-to-noise ratio in the 25th to 90th percentile of all unblended 1-component fits. 2-component fits shown include unblended transitions in which the low velocity component has a signal-to-noise ratio in the 25th to 90th percentile of the low velocity components of all 2-component lines.

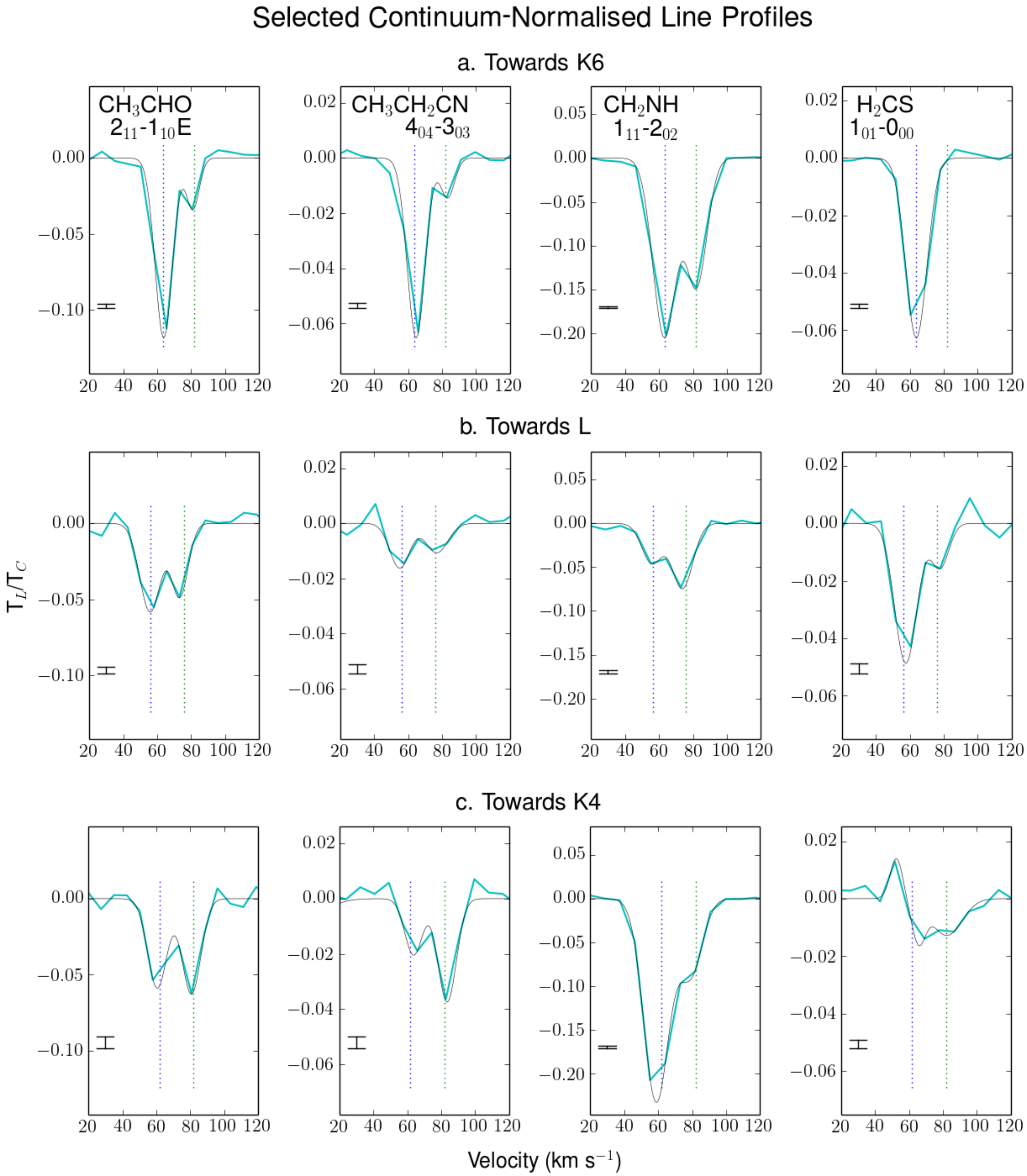

**Figure 13.** Line profiles of $CH_3CHO$ $2_{11}$-$1_{10}$E (39362 MHz), $CH_3CH_2CN$ $4_{04}$-$3_{03}$ (35722 MHz), $CH_2NH$ $1_{11}$-$2_{02}$ (33704 MHz), and $H_2CS$ $1_{01}$-$0_{00}$ (34351 MHz) reveal differences in the line optical depth ratios between all spatial positions and all velocity components. The data (cyan) are overlaid with the automated line fits (black), and vertical dotted lines indicate the velocities associated with the low and high velocity gas towards each spatial region as reported in Table 8. **a.** In K6, while $CH_3CHO$ and $CH_3CH_2CN$ have similar line profiles, the selected transition of $CH_2NH$ has a comparatively enhanced line strength in K6: 82 $\mathrm{km\,s^{-1}}$. Further, the line radiation by $H_2CS$ in the K6: 82 $\mathrm{km\,s^{-1}}$ is significantly depleted to below the detection threshold. Towards L (**b.**) and K4 (**c.**) the line profiles vary significantly, and line strengths do not scale linearly with the strengths observed towards K6. The scale of the ordinate is the same for each line towards all three regions, and the scale is set relative to the normalised line height in the K6: 62 $\mathrm{km\,s^{-1}}$ component. The root-mean-squared values of the extracted spectra are shown in the lower left corner of each panel.

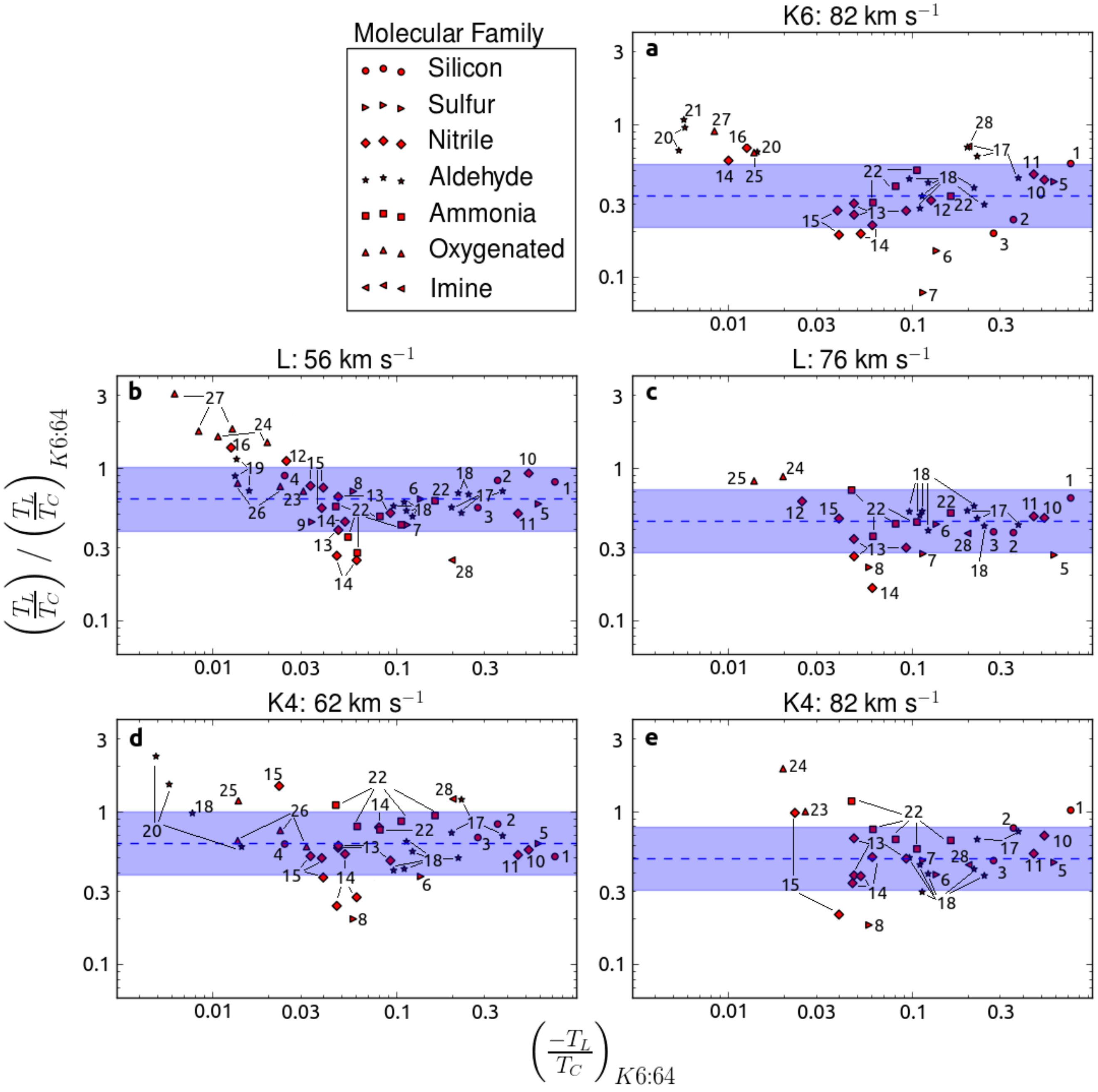

**Figure 14.** Line height ratios with respect to the K6: 64 km s$^{-1}$ component indicate statistically significant differences in gas phase molecular abundances or excitation between different spatial positions. In the plot, the abscissa shows the line height-to-continuum ratios of lines detected in K6: 64 km s$^{-1}$. Given the low excitation temperatures observed in this gas and the high background continuum temperature, this provides a proxy of the line optical depth towards K6: 64 km s$^{-1}$. The ordinate provides the normalized line ratios (NLRs) of the lines in the relevant gas component with respect to K6: 64 km s$^{-1}$. For all but the strongest lines, the y-axis values are proportional to the line optical depth ratio with respect to K6: 64 km s$^{-1}$. The median ratio is represented with the dashed line, and shading indicates the $\pm 3\sigma$ range. Represented data only include lines within the high spatial resolution portion of the spectrum (from 30 - 44.6 GHz) for selected families of molecules. Species are numbered as follows: 1 - 4 are SiO, $^{29}$SiO, $^{30}$SiO, and SiS. 5 - 9 are sulfur-bearing species SO, CCS, HCS$^+$, $H_2CS$, and OCS. 10 - 16 are nitrile species $HC_3N$, $CH_3CN$, $CH_2CN$, $CH_2CHCN$, $CH_3CH_2CN$, $HC_5N$, and CCCN. 17 - 21 are aldehyde species $NH_2CHO$, $CH_3CHO$, $CH_3OCHO$, *cis*-$CH_2OHCHO$, and *t*-$CH_2CHCHO$. 22 is $NH_3$. 23 - 27 are non-aldehyde oxygenated species $H_2CCO$, *c*-$H_2C_3O$, $H_2COH^+$, $CH_3OCH_3$, and *t*-$CH_3CH_2OH$. 28 is the imine species $CH_2NH$. Note that the apparent slope towards the low optical depth segment of the panels is related to the detection limit; because K6: 64 km s$^{-1}$ has the highest optical depth, lines that are weakly detected towards K6: 64 km s$^{-1}$ are detected towards other components only if they have higher than the median line optical depth. This does not imply that these points are unreliable, but implies that the lower left corners of each panel are below the detection threshold.

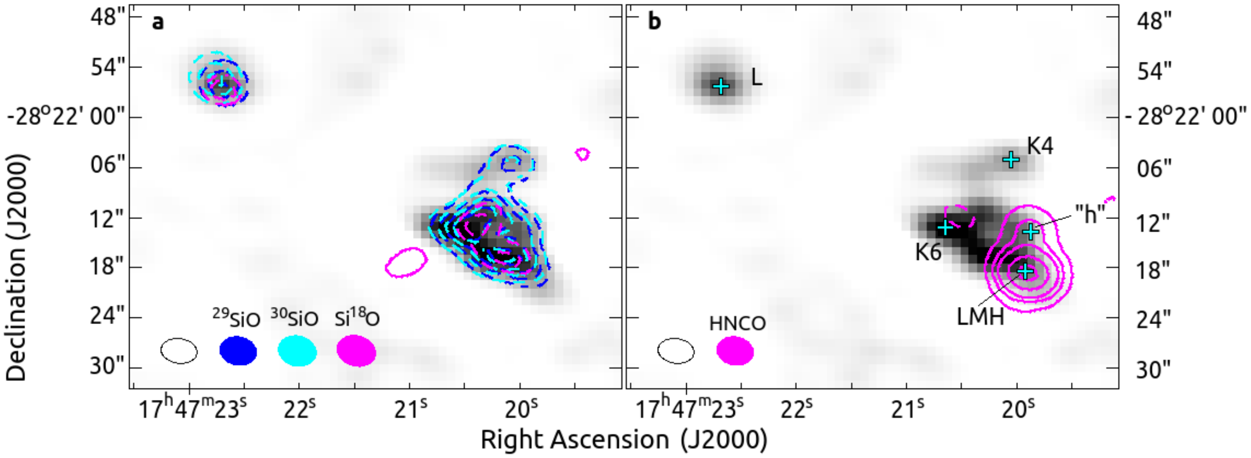

**Figure 15.** Integrated line contours of the (1-0) transitions of SiO isotopologues are anticorrelated with the $2_{02}$-$1_{01}$ transition of HNCO. **a.** $^{29}$SiO, $^{30}$SiO, and Si$^{18}$O are observed in absorption (dashed contours) against the continuum and exhibit no emission associated with the hot cores. **b.** HNCO is present in emission towards the LMH and "h" hot cores. A very weak absorption feature (with a contour at 2.5% of the peak line strength) is detected slightly north of K6. The crosses indicate the center positions of the elliptical regions from which spectra were extracted. The synthesized beams for the continuum and line images are shown in the lower left corner.

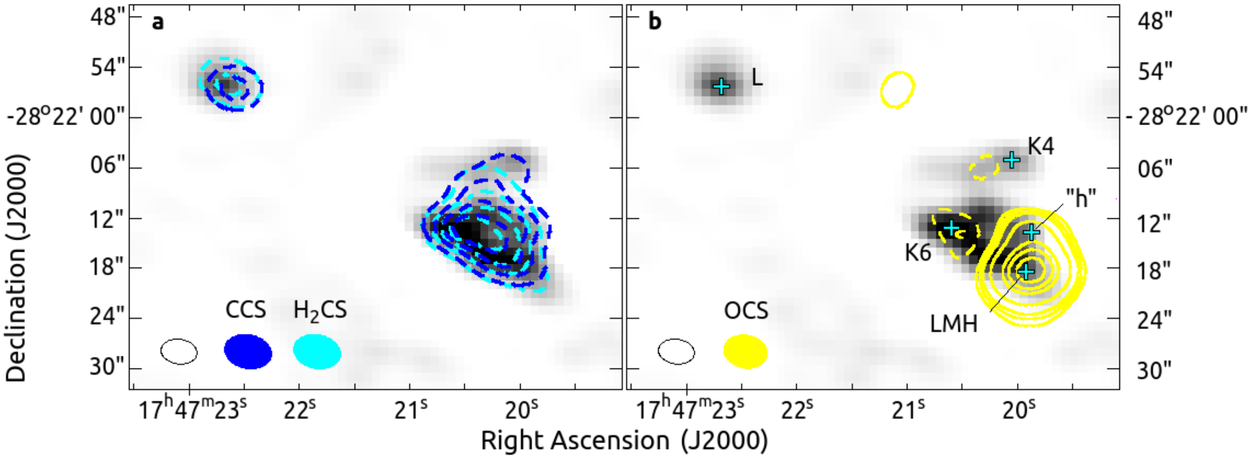

**Figure 16.** Integrated line contours of $H_2CS$ ($1_{01}$-$0_{00}$), CCS ($3_2$-$3_1$), and OCS (3-2). **a.** $H_2CS$ and CCS are observed in absorption (dashed contours) against K4, K5, K6, and L, with no detected emission from hot core regions. Contour levels are at 20, 40, 60, and 80 % of the peak line strength. **b.** OCS appears in emission from the hot core regions, the LMH and "h", with very weak absorption observed towards K6 and near K4. The contour levels are at 4.5, 7, 20, 40, 60, and 80 % of the peak line strength. The crosses indicate the center positions of the elliptical regions from which spectra were extracted. The synthesized beams for the continuum and line images are shown in the lower left corner.

This paper has been typeset from a TEX/ LATEX file prepared by the author.

## APPENDIX A
## AUTOMATED LINE FITTER CODE RELEASE

All scripts used for automated line fitting and semi-automated line identification are provided in the online journal and in GitHub at https://github.com/jfc2113/MicrowaveLineFitter. We provide instructions for use including a description of the input and output files and system requirements.

The scripts have been tested in IPYTHON version 0.12.1 with PYTHON 2.7.3, NUMPY 1.6.1, and MATPLOTLIB 1.1.1rc. PYTHON 2.7.3 includes the MATH and CSV modules that are used in the scripts.

The packaged file provided in the journal includes eight scripts, spectra characterized in this work, and csv files holding line data. Two of the scripts are run directly, namely 'FullCode.py' is run before 'VelocityFileMaker.py'. After optional adjustments by the user, 'VelocityFileMaker.py' uses the output of 'FullCode.py' to generate a final csv file that contains Gaussian fits to the full spectrum and line identifications. Of the remaining six scripts, five contain modules called in 'FullCode.py'. The modules and their primary purposes include:

- 'LineFind.py' grabs segments of the spectrum that contain lines, detecting "line-channels" with single-channel intensity values greater than $\sigma_{rms}\times$ an input threshold. The module also selects a set number of channels on either side of line-channels. The number of neighboring channels has a default value of 5, but can be adjusted when LineFind is called.
- 'FTinterp.py' interpolates a segment of the spectrum, outputting a spectrum with a factor of 3 improvement in the spectral resolution. It performs the interpolation by Fourier-domain zero padding. This should only be used for data with poor spectral resolution compared to the linewidths.
- 'Gfit.py' provides the most essential functionality; through 'FullCode.py', the function Gfit.GauFit is passed a single segment of the spectrum that contains one or more lines. Gfit.GauFit returns a 1- or 2-component Gaussian fit to a spectral feature within the segment. The script selects a specific portion of the line-containing segment and first attempts a one-component fit. It then follows an algorithm to adjust the section of the segment used for line-fitting and re-fit 1-component Gaussians. It passes information to 'G2criteria.py', which evaluates the fit against a set of criteria to determine whether a 2-component Gaussian fit is justified. The output of G2criteria determines whether Gfit.GauFit fits a 2-component Gaussian, following an algorithm to adjust the section used for line-fitting and attempting 2-component Gaussian fits.
- 'G2criteria.py' determines if a 2-component Gaussian fit is required. Gfit.GauFit provides G2criteria with information about the data and the best 1-component Gaussian fit achieved; G2criteria then determines if the data differs significantly from the 1-component fit, requiring a 2-component fit. G2criteria takes into account the signal-to-noise ratio of the line in question and the degree to which the data differs from the 1-component Gaussian fit. The primary factors considered include (1) the difference between the position of the absolute maximum of the data and the position of the 1-component Gaussian center; (2) the maximum residual between the data and the fit, compared to the rms noise level at that frequency tuning; (3) the mean residual between the data and the fit, compared to the rms noise level; (4) the width of the fit compared to the typical width of features. The criteria, mostly empirically determined, works very well for this dataset. However, we advise inspecting results obtained on other datasets carefully and likely adjusting the criteria, as they will change with the parameters of the data.
- 'LineID.py' provides semi-automated line identification of features fit over the full spectrum. FullCode compiles the output of Gfit.py and passes it to LineID, along with one or two csv files containing spectral line catalog data. The input csv files can quickly and easily be output from the ALMA Spectral Line Catalogue - Splatalogue[2] after selecting a set of molecules that might appear in your spectrum.

FullCode manages the full data spectrum, compiles the results of Gfit.GauFit, and calls LineID to output the data. All of the modules except G2criteria are written to be easily tunable, and the main parameters that users will want to adjust are specified and explained in the first section of FullCode. These parameters include: whether the results should be output; what plots should be produced; the names of input files; whether data interpolation is desired; information about the source including guidelines for appropriate linewidths and line velocities; and information about the data structure (e.g. how many separate data sections are in a single spectrum; in this work, the line-fitter inspected a spectrum including 11 tunings, each of which had different $\sigma_{rms}$ noise levels. If all tunings have the same noise level in the intensity units you are using, they can be treated as a single section).

FullCode requires a spectrum input in standard ascii format with frequency and baseline subtracted intensity. The file 'K6_fullSpec.txt', provided with the scripts, is in the correct format. If the user chooses to perform line identification, the script requires files containing recombination line or molecular line data output in csv format from any spectral line catalog. The line data should be formatted similarly to the files 'recombLines.csv' and 'molecularLines.csv', provided. If your source has recombination lines, we recommend preserving the file name of 'recombLines.csv', but including lines that are relevant for your frequency range. All csv files read into the code should be text csv files with UNICODE UTF-8 characters and a colon (:) as the field delimiter. The code outputs csv file data with this format as well.

FullCode plots the full data spectrum with the line fits overlaid, marking the locations of lines from the input catalogue data that are near the fit frequency centers. The code can output a csv file containing Gaussian line fits and possible line assignments. This output of FullCode is named ALLFITS_(r).csv, where (r) is the name of the source or region targeted. It contains:

- Gaussian line fit parameters (height, center frequency, and width in frequency units) of all features.
- two measures of the quality of the fit. First, the rms residual between the data and the fit; second, for 1-component fits, the file provides the offset between the frequency at which the data has its maximum absolute value and the Gaussian center frequency. Fits with abnormally large values may be suspect.
- the 'bin' indicates how the line was handled in Gfit.GauFit. Lines with bin = 0 are 1-component fits that were deemed appropriate. Lines with bin = 1 are 2-component fits that were found to be reasonable. For lines with bin = 2, the data significantly differed from the best 1-component fit obtained, however Gfit.GauFit was unable to obtain a reasonable 2-component fit and therefore used the best 1-component fit obtained. These should be inspected and possibly re-fit manually. For bin = 3 lines, the residual between the data and the fit is significantly larger than the noise level of the

---

[2] Available at www.splatalogue.net; Remijan et al. (2007)

spectrum. These should be inspected and possibly re-fit manually. Bin = 5 lines are entirely unreasonable, with very broad line widths or unreasonable line heights. They are used as placeholders to enable the code to proceed, and they will need to be re-fit. Of 617 components used to fit the spectrum towards K6, 360 have bin = 0, 242 have bin = 1, 1 has bin = 2, 12 have bin = 3, and 2 have bin = 5.

- possible atomic or molecular carriers of the detected Gaussian features. The output file lists any transitions from the input recombLines.csv and molecularLines.csv files that are within a specified velocity range of the detected features. It does not choose the most probable line at this step, but does so when the second code is run. These can be prioritized before running VelocityFileMaker.py to obtain the final line results.

Upon inspection of the results and manual updates to any bad fits, run VelocityFileMaker to generate a final output csv file containing line identifications and Gaussian fit parameters, with parameters listed in velocity space. VelocityFileMaker generates an output csv file entitled ‘velocity_ALL_(r).csv’. The file contains line rest frequencies, species, transitions, Gaussian fit velocities, heights, widths (in velocity units), center frequencies, and line types.

Before running VelocityFileMaker, edit parameters in ‘velEDIT.py’. Specify the names of the positions from which you extracted spectra, csv file input names, and velocity ranges that are appropriate for different types of lines, including recombination lines, molecular lines from the primary source, and additional lines observed in absorption by foreground diffuse or translucent clouds. The latter are only relevant in some lines-of-sight.

The code implements primarily kinematics-based consistency checks for line identifications, and can use one or two optional input csv files to prioritize line identifications. In order to minimize mis-identification, the final line-identification process operates on a priority system as follows:

- Priority 1: The code first inspects identified recombination lines for kinematic consistency and consistent line-intensities. This step requires a sufficiently large number of recombination lines to work well ($>$10 high signal-to-noise lines or $>$20 lines recommended), as it derives the mean Gaussian fit parameters and standard deviations in order to evaluate consistency. Lines that are self-consistent with the mean and standard deviations are output as firm line identifications, and assigned a “LineType” of either “H Recomb” or “He Recomb”. The script is not presently equipped to handle carbon recombination lines or absorption by recombination lines, but could be easily adjusted to do so. Features that are inconsistent with recombination lines include absorption lines, features that are significantly more broad or narrow than the mean, features that are too far from the mean center frequency, and lines that are significantly too strong or weak (e.g. an H$\,\gamma$ line is as strong as most H$\,\alpha$ lines). These may be output as tentative line identifications, which the user should inspect for line blending or data issues. If you do not have recombination lines, the code will simply move to Priority 2.
- Priority 2: The user has the option of specifying a file entitled ‘strongLines.csv’. (Of course, the file name can be changed per the users preference). The file “strongLines.csv” contains the strongest lines, which can be firmly identified prior to identifying weaker molecular lines. Lines that fall within the velocity range set in the function vEDIT.strongVrange are output as firmly identified, and assigned “LineType = strong”. Verify that the first two columns of your strongLines file are formatted the same as the file included in the package.
- Priority 3: The user can use a file entitled ‘SAClines.csv’, which indicates which transitions that may be observed in foreground absorption by diffuse and translucent cloud material, often referred to as Spiral Arm Clouds (abbreviated SAC). The foreground absorption components are at velocities that are inconsistent with the targeted cloud, and must be constrained in VelocityEditFile. Lines that fall within the velocity range set in the function vEDIT.SACvRange are output as firmly identified, and assigned the “LineType = SAC”. Verify that the first two columns of your SAClines file are formatted the same as the file included in the package.
- Priority 4: The code then assigns remaining lines tentatively assigned in ALLFITS_(r). In cases where multiple transitions are near the Gaussian center frequency, the line with the best kinematic match to the velocity, as specified in VelocityEditFile, is output. While this typically works well at centimeter wavelengths, we recommend inspecting lines that have multiple line entries in ALLFITS_(r), especially at higher frequency. If the code gets the “wrong” answer at this point, mark the line as blended, and consider only keeping the preferred line in ALLFITS_(r)
- Priority 5: Finally, the code outputs all fits that were not firmly identified in Priorities 1-4. These are given a Line Type of “Unidentified”. If a fit was associated with a known transition in ALLFITS_(r), the transition parameters will be output so that the user can decide whether or not to adopt the transition as identified.

While FullCode.py can fit most blended lines well, VelocityFileMaker does not handle identification of blended lines with much sophistication; however the prioritization system significantly improves the likelihood that most of the line radiation can be ascribed to the identified carrier transition. The user is responsible for inspecting the output of ALLFITS_(r) and velocity_ALL_(r) to ensure that any lines that may be blended (which should have multiple transitions listed in ALLFITS_(r)) are handled appropriately.

Within each priority, the script also handles wing components. As described in §3.2, numerous spectral features are non-Gaussian, including recombination lines, strongly masing lines, and optically thick molecular lines. In FullCode, in which the line fitting is conducted, after subtracting a best-fit 1- or 2-component Gaussian fits from the raw data (called the primary component(s)), high signal-to-noise lines may have wing components with intensities exceeding the detection threshold. Such wing features, which are typically weak as compared to the primary 1- or 2-component fit, are fit to the residual. VelocityFileMaker selects these features to prevent them from incorrectly being assigned to other molecular carriers or labelled as unidentified. Wing features are selected based on (1) their separation from the primary line component as compared to the width of the primary line component and (2) their height as compared to the primary line component. If a feature meets either of the following criteria, it is identified as a wing of an identified line and the velocity is calculated with respect to the rest frequency of that line. The criteria include:

(i) $\frac{H_{\rm Feature}}{H_{\rm Primary}} < 0.22$ and $v_{\rm Feature} - v_{\rm Primary} < \Delta v_{\rm Primary}$

(ii) $\frac{H_{\rm Feature}}{H_{\rm Primary}} < 0.05$ and $v_{\rm Feature} - v_{\rm Primary} < 1.5 \times \Delta v_{\rm Primary}$,

for the line heights, velocity centers, and FWHM widths $H$, $v$, and $\Delta v_{\rm Primary}$, respectively. These are assigned “LineType = wing”. Within each priority, VelocityFileMaker identifies the primary components, which must be consistent with the kinematic information input, and then selects any wings associated with these lines. As such, the recombination lines and wings of recombination lines are identified, followed by designated “strong lines” and the wings of strong lines, etc.

## APPENDIX B
## FULL SPECTRA AND LINE IDENTIFICATION FIGURES

The raw data spectra extracted towards K6, L, and K4 are provided with the output of the line fitter overlaid and line identifications labeled. All data are frequency shifted to the nominal source velocity of 64 $\mathrm{km\,s^{-1}}$. The following conventions are used in all figures. Tentative identifications are noted with a '?', as are unidentified lines suspected to be artifacts. Strong masing transitions are marked with '$Maser$', blended lines are marked with '$Blend$', and line fits that have been adjusted from the output of the line fitter are marked with '$Adj$'. In cases where the line-fitter determined a 1-component fit that we suspect to be a 2-component transition with insufficient signal-to-noise to be identified as such by the fitter, the species is marked with '$BC$'.

For cases in which a transition has blended spectral structure (such as blended transitions of A and E states), the listed transition indicates what components are expected to be blended, with the first listed component corresponding to the state that is strongest or best matches the expected source velocity. The transition listed first sets the rest frequency in Column 1 in the table provided in Appendix C.

Recombination lines are marked at 75, 76, and 64 $\mathrm{km\,s^{-1}}$ for K6, L, and K4, respectively. Identified molecular line components are marked at the following velocity components:

K6: Primary velocity components are at 64 and 82 $\mathrm{km\,s^{-1}}$; translucent cloud components are at 6, -30, -73, and -106 $\mathrm{km\,s^{-1}}$.
L: Primary: 56 and 76 $\mathrm{km\,s^{-1}}$; translucent cloud: 35, 20, -5, -35, -75, and -106 $\mathrm{km\,s^{-1}}$.
K4: Primary: 62 and 82 $\mathrm{km\,s^{-1}}$; translucent cloud: 2 $\mathrm{km\,s^{-1}}$.

Tentatively identified velocity components of firmly identified transitions are marked with a dashed pointer. For lines identified in the high velocity gas but not in the low velocity gas, the low velocity component is marked with a dotted line. Figure 17 illustrates these conventions.

### Notes on U-lines, Tentative U-lines, and Line Contamination

The figures and tables in Appendices B and C include firmly identified features, contamination from flux originating from other locations on the image ("contam"), tentatively identified features (marked with a "?"), unidentified lines (marked with "U" in figures and tables and referred to as U-lines), and tentative U-lines (marked with "U?" in figures and tables and referred to as "U?-lines").

Nearly all instances of line contamination are present in the spectrum of K6 and are lines that originate in the LMH or "h" hot cores. In spectra extracted from the high spatial resolution data (29.8 to 44.6 GHz), the hot cores are sufficiently separated from the elliptical region placed on K6. As a result, the line emission from the hot cores does not generate artifacts in the spectra towards the regions characterised here for frequencies $\nu < 44.6$ GHz. In this region of the spectrum, we have carefully inspected the images and spectra to verify that strong lines in the hot cores do not have imaging artifacts including negative bowls that are detected in K6, K4, and L. In the spectra extracted from the low resolution data (towards K6 and L), no imaging artifacts are observed towards L, while 30 imaging artifacts are present in the spectrum of K6. The authors have carefully inspected the images and spectra to verify that these are properly handled. The instances of contamination occur more frequently in the lowest resolution image (from 44.6 - 46.5 GHz) than in any other image, as would be expected. In cases where line absorption is observed towards K6 and line emission is produced in the LMH and/or "h", the line profiles in the low resolution spectra will not be representative of the true line flux towards K6. For this reason, we excluded low resolution spectra from the analysis of line ratios.

In addition to the imaging artifacts towards K6, a single feature is labeled as contamination towards L in the high spatial resolution portion of the spectrum. The methanol masing transition at 36 GHz appears as an absorption feature in the spectrum of L. Inspecting the image however, it is clear that imaging artifacts are implicated, as the very strong masing transition has limited dynamic range and image fidelity. We have inspected the images and spectra to ensure that the masing features identified towards K4 and K6 appear to arise from these regions. No instances of line contamination were observed towards K4.

Tentative U-lines (U?-lines) are features that meet the detection threshold, but upon inspecting the spectra and images, the authors remain unconvinced that a real line is present. As noted in §3.2, with the established threshold of $3.5\sigma$, one channel in 2149 line-free channels should meet the detection threshold assuming perfect baseline subtraction and frequency-independent noise within each tuning. With minor baseline residuals, it is reasonable to expect an average of $\sim$1 falsely detected feature per tuning. In the spectra of K6 and L, composed of 11 tunings, we report 11 and 10 U?-lines respectively consistent with this expectation; in the spectrum of K4, composed of 7 tunings, we report 11 U?-lines. The number in emission and absorption are similar, as would be expected for random noise and baseline variations.

As is typical of line surveys of Sgr B2, unidentified transitions are detected in the spectra towards all three positions. However, while a large fraction of detected lines are unidentified in most surveys of the LMH hot core (see e.g. Belloche et al. 2013; Nummelin et al. 1998), roughly 90% of all detected features are confidently assigned towards K6, L, and K4. Of the 496 features detected towards K6 (excluding contamination from the LMH and "h"), 89% are confidently assigned, while tentative assignments, U-lines, and U?-lines compose 2, 7, and 2% of the detected features, respectively. Towards K6, three of the U-lines are observed at two velocity components, with velocities consistent with the 64 and 82 $\mathrm{km\,s^{-1}}$ components characterised in §3.2. An additional 23 lines are observed in absorption at a single velocity component, and 4 are observed in emission. The fraction of U-lines in emission is thus $\sim$12%, significantly larger than the 1% and 2.5% observed for firmly assigned molecular lines (excluding the methanol masing transitions) in the low and high velocity gas, respectively.

Towards L, 93% of the 273 detected features (excluding contamination) are firmly identified. Tentative assignments, U-lines, and U?-lines compose 2.6, 1.1, and 3.7% of the transitions, respectively. Only three U-lines are reported towards L, and all are in absorption. Two of the three U-lines in L are detected in absorption towards K6, and the third does not meet the detection threshold in K6, but a clear absorption feature is present towards K6. Excluding recombination lines and U?-lines, all detected molecular lines are in absorption towards L. Neither strong maser transitions nor weakly masing transitions are detected towards L.

Of the 192 lines detected towards K4, 90% are firmly identified; tentative assignments, U-lines, and U?-lines compose 1.6, 2.6, and 5.8% respectively. Weak masing constitutes 3 and 2% of the firmly detected molecular lines in the low and high velocity gas, respectively, in K4, and one of the five U-lines observed towards K4 appears in emission. Two of the absorbing U-lines detected in K4 are also detected in K6, but K4 and L have no U-lines in common with one another. It is possible that the U-line observed in emission towards K4 is produced by $H_2CS$ at the same velocity as the methanol masers towards K4.

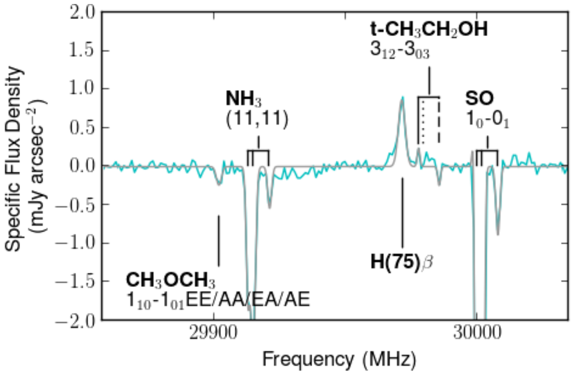

**Figure 17.** A segment of the spectrum towards K4 illustrates the marking conventions used in this appendix. The t-CH$_3$CH$_2$OH transition is firmly detected at 82 km s$^{-1}$, indicated by the solid line pointer. No emission or absorption is detected at 62 km s$^{-1}$, although this component is typically the most prominent. The dotted line marks 62 km s$^{-1}$ , at which we surprisingly detect no line radiation. Additionally, a 2 km s$^{-1}$ component is tentatively detected, producing a dashed pointer. The transitions of SO and NH$_3$ each have three firmly identified velocity components marked by pointers at 82, 62, and 2 km s$^{-1}$. The position of CH$_3$OCH$_3$ at 62 km s$^{-1}$is marked by the single pointer at 62 km s$^{-1}$. Pointers for recombination lines are at 65 km s$^{-1}$.

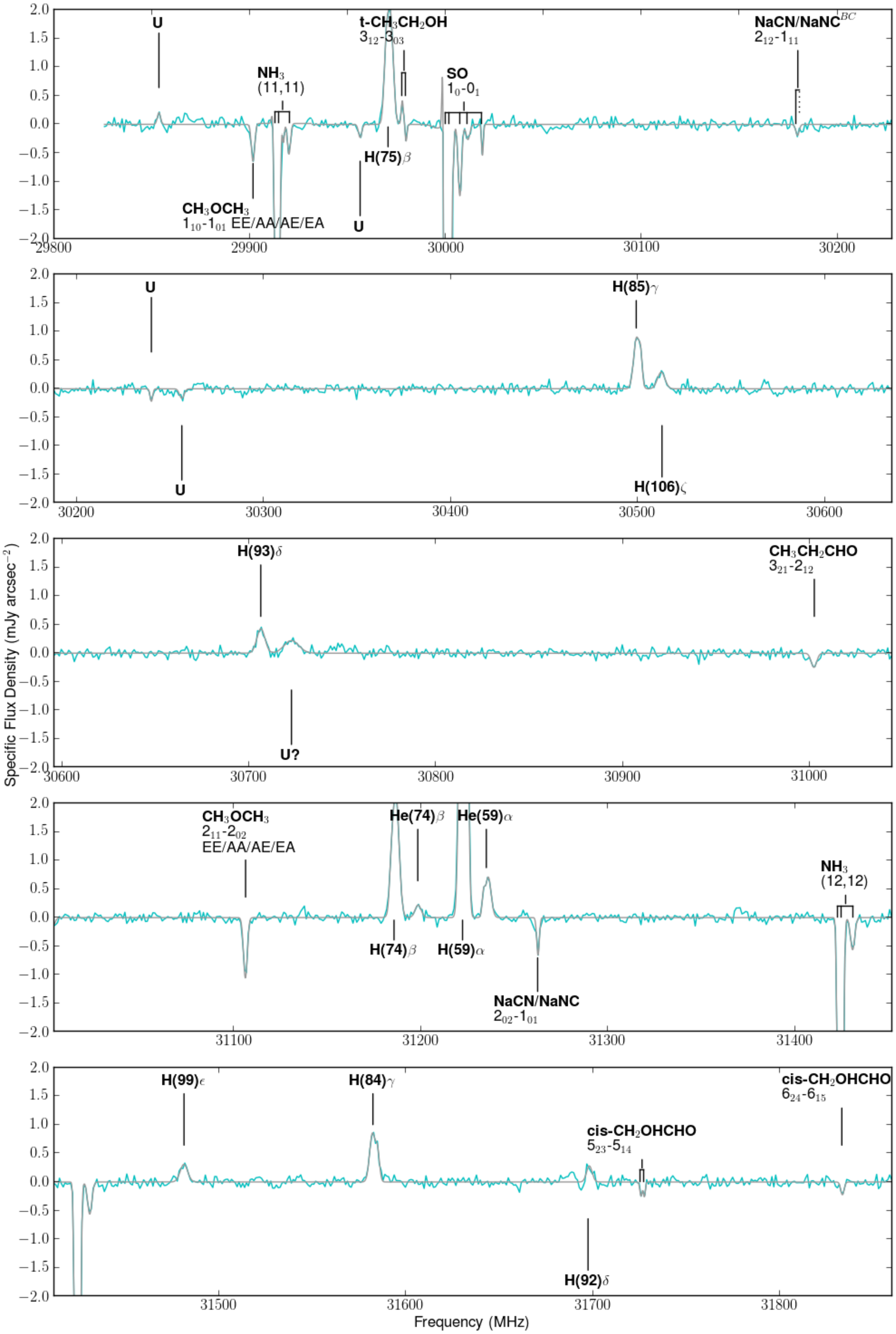

**Figure 18.** Spectrum Towards K6.

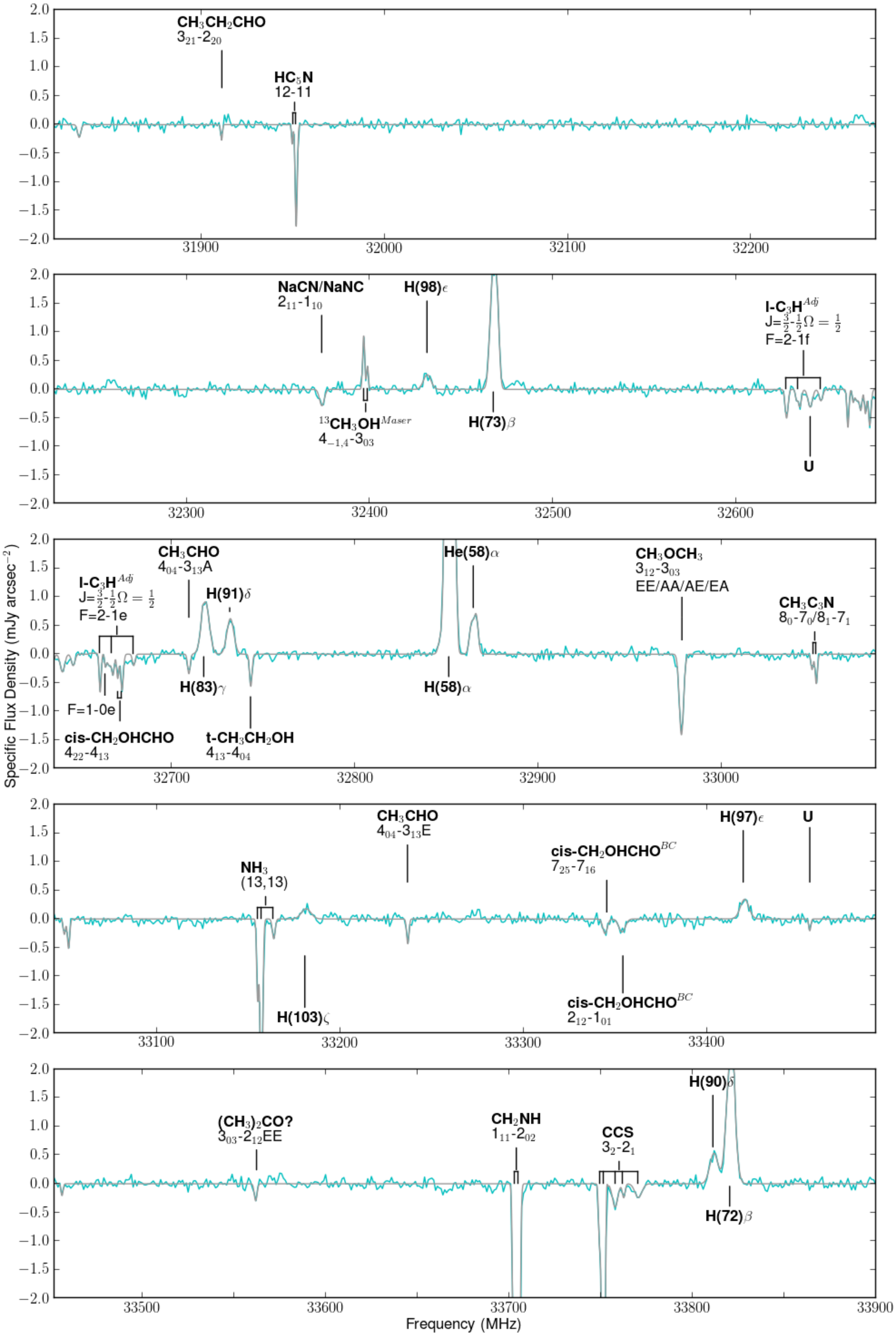

**Figure 19.** Spectrum Towards K6.

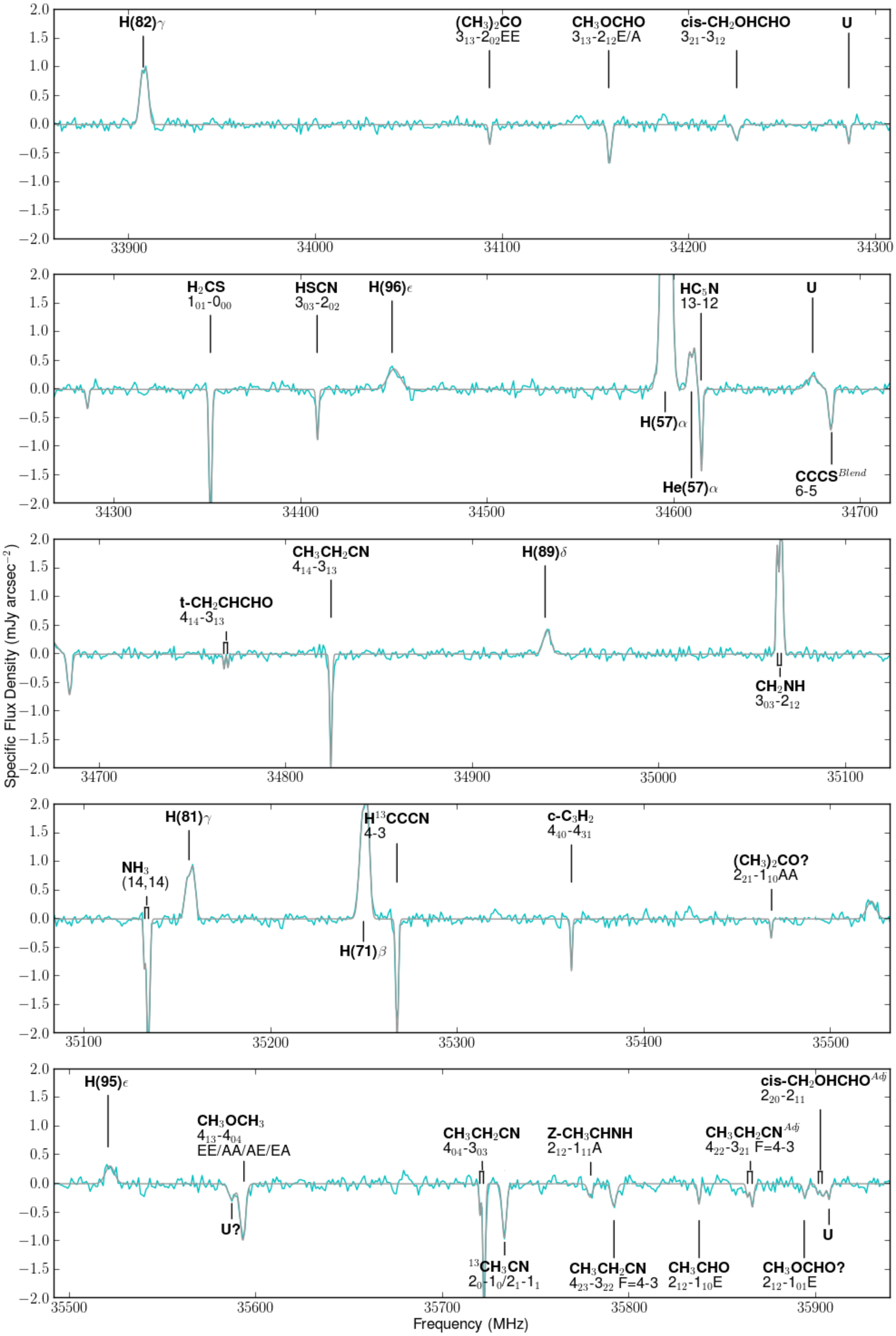

**Figure 20.** Spectrum Towards K6.

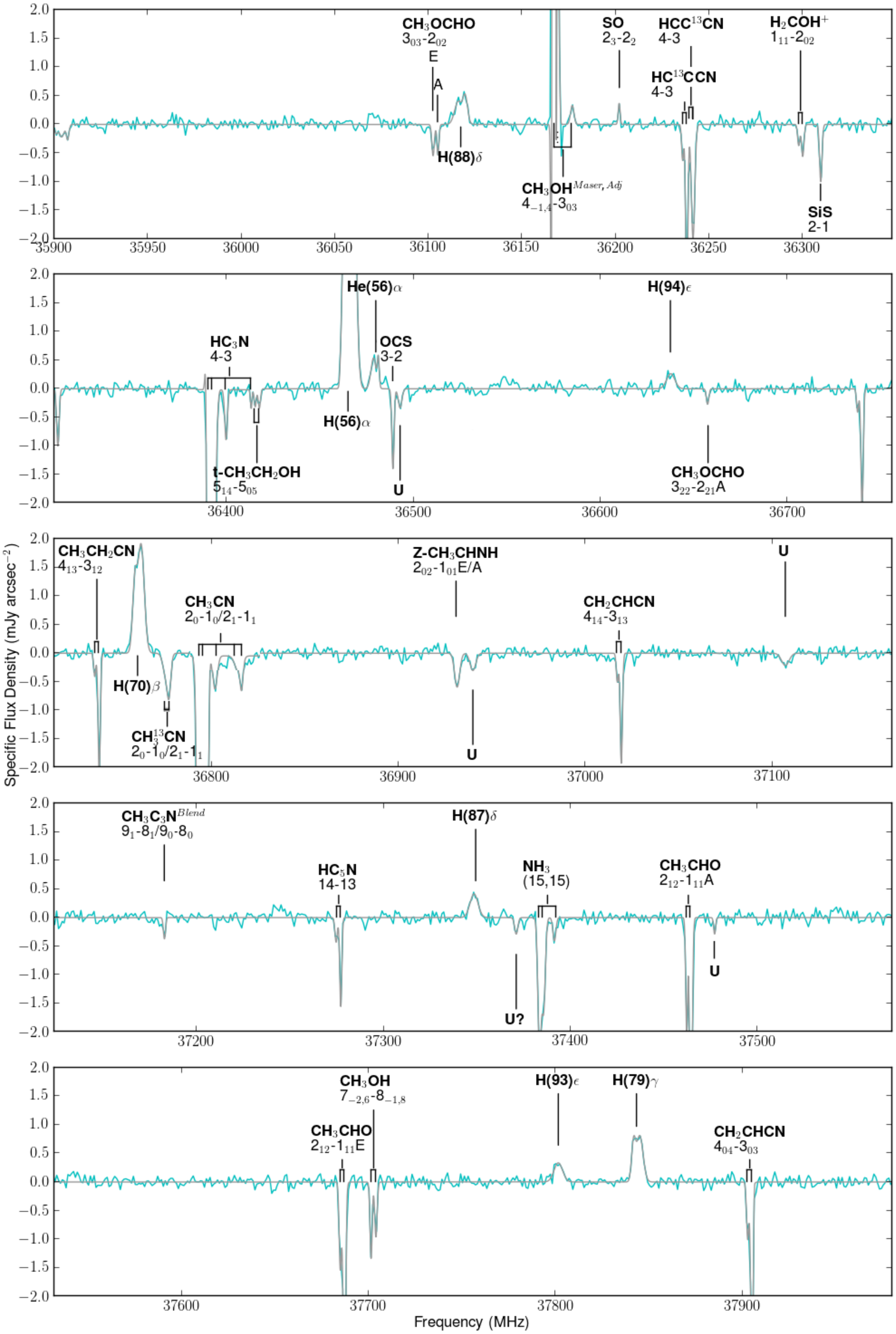

**Figure 21.** Spectrum Towards K6.

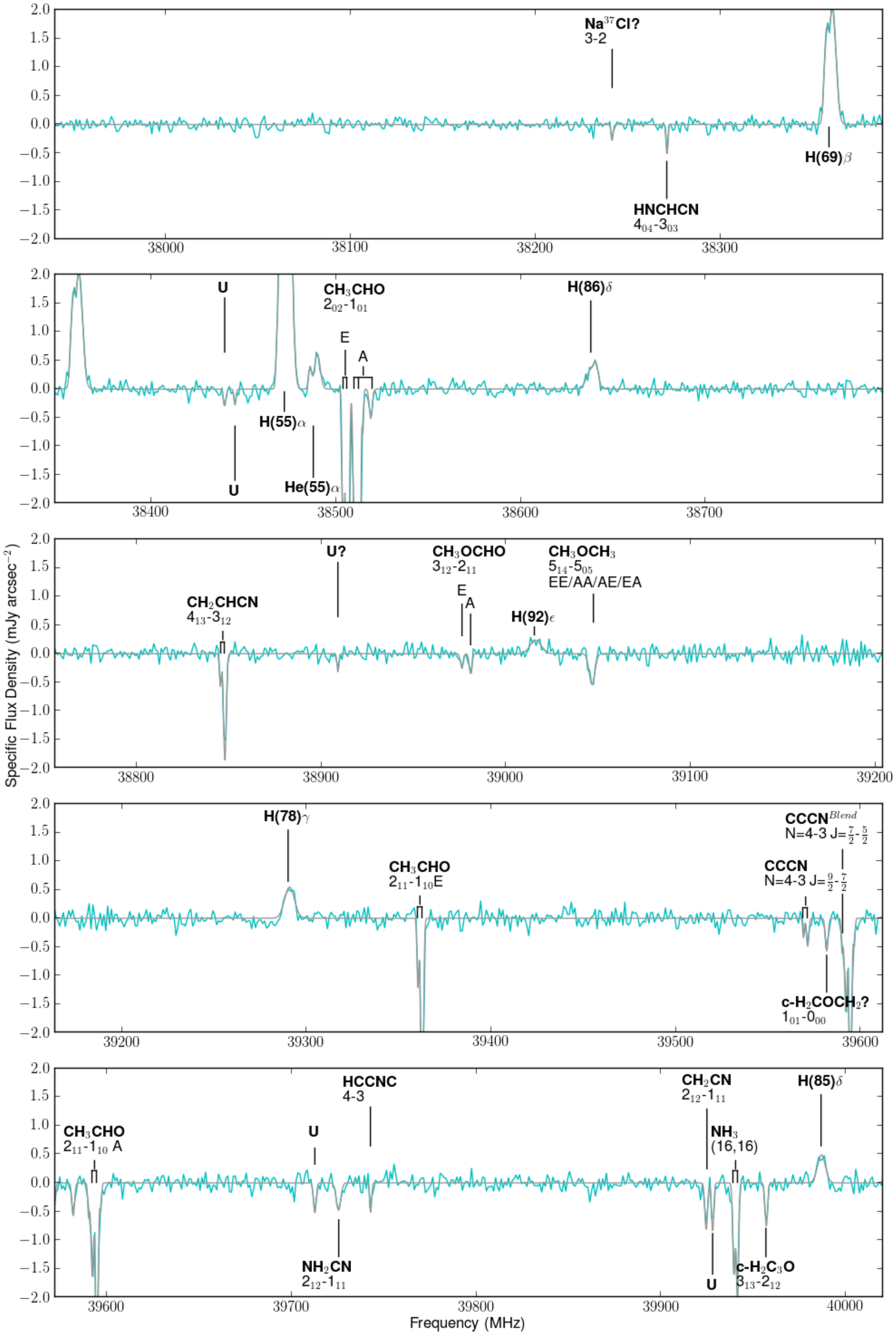

**Figure 22.** Spectrum Towards K6.

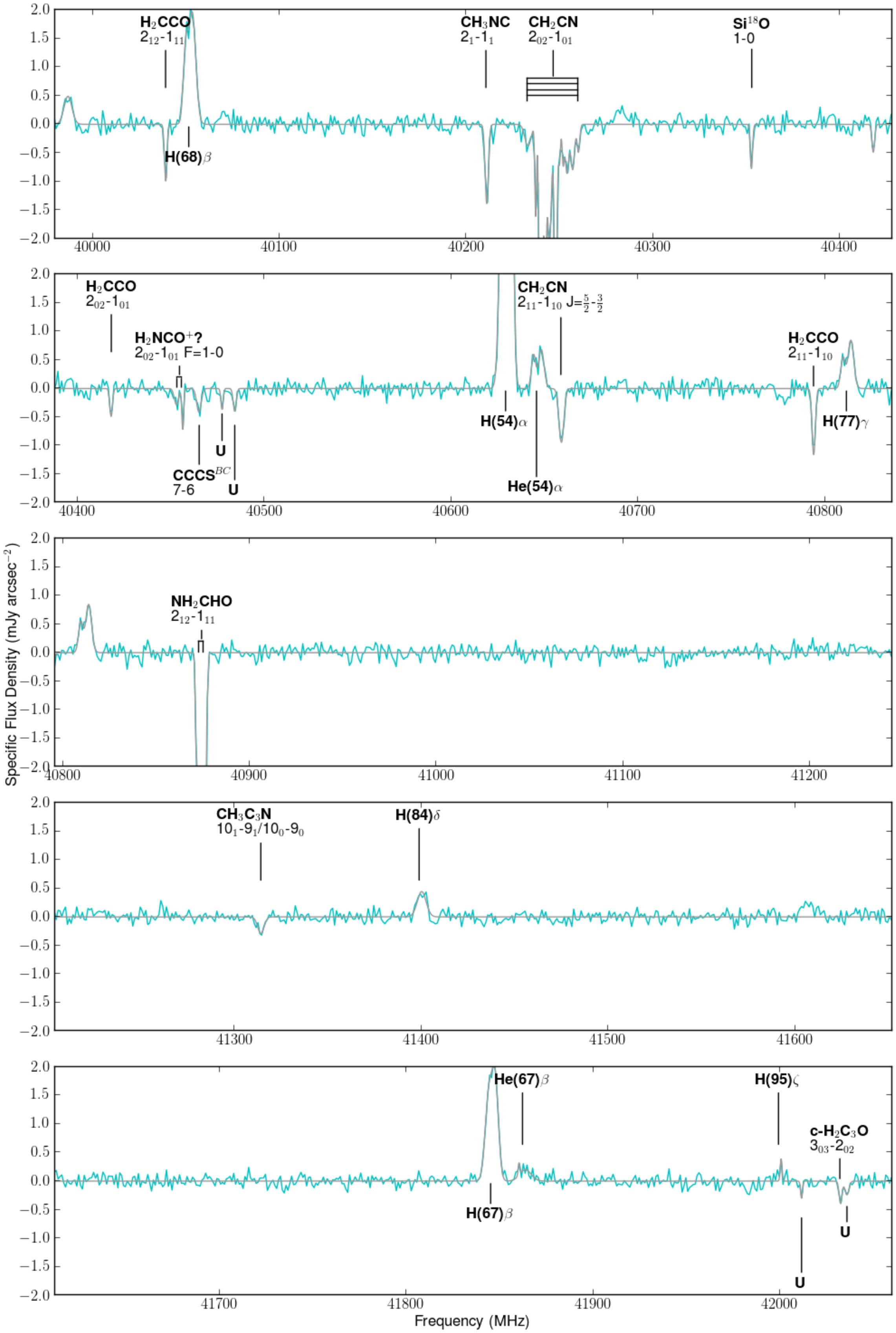

**Figure 23.** Spectrum Towards K6.

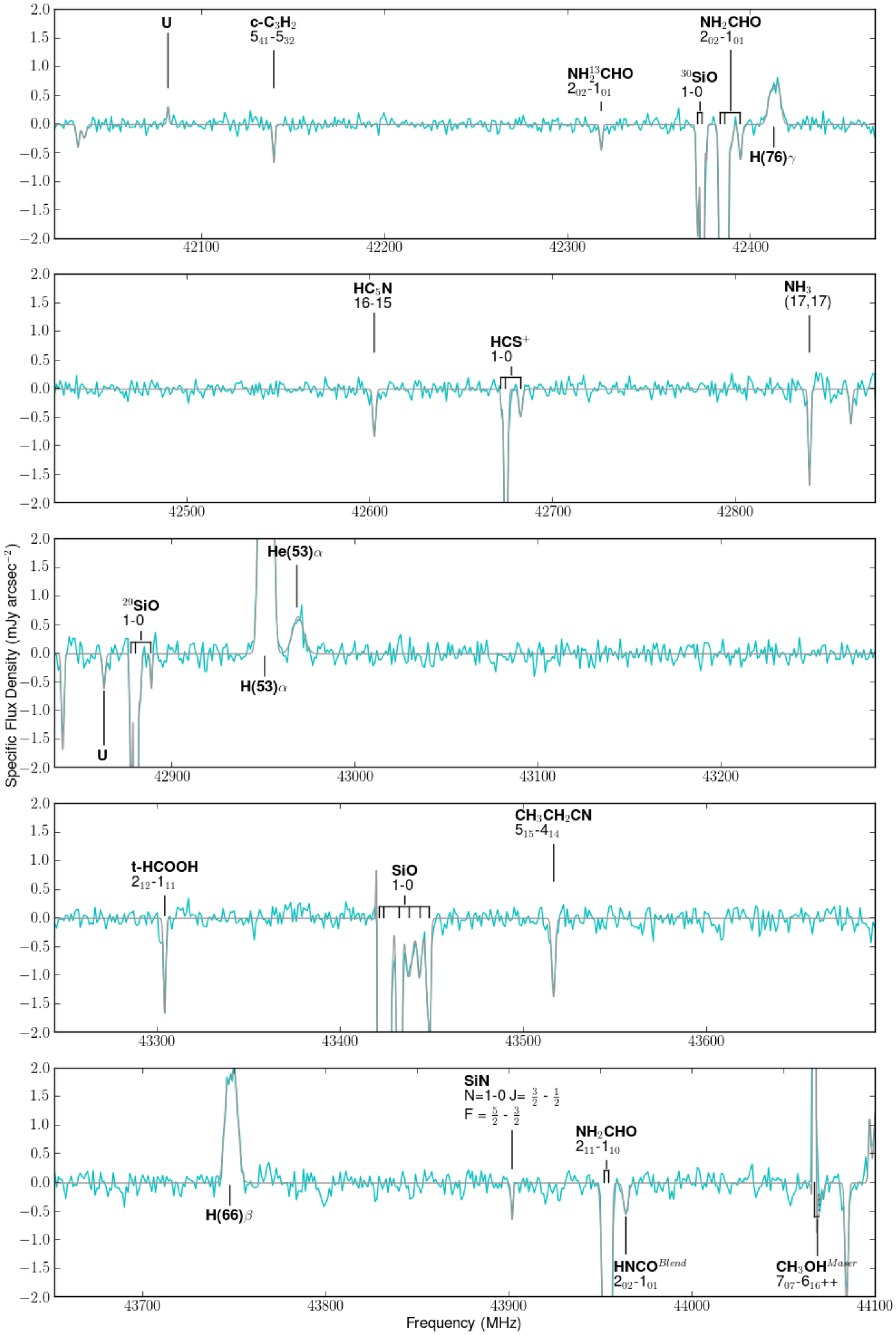

**Figure 24.** Spectrum Towards K6.

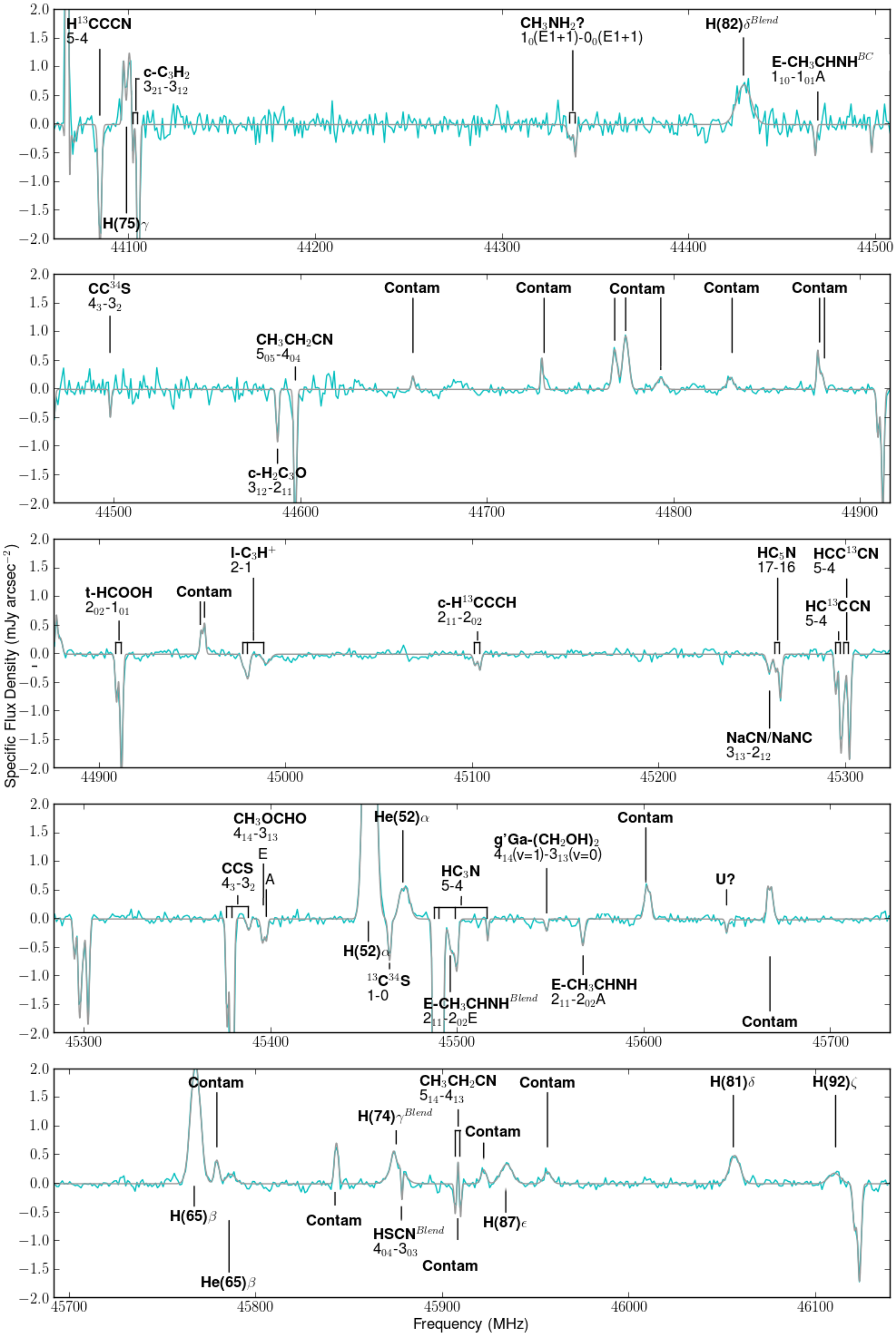

**Figure 25.** Spectrum Towards K6.

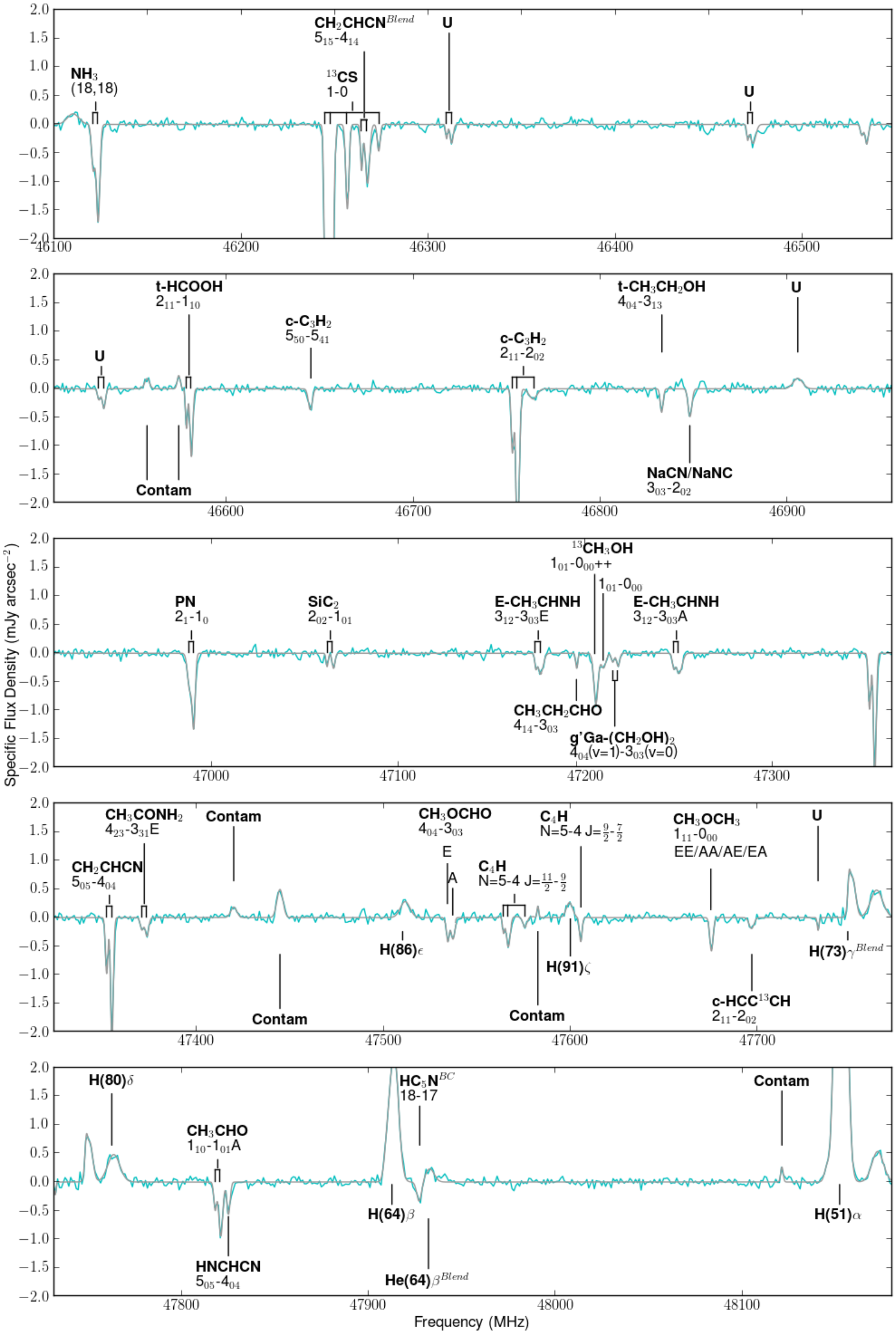

**Figure 26.** Spectrum Towards K6.

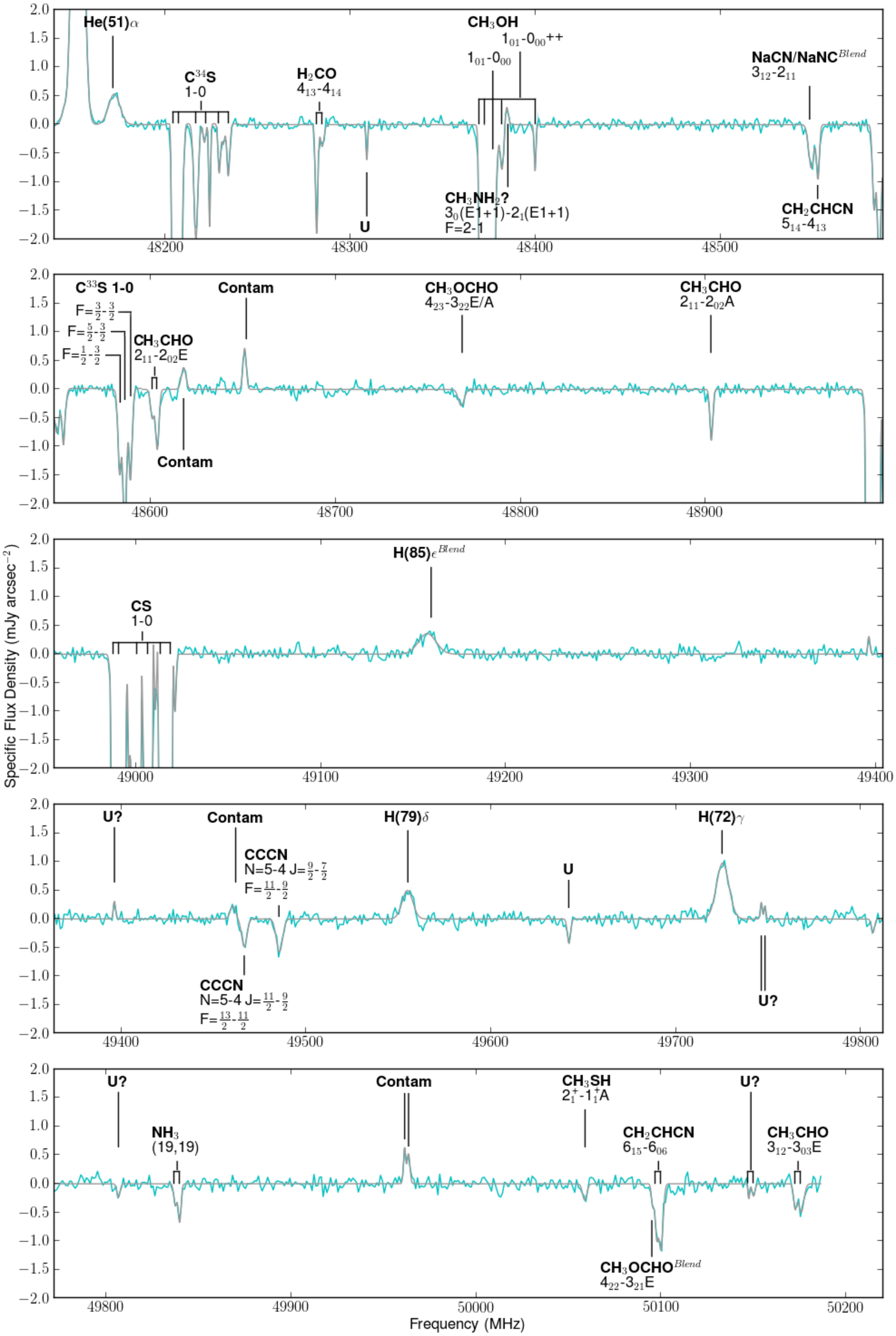

**Figure 27.** Spectrum Towards K6.

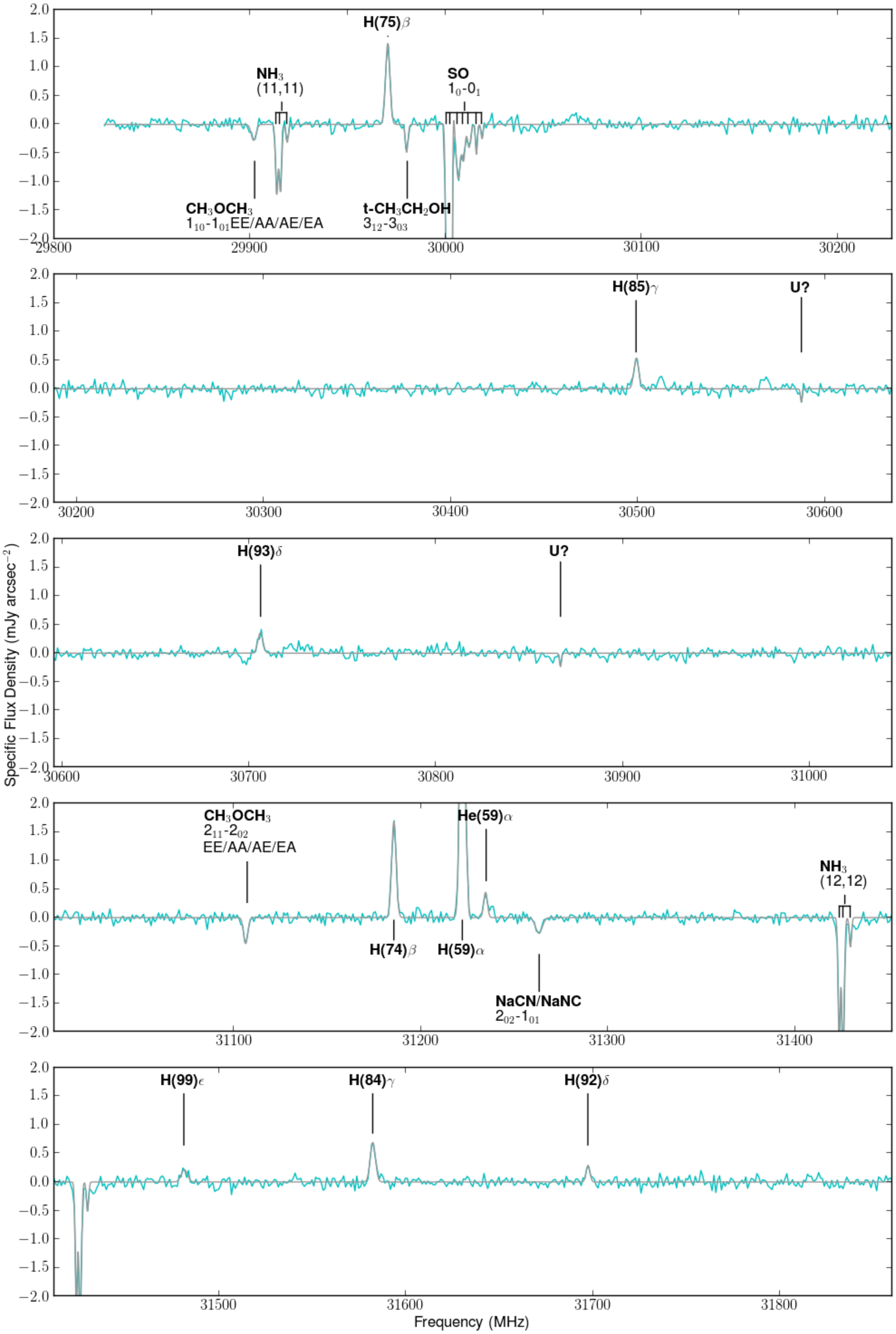

**Figure 28.** Spectrum Towards L.

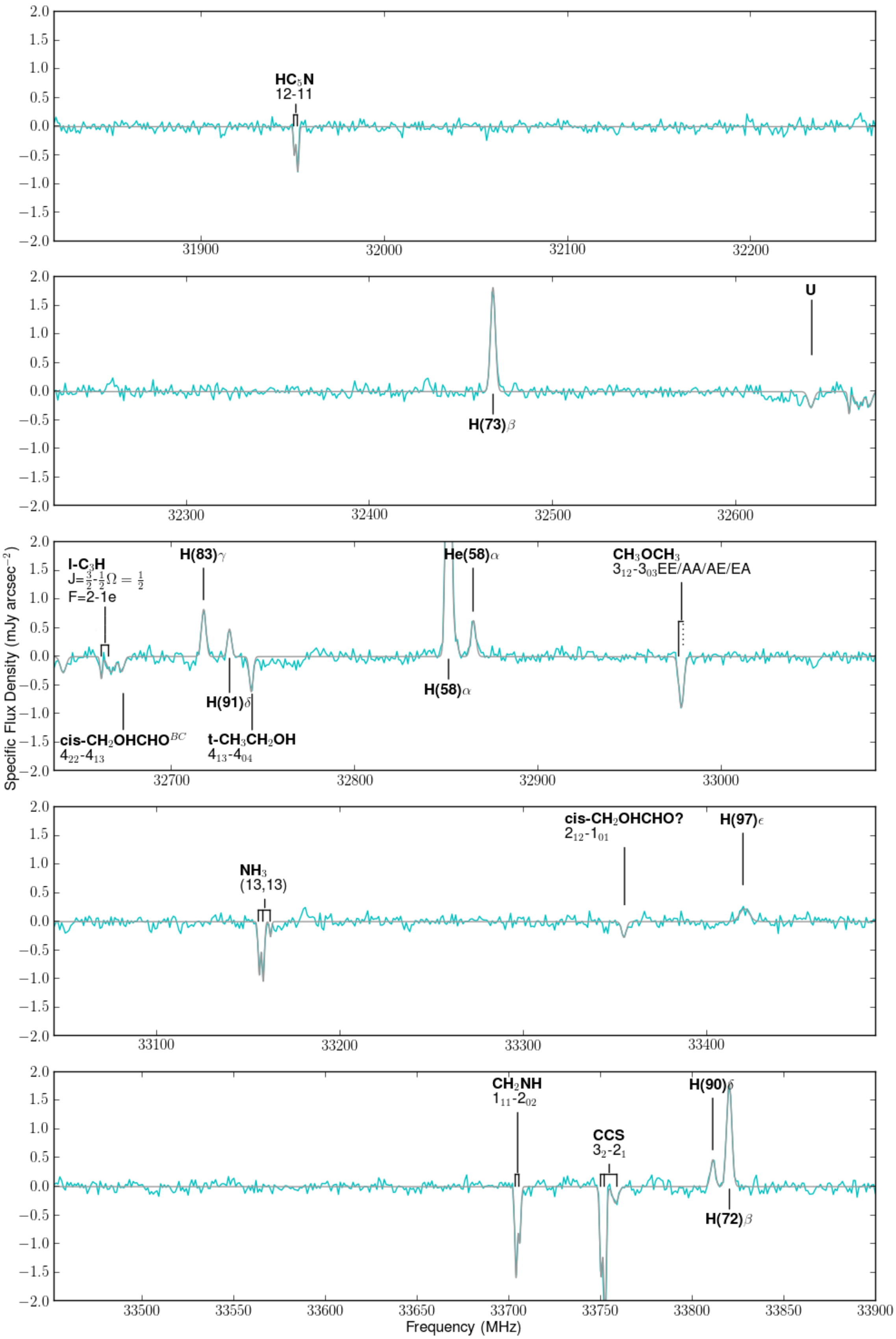

**Figure 29.** Spectrum Towards L.

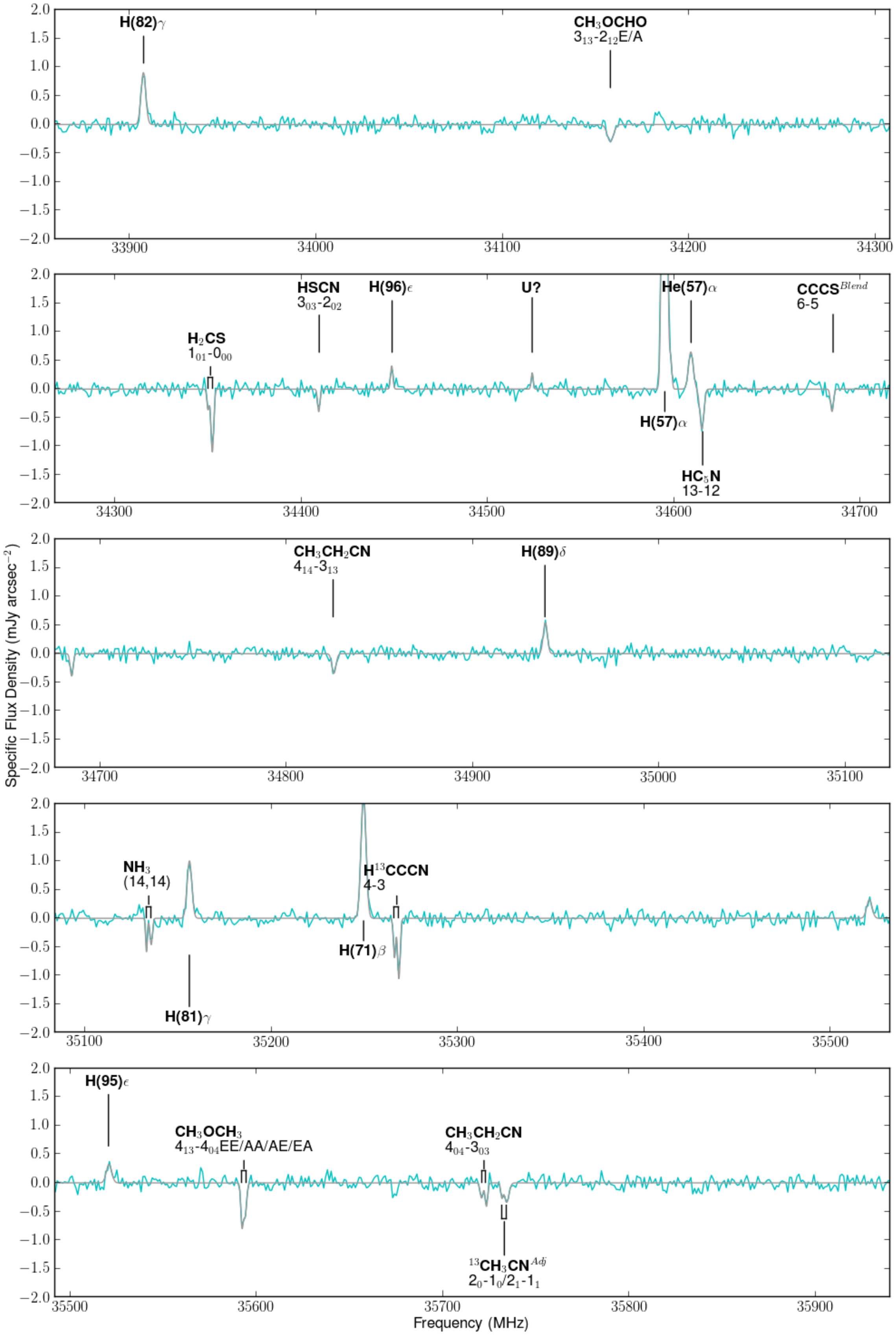

**Figure 30.** Spectrum Towards L.

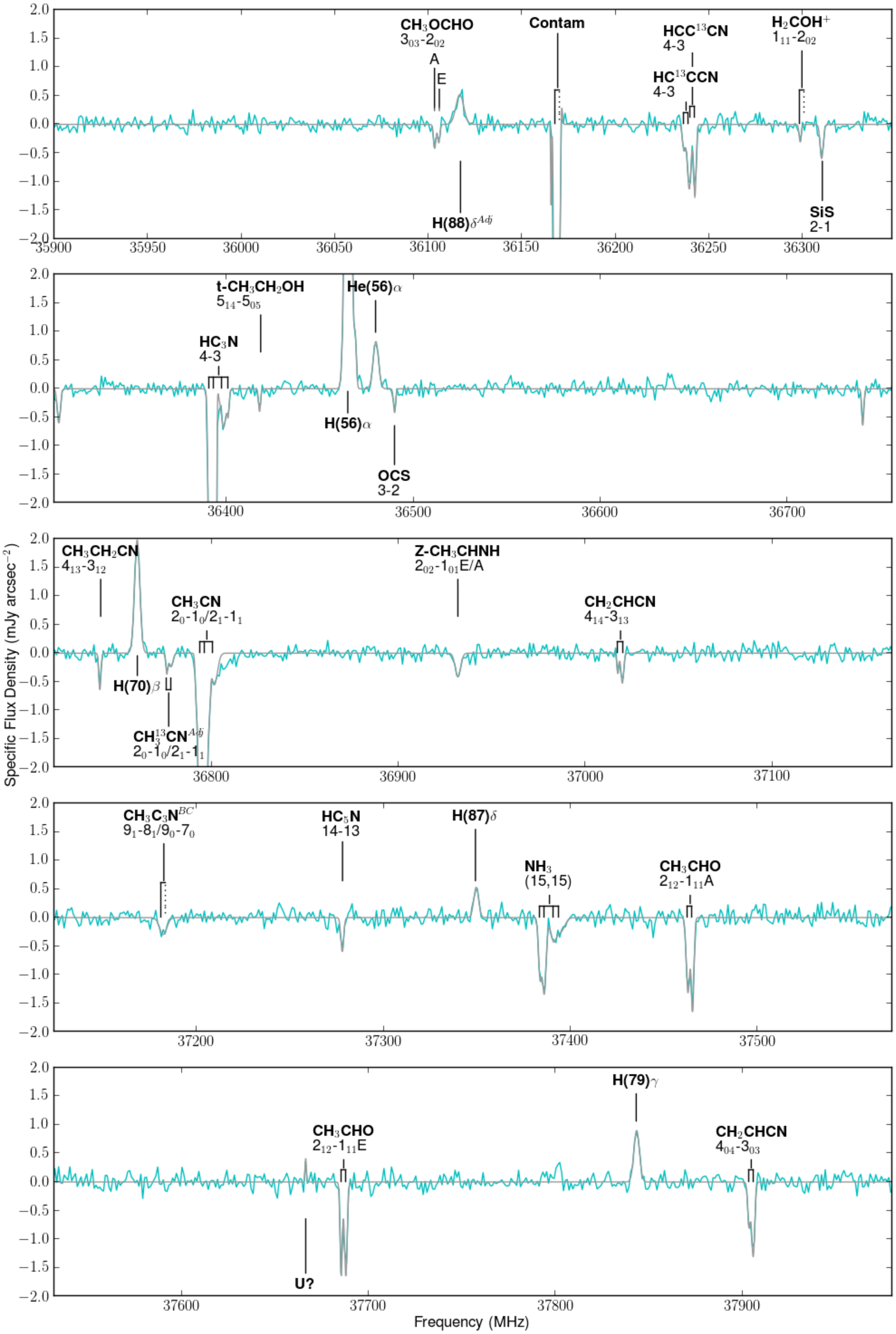

**Figure 31.** Spectrum Towards L.

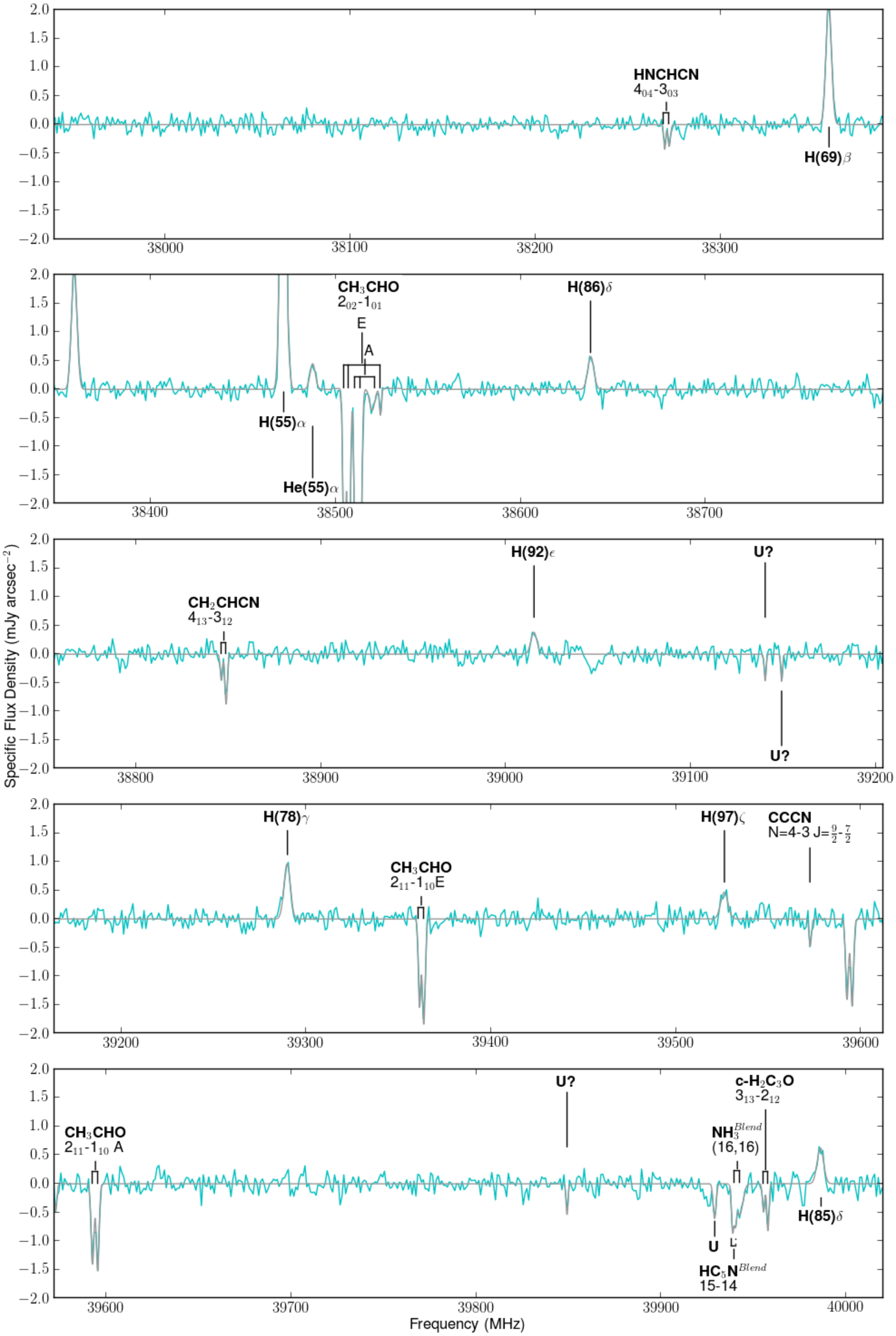

**Figure 32.** Spectrum Towards L.

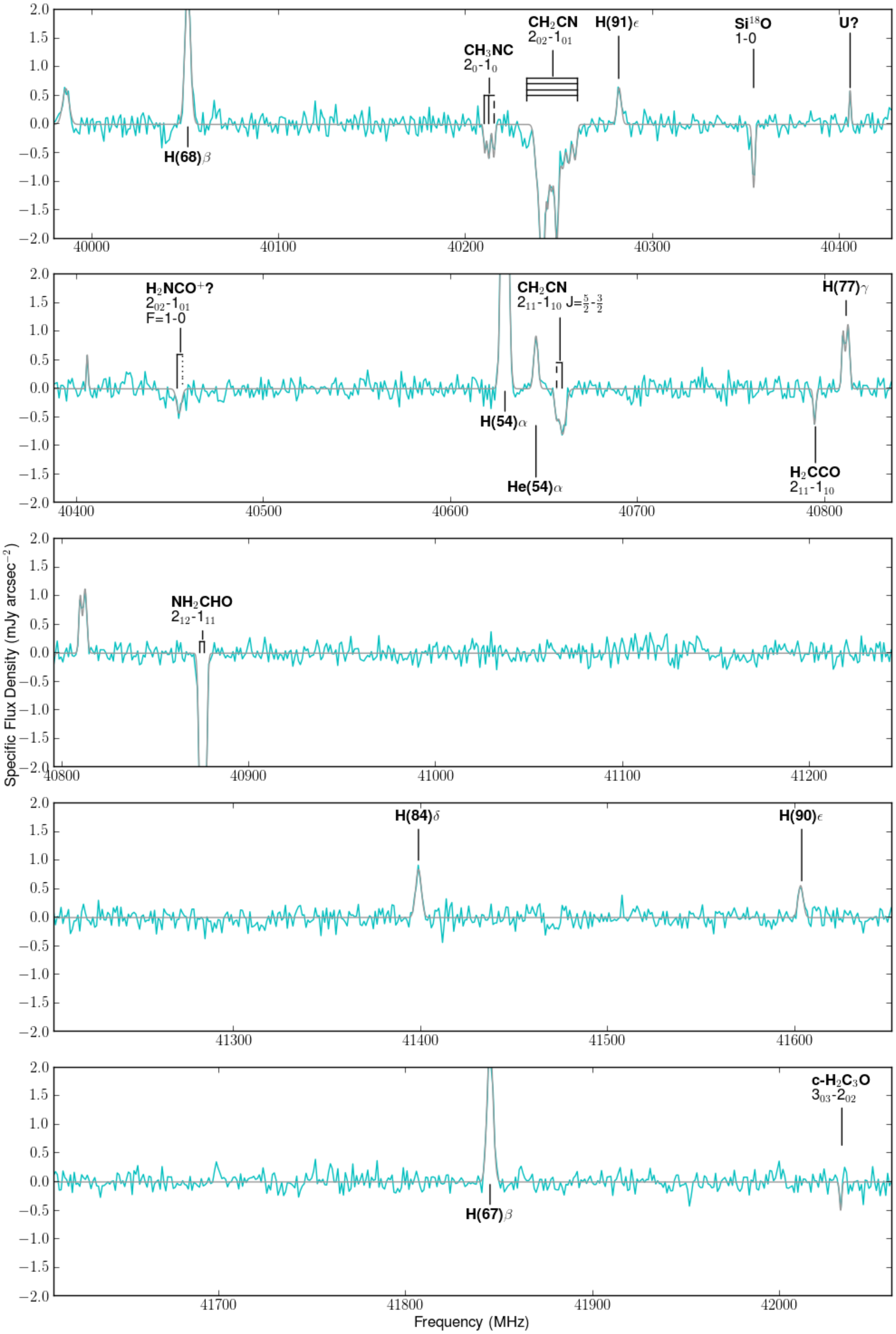

**Figure 33.** Spectrum Towards L.

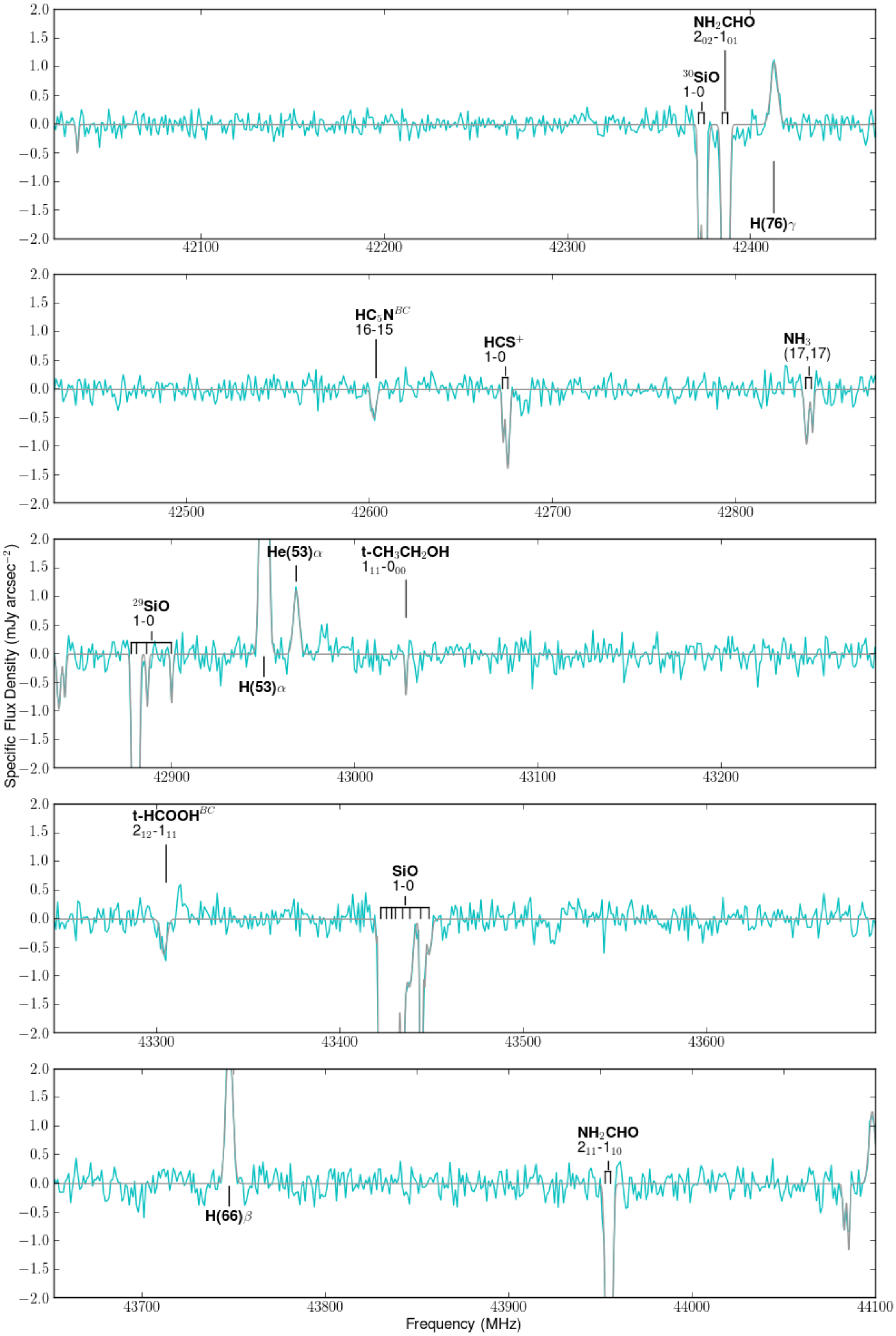

**Figure 34.** Spectrum Towards L.

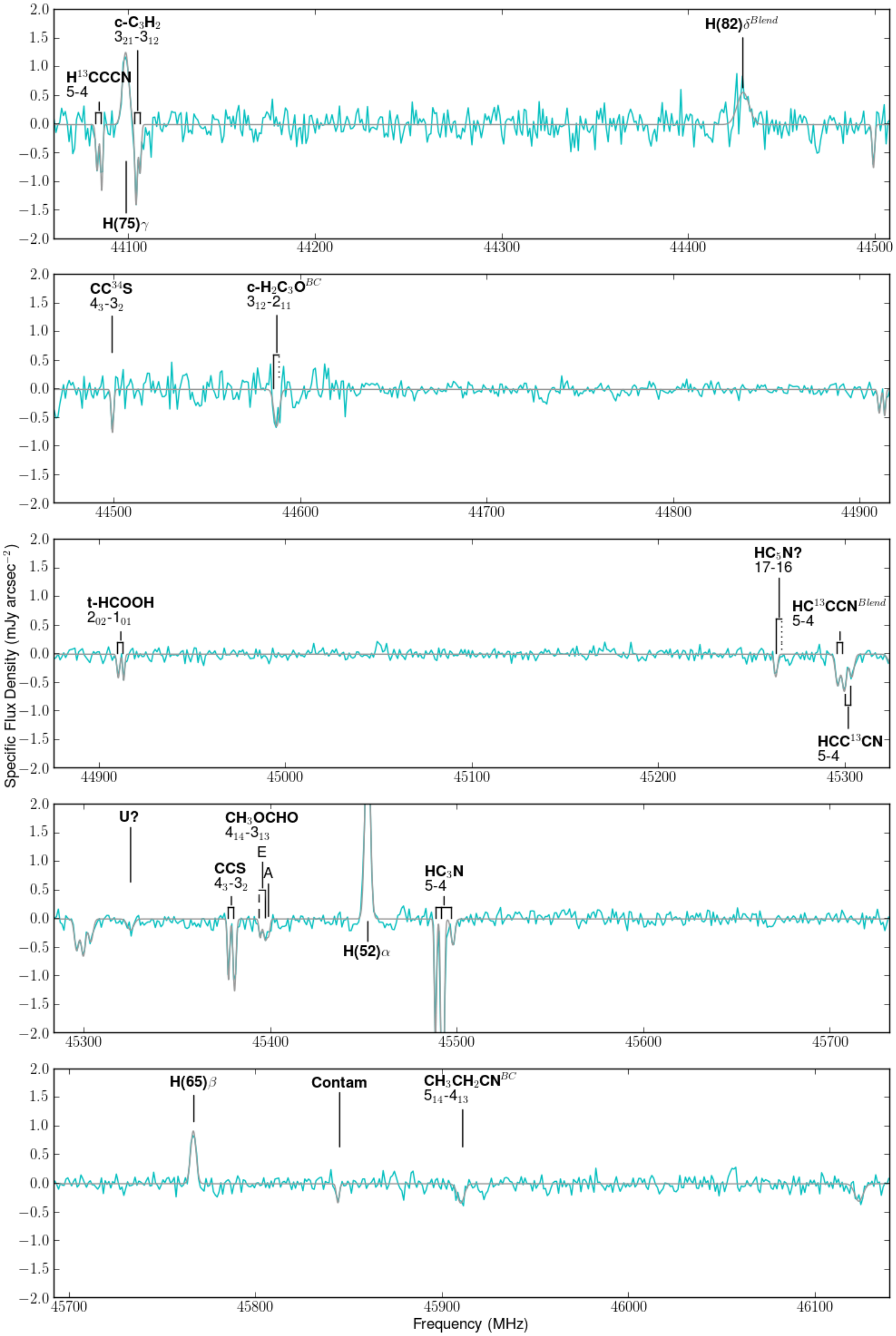

**Figure 35.** Spectrum Towards L.

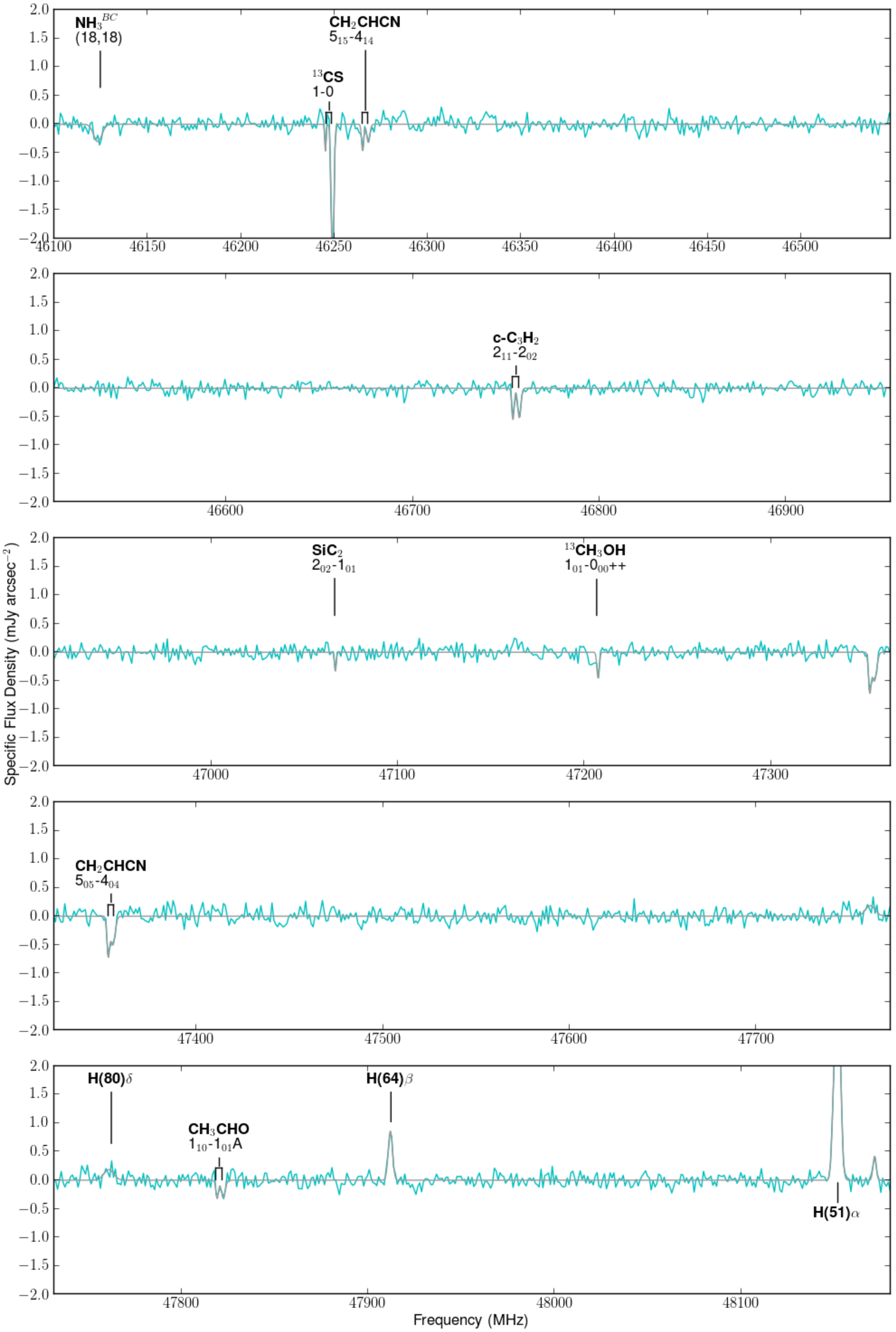

**Figure 36.** Spectrum Towards L.

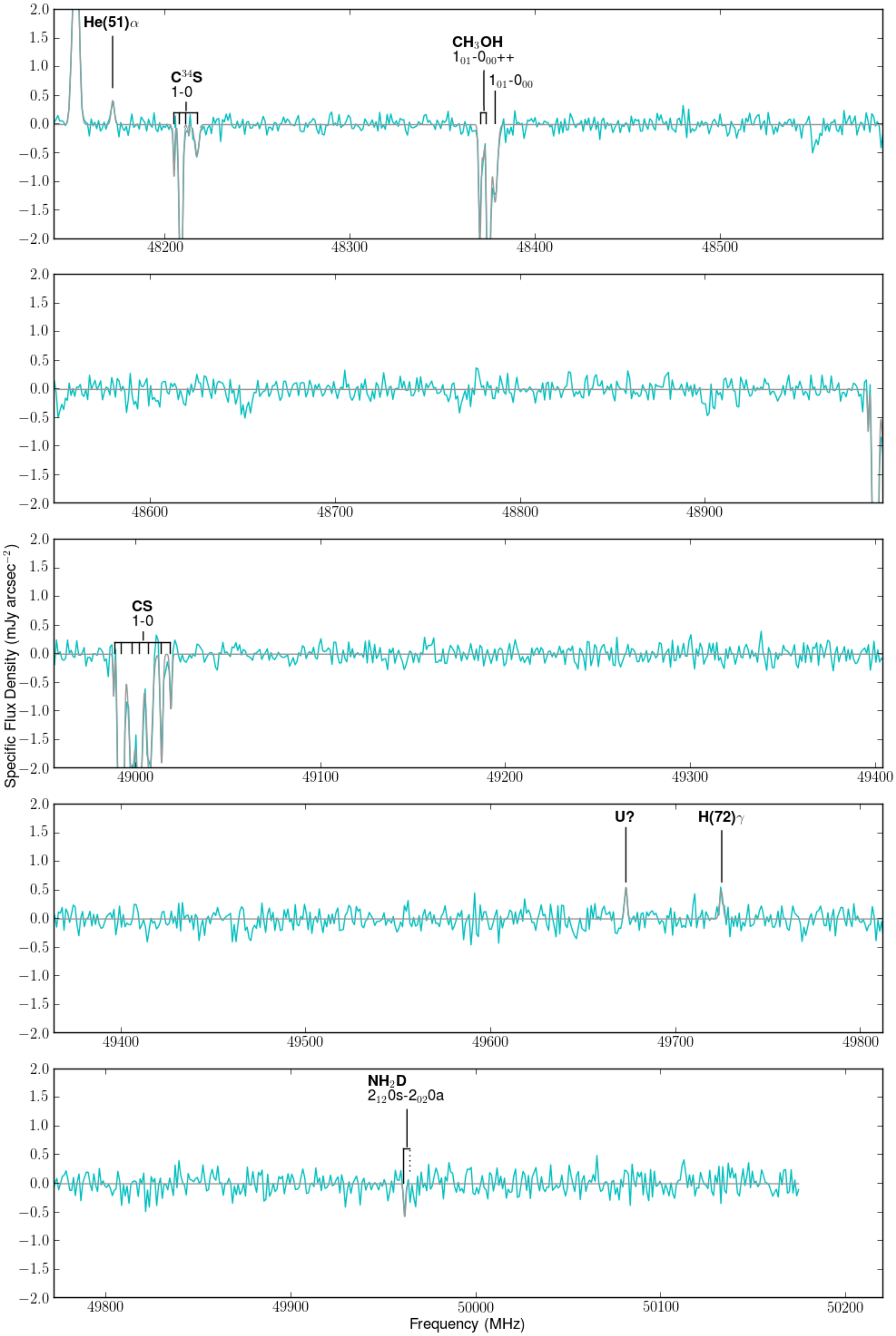

**Figure 37.** Spectrum Towards L.

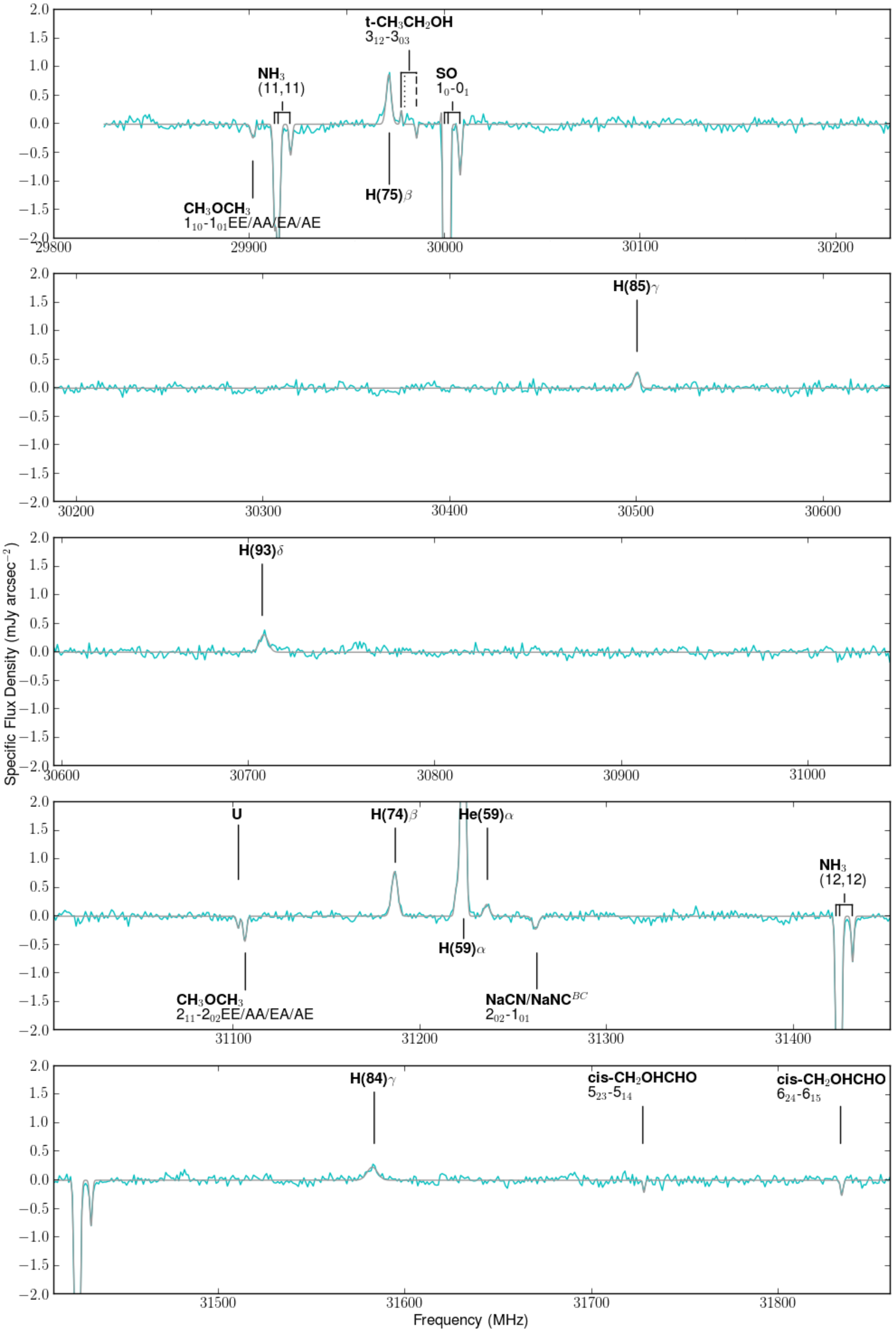

**Figure 38.** Spectrum Towards K4.

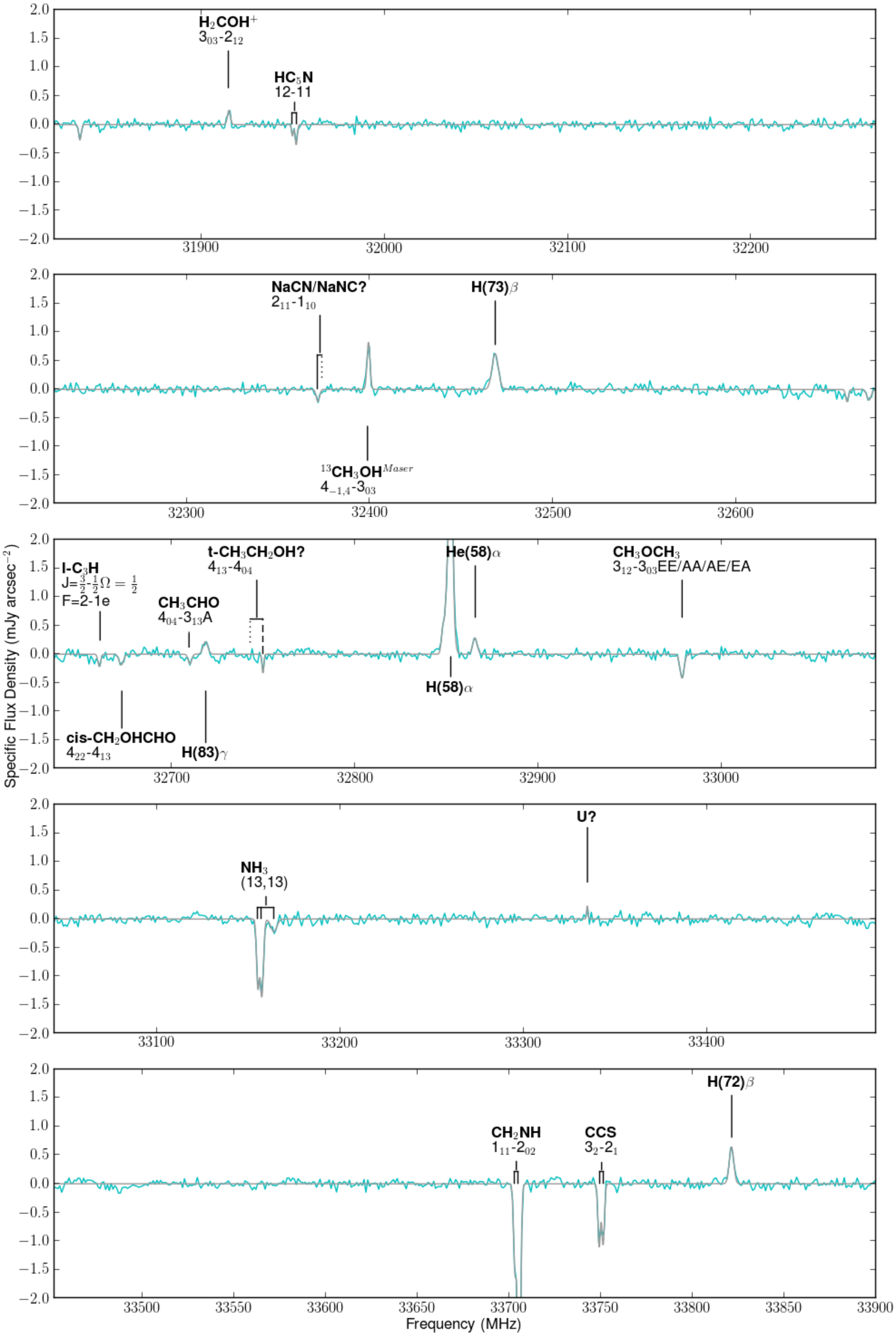

**Figure 39.** Spectrum Towards K4.

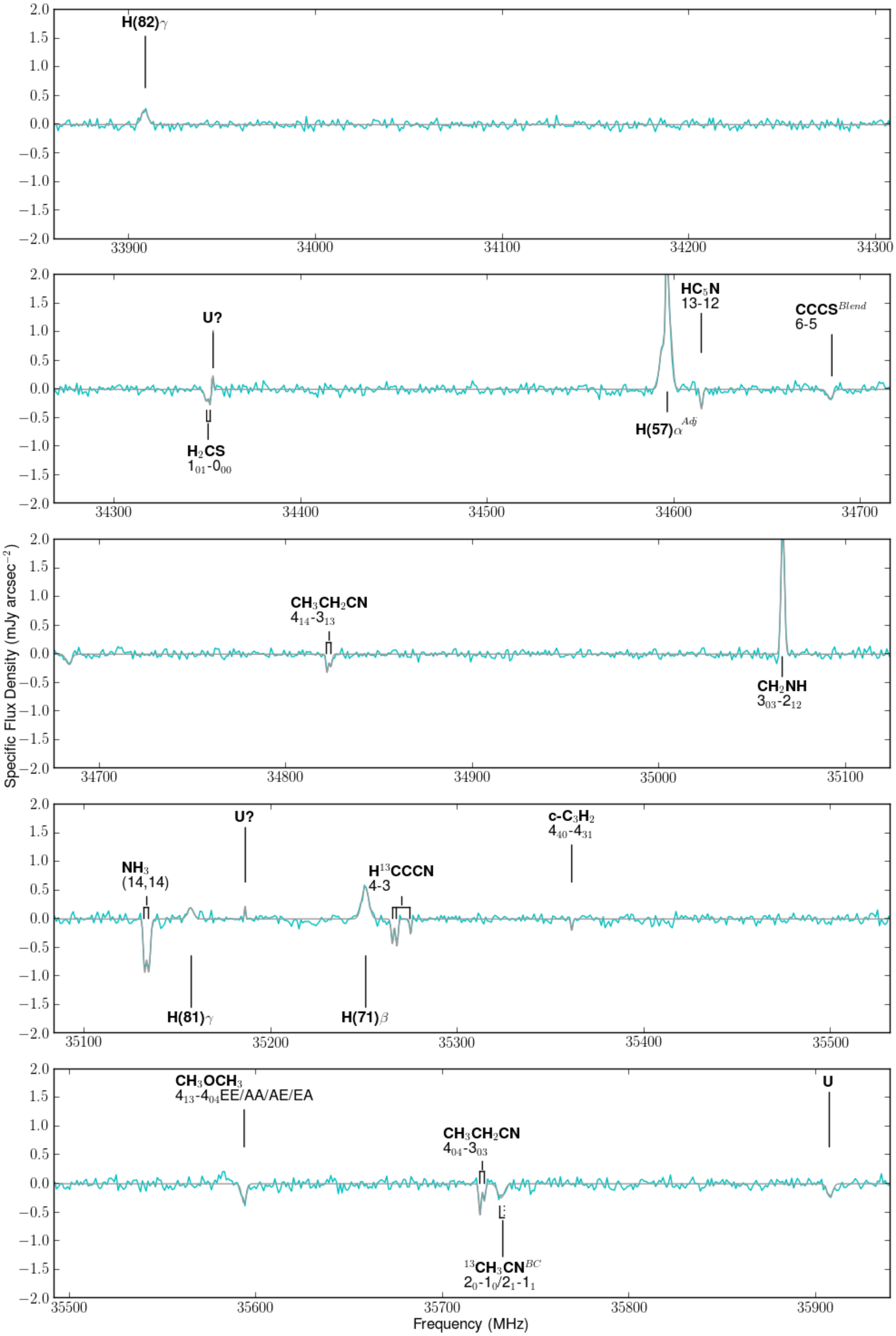

**Figure 40.** Spectrum Towards K4.

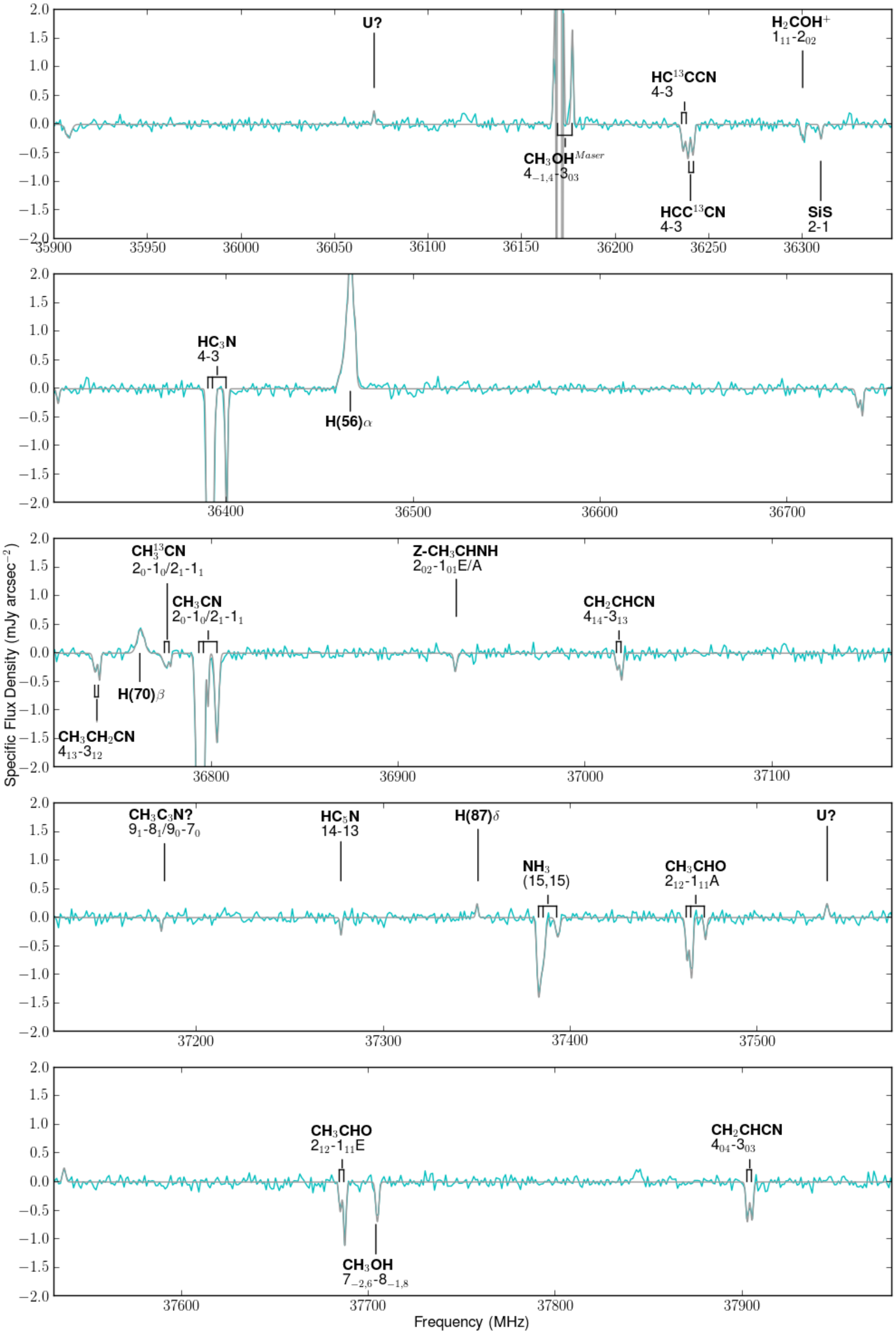

**Figure 41.** Spectrum Towards K4.

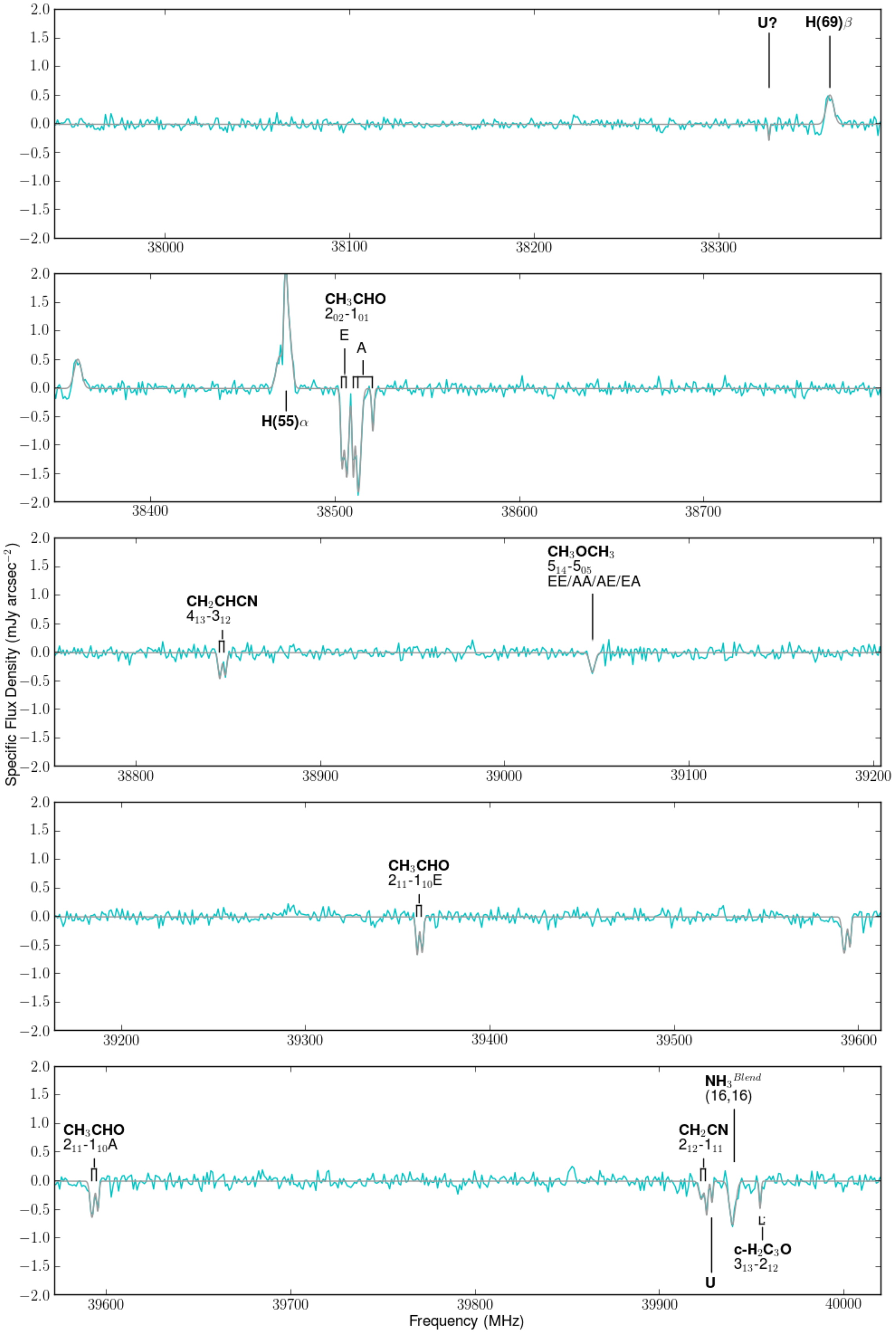

**Figure 42.** Spectrum Towards K4.

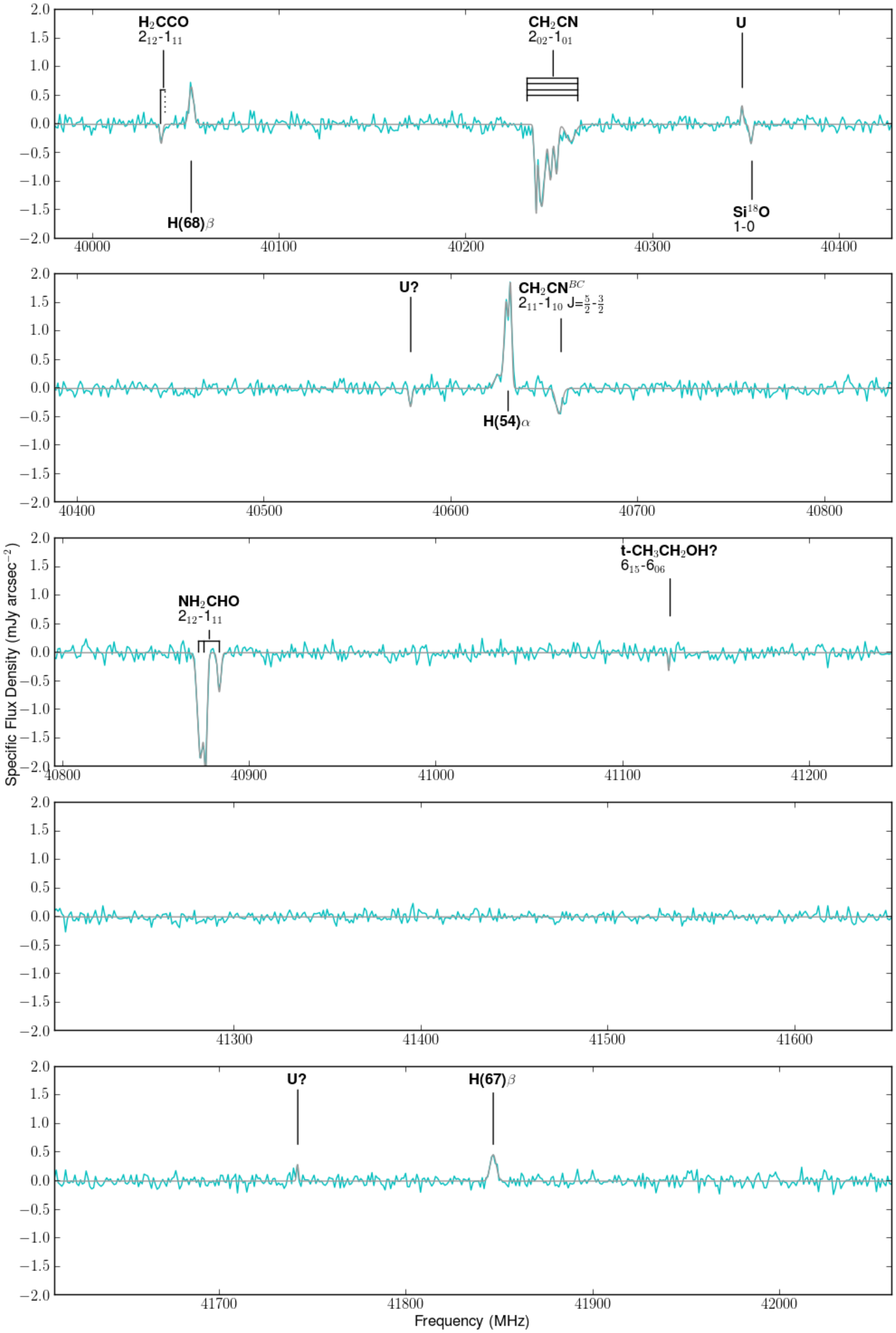

**Figure 43.** Spectrum Towards K4.

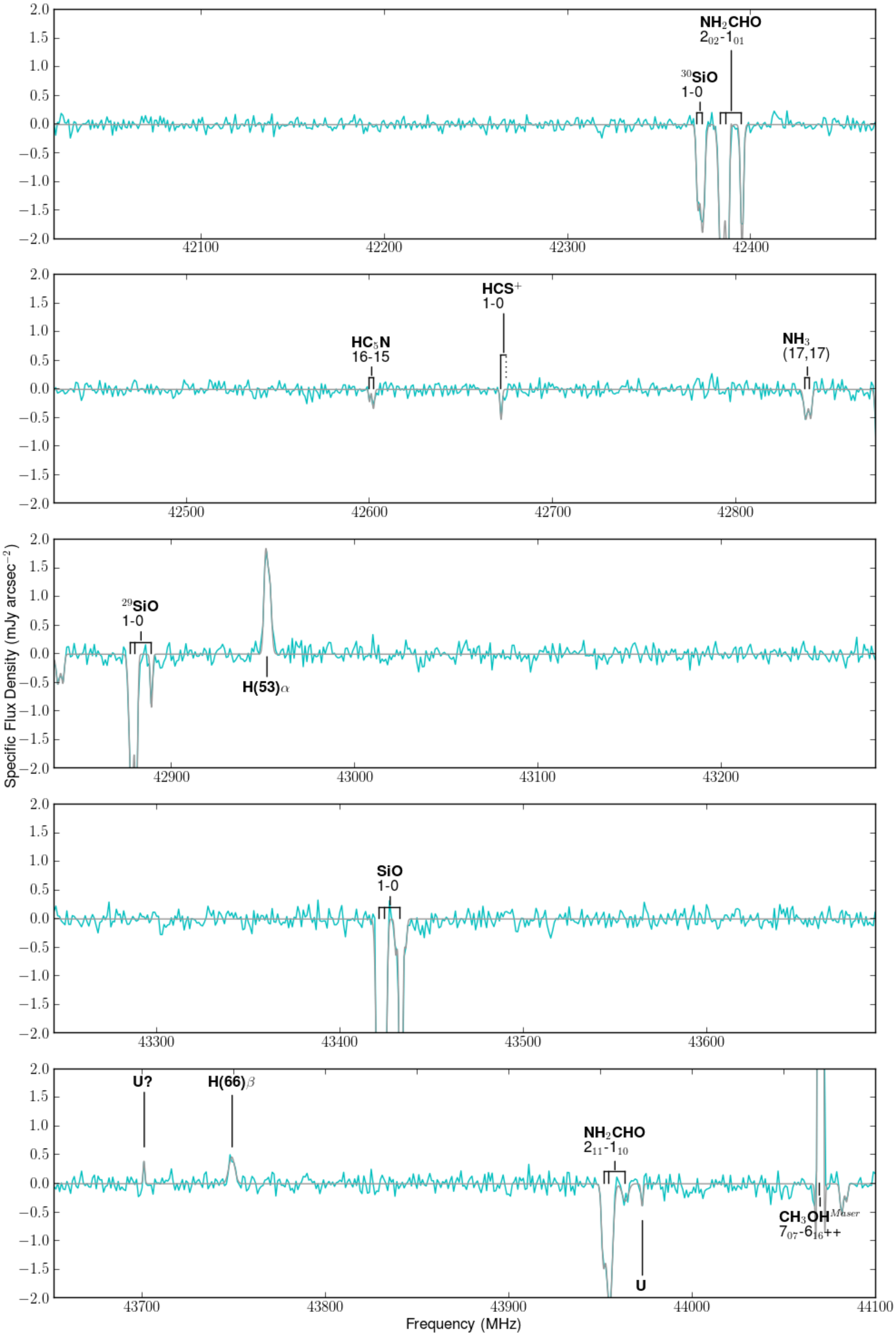

**Figure 44.** Spectrum Towards K4.

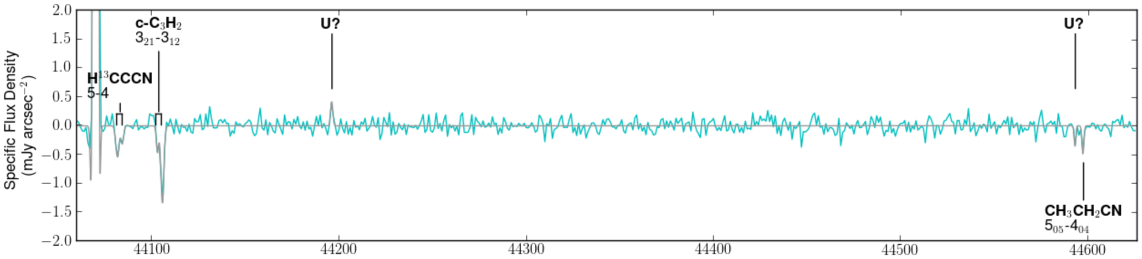

**Figure 45.** Spectrum Towards K4.

## APPENDIX C
## LINE IDENTIFICATION AND GAUSSIAN FIT TABLES

Line identifications and Gaussian fit parameters, including velocity center, height, width, and integrated flux towards K6, L, and K4 are provided. The following conventions are used in all tables. Tentative identifications are noted with a '?', as are unidentified lines (U-lines) suspected to be artifacts. Strong masing transitions are marked with '$Maser$', blended lines are marked with '$B$', and line fits that have been adjusted from the output of the line fitter are marked with '$Adj$'. In cases where the line-fitter determined a 1-component fit that we suspect to be a 2-component transition with insufficient signal-to-noise to be identified as such by the fitter, the species is marked with '$BC$'. Footnotes, linked from the velocity column, provide notes on any other notable aspects of lines.

We have applied the following rules to assigning the rest frequencies and velocities to U-lines. U-lines detected towards K6 are treated as follows:

(i) 1-component transitions detected towards K6 are assumed to be at a velocity of 64.0 $\mathrm{km\,s^{-1}}$.
(ii) For 2-component transitions, we assume that the lower velocity component is at 64.0 $\mathrm{km\,s^{-1}}$.

U-lines detected towards L and K4 are treated as follows:

(i) If the U-line is detected towards K6, we use the rest frequency determined above.
(ii) If the U-line is not detected towards K6, we assume the velocity of the low velocity gas component, namely 56 and 62 $\mathrm{km\,s^{-1}}$ for L and K4 respectively.

For cases in which a transition has blended spectral structure (such as blended transitions of A- and E-states), the listed transition indicates what components are expected to be blended, with the first listed component corresponding to the transition rest frequency in the first column.

Table 9: Line identifications and fit parameters towards K6.

| Line Rest Freq (MHz) | Species | Transition | Fit Velocity ( km s$^{-1}$) | Height (mJy arcsec$^{-2}$) | Width ( km s$^{-1}$) | $\int I_v dv$ (mJy arcsec$^{-2}$ × km s$^{-1}$) |
|---|---|---|---|---|---|---|
| 29853.31 | U | —— | 64.0 | 0.20 | 19.7 | 4.3 |
| 29901.40 | $CH_3OCH_3$ | $1_{10}$-$1_{01}$EE/AA/AE/EA | 64.2 | -0.64 | 20.2 | -13.9 |
| 29914.49 | $NH_3$ | (11,11) | 83.4 | -2.51 | 12.5 | -29.5 |
| | | | 64.6 | -4.96 | 15.9 | -83.5 |
| | | | 11.3 | -0.52 | 18.6 | -11.4 |
| 29956.11 | U | —— | 64.0 | -0.23 | 20.1 | -4.9 |
| 29971.48 | Hydrogen | H(75)$\beta$ | 84.6 | 1.20 | 26.2 | 33.6 |
| | | | 61.8 | 1.82 | 32.3 | 62.7 |
| 29979.38 | *t*-$CH_3CH_2OH$ | $3_{12}$-$3_{03}$ | [1]81.2 | 0.41 | 12.5 | 5.5 |
| | | | 62.0 | -0.29 | 11.5 | -3.6 |
| 30001.55 | SO | $1_0$-$0_1$ | 84.4 | -11.73 | 13.5 | -150.3 |
| | | | 64.2 | -27.56 | 15.4 | -451.7 |
| | | | 8.9 | -1.25 | 21.2 | -30.5 |
| | | | -32.4 | -0.27 | 22.9 | -6.5 |
| | | | -106.3 | -0.54 | 10.9 | -6.3 |
| 30180.60 | NaCN/NaNC$^{BC}$ | $2_{12}$-$1_{11}$ | 74.4 | -0.19 | 20.4 | -4.2 |
| 30239.76 | U | —— | 64.0 | -0.22 | 16.1 | -3.8 |
| 30256.04 | U | —— | 64.0 | -0.17 | 28.6 | -5.1 |
| 30500.20 | Hydrogen | H(85)$\gamma$ | 72.9 | 0.90 | 37.3 | 35.6 |
| | | | 51.1 | 0.38 | 18.6 | 7.5 |
| 30513.96 | Hydrogen | H(106)$\zeta$ | 79.1 | 0.29 | 46.4 | 14.4 |
| 30707.38 | Hydrogen | H(93)$\delta$ | 74.3 | 0.43 | 49.7 | 22.7 |
| 30722.67 | U? | —— | 64.0 | 0.22 | 90.9 | 21.3 |
| 31002.30 | $CH_3CH_2CHO$ | $3_{21}$-$2_{12}$ | 65.9 | -0.25 | 33.6 | -8.9 |
| 31106.15 | $CH_3OCH_3$ | $2_{11}$-$2_{02}$EE/AA/AE/EA | 65.1 | -1.06 | 23.2 | -26.1 |
| 31186.68 | Hydrogen | H(74)$\beta$ | 66.8 | 2.23 | 39.9 | 102.6 |
| 31199.39 | Helium | He(74)$\beta$ | 73.5 | 0.22 | 36.9 | 8.7 |
| 31223.31 | Hydrogen | H(59)$\alpha$ | 78.3 | 7.51 | 29.2 | 233.7 |
| | | | 55.7 | 5.95 | 23.1 | 146.5 |
| 31236.04 | Helium | He(59)$\alpha$ | 89.7 | 0.32 | 16.6 | 5.7 |
| | | | 65.3 | 0.71 | 34.8 | 26.2 |
| 31262.33 | NaCN/NaNC | $2_{02}$-$1_{01}$ | 62.0 | -0.66 | 15.8 | -11.1 |
| 31424.94 | $NH_3$ | (12,12) | 84.5 | -2.50 | 13.3 | -35.5 |
| | | | 65.2 | -7.30 | 19.4 | -150.5 |
| | | | 8.2 | -0.56 | 25.6 | -15.4 |
| 31482.38 | Hydrogen | H(99)$\epsilon$ | 75.6 | 0.31 | 45.0 | 14.8 |
| 31583.40 | Hydrogen | H(84)$\gamma$ | 77.7 | 0.84 | 33.4 | 30.0 |
| | | | 51.2 | 0.49 | 23.6 | 12.2 |
| 31698.47 | Hydrogen | H(92)$\delta$ | 68.7 | 0.28 | 33.6 | 10.1 |
| 31727.07 | *cis*-$CH_2OHCHO$ | $5_{23}$-$5_{14}$ | 77.6 | -0.25 | 13.7 | -3.6 |
| | | | 60.9 | -0.26 | 11.7 | -3.2 |
| 31833.03 | *cis*-$CH_2OHCHO$ | $6_{24}$-$6_{15}$ | 61.2 | -0.22 | 20.1 | -4.8 |
| 31911.20 | $CH_3CH_2CHO$ | $3_{21}$-$2_{20}$ | 65.4 | -0.27 | 10.0 | -2.9 |
| 31951.78 | $HC_5N$ | 12-11 | 84.8 | -0.34 | 8.6 | -3.1 |
| | | | 64.2 | -1.78 | 12.6 | -23.9 |
| 32373.67 | NaCN/NaNC | $2_{11}$-$1_{10}$ | 62.8 | -0.29 | 28.1 | -8.6 |
| 32398.56 | $^{13}CH_3OH^{Maser}$ | $4_{-1,4}$-$3_{03}$ | 82.3 | 0.93 | 12.6 | 12.5 |
| | | | 62.8 | 0.40 | 10.7 | 4.6 |
| 32432.32 | Hydrogen | H(98)$\epsilon$ | 74.0 | 0.26 | 44.3 | 12.1 |
| 32468.48 | Hydrogen | H(73)$\beta$ | 78.2 | 1.92 | 32.8 | 66.8 |
| | | | 55.1 | 1.36 | 23.8 | 34.4 |
| 32627.30 | *l*-$C_3H^{Adj}$ | J=$\frac{3}{2}$-$\frac{1}{2}$ $\Omega$=$\frac{1}{2}$ F=2-1f | 63.7 | -0.50 | 17.2 | -9.2 |
| | | | 14.5 | -0.16 | 12.0 | -2.1 |
| | | | [2]-2.5 | -0.31 | 18.8 | -6.1 |
| 32640.21 | U | —— | [3]64.0 | -0.31 | 26.2 | -8.7 |
| 32627.30 | *l*-$C_3H$ | J=$\frac{3}{2}$-$\frac{1}{2}$ $\Omega$=$\frac{1}{2}$ F=2-1f | -108.5 | -0.20 | 21.1 | -4.5 |
| 32660.65 | *l*-$C_3H^{Adj}$ | J=$\frac{3}{2}$-$\frac{1}{2}$ $\Omega$=$\frac{1}{2}$ F=2-1e | 62.6 | -0.66 | 11.7 | -8.3 |
| 32663.38 | *l*-$C_3H^{Adj}$ | J=$\frac{3}{2}$-$\frac{1}{2}$ $\Omega$=$\frac{1}{2}$ F=1-0e | 61.8 | -0.19 | 10.5 | -2.1 |
| 32660.65 | *l*-$C_3H^{Adj}$ | J=$\frac{3}{2}$-$\frac{1}{2}$ $\Omega$=$\frac{1}{2}$ F=2-1e | 17.4 | -0.20 | 24.8 | -5.3 |
| | | | [4]-2.1 | -0.33 | 14.7 | -5.2 |
| 32672.52 | *cis*-$CH_2OHCHO$ | $4_{22}$-$4_{13}$ | 83.8 | -0.42 | 12.1 | -5.4 |

Continued on next page

**Table 9 – Line Identifications and Fit Parameters towards K6**

| Line Rest Freq (MHz) | Species | Transition | Fit Velocity ( $km\,s^{-1}$ ) | Height (mJy arcsec$^{-2}$) | Width ( $km\,s^{-1}$ ) | $\int I_v dv$ (mJy arcsec$^{-2}$ × $km\,s^{-1}$ ) |
|---|---|---|---|---|---|---|
| | | | 62.3 | -0.63 | 16.0 | -10.8 |
| 32660.65 | *l*-$C_3H$ | $J=\frac{3}{2}-\frac{1}{2}$ $\Omega=\frac{1}{2}$ F=2-1e | -105.6 | -0.20 | 15.5 | -3.3 |
| 32709.18 | $CH_3CHO$ | $4_{04}$-$3_{13}$A | 63.8 | -0.34 | 15.3 | -5.6 |
| 32718.50 | Hydrogen | H(83)$\gamma$ | 66.7 | 0.92 | 45.5 | 46.0 |
| 32732.67 | Hydrogen | H(91)$\delta$ | 71.7 | 0.62 | 40.6 | 26.8 |
| 32742.82 | *t*-$CH_3CH_2OH$ | $4_{13}$-$4_{04}$ | 62.5 | -0.56 | 15.1 | -9.0 |
| 32852.20 | Hydrogen | H(58)$\alpha$ | 83.7 | 5.60 | 27.2 | 169.2 |
| | | | 60.0 | 8.10 | 28.0 | 244.9 |
| 32865.58 | Helium | He(58)$\alpha$ | 83.5 | 0.52 | 25.5 | 14.2 |
| | | | 60.3 | 0.65 | 23.4 | 16.1 |
| 32978.23 | $CH_3OCH_3$ | $3_{12}$-$3_{03}$EE/AA/AE/EA | 66.5 | -1.41 | 25.0 | -37.5 |
| 33051.62 | $CH_3C_3N$ | $8_0$-$7_0$/$8_1$-$7_1$ | 85.6 | -0.27 | 12.8 | -3.7 |
| | | | 64.7 | -0.52 | 13.6 | -7.4 |
| 33156.85 | $NH_3$ | (13,13) | 83.1 | -1.40 | 11.7 | -17.4 |
| | | | 64.7 | -3.52 | 14.7 | -54.9 |
| | | | 3.8 | -0.35 | 16.2 | -6.0 |
| 33181.67 | Hydrogen | H(103)$\zeta$ | 68.4 | 0.18 | 54.8 | 10.5 |
| 33236.47 | $CH_3CHO$ | $4_{04}$-$3_{13}$E | 62.4 | -0.43 | 13.4 | -6.2 |
| 33345.23 | *cis*-$CH_2OHCHO^{BC}$ | $7_{25}$-$7_{16}$ | 72.5 | -0.26 | 25.9 | -7.1 |
| 33354.01 | *cis*-$CH_2OHCHO^{BC}$ | $2_{12}$-$1_{01}$ | 68.1 | -0.23 | 37.7 | -9.1 |
| 33420.88 | Hydrogen | H(97)$\epsilon$ | 68.2 | 0.34 | 49.7 | 18.2 |
| 33455.99 | U | —— | 64.0 | -0.21 | 11.8 | -2.6 |
| 33562.12 | $(CH_3)_2CO$? | $3_{03}$-$2_{12}$EE | [5]68.3 | -0.30 | 16.0 | -5.1 |
| 33704.82 | $CH_2NH$ | $1_{11}$-$2_{02}$ | 82.1 | -5.77 | 14.5 | -89.3 |
| | | | 63.2 | -8.11 | 15.9 | -137.5 |
| 33751.37 | CCS | $3_2$-$2_1$ | 83.7 | -0.87 | 10.8 | -10.0 |
| | | | 64.0 | -5.79 | 17.7 | -107.5 |
| | | | 7.3 | -0.41 | 30.6 | -10.7 |
| | | | -34.5 | -0.24 | 15.4 | -4.0 |
| | | | -105.7 | -0.24 | 39.5 | -10.2 |
| 33812.37 | Hydrogen | H(90)$\delta$ | 69.8 | 0.53 | 46.8 | 26.5 |
| 33821.51 | Hydrogen | H(72)$\beta$ | 70.3 | 2.22 | 46.9 | 116.9 |
| 33908.67 | Hydrogen | H(82)$\gamma$ | 82.4 | 0.77 | 27.4 | 22.3 |
| | | | 59.2 | 0.84 | 26.4 | 23.5 |
| 34092.97 | $(CH_3)_2CO$ | $3_{13}$-$2_{02}$EE | 62.7 | -0.35 | 13.3 | -4.9 |
| 34156.88 | $CH_3OCHO$ | $3_{13}$-$2_{12}$E/A | 60.1 | -0.67 | 21.2 | -15.2 |
| 34225.47 | *cis*-$CH_2OHCHO$ | $3_{21}$-$3_{12}$ | 64.9 | -0.26 | 25.3 | -7.1 |
| 34285.54 | U | —— | 64.0 | -0.34 | 14.3 | -5.2 |
| 34351.45 | $H_2CS$ | $1_{01}$-$0_{00}$ | 63.8 | -2.46 | 14.7 | -38.5 |
| 34408.63 | HSCN | $3_{03}$-$2_{02}$ | 62.3 | -0.88 | 13.2 | -12.4 |
| 34450.03 | Hydrogen | H(96)$\epsilon$ | 65.7 | 0.36 | 67.9 | 25.7 |
| 34596.38 | Hydrogen | H(57)$\alpha$ | 90.0 | 3.08 | 18.9 | 70.3 |
| | | | 64.5 | 8.28 | 37.5 | 332.2 |
| 34610.48 | Helium | He(57)$\alpha$ | 82.9 | 0.65 | 21.7 | 14.9 |
| | | | 61.0 | 0.68 | 17.8 | 12.9 |
| 34614.38 | $HC_5N$ | 13-12 | 62.4 | -1.43 | 13.5 | -20.5 |
| 34674.19 | U | —— | 64.0 | 0.23 | 59.2 | 14.8 |
| 34684.37 | $CCCS^B$ | 6-5 | [6]67.8 | -0.71 | 22.4 | -16.9 |
| 34768.97 | *t*-$CH_2CHCHO$ | $4_{14}$-$3_{13}$ | 83.5 | -0.26 | 9.3 | -2.6 |
| | | | 65.2 | -0.24 | 9.5 | -2.4 |
| 34824.07 | $CH_3CH_2CN$ | $4_{14}$-$3_{13}$ | 64.6 | -1.98 | 12.4 | -26.1 |
| 34940.09 | Hydrogen | H(89)$\delta$ | 66.0 | 0.42 | 40.7 | 18.2 |
| 35065.73 | $CH_2NH$ | $3_{03}$-$2_{12}$ | [1]85.7 | 1.82 | 13.1 | 25.3 |
| | | | [1]67.0 | 2.37 | 17.0 | 42.9 |
| 35134.30 | $NH_3$ | (14,14) | 83.7 | -0.79 | 9.6 | -8.0 |
| | | | 65.7 | -2.54 | 16.1 | -43.5 |
| 35157.27 | Hydrogen | H(81)$\gamma$ | 83.8 | 0.64 | 27.7 | 18.7 |
| | | | 57.3 | 0.87 | 27.9 | 25.7 |
| 35250.77 | Hydrogen | H(71)$\beta$ | 78.2 | 1.79 | 35.4 | 67.5 |
| | | | 54.5 | 1.42 | 24.1 | 36.5 |
| 35267.41 | $H^{13}CCCN$ | 4-3 | 63.4 | -2.09 | 14.4 | -32.1 |
| 35360.93 | *c*-$C_3H_2$ | $4_{40}$-$4_{31}$ | 64.1 | -0.91 | 10.2 | -9.8 |
| 35468.17 | $(CH_3)_2CO$? | $2_{21}$-$1_{10}$AA | [7]65.8 | -0.34 | 10.2 | -3.7 |

Continued on next page

**Table 9 – Line Identifications and Fit Parameters towards K6**

| Line Rest Freq (MHz) | Species | Transition | Fit Velocity ( km s$^{-1}$) | Height (mJy arcsec$^{-2}$) | Width ( km s$^{-1}$) | $\int I_v dv$ (mJy arcsec$^{-2}$ × km s$^{-1}$) |
|---|---|---|---|---|---|---|
| 35521.88 | Hydrogen | H(95)$\epsilon$ | 66.8 | 0.31 | 49.1 | 16.3 |
| 35586.91 | U? | —— | 64.0 | -0.27 | 34.5 | -10.0 |
| 35593.41 | $CH_3OCH_3$ | $4_{13}$-$4_{04}$EE/AA/AE/EA | 60.8 | -0.98 | 28.9 | -30.3 |
| 35722.21 | $CH_3CH_2CN$ | $4_{04}$-$3_{03}$ | 83.3 | -0.55 | 9.7 | -5.7 |
| | | | 64.8 | -2.49 | 12.4 | -32.7 |
| 35733.12 | $^{13}CH_3CN$ | $2_0$-$1_0$/$2_1$-$1_1$ | 65.4 | -0.94 | 22.6 | -22.7 |
| 35779.25 | *Z*-$CH_3CHNH$ | $2_{12}$-$1_{11}$A | 66.6 | -0.24 | 25.3 | -6.3 |
| 35791.73 | $CH_3CH_2CN$ | $4_{23}$-$3_{22}$ F=4-3 | 64.9 | -0.39 | 27.4 | -11.4 |
| 35837.33 | $CH_3CHO$ | $2_{12}$-$1_{10}$E | 64.6 | -0.36 | 13.5 | -5.1 |
| 35865.83 | $CH_3CH_2CN^{Adj}$ | $4_{22}$-$3_{21}$ F=4-3 | 85.3 | -0.24 | 14.1 | -3.5 |
| | | | 63.8 | -0.41 | 15.8 | -6.8 |
| 35893.63 | $CH_3OCHO$? | $2_{12}$-$1_{01}$E | [8]61.0 | -0.24 | 20.0 | -5.1 |
| 35903.32 | *cis*-$CH_2OHCHO^{Adj}$ | $2_{20}$-$2_{11}$ | 85.0 | -0.15 | 16.3 | -2.6 |
| | | | 60.1 | -0.22 | 25.1 | -5.9 |
| 35906.98 | U | —— | 64.0 | -0.26 | 13.8 | -3.8 |
| 36102.22 | $CH_3OCHO$ | $3_{03}$-$2_{02}$E | 62.3 | -0.55 | 12.8 | -7.5 |
| 36104.79 | $CH_3OCHO$ | $3_{03}$-$2_{02}$A | 62.2 | -0.54 | 10.9 | -6.2 |
| 36118.53 | Hydrogen | H(88)$\delta$ | 86.4 | 0.40 | 37.5 | 16.0 |
| | | | 55.1 | 0.47 | 24.9 | 12.5 |
| 36169.29 | $CH_3OH^{Maser,Adj}$ | $4_{-1,4}$-$3_{03}$ | 82.9 | 182.10 | 9.2 | 1614.3 |
| | | | 1.5 | 0.33 | 17.9 | 6.6 |
| 36202.04 | SO | $2_3$-$2_2$ | [9]64.9 | 0.37 | 10.1 | 3.9 |
| 36237.99 | $HC^{13}CCN$ | 4-3 | 81.4 | -0.63 | 10.5 | -7.0 |
| | | | [10]63.3 | -2.95 | 11.9 | -37.4 |
| 36241.44 | $HCC^{13}CN$ | 4-3 | 64.0 | -1.99 | 18.0 | -38.1 |
| 36299.95 | $H_2COH^+$ | $1_{11}$-$2_{02}$ | 80.4 | -0.37 | 11.4 | -4.5 |
| | | | 62.8 | -0.56 | 12.6 | -7.5 |
| 36309.63 | SiS | 2-1 | 62.9 | -1.00 | 12.9 | -13.8 |
| 36392.32 | $HC_3N$ | 4-3 | 82.5 | -9.27 | 11.3 | -102.3 |
| | | | 62.8 | -21.17 | 16.4 | -370.7 |
| | | | 3.6 | -0.89 | 13.9 | -20.8 |
| | | | -107.2 | -0.34 | 8.0 | -3.0 |
| 36417.24 | *t*-$CH_3CH_2OH$ | $5_{14}$-$5_{05}$ | 80.1 | -0.31 | 11.0 | -3.7 |
| | | | 62.0 | -0.34 | 11.8 | -4.3 |
| 36466.26 | Hydrogen | H(56)$\alpha^B$ | [11]87.3 | 5.15 | 20.1 | 115.2 |
| | | | [11]60.2 | 8.66 | 34.5 | 317.6 |
| 36481.12 | Helium | He(56)$\alpha$ | 84.7 | 0.54 | 27.1 | 15.6 |
| | | | 63.9 | 0.48 | 9.6 | 4.9 |
| 36488.81 | OCS | 3-2 | [12]62.8 | -1.40 | 11.5 | -17.1 |
| 36492.76 | U | —— | 64.0 | -0.33 | 19.0 | -6.7 |
| 36638.68 | Hydrogen | H(94)$\epsilon$ | 73.6 | 0.26 | 42.2 | 11.9 |
| 36657.47 | $CH_3OCHO$ | $3_{22}$-$2_{21}$A | 65.9 | -0.27 | 12.4 | -3.6 |
| 36739.67 | $CH_3CH_2CN$ | $4_{13}$-$3_{12}$ | 82.0 | -0.41 | 10.7 | -4.7 |
| | | | 62.6 | -2.11 | 11.6 | -26.0 |
| 36761.72 | Hydrogen | H(70)$\beta$ | 87.1 | 1.16 | 23.4 | 29.0 |
| | | | 59.6 | 1.89 | 32.7 | 65.9 |
| 36777.28 | $CH_3^{13}CN$ | $2_0$-$1_0$/$2_1$-$1_1$ | 76.1 | -0.44 | 30.7 | -14.4 |
| | | | 64.2 | -0.50 | 17.3 | -9.2 |
| 36795.47 | $CH_3CN$ | $2_0$-$1_0$/$2_1$-$1_1$ | 79.3 | -8.75 | 21.4 | -199.7 |
| | | | 64.1 | -18.38 | 18.2 | -355.9 |
| | | | 12.4 | -0.63 | 22.9 | -43.8 |
| | | | -89.4 | -0.28 | 34.1 | -10.3 |
| | | | -103.6 | -0.47 | 14.6 | -7.4 |
| 36930.70 | *Z*-$CH_3CHNH$ | $2_{02}$-$1_{01}$E/A | 59.2 | -0.59 | 25.8 | -16.3 |
| 36939.70 | U | —— | 64.0 | -0.30 | 29.0 | -9.4 |
| 37018.92 | $CH_2CHCN$ | $4_{14}$-$3_{13}$ | 79.7 | -0.50 | 10.9 | -5.8 |
| | | | 62.8 | -1.93 | 11.5 | -23.6 |
| 37106.79 | U | —— | 64.0 | -0.21 | 38.3 | -8.7 |
| 37182.66 | $CH_3C_3N^B$ | $9_1$-$8_1$/$9_0$-$7_0$ | [13]63.4 | -0.37 | 10.8 | -4.3 |
| 37276.99 | $HC_5N$ | 14-13 | 83.4 | -0.43 | 12.2 | -5.6 |
| | | | 63.6 | -1.56 | 10.7 | -17.7 |
| 37350.57 | Hydrogen | H(87)$\delta$ | 82.1 | 0.42 | 40.5 | 17.9 |
| 37370.88 | U? | —— | 64.0 | -0.29 | 16.1 | -4.9 |

Continued on next page

**Table 9 – Line Identifications and Fit Parameters towards K6**

| Line Rest Freq (MHz) | Species | Transition | Fit Velocity ( $\mathrm{km\,s^{-1}}$ ) | Height (mJy $\mathrm{arcsec^{-2}}$ ) | Width ( $\mathrm{km\,s^{-1}}$ ) | $\int I_v dv$ (mJy $\mathrm{arcsec^{-2}}$ $\times$ $\mathrm{km\,s^{-1}}$ ) |
|---|---|---|---|---|---|---|
| 37385.12 | $NH_3^B$ | (15,15) | [14]78.4 | -2.33 | 16.1 | -39.8 |
| | | | [14]60.8 | -1.61 | 17.2 | -29.4 |
| | | | 14.5 | -0.41 | 15.2 | -6.6 |
| 37464.17 | $CH_3CHO$ | $2_{12}$-$1_{11}$A | 80.8 | -2.03 | 10.1 | -20.9 |
| | | | 63.3 | -4.84 | 12.8 | -64.4 |
| 37476.99 | U | —— | [15]64.0 | -0.29 | 9.9 | -3.0 |
| 37686.87 | $CH_3CHO$ | $2_{12}$-$1_{11}$E | 80.4 | -1.53 | 11.8 | -19.2 |
| | | | 62.6 | -4.47 | 12.7 | -58.4 |
| 37703.70 | $CH_3OH$ | $7_{-2,6}$-$8_{-1,8}$ | 83.4 | -1.34 | 10.8 | -15.5 |
| | | | 62.8 | -0.96 | 12.1 | -12.4 |
| 37802.79 | Hydrogen | H(93)$\epsilon$ | 75.2 | 0.33 | 42.7 | 15.2 |
| 37844.59 | Hydrogen | H(79)$\gamma$ | 87.6 | 0.64 | 19.6 | 13.4 |
| | | | 61.2 | 0.81 | 33.6 | 29.0 |
| 37904.85 | $CH_2CHCN$ | $4_{04}$-$3_{03}$ | 81.0 | -1.00 | 11.7 | -12.4 |
| | | | 63.2 | -3.64 | 11.9 | -44.0 |
| 38241.47 | $Na^{37}Cl$? | 3-2 | 64.1 | -0.27 | 10.2 | -3.0 |
| 38271.02 | $E$-HNCHCN | $4_{04}$-$3_{03}$ | 63.0 | -0.51 | 9.7 | -5.3 |
| 38360.27 | Hydrogen | H(69)$\beta$ | 87.4 | 1.26 | 20.2 | 27.0 |
| | | | 60.0 | 2.04 | 34.9 | 75.8 |
| 38439.65 | U | —— | 64.0 | -0.29 | 12.6 | -3.9 |
| 38445.25 | U | —— | 64.0 | -0.27 | 10.4 | -3.0 |
| 38473.36 | Hydrogen | H(55)$\alpha$ | 88.7 | 4.26 | 19.6 | 91.7 |
| | | | 62.6 | 7.63 | 34.6 | 281.1 |
| 38489.04 | Helium | He(55)$\alpha$ | 88.8 | 0.38 | 14.4 | 5.8 |
| | | | 58.0 | 0.62 | 28.0 | 18.4 |
| 38506.04 | $CH_3CHO$ | $2_{02}$-$1_{01}$E | 81.1 | -3.27 | 9.8 | -33.6 |
| | | | 63.4 | -8.42 | 13.3 | -113.7 |
| 38512.11 | $CH_3CHO$ | $2_{02}$-$1_{01}$A | 81.1 | -2.89 | 12.5 | -38.1 |
| | | | 63.1 | -9.58 | 12.6 | -125.5 |
| | | | 12.5 | -0.51 | 14.6 | -13.4 |
| 38639.30 | Hydrogen | H(86)$\delta$ | 74.4 | 0.33 | 44.9 | 16.0 |
| | | | 52.7 | 0.29 | 23.1 | 7.2 |
| 38847.73 | $CH_2CHCN$ | $4_{13}$-$3_{12}$ | 82.6 | -0.57 | 9.6 | -5.8 |
| | | | 63.7 | -1.86 | 13.4 | -26.5 |
| 38908.94 | U? | —— | 64.0 | -0.32 | 9.1 | -3.1 |
| 38976.13 | $CH_3OCHO$ | $3_{12}$-$2_{11}$E | 64.3 | -0.25 | 14.2 | -3.7 |
| 38980.81 | $CH_3OCHO$ | $3_{12}$-$2_{11}$A | 63.9 | -0.35 | 13.4 | -5.0 |
| 39016.76 | Hydrogen | H(92)$\epsilon$ | 69.6 | 0.24 | 54.2 | 13.6 |
| 39047.30 | $CH_3OCH_3$ | $5_{14}$-$5_{05}$EE/AA/AE/EA | 69.9 | -0.54 | 27.7 | -15.8 |
| 39291.42 | Hydrogen | H(78)$\gamma$ | 69.2 | 0.55 | 48.0 | 27.8 |
| 39362.50 | $CH_3CHO$ | $2_{11}$-$1_{10}$E | 81.0 | -1.20 | 8.9 | -11.4 |
| | | | 63.9 | -4.21 | 12.0 | -53.7 |
| 39571.33 | CCCN | N=4-3 J=$\frac{9}{2}$-$\frac{7}{2}$ | 81.1 | -0.34 | 7.7 | -2.8 |
| | | | 64.1 | -0.48 | 11.1 | -5.7 |
| 39581.58 | $c$-$H_2COCH_2$? | $1_{01}$-$0_{00}$ | 63.6 | -0.57 | 12.9 | -7.9 |
| 39590.21 | $CCCN^B$ | N=4-3 J=$\frac{7}{2}$-$\frac{5}{2}$ | [16]66.0 | -0.57 | 8.2 | -5.0 |
| 39594.29 | $CH_3CHO$ | $2_{11}$-$1_{10}$A | 81.8 | -1.63 | 13.0 | -22.5 |
| | | | 63.1 | -3.67 | 11.7 | -49.9 |
| 39712.47 | U | —— | 64.0 | -0.52 | 13.2 | -7.4 |
| 39725.38 | $NH_2CN$ | $2_{12}$-$1_{11}$ | 64.7 | -0.48 | 21.7 | -11.1 |
| 39742.55 | HCCNC | 4-3 | 62.9 | -0.51 | 8.9 | -4.9 |
| 39924.77 | $CH_2CN$ | $2_{12}$-$1_{11}$ | 67.1 | -0.81 | 13.0 | -11.2 |
| 39927.87 | U | —— | [17]64.0 | -0.84 | 10.7 | -9.6 |
| 39941.41 | $NH_3^B$ | (16,16) | [18]79.0 | -1.58 | 11.6 | -19.6 |
| | | | 64.7 | -2.06 | 10.8 | -23.7 |
| 39956.70 | $c$-$H_2C_3O$ | $3_{13}$-$2_{12}$ | 62.4 | -0.75 | 12.7 | -10.2 |
| 39988.02 | Hydrogen | H(85)$\delta$ | 73.5 | 0.49 | 37.6 | 19.6 |
| 40039.02 | $H_2CCO$ | $2_{12}$-$1_{11}$ | 63.4 | -0.99 | 12.2 | -12.9 |
| 40052.88 | Hydrogen | H(68)$\beta$ | 87.4 | 1.20 | 23.0 | 29.3 |
| | | | 60.9 | 1.94 | 33.1 | 68.3 |
| 40210.49 | $CH_3NC$ | $2_1$-$1_1$ | 60.6 | -1.39 | 15.9 | -23.4 |
| 40232.80 | $CH_2CN$ | $2_{02}$-$1_{01}$ J=$\frac{3}{2}$-$\frac{1}{2}$<br>F1=$\frac{3}{2}$-$\frac{1}{2}$ F=$\frac{5}{2}$-$\frac{3}{2}$ | [19]62.6 | -0.38 | 29.6 | -12.0 |

Continued on next page

**Table 9 – Line Identifications and Fit Parameters towards K6**

| Line Rest Freq (MHz) | Species | Transition | Fit Velocity ( km s$^{-1}$) | Height (mJy arcsec$^{-2}$) | Width ( km s$^{-1}$) | $\int I_v dv$ (mJy arcsec$^{-2}$ × km s$^{-1}$) |
|---|---|---|---|---|---|---|
| 40239.70 | $CH_2CN$ | $2_{02}$-$1_{01}$ J=$\frac{5}{2}$-$\frac{3}{2}$ | [19]83.3 | -1.53 | 8.2 | -12.8 |
| | | F1=$\frac{7}{2}$-$\frac{5}{2}$ F=$\frac{7}{2}$-$\frac{5}{2}$ | [18]62.8 | -4.76 | 16.7 | -81.6 |
| 40242.22 | $CH_2CN$ | $2_{02}$-$1_{01}$ J=$\frac{5}{2}$-$\frac{3}{2}$<br>F1=$\frac{5}{2}$-$\frac{3}{2}$ F=$\frac{5}{2}$-$\frac{3}{2}$ | [19]63.4 | -2.56 | 9.5 | -26.0 |
| 40244.34 | $CH_2CN$ | $2_{02}$-$1_{01}$ J=$\frac{5}{2}$-$\frac{3}{2}$<br>F1=$\frac{5}{2}$-$\frac{3}{2}$ F=$\frac{7}{2}$-$\frac{5}{2}$ | [19]63.1 | -2.16 | 18.3 | -42.0 |
| 40247.54 | $CH_2CN$ | $2_{02}$-$1_{01}$ J=$\frac{3}{2}$-$\frac{1}{2}$<br>F1=$\frac{5}{2}$-$\frac{3}{2}$ F=$\frac{5}{2}$-$\frac{3}{2}$ | [19]62.2 | -3.63 | 12.5 | -48.1 |
| 40249.34 | $CH_2CN$ | $2_{02}$-$1_{01}$ J=$\frac{3}{2}$-$\frac{3}{2}$<br>F1=$\frac{5}{2}$-$\frac{3}{2}$ F=$\frac{5}{2}$-$\frac{5}{2}$ | [19]60.1 | -0.66 | 9.2 | -6.5 |
| 40251.86 | $CH_2CN$ | $2_{02}$-$1_{01}$ J=$\frac{3}{2}$-$\frac{3}{2}$<br>F1=$\frac{5}{2}$-$\frac{3}{2}$ F=$\frac{5}{2}$-$\frac{5}{2}$ | [19]64.4 | -0.64 | 9.5 | -6.5 |
| 40253.88 | $CH_2CN$ | $2_{02}$-$1_{01}$ J=$\frac{3}{2}$-$\frac{1}{2}$<br>F1=$\frac{5}{2}$-$\frac{3}{2}$ F=$\frac{3}{2}$-$\frac{3}{2}$ | [19]63.9 | -0.85 | 17.1 | -15.5 |
| 40256.79 | $CH_2CN$ | $2_{02}$-$1_{01}$ J=$\frac{3}{2}$-$\frac{1}{2}$<br>F1=$\frac{3}{2}$-$\frac{3}{2}$ F=$\frac{5}{2}$-$\frac{5}{2}$ | [19]62.9 | -0.79 | 17.5 | -14.7 |
| 40259.84 | $CH_2CN$ | $2_{02}$-$1_{01}$ J=$\frac{3}{2}$-$\frac{3}{2}$<br>F1=$\frac{3}{2}$-$\frac{5}{2}$ F=$\frac{3}{2}$-$\frac{5}{2}$ | [19]62.8 | -0.48 | 12.4 | -6.4 |
| 40352.77 | $Si^{18}O$ | 1-0 | 65.1 | -0.77 | 10.6 | -8.8 |
| 40417.95 | $H_2CCO$ | $2_{02}$-$1_{01}$ | 64.7 | -0.49 | 12.8 | -6.7 |
| 40455.62 | $H_2NCO^+$? | $2_{02}$-$1_{01}$ F=1-0 | 84.7 | -0.28 | 20.1 | -6.0 |
| | | | 59.7 | -0.71 | 8.9 | -6.7 |
| 40465.01 | $CCCS^{BC}$ | 7-6 | 65.3 | -0.41 | 21.1 | -9.2 |
| 40477.24 | U | —— | 64.0 | -0.36 | 10.5 | -4.1 |
| 40484.03 | U | —— | 64.0 | -0.40 | 14.3 | -6.1 |
| 40630.50 | Hydrogen | H(54)$\alpha$ | 81.5 | 6.30 | 31.6 | 211.9 |
| | | | 55.4 | 5.76 | 23.8 | 145.9 |
| 40647.06 | Helium | He(54)$\alpha$ | 86.6 | 0.58 | 20.0 | 12.4 |
| | | | 56.1 | 0.68 | 25.7 | 18.6 |
| 40658.60 | $CH_2CN$ | $2_{11}$-$1_{10}$ J=$\frac{5}{2}$-$\frac{3}{2}$ | 61.7 | -0.94 | 22.8 | -22.9 |
| 40793.84 | $H_2CCO$ | $2_{11}$-$1_{10}$ | 63.3 | -1.16 | 15.2 | -18.8 |
| 40812.95 | Hydrogen | H(77)$\gamma$ | 88.7 | 0.53 | 20.7 | 11.7 |
| | | | 57.5 | 0.85 | 27.4 | 24.7 |
| 40875.44 | $NH_2CHO$ | $2_{12}$-$1_{11}$ | 80.1 | -5.32 | 15.9 | -98.4 |
| | | | 62.4 | -7.41 | 12.5 | -102.1 |
| 41313.99 | $CH_3C_3N$ | $10_1$-$9_1$/$10_0$-$9_0$ | 63.8 | -0.29 | 29.2 | -9.0 |
| 41400.26 | Hydrogen | H(84)$\delta$ | 65.2 | 0.44 | 40.6 | 19.2 |
| 41846.55 | Hydrogen | H(67)$\beta$ | 81.4 | 1.52 | 33.1 | 53.7 |
| | | | 56.3 | 1.60 | 28.4 | 48.4 |
| 41863.60 | Helium | He(67)$\beta$ | 88.5 | 0.21 | 7.6 | 1.7 |
| | | | 63.9 | 0.20 | 51.8 | 11.1 |
| 42000.64 | Hydrogen | H(95)$\zeta$ | 65.0 | 0.39 | 8.2 | 3.4 |
| 42011.43 | U | —— | 64.0 | -0.30 | 8.8 | -2.8 |
| 42031.94 | $c$-$H_2C_3O$ | $3_{03}$-$2_{02}$ | 61.3 | -0.39 | 13.1 | -5.5 |
| 42035.74 | U | —— | 64.0 | -0.24 | 18.0 | -4.6 |
| 42081.49 | U | —— | 64.0 | 0.31 | 9.9 | 3.3 |
| 42139.19 | $c$-$C_3H_2$ | $5_{41}$-$5_{32}$ | 63.3 | -0.66 | 10.0 | -7.1 |
| 42318.18 | $NH_2^{13}CHO$ | $2_{02}$-$1_{01}$ | 63.8 | -0.45 | 10.9 | -5.2 |
| 42373.34 | $^{30}SiO$ | 1-0 | 81.4 | -1.96 | 11.2 | -23.4 |
| | | | 63.1 | -10.02 | 10.6 | -117.5 |
| 42386.06 | $NH_2CHO$ | $2_{02}$-$1_{01}$ | 80.4 | -6.15 | 13.9 | -91.3 |
| | | | 62.5 | -13.66 | 12.9 | -187.0 |
| | | | 6.0 | -0.62 | 14.2 | -14.5 |
| 42414.09 | Hydrogen | H(76)$\gamma$ | 85.8 | 0.58 | 28.5 | 17.7 |
| | | | 58.9 | 0.67 | 26.0 | 18.6 |
| 42602.15 | $HC_5N$ | 16-15 | 63.3 | -0.83 | 13.4 | -11.9 |
| 42674.19 | $HCS^+$ | 1-0 | 81.8 | -0.33 | 7.4 | -2.6 |
| | | | 64.4 | -4.12 | 13.2 | -57.8 |
| | | | 8.4 | -0.49 | 15.8 | -8.2 |
| 42839.92 | $NH_3$ | (17,17) | 63.5 | -1.68 | 11.5 | -20.6 |
| 42862.60 | U | —— | 64.0 | -0.61 | 12.0 | -7.8 |
| 42879.94 | $^{29}SiO$ | 1-0 | 82.1 | -3.06 | 9.2 | -28.9 |

Continued on next page

**Table 9 – Line Identifications and Fit Parameters towards K6**

| Line Rest Freq (MHz) | Species | Transition | Fit Velocity ( km s$^{-1}$) | Height (mJy arcsec$^{-2}$) | Width ( km s$^{-1}$) | $\int I_v dv$ (mJy arcsec$^{-2}$ × km s$^{-1}$) |
|---|---|---|---|---|---|---|
| | | | 64.3 | -12.73 | 11.6 | -154.9 |
| | | | 4.8 | -0.61 | 8.3 | -13.5 |
| 42951.97 | Hydrogen | H(53)$\alpha$ | 84.2 | 6.67 | 28.5 | 202.1 |
| | | | 56.7 | 7.66 | 27.8 | 226.9 |
| 42969.47 | Helium | He(53)$\alpha$ | 70.2 | 0.65 | 49.2 | 33.8 |
| 43303.71 | *t*-HCOOH | $2_{12}$-$1_{11}$ | 64.2 | -1.67 | 10.6 | -18.8 |
| 43423.85 | SiO$^{Adj}$ | 1-0 | 83.8 | -14.45 | 9.8 | -137.4 |
| | | | 62.5 | -25.83 | 26.0 | -707.5 |
| | | | 15.3 | -2.99 | 11.5 | -38.7 |
| | | | 3.1 | -6.16 | 10.3 | -67.5 |
| | | | -28.4 | -1.02 | 31.0 | -33.8 |
| | | | -67.9 | -1.03 | 20.7 | -22.8 |
| | | | -99.3 | -1.66 | 17.0 | -30.1 |
| | | | -108.1 | -1.48 | 7.9 | -12.4 |
| 43516.19 | $CH_3CH_2CN$ | $5_{15}$-$4_{14}$ | 64.4 | -1.37 | 15.2 | -22.2 |
| 43748.95 | Hydrogen | H(66)$\beta$ | 86.9 | 1.38 | 25.9 | 38.0 |
| | | | 59.1 | 1.91 | 34.0 | 69.2 |
| 43901.51 | SiN | N=1-0 J= $\frac{3}{2}$ - $\frac{1}{2}$<br>F = $\frac{5}{2}$ - $\frac{3}{2}$ | 64.0 | -0.64 | 9.3 | -6.3 |
| 43954.45 | $NH_2CHO$ | $2_{11}$-$1_{10}$ | 78.3 | -4.96 | 21.0 | -110.8 |
| | | | 61.7 | -7.95 | 13.4 | -113.3 |
| 43963.04 | HNCO$^{B}$ | $2_{02}$-$1_{01}$ | [20]60.0 | -0.55 | 20.2 | -11.9 |
| 44069.48 | $CH_3OH^{Maser}$ | $7_{07}$-$6_{16}$++ | 83.2 | 35.09 | 7.6 | 244.6 |
| 44084.17 | H$^{13}$CCCN | 5-4 | 63.5 | -2.18 | 13.2 | -30.5 |
| 44100.09 | Hydrogen | H(75)$\gamma$ | 85.3 | 1.11 | 11.3 | 13.3 |
| | | | 64.9 | 1.25 | 14.7 | 19.6 |
| 44104.78 | *c*-$C_3H_2$ | $3_{21}$-$3_{12}$ | 83.5 | -0.80 | 6.3 | -5.3 |
| | | | 64.1 | -3.89 | 10.0 | -41.3 |
| 44338.89 | $CH_3NH_2$? | $1_0$E1+1-$0_0$E1+1 | 81.1 | -0.26 | 21.5 | -6.0 |
| | | | 62.6 | -0.53 | 8.8 | -5.0 |
| 44430.71 | Hydrogen$^{B}$ | H(82)$\delta$ | [21]73.2 | 0.70 | 61.6 | 45.6 |
| 44469.22 | *E*-$CH_3CHNH^{BC}$ | $1_{10}$-$1_{01}$A | [22]74.9 | -0.54 | 9.8 | -5.6 |
| 44497.60 | CC$^{34}$S | $4_3$-$3_2$ | 62.7 | -0.49 | 8.1 | -4.2 |
| 44587.40 | *c*-$H_2C_3O$ | $3_{12}$-$2_{11}$ | 64.0 | -0.92 | 10.6 | -10.3 |
| 44596.99 | $CH_3CH_2CN$ | $5_{05}$-$4_{04}$ | 64.5 | -2.80 | 10.8 | -32.1 |
| 44659.99 | Contam | —— | 64.0 | 0.24 | 11.8 | 3.0 |
| 44730.27 | Contam | —— | 71.8 | 0.55 | 10.0 | 5.9 |
| 44768.91 | Contam | —— | 69.5 | 0.71 | 20.1 | 15.0 |
| 44773.87 | Contam | —— | 62.9 | 0.94 | 24.8 | 24.8 |
| 44792.73 | Contam | —— | 64.0 | 0.20 | 31.0 | 6.5 |
| 44831.00 | Contam | —— | 70.3 | 0.21 | 27.1 | 6.0 |
| 44878.10 | Contam | —— | 72.0 | 0.66 | 10.0 | 7.0 |
| 44879.04 | Contam | —— | 64.0 | 0.28 | 15.7 | 4.7 |
| 44911.75 | *t*-HCOOH | $2_{02}$-$1_{01}$ | 81.1 | -0.84 | 10.9 | -9.7 |
| | | | 63.9 | -2.23 | 11.1 | -26.4 |
| 44955.78 | Contam | —— | 75.9 | 0.41 | 10.1 | 4.4 |
| | | | 64.0 | 0.54 | 10.0 | 5.7 |
| 44979.54 | *l*-$C_3H$+ $^{Adj}$ | $2-1$ | 80.0 | -0.21 | 15.0 | -3.3 |
| | | | 64.7 | -0.42 | 15.2 | -6.8 |
| | | | -2.4 | -0.16 | 30.5 | -5.3 |
| 45103.87 | *c*-H$^{13}$CCCH$^{Adj}$ | $2_{11}$-$2_{02}$ | 81.0 | -0.20 | 14.4 | -3.1 |
| | | | 64.0 | -0.28 | 10.8 | -3.2 |
| 45259.08 | NaCN/NaNC | $3_{13}$-$2_{12}$ | 65.2 | -0.32 | 17.5 | -5.9 |
| 45264.72 | $HC_5N$ | 17-16 | 79.2 | -0.31 | 10.7 | -3.5 |
| | | | 63.0 | -0.77 | 12.4 | -10.2 |
| 45297.35 | HC$^{13}$CCN | 5-4 | 82.3 | -0.70 | 10.5 | -7.8 |
| | | | 64.1 | -1.64 | 11.6 | -20.2 |
| 45301.71 | HCC$^{13}$CN | 5-4 | 81.7 | -0.67 | 12.9 | -9.2 |
| | | | 62.9 | -1.84 | 11.2 | -21.9 |
| 45379.03 | CCS | $4_3$-$3_2$ | 81.2 | -1.86 | 10.1 | -19.9 |
| | | | 64.2 | -6.03 | 12.4 | -77.8 |
| | | | 5.2 | -0.20 | 15.9 | -3.3 |
| 45395.79 | $CH_3OCHO^{B}$ | $4_{14}$-$3_{13}$E | [23]66.4 | -0.42 | 13.6 | -6.1 |

Continued on next page

**Table 9 – Line Identifications and Fit Parameters towards K6**

| Line Rest Freq (MHz) | Species | Transition | Fit Velocity ( km s$^{-1}$) | Height (mJy arcsec$^{-2}$) | Width ( km s$^{-1}$) | $\int I_v dv$ (mJy arcsec$^{-2}$ × km s$^{-1}$) |
|---|---|---|---|---|---|---|
| 45397.38 | $CH_3OCHO$ | $4_{14}$-$3_{13}$A | 63.3 | -0.36 | 10.1 | -3.9 |
| 45453.72 | Hydrogen | H(52)$\alpha$ | 84.7 | 3.28 | 28.3 | 99.0 |
| | | | 64.6 | 6.79 | 33.2 | 240.0 |
| 45463.42 | $^{13}C^{34}S$ | 1-0 | 63.8 | -0.73 | 12.3 | -9.5 |
| 45472.24 | Helium | He(52)$\alpha$ | 85.9 | 0.19 | 17.1 | 3.5 |
| | | | 66.1 | 0.55 | 35.5 | 20.7 |
| 45490.34 | $HC_3N$ | 5-4 | 81.0 | -8.94 | 12.2 | -115.9 |
| | | | 63.1 | -15.77 | 14.7 | -246.3 |
| 45495.97 | *E*-$CH_3CHNH^B$ | $2_{11}$-$2_{02}$E | [24]57.2 | -0.60 | 25.8 | -16.5 |
| 45490.34 | $HC_3N$ | 5-4 | 3.4 | -0.72 | 12.1 | -12.6 |
| | | | -105.3 | -0.38 | 8.1 | -3.3 |
| 45547.64 | *g'Ga*-$(CH_2OH)_2$ | $4_{14}$v=1-$3_{13}$v=0 | 64.4 | -0.21 | 11.9 | -2.7 |
| 45566.66 | *E*-$CH_3CHNH$ | $2_{11}$-$2_{02}$A | 61.8 | -0.47 | 14.2 | -7.1 |
| 45600.79 | Contam | —— | 61.6 | 0.59 | 18.7 | 11.8 |
| | | | 47.2 | 0.31 | 10.8 | 3.6 |
| 45644.07 | U? | | 64.0 | -0.23 | 11.3 | -2.8 |
| 45667.55 | Contam | —— | 73.6 | 0.47 | 9.8 | 5.0 |
| | | | 61.1 | 0.56 | 15.2 | 9.0 |
| 45768.44 | Hydrogen | H(65)$\beta$ | 70.5 | 2.11 | 40.7 | 91.5 |
| 45778.89 | Contam | —— | 64.0 | 0.41 | 19.5 | 8.5 |
| 45787.10 | Helium | He(65)$\beta$ | 68.5 | 0.17 | 37.9 | 6.7 |
| 45842.95 | Contam | —— | 64.0 | 0.72 | 15.2 | 11.7 |
| 45876.67 | Hydrogen$^B$ | H(74)$\gamma$ | [25]84.7 | 0.25 | 16.1 | 4.4 |
| | | | [25]73.8 | 0.34 | 59.4 | 21.8 |
| 45877.81 | $HSCN^B$ | $4_{04}$-$3_{03}$ | 62.1 | -0.53 | 7.0 | -4.0 |
| 45909.51 | $CH_3CH_2CN^B$ | $5_{14}$-$4_{13}$ | [26]82.9 | -0.53 | 8.1 | -4.5 |
| | | | [26]72.9 | 0.39 | 7.1 | 2.9 |
| | | | [26]63.8 | -0.58 | 6.9 | -4.3 |
| 45921.88 | Contam | —— | 64.0 | 0.24 | 22.4 | 5.8 |
| 45935.39 | Hydrogen | H(87)$\epsilon$ | 71.9 | 0.34 | 47.3 | 17.3 |
| 45956.07 | Contam | —— | 64.0 | 0.21 | 30.9 | 6.9 |
| 46057.33 | Hydrogen | H(81)$\delta$ | 70.1 | 0.50 | 42.9 | 22.6 |
| 46112.17 | Hydrogen | H(92)$\zeta$ | 79.0 | 0.19 | 47.7 | 9.4 |
| 46123.30 | $NH_3$ | (18,18) | 81.2 | -0.79 | 13.6 | -11.4 |
| | | | 64.1 | -1.69 | 14.2 | -25.5 |
| 46247.56 | $^{13}CS$ | 1-0 | 81.1 | -3.54 | 10.9 | -41.1 |
| | | | 64.3 | -11.24 | 14.4 | -172.0 |
| | | | 5.6 | -1.48 | 13.1 | -24.2 |
| 46266.93 | $CH_2CHCN^B$ | $5_{15}$-$4_{14}$ | [27]81.8 | -0.79 | 9.3 | -7.8 |
| | | | [27]61.3 | -1.03 | 16.9 | -18.6 |
| 46247.56 | $^{13}CS$ | $1-0$ | -103.2 | -0.47 | 11.8 | -5.9 |
| 46312.34 | U | —— | 81.3 | -0.25 | 7.8 | -2.1 |
| | | | 64.0 | -0.33 | 12.8 | -4.5 |
| 46473.52 | U | —— | 82.5 | -0.23 | 7.8 | -1.9 |
| | | | 64.0 | -0.33 | 22.0 | -7.8 |
| 46534.34 | U | —— | 80.8 | -0.19 | 11.7 | -2.4 |
| | | | 64.0 | -0.35 | 12.8 | -4.7 |
| 46557.44 | Contam | —— | 64.0 | 0.18 | 19.5 | 3.7 |
| 46574.40 | Contam | —— | 64.0 | 0.23 | 12.3 | 3.0 |
| 46581.23 | *t*-HCOOH | $2_{11}$-$1_{10}$ | 81.3 | -0.69 | 8.5 | -6.3 |
| | | | 64.5 | -1.19 | 11.5 | -14.5 |
| 46645.05 | *c*-$C_3H_2$ | $5_{50}$-$5_{41}$ | 65.9 | -0.37 | 15.9 | -6.2 |
| 46755.61 | *c*-$C_3H_2$ | $2_{11}$-$2_{02}$ | 81.5 | -1.11 | 10.6 | -12.6 |
| | | | 64.2 | -2.79 | 12.9 | -38.3 |
| | | | 11.1 | -0.18 | 31.0 | -5.9 |
| 46832.80 | *t*-$CH_3CH_2OH$ | $4_{04}$-$3_{13}$ | 64.7 | -0.41 | 11.7 | -5.1 |
| 46847.73 | NaCN/NaNC | $3_{03}$-$2_{02}$ | 63.5 | -0.49 | 15.4 | -8.0 |
| 46905.49 | U | —— | 64.0 | 0.18 | 38.1 | 7.4 |
| 46990.54 | PN | N = 1-0 J=2-1 | [28]78.4 | -0.64 | 17.5 | -11.8 |
| | | | 64.7 | -1.21 | 12.0 | -15.5 |
| 47064.81 | $SiC_2$ | $2_{02}$-$1_{01}$ | 83.6 | -0.24 | 8.6 | -2.2 |
| | | | 61.6 | -0.27 | 11.8 | -3.3 |
| 47176.01 | *E*-$CH_3CHNH^{Adj}$ | $3_{12}$-$3_{03}$E | 80.8 | -0.21 | 8.3 | -1.9 |

Continued on next page

**Table 9 – Line Identifications and Fit Parameters towards K6**

| Line Rest Freq (MHz) | Species | Transition | Fit Velocity ( km s$^{-1}$) | Height (mJy arcsec$^{-2}$) | Width ( km s$^{-1}$) | $\int I_v dv$ (mJy arcsec$^{-2}$ × km s$^{-1}$) |
|---|---|---|---|---|---|---|
| | | | 64.5 | -0.35 | 21.6 | -8.1 |
| 47195.10 | $CH_3CH_2CHO$ | $4_{14}$-$3_{03}$ | 63.2 | -0.27 | 8.4 | -2.4 |
| 47205.21 | $^{13}CH_3OH$ | $1_{01}$-$0_{00}$++ | 61.9 | -0.88 | 16.9 | -15.8 |
| 47209.55 | $^{13}CH_3OH$ | $1_{01}$-$0_{00}$ | 63.9 | -0.26 | 18.6 | -5.2 |
| 47217.41 | *g'Ga*-$(CH_2OH)_2$ | $4_{04}$v=1-$3_{03}$v=0 | 82.2 | -0.16 | 11.7 | -2.0 |
| | | | 64.2 | -0.23 | 12.1 | -3.0 |
| 47249.91 | *E*-$CH_3CHNH$ | $3_{12}$-$3_{03}$A | 82.1 | -0.22 | 10.5 | -2.4 |
| | | | 63.4 | -0.36 | 23.7 | -9.0 |
| 47354.65 | $CH_2CHCN$ | $5_{05}$-$4_{04}$ | 81.8 | -0.98 | 9.9 | -10.3 |
| | | | 63.9 | -2.19 | 11.0 | -25.6 |
| 47373.32 | $CH_3CONH_2$ | $4_{23}$-$3_{31}$E | 80.6 | -0.21 | 12.8 | -2.9 |
| | | | 63.6 | -0.33 | 13.8 | -4.8 |
| 47419.79 | Contam | —— | 63.9 | 0.18 | 24.0 | 4.7 |
| 47444.51 | Contam | —— | 64.0 | 0.49 | 23.9 | 12.5 |
| 47511.87 | Hydrogen | H(86)$\epsilon$ | 66.6 | 0.28 | 37.8 | 11.3 |
| 47534.09 | $CH_3OCHO$ | $4_{04}$-$3_{03}$E | 62.8 | -0.41 | 11.1 | -4.9 |
| 47536.94 | $CH_3OCHO$ | $4_{04}$-$3_{03}$A | 63.2 | -0.38 | 15.4 | -6.2 |
| 47566.80 | $C_4H$ | N=5-4 J=$\frac{11}{2}$-$\frac{9}{2}$ | 81.3 | -0.26 | 8.3 | -2.3 |
| | | | 65.0 | -0.51 | 14.7 | -8.0 |
| | | | 9.2 | -0.17 | 17.2 | -3.1 |
| 47582.44 | Contam | —— | 64.0 | 0.20 | 7.3 | 1.6 |
| 47601.58 | Hydrogen | H(91)$\zeta$ | 78.1 | 0.26 | 25.2 | 7.0 |
| 47605.49 | $C_4H$ | N=5-4 J=$\frac{9}{2}$-$\frac{7}{2}$ | 64.7 | -0.42 | 10.4 | -4.7 |
| 47674.96 | $CH_3OCH_3$ | $1_{11}$-$0_{00}$EE/AA/AE/EA | 61.9 | -0.58 | 13.1 | -8.2 |
| 47696.89 | *c*-$HCC^{13}CH$ | $2_{11}$-$2_{02}$ | 65.0 | -0.19 | 19.0 | -3.9 |
| 47732.32 | U | —— | 64.0 | -0.22 | 6.9 | -1.6 |
| 47749.98 | Hydrogen$^{B}$ | H(73)$\gamma$ | [29] 70.9 | 0.45 | 10.0 | 4.8 |
| | | | 59.1 | 0.70 | 24.3 | 18.1 |
| 47764.35 | Hydrogen | H(80)$\delta$ | 68.6 | 0.48 | 48.1 | 24.6 |
| 47820.62 | $CH_3CHO$ | $1_{10}$-$1_{01}$A | 81.3 | -0.48 | 10.7 | -5.5 |
| | | | 62.4 | -0.95 | 15.7 | -15.8 |
| 47824.96 | *E*-HNCHCN | $5_{05}$-$4_{04}$ | 63.7 | -0.56 | 12.8 | -7.7 |
| 47914.18 | Hydrogen | H(64)$\beta$ | 68.0 | 2.27 | 34.9 | 92.8 |
| 47927.28 | $HC_5N^{BC}$ | 18-17 | 65.8 | -0.34 | 19.3 | -7.0 |
| 47933.71 | Helium$^{B}$ | He(64)$\beta$ | [30] 70.4 | 0.23 | 34.2 | 8.3 |
| 48120.99 | Contam | —— | 64.0 | 0.26 | 9.6 | 2.7 |
| 48153.60 | Hydrogen | H(51)$\alpha$ | 85.5 | 3.42 | 26.0 | 100.1 |
| | | | 64.0 | 6.29 | 32.6 | 218.0 |
| 48173.22 | Helium | He(51)$\alpha$ | 70.4 | 0.53 | 45.0 | 25.6 |
| 48206.94 | $C^{34}S$ | 1-0 | 81.3 | -4.63 | 11.4 | -54.1 |
| | | | 64.3 | -12.98 | 15.4 | -213.2 |
| | | | 5.6 | -1.99 | 15.8 | -38.1 |
| | | | -23.1 | -0.31 | 10.1 | -3.4 |
| | | | -40.4 | -1.78 | 7.0 | -13.2 |
| | | | -72.9 | -0.84 | 9.8 | -8.8 |
| | | | -86.2 | -0.34 | 10.7 | -3.9 |
| | | | -103.4 | -0.90 | 11.4 | -10.8 |
| 48284.52 | $H_2CO$ | $4_{13}$-$4_{14}$ | 81.8 | -1.90 | 9.7 | -19.2 |
| | | | 63.1 | -0.38 | 13.8 | -5.7 |
| 48308.75 | U | —— | 64.0 | -0.61 | 6.7 | -4.4 |
| 48372.46 | $CH_3OH$ | $1_{01}$-$0_{00}$++ | 80.8 | -2.20 | 7.3 | -17.1 |
| | | | 61.5 | -11.79 | 20.0 | -249.5 |
| 48376.89 | $CH_3OH$ | $1_{01}$-$0_{00}$ | 62.6 | -6.59 | 12.7 | -88.8 |
| 48372.46 | $CH_3OH$ | $1_{01}$-$0_{00}$++ | 6.0 | -0.78 | 14.6 | -16.7 |
| 48385.60 | $CH_3NH_2$? | $3_0$E1+1-$2_1$E1+1 F=2-1 | 72.1 | 0.35 | 11.0 | 4.1 |
| 48372.46 | $CH_3OH$ | $1_{01}$-$0_{00}$++ | -105.1 | -0.81 | 7.3 | -6.3 |
| 48548.22 | NaCN/NaNC$^{B}$ | $3_{12}$-$2_{11}$ | [31] 58.3 | -0.76 | 21.2 | -17.2 |
| 48552.56 | $CH_2CHCN$ | $5_{14}$-$4_{13}$ | 62.8 | -0.93 | 11.2 | -11.1 |
| 48583.29 | $C^{33}S$ | 1-0 F=$\frac{1}{2}$-$\frac{3}{2}$ | 65.2 | -1.46 | 12.6 | -19.6 |
| 48585.92 | $C^{33}S$ | 1-0 F=$\frac{5}{2}$-$\frac{3}{2}$ | 64.3 | -2.70 | 13.6 | -39.2 |
| 48589.07 | $C^{33}S$ | 1-0 F=$\frac{3}{2}$-$\frac{3}{2}$ | 64.6 | -1.57 | 12.5 | -20.9 |
| 48603.47 | $CH_3CHO$ | $2_{11}$-$2_{02}$E | 80.8 | -0.50 | 13.9 | -7.4 |
| | | | 64.0 | -1.04 | 13.2 | -14.7 |

Continued on next page

**Table 9 – Line Identifications and Fit Parameters towards K6**

| Line Rest Freq (MHz) | Species | Transition | Fit Velocity ( $\mathrm{km\,s^{-1}}$) | Height (mJy arcsec$^{-2}$) | Width ( $\mathrm{km\,s^{-1}}$) | $\int I_v dv$ (mJy arcsec$^{-2}$ $\times$ $\mathrm{km\,s^{-1}}$) |
|---|---|---|---|---|---|---|
| 48617.69 | Contam | —— | 64.0 | 0.38 | 17.9 | 7.3 |
| 48651.60 | Contam | —— | 69.7 | 0.72 | 13.1 | 10.0 |
| 48768.30 | $CH_3OCHO$ | $4_{23}$-$3_{22}$E/A | 66.8 | -0.29 | 22.8 | -6.9 |
| 48902.83 | $CH_3CHO$ | $2_{11}$-$2_{02}$A | 62.5 | -0.89 | 11.4 | -10.8 |
| 48990.95 | CS | 1-0 | 80.3 | -11.93 | 15.3 | -188.6 |
| | | | 61.5 | -18.43 | 23.0 | -451.1 |
| | | | 32.7 | -1.54 | 5.5 | -1.9 |
| | | | 6.4 | -13.54 | 19.2 | -288.5 |
| | | | -21.6 | -3.61 | 10.1 | -36.9 |
| | | | -38.3 | -11.27 | 11.6 | -144.1 |
| | | | -76.6 | -6.29 | 18.3 | -119.6 |
| | | | -94.1 | -3.16 | 6.1 | -16.7 |
| | | | -105.3 | -8.17 | 11.0 | -94.1 |
| 49161.34 | Hydrogen$^B$ | H(85)$\epsilon$ | [32] 87.8 | 0.36 | 68.4 | 26.2 |
| 49396.29 | U? | —— | 64.0 | 0.31 | 8.4 | 2.7 |
| 49461.85 | Contam | —— | 69.0 | 0.23 | 19.8 | 4.8 |
| 49466.46 | CCCN | N=5-4 J=$\frac{11}{2}$-$\frac{9}{2}$ | 63.6 | -0.48 | 20.4 | -10.5 |
| 49485.25 | CCCN | N=5-4 J=$\frac{9}{2}$-$\frac{7}{2}$ | 62.6 | -0.58 | 24.1 | -14.8 |
| 49556.79 | Hydrogen | H(79)$\delta$ | 76.4 | 0.50 | 40.6 | 21.5 |
| 49642.06 | U | U-49643.86 | [33] 64.0 | -0.42 | 12.3 | -5.6 |
| 49726.70 | Hydrogen | H(72)$\gamma$ | 73.0 | 0.98 | 47.6 | 49.6 |
| 49746.08 | U? | —— | 64.0 | 0.29 | 7.7 | 2.3 |
| 49748.08 | U? | —— | 64.0 | 0.23 | 7.0 | 1.7 |
| 49806.46 | U? | —— | 64.0 | -0.24 | 12.1 | -3.1 |
| 49839.64 | $NH_3$ | (19,19) | 78.5 | -0.38 | 11.7 | -4.7 |
| | | | 64.5 | -0.67 | 10.9 | -7.8 |
| 49962.84 | Contam | —— | 73.8 | 0.61 | 9.0 | 5.8 |
| | | | 61.0 | 0.52 | 10.8 | 6.0 |
| 50058.80 | $CH_3SH$ | $2_1$+-$1_1$+A | 65.3 | -0.29 | 16.5 | -5.1 |
| 50094.90 | $CH_3OCHO^B$ | $4_{22}$-$3_{21}$E | 61.0 | -0.39 | 10.2 | -4.2 |
| 50099.91 | $CH_2CHCN$ | $6_{15}$-$6_{06}$ | 78.6 | -0.84 | 11.1 | -9.9 |
| | | | 64.7 | -1.15 | 15.9 | -19.5 |
| 50149.90 | U? | —— | 79.1 | -0.26 | 6.6 | -1.8 |
| | | | 64.0 | -0.22 | 11.0 | -2.5 |
| 50175.41 | $CH_3CHO$ | $3_{12}$-$3_{03}$E | 82.0 | -0.42 | 11.7 | -5.2 |
| | | | 62.5 | -0.50 | 20.1 | -10.7 |

[1] Weakly masing.
[2] The line-of-sight absorption of the F=(2-1f) transition is blended with the F=(1-1f) transition and the F=(1-0f) transitions.
[3] This could be l-$C_3H$ F=(1-0f) at 10 $\mathrm{km\,s^{-1}}$or F=(2-1f) at -54 $\mathrm{km\,s^{-1}}$. The feature is detected towards L and is evident, but not detected towards K4. If this is a U-line, the line should be shifted to 56 or 76 $\mathrm{km\,s^{-1}}$ towards L;however it is not significantly shifted. If the feature is a spiral arm cloud component, we would not expect to see it towards K4 at these velocities, as strong foreground absorption is only detected towards K4 at $\sim$2 $\mathrm{km\,s^{-1}}$.
[4] Blended with the 64 $\mathrm{km\,s^{-1}}$ component of the F=(1-1) transition.
[5] Tentative because the velocity is unusual for this source.
[6] Blended with $CH_3OCH_3$ $2_{20}$-$3_{13}$.
[7] Tentative because the stronger EE transition is not detected.
[8] Tentative because the A-state transition is not detected.
[9] Generally arising from LMH, with some emission in the base of the K5 shell.
[10] The 64 $\mathrm{km\,s^{-1}}$ component of $HC^{13}CCN$ is blended with the 82 $\mathrm{km\,s^{-1}}$ component of $HCC^{1}3CN$.
[11] Blended with H(80)$\gamma$.
[12] This may be line-of-sight absorption by OCS at $\sim$35 $\mathrm{km\,s^{-1}}$.
[13] Blended with $CH_3OCHO$ $3_{21}$-$2_{20}$.
[14] Blended with $CH_3OCHO$ $3_{21}$-$2_{21}$E.
[15] This may be line-of-sight absorption by $CH_3CHO$ at -39 $\mathrm{km\,s^{-1}}$.
[16] Blended with the wing of $CH_3CHO$ $2_{11}$-$1_{10}$E.
[17] Detected in K6, L, and K4.
[18] Blended with $HC_5N$ J=(15-14).
[19] Multiple hyperfine components are blended.
[20] Possibly blended with $NH_2CHO$ at $\sim$0 $\mathrm{km\,s^{-1}}$.
[21] Blended with H(88)$\epsilon$.
[22] Unusual velocity, perhaps due to poor S:N or baseline issues.
[23] May be blended with line-of-sight absorption of CCS.
[24] Blended with line-of-sight absorption of $HC_3N$.

Continued on next page

**Table 9 – Line Identifications and Fit Parameters towards K6**

| Line Rest Freq (MHz) | Species | Transition | Fit Velocity ( $km\,s^{-1}$ ) | Height (mJy $arcsec^{-2}$ ) | Width ( $km\,s^{-1}$ ) | $\int I_v dv$ (mJy $arcsec^{-2}$ $\times$ $km\,s^{-1}$ ) |
|---|---|---|---|---|---|---|

[25] Blended with HSCN $4_{04}$-$3_{03}$ towards K6.
[26] Due to line emission from ‘h’ (at 73 $km\,s^{-1}$ ) and the LMH, the line profile is not representative of the gas kinematics towards K6.
[27] Blended with line-of-sight absorption of $^{13}$CS.
[28] Blended with the N=1-0 J=1-1 transition.
[29] Blended with $CH_3CHO$ $1_{10}$-$1_{01}$E.
[30] Blended with $HC_5N$ J=(18-17).
[31] Blended with the 82 $km\,s^{-1}$ component of $CH_2CHCN$.
[32] Blend of H(85)$\epsilon$, H(90)$\zeta$, and $CH_3OCHO$ $4_{31}$-$3_{03}$E.
[33] This is at 74.9 $km\,s^{-1}$ with respect to a U-line at 49643.86 MHz in the LOVAS catalog.

Table 10: Line identifications and fit parameters towards L.

| Line Rest Freq (MHz) | Species | Transition | Fit Velocity ( $km\,s^{-1}$ ) | Height (mJy $arcsec^{-2}$ ) | Width ( $km\,s^{-1}$ ) | $\int I_v dv$ (mJy $arcsec^{-2}$ $\times$ $km\,s^{-1}$ ) |
|---|---|---|---|---|---|---|
| 29901.40 | $CH_3OCH_3$ | $1_{10}$-$1_{01}$EE/AA/AE/EA | [1]61.2 | -0.28 | 28.7 | -8.5 |
| 29914.49 | $NH_3$ | (11,11) | 74.0 | -1.21 | 14.9 | -19.2 |
| | | | 54.9 | -1.16 | 15.3 | -19.0 |
| | | | 20.2 | -0.31 | 14.5 | -4.8 |
| 29971.48 | Hydrogen | H(75)$\beta$ | 76.6 | 1.42 | 26.2 | 39.5 |
| 29979.38 | *t*-$CH_3CH_2OH$ | $3_{12}$-$3_{03}$ | 59.1 | -0.49 | 15.8 | -8.2 |
| 30001.55 | SO | $1_0$-$0_1$ | 73.7 | -4.10 | 17.1 | -70.1 |
| | | | 56.1 | -8.86 | 14.2 | -133.1 |
| | | | 16.7 | -0.96 | 26.1 | -18.0 |
| | | | -10.4 | -0.59 | 17.4 | -10.9 |
| | | | -38.1 | -0.40 | 20.1 | -8.7 |
| | | | -75.6 | -0.52 | 11.4 | -6.3 |
| | | | -104.3 | -0.25 | 11.8 | -3.1 |
| 30500.20 | Hydrogen | H(85)$\gamma$ | 74.6 | 0.54 | 29.8 | 17.0 |
| 30586.57 | U? | —— | 56.0 | -0.24 | 11.2 | -2.8 |
| 30707.38 | Hydrogen | H(93)$\delta$ | 77.1 | 0.36 | 31.3 | 11.9 |
| 30865.74 | U? | —— | 56.0 | -0.23 | 12.0 | -3.0 |
| 31106.15 | $CH_3OCH_3$ | $2_{11}$-$2_{02}$EE/AA/AE/EA | [1]63.6 | -0.46 | 25.3 | -12.3 |
| 31186.68 | Hydrogen | H(74)$\beta$ | 75.6 | 1.68 | 27.2 | 48.7 |
| 31223.31 | Hydrogen | H(59)$\alpha$ | 76.3 | 6.55 | 26.3 | 189.8 |
| 31236.04 | Helium | He(59)$\alpha$ | 79.1 | 0.44 | 22.0 | 10.3 |
| 31262.33 | NaCN/NaNC | $2_{02}$-$1_{01}$ | 57.5 | -0.27 | 40.4 | -11.8 |
| 31424.94 | $NH_3$ | (12,12) | 76.8 | -2.15 | 13.4 | -30.7 |
| | | | 57.0 | -2.58 | 14.9 | -41.0 |
| | | | 19.4 | -0.51 | 13.4 | -7.3 |
| 31482.38 | Hydrogen | H(99)$\epsilon$ | 73.5 | 0.21 | 37.6 | 8.6 |
| 31583.40 | Hydrogen | H(84)$\gamma$ | 75.3 | 0.69 | 31.2 | 23.0 |
| 31698.47 | Hydrogen | H(92)$\delta$ | 75.2 | 0.29 | 22.3 | 6.9 |
| 31951.78 | $HC_5N$ | 12-11 | 73.9 | -0.49 | 10.6 | -5.6 |
| | | | 56.3 | -0.78 | 14.0 | -11.7 |
| 32468.48 | Hydrogen | H(73)$\beta$ | 76.5 | 1.82 | 28.3 | 54.8 |
| 32640.21 | U | —— | 59.9 | -0.28 | 33.2 | -9.9 |
| 32660.65 | *l*-$C_3H$ | J=$\frac{3}{2}$-$\frac{1}{2}$ $\Omega$=$\frac{1}{2}$ F=2-1e | 57.0 | -0.38 | 13.3 | -5.4 |
| | | | [2]7.7 | -0.27 | 44.1 | -12.7 |
| 32672.52 | *cis*-$CH_2OHCHO^{BC}$ | $4_{22}$-$4_{13}$ | 63.5 | -0.26 | 28.1 | -7.7 |
| 32718.50 | Hydrogen | H(83)$\gamma$ | 75.2 | 0.83 | 26.5 | 23.3 |

Continued on next page

**Table 10 – Line Identifications and Fit Parameters towards L**

| Line Rest Freq (MHz) | Species | Transition | Fit Velocity ( km s$^{-1}$) | Height (mJy arcsec$^{-2}$) | Width ( km s$^{-1}$) | $\int I_v dv$ (mJy arcsec$^{-2}$ × km s$^{-1}$) |
|---|---|---|---|---|---|---|
| 32732.67 | Hydrogen | H(91)$\delta$ | 76.1 | 0.48 | 24.1 | 12.3 |
| 32742.82 | *t*-$CH_3CH_2OH$ | $4_{13}$-$4_{04}$ | 60.2 | -0.61 | 21.9 | -14.3 |
| 32852.20 | Hydrogen | H(58)$\alpha$ | 75.8 | 7.08 | 27.3 | 214.5 |
| 32865.58 | Helium | He(58)$\alpha$ | 74.4 | 0.63 | 28.5 | 19.1 |
| 32978.23 | $CH_3OCH_3$ | $3_{12}$-$3_{03}$EE/AA/AE/EA | [1]67.0 | -0.89 | 28.8 | -27.2 |
| 33156.85 | $NH_3$ | (13,13) | 74.9 | -0.93 | 13.9 | -13.7 |
| | | | 55.6 | -1.04 | 14.3 | -15.8 |
| | | | 19.8 | -0.26 | 11.7 | -3.3 |
| 33354.01 | *cis*-$CH_2OHCHO$? | $2_{12}$-$1_{01}$ | 58.6 | -0.27 | 26.6 | -7.8 |
| 33420.88 | Hydrogen | H(97)$\epsilon$ | 68.3 | 0.22 | 56.0 | 13.3 |
| 33704.82 | $CH_2NH$ | $1_{11}$-$2_{02}$ | 73.8 | -1.58 | 14.4 | -24.3 |
| | | | 55.9 | -0.97 | 14.0 | -14.4 |
| 33751.37 | CCS | $3_2$-$2_1$ | 75.3 | -1.55 | 15.4 | -25.4 |
| | | | 56.1 | -2.26 | 15.2 | -36.7 |
| | | | 5.1 | -0.29 | 33.1 | -10.2 |
| 33812.37 | Hydrogen | H(90)$\delta$ | 75.1 | 0.47 | 26.2 | 13.1 |
| 33821.51 | Hydrogen | H(72)$\beta$ | 77.0 | 1.83 | 29.1 | 56.5 |
| 33908.67 | Hydrogen | H(82)$\gamma$ | 76.9 | 0.91 | 26.6 | 25.7 |
| 34156.88 | $CH_3OCHO$ | $3_{13}$-$2_{12}$E/A | 56.2 | -0.30 | 34.8 | -11.0 |
| 34351.45 | $H_2CS$ | $1_{01}$-$0_{00}$ | 77.7 | -0.35 | 12.3 | -4.6 |
| | | | 57.6 | -1.10 | 15.4 | -18.0 |
| 34408.63 | HSCN | $3_{03}$-$2_{02}$ | 58.2 | -0.40 | 12.9 | -5.4 |
| 34450.03 | Hydrogen | H(96)$\epsilon$ | 77.7 | 0.41 | 12.8 | 5.5 |
| 34522.90 | U? | | 56.0 | 0.28 | 11.2 | 3.4 |
| 34596.38 | Hydrogen | H(57)$\alpha$ | [3]85.2 | 4.80 | 17.5 | 89.5 |
| | | | [3]71.5 | 6.37 | 17.9 | 128.6 |
| 34610.48 | Helium | He(57)$\alpha$ | 77.2 | 0.65 | 25.9 | 17.9 |
| 34614.38 | $HC_5N$ | 13-12 | 59.7 | -0.70 | 22.0 | -16.4 |
| 34684.37 | $CCCS^B$ | 6-5 | [4]61.1 | -0.39 | 16.0 | -6.7 |
| 34824.07 | $CH_3CH_2CN$ | $4_{14}$-$3_{13}$ | 52.3 | -0.34 | 22.3 | -8.2 |
| 34940.09 | Hydrogen | H(89)$\delta$ | 74.4 | 0.55 | 22.3 | 13.0 |
| 35134.30 | $NH_3$ | (14,14) | 76.3 | -0.59 | 9.3 | -5.8 |
| | | | 54.7 | -0.46 | 13.6 | -6.7 |
| 35157.27 | Hydrogen | H(81)$\gamma$ | 75.5 | 1.00 | 25.4 | 27.2 |
| 35250.77 | Hydrogen | H(71)$\beta$ | 76.4 | 2.18 | 26.8 | 62.1 |
| 35267.41 | $H^{13}CCCN$ | 4-3 | 76.6 | -0.69 | 12.2 | -8.9 |
| | | | 56.4 | -1.06 | 13.9 | -15.7 |
| 35521.88 | Hydrogen | H(95)$\epsilon$ | 73.5 | 0.33 | 28.4 | 9.9 |
| 35593.40 | $CH_3OCH_3$ | $4_{13}$-$4_{04}$EE/AA/AE/EA | [1]74.9 | -0.73 | 12.9 | -10.0 |
| | | | 60.8 | -0.58 | 15.7 | -9.8 |
| 35722.21 | $CH_3CH_2CN$ | $4_{04}$-$3_{03}$ | 76.9 | -0.27 | 15.4 | -4.3 |
| | | | 55.1 | -0.41 | 13.8 | -6.0 |
| 35733.12 | $^{13}CH_3CN^{Adj}$ | $2_0$-$1_0$/$2_1$-$1_1$ | 77.3 | -0.23 | 11.8 | -2.9 |
| | | | 55.5 | -0.34 | 24.4 | -8.9 |
| 36102.22 | $CH_3OCHO$ | $3_{03}$-$2_{02}$A | 55.2 | -0.42 | 12.7 | -5.7 |
| 36104.79 | $CH_3OCHO$ | $3_{03}$-$2_{02}$E | 58.3 | -0.32 | 11.5 | -4.0 |
| 36118.53 | Hydrogen$^{Adj}$ | H(88)$\delta$ | 79.1 | 0.52 | 40.6 | 22.6 |
| 36169.29 | Contam | —— | 74.9 | -17.01 | 11.7 | -239.9 |
| 36237.99 | $HC^{13}CCN$ | 4-3 | 75.9 | -0.44 | 15.2 | -7.1 |
| | | | [5]52.2 | -1.13 | 20.0 | -24.0 |
| 36241.48 | $HCC^{13}CN$ | 4-3 | 55.9 | -1.25 | 12.7 | -16.9 |
| 36299.95 | $H_2COH^+$ | $1_{11}$-$2_{02}$ | 73.8 | -0.31 | 11.4 | -3.7 |
| 36309.63 | SiS | 2-1 | 58.8 | -0.60 | 16.5 | -10.5 |
| 36392.32 | $HC_3N$ | 4-3 | 73.1 | -6.73 | 14.9 | -106.6 |
| | | | 55.8 | -13.17 | 15.2 | -213.7 |
| | | | 14.1 | -0.67 | 27.1 | -14.5 |
| | | | -6.1 | -0.36 | 9.7 | -3.7 |
| 36417.24 | *t*-$CH_3CH_2OH$ | $5_{14}$-$5_{05}$ | 61.1 | -0.40 | 10.3 | -4.3 |
| 36466.26 | Hydrogen | H(56)$\alpha^B$ | [6]74.3 | 7.86 | 28.6 | 264.2 |
| 36467.94 | Hydrogen | H(80)$\gamma$ | 56.4 | 0.71 | 11.2 | 8.5 |
| 36481.12 | Helium | He(56)$\alpha$ | 74.8 | 0.83 | 28.0 | 24.7 |
| 36488.81 | OCS | 3-2 | 55.8 | -0.42 | 11.3 | -5.0 |
| 36739.67 | $CH_3CH_2CN$ | $4_{13}$-$3_{12}$ | 59.5 | -0.64 | 10.8 | -7.4 |

Continued on next page

**Table 10 – Line Identifications and Fit Parameters towards L**

| Line Rest Freq (MHz) | Species | Transition | Fit Velocity ( $\mathrm{km\,s^{-1}}$) | Height (mJy arcsec$^{-2}$) | Width ( $\mathrm{km\,s^{-1}}$) | $\int I_v dv$ (mJy arcsec$^{-2}$ × $\mathrm{km\,s^{-1}}$) |
|---|---|---|---|---|---|---|
| 36761.72 | Hydrogen | H(70)$\beta$ | 76.6 | 1.98 | 27.1 | 57.3 |
| 36777.28 | $CH_3^{13}CN^{Adj}$ | $2_0$-$1_0$/$2_1$-$1_1$ | 74.1 | -0.33 | 11.2 | -3.9 |
| | | | 55.7 | -0.24 | 19.2 | -4.9 |
| 36795.47 | $CH_3CN$ | $2_0$-$1_0$/$2_1$-$1_1$ | 72.7 | -6.05 | 21.6 | -144.7 |
| | | | 57.4 | -6.31 | 19.5 | -130.7 |
| | | | 15.6 | -0.55 | 31.4 | -26.4 |
| 36930.70 | *Z*-$CH_3CHNH$ | $2_{02}$-$1_{01}$E/A | 55.9 | -0.42 | 27.5 | -12.2 |
| 37018.92 | $CH_2CHCN$ | $4_{14}$-$3_{13}$ | 77.6 | -0.35 | 9.8 | -3.7 |
| | | | 58.2 | -0.52 | 14.2 | -7.9 |
| 37182.66 | $CH_3C_3N^{BC}$ | $9_1$-$8_1$/$9_0$-$7_0$ | 68.8 | -0.30 | 36.7 | -11.6 |
| 37276.99 | $HC_5N$ | 14-13 | 57.2 | -0.59 | 14.6 | -9.2 |
| 37350.57 | Hydrogen | H(87)$\delta$ | 72.8 | 0.53 | 24.6 | 13.9 |
| 37385.12 | $NH_3$ | (15, 15) | 76.4 | -0.99 | 15.1 | -15.9 |
| | | | 58.0 | -1.33 | 19.1 | -27.0 |
| | | | 19.0 | -0.36 | 27.8 | -10.8 |
| | | | -11.3 | -0.25 | 41.6 | -11.0 |
| 37464.17 | $CH_3CHO$ | $2_{12}$-$1_{11}$A | 75.4 | -1.31 | 16.9 | -23.6 |
| | | | 55.8 | -1.62 | 13.8 | -23.7 |
| 37665.30 | U? | —— | 56.0 | 0.41 | 6.7 | 2.9 |
| 37686.87 | $CH_3CHO$ | $2_{12}$-$1_{11}$E | 76.5 | -1.63 | 11.5 | -20.0 |
| | | | 57.0 | -1.64 | 14.0 | -24.4 |
| 37844.59 | Hydrogen | H(79)$\gamma$ | 74.2 | 0.90 | 27.5 | 26.4 |
| 37904.85 | $CH_2CHCN$ | $4_{04}$-$3_{03}$ | 75.5 | -0.77 | 13.3 | -10.9 |
| | | | 57.9 | -1.30 | 15.3 | -21.2 |
| 38271.02 | *E*-HNCHCN | $4_{04}$-$3_{03}$ | 73.0 | -0.43 | 9.6 | -4.4 |
| | | | 54.0 | -0.38 | 12.5 | -5.0 |
| 38360.27 | Hydrogen | H(69)$\beta$ | 77.4 | 2.15 | 27.0 | 61.9 |
| 38473.36 | Hydrogen | H(55)$\alpha$ | 77.3 | 7.86 | 27.2 | 222.6 |
| 38489.04 | Helium | He(55)$\alpha$ | 76.1 | 0.45 | 26.3 | 12.6 |
| 38506.04 | $CH_3CHO$ | $2_{02}$-$1_{01}$E | 75.1 | -3.39 | 13.4 | -48.3 |
| | | | 55.9 | -4.12 | 13.4 | -58.6 |
| 38512.11 | $CH_3CHO$ | $2_{02}$-$1_{01}$A | 76.6 | -2.86 | 12.7 | -38.5 |
| | | | 57.5 | -4.60 | 16.0 | -78.5 |
| | | | 5.4 | -0.37 | 25.5 | -9.9 |
| 38506.04 | $CH_3CHO$? | $2_{02}$-$1_{01}$E | -77.0 | -0.45 | 10.1 | -4.8 |
| 38639.30 | Hydrogen | H(86)$\delta$ | 75.0 | 0.57 | 30.0 | 18.3 |
| 38847.73 | $CH_2CHCN$ | $4_{13}$-$3_{12}$ | 76.7 | -0.46 | 10.9 | -5.3 |
| | | | 56.6 | -0.87 | 11.6 | -10.7 |
| 39016.76 | Hydrogen | H(92)$\epsilon$ | 76.7 | 0.38 | 29.6 | 12.0 |
| 39139.14 | U? | —— | 56.0 | -0.46 | 9.6 | -4.7 |
| 39148.05 | U? | —— | 56.0 | -0.48 | 8.9 | -4.5 |
| 39291.42 | Hydrogen | H(78)$\gamma$ | 77.4 | 0.96 | 30.9 | 31.7 |
| 39362.50 | $CH_3CHO$ | $2_{11}$-$1_{10}$E | 73.3 | -1.51 | 11.7 | -18.9 |
| | | | 55.9 | -1.84 | 14.5 | -28.3 |
| 39527.73 | Hydrogen | H(97)$\zeta$ | 76.4 | 0.47 | 35.0 | 17.3 |
| 39571.33 | CCCN | N=4-3 J=$\frac{9}{2}$-$\frac{7}{2}$ | 54.8 | -0.48 | 11.1 | -5.6 |
| 39594.29 | $CH_3CHO$ | $2_{11}$-$1_{10}$ A | 77.9 | -1.40 | 14.2 | -21.3 |
| | | | 56.9 | -1.52 | 13.7 | -22.2 |
| 39847.97 | U? | —— | 56.0 | -0.54 | 9.3 | -5.3 |
| 39927.87 | U | —— | [7]56.7 | -0.61 | 14.0 | -9.1 |
| 39939.57 | $HC_5N^{B,Adj}$ | 15-14 | [8]71.1 | -0.80 | 11.6 | -9.9 |
| 39941.41 | $NH_3^{B,Adj}$ | (16,16) | [9]73.7 | -0.51 | 10.1 | -5.5 |
| | | | 56.3 | -0.54 | 29.5 | -16.9 |
| 39956.70 | *c*-$H_2C_3O$ | $3_{13}$-$2_{12}$ | 74.3 | -0.49 | 11.0 | -5.7 |
| | | | 56.8 | -0.82 | 10.6 | -9.3 |
| 39988.02 | Hydrogen | H(85)$\delta$ | 79.0 | 0.63 | 31.0 | 20.7 |
| 40052.88 | Hydrogen | H(68)$\beta$ | 76.6 | 2.40 | 26.3 | 67.3 |
| 40211.39 | $CH_3NC$ | $2_0$-$1_0$ | 73.7 | -0.49 | 10.1 | -5.3 |
| | | | 57.8 | -0.59 | 12.9 | -8.2 |
| | | | 37.8 | -0.57 | 10.6 | -6.5 |
| 40239.70 | $CH_2CN^B$ | $2_{02}$-$1_{01}$ J=$\frac{5}{2}$-$\frac{3}{2}$ | 77.1 | -0.72 | 22.0 | -16.9 |
| | | F1=$\frac{7}{2}$-$\frac{5}{2}$ F=$\frac{7}{2}$-$\frac{5}{2}$ | 54.2 | -2.70 | 25.1 | -72.2 |
| 40242.22 | $CH_2CN^B$ | $2_{02}$-$1_{01}$ J=$\frac{5}{2}$-$\frac{3}{2}$ | 52.4 | -0.77 | 9.1 | -7.5 |

Continued on next page

**Table 10 – Line Identifications and Fit Parameters towards L**

| Line Rest Freq (MHz) | Species | Transition | Fit Velocity ( km s$^{-1}$) | Height (mJy arcsec$^{-2}$) | Width ( km s$^{-1}$) | $\int I_v dv$ (mJy arcsec$^{-2}$ × km s$^{-1}$) |
|---|---|---|---|---|---|---|
| | | F1=$\frac{5}{2}$-$\frac{3}{2}$ F=$\frac{5}{2}$-$\frac{3}{2}$ | | | | |
| 40244.34 | CH$_2$CN$^B$ | $2_{02}$-$1_{01}$ J=$\frac{5}{2}$-$\frac{3}{2}$<br>F1=$\frac{5}{2}$-$\frac{3}{2}$ F=$\frac{7}{2}$-$\frac{5}{2}$ | 54.5 | -1.13 | 19.4 | -23.3 |
| 40247.54 | CH$_2$CN$^B$ | $2_{02}$-$1_{01}$ J=$\frac{3}{2}$-$\frac{1}{2}$<br>F1=$\frac{5}{2}$-$\frac{3}{2}$ F=$\frac{5}{2}$-$\frac{3}{2}$ | 56.2 | -2.05 | 18.0 | -39.2 |
| 40250.43 | CH$_2$CN$^B$ | $2_{02}$-$1_{01}$ J=$\frac{3}{2}$-$\frac{3}{2}$<br>F1=$\frac{3}{2}$-$\frac{1}{2}$ F=$\frac{1}{2}$-$\frac{1}{2}$ | 54.0 | -0.75 | 20.6 | -16.4 |
| 40253.88 | CH$_2$CN$^B$ | $2_{02}$-$1_{01}$ J=$\frac{3}{2}$-$\frac{1}{2}$<br>F1=$\frac{5}{2}$-$\frac{3}{2}$ F=$\frac{3}{2}$-$\frac{3}{2}$ | 54.9 | -0.67 | 19.6 | -13.9 |
| 40256.79 | CH$_2$CN$^B$ | $2_{02}$-$1_{01}$ J=$\frac{3}{2}$-$\frac{1}{2}$<br>F1=$\frac{3}{2}$-$\frac{3}{2}$ F=$\frac{5}{2}$-$\frac{5}{2}$ | 52.4 | -0.61 | 15.8 | -10.3 |
| 40283.29 | Hydrogen | H(91)$\epsilon$ | 74.2 | 0.64 | 20.3 | 13.8 |
| 40352.77 | Si$^{18}$O | 1-0 | 55.8 | -1.10 | 12.6 | -14.8 |
| 40404.39 | U? | —— | 56.0 | 0.59 | 8.8 | 5.6 |
| 40455.62 | H$_2$NCO$^+$? | $2_{02}$-$1_{01}$ F=1-0 | 71.8 | -0.43 | 22.8 | -10.4 |
| 40630.50 | Hydrogen | H(54)$\alpha$ | 76.6 | 8.65 | 26.4 | 242.5 |
| 40647.06 | Helium | He(54)$\alpha$ | 75.8 | 0.92 | 19.6 | 19.2 |
| 40658.60 | CH$_2$CN? | $2_{11}$-$1_{10}$ J=$\frac{5}{2}$-$\frac{3}{2}$ | 80.3 | -0.43 | 15.6 | -7.2 |
| | | | 55.9 | -0.79 | 28.8 | -24.4 |
| 40793.84 | H$_2$CCO | $2_{11}$-$1_{10}$ | 59.5 | -0.62 | 11.8 | -7.8 |
| 40812.95 | Hydrogen | H(77)$\gamma$ | [3]87.7 | 0.98 | 12.5 | 13.0 |
| | | | 68.9 | 1.12 | 16.6 | 19.9 |
| 40875.44 | NH$_2$CHO | $2_{12}$-$1_{11}$ | 74.6 | -2.96 | 15.5 | -48.7 |
| | | | 56.0 | -3.11 | 15.1 | -49.9 |
| 41400.26 | Hydrogen | H(84)$\delta$ | 75.9 | 0.84 | 25.9 | 23.3 |
| 41605.24 | Hydrogen | H(90)$\epsilon$ | 80.2 | 0.56 | 23.2 | 13.8 |
| 41846.55 | Hydrogen$^{Adj}$ | H(67)$\beta$ | 75.8 | 2.52 | 26.0 | 69.6 |
| 42031.94 | *c*-H$_2$C$_3$O | $3_{03}$-$2_{02}$ | 60.8 | -0.49 | 9.4 | -5.0 |
| 42373.34 | $^{30}$SiO | 1-0 | 76.2 | -3.02 | 10.6 | -34.1 |
| | | | 54.9 | -4.35 | 19.0 | -88.2 |
| 42386.06 | NH$_2$CHO | $2_{02}$-$1_{01}$ | 72.8 | -4.58 | 15.8 | -77.2 |
| | | | 57.7 | -7.60 | 15.6 | -126.1 |
| 42414.09 | Hydrogen | H(76)$\gamma$ | 74.4 | 1.09 | 31.6 | 36.8 |
| 42602.15 | HC$_5$N$^{BC}$ | 16-15 | 64.5 | -0.50 | 21.1 | -11.3 |
| 42674.19 | HCS$^+$ | 1-0 | 74.8 | -0.90 | 9.5 | -9.1 |
| | | | 56.4 | -1.39 | 15.6 | -23.0 |
| 42839.92 | NH$_3$ | (17,17) | 75.6 | -0.96 | 15.6 | -15.9 |
| | | | 52.8 | -0.75 | 10.9 | -8.7 |
| 42879.94 | $^{29}$SiO | 1-0 | 73.6 | -3.84 | 11.9 | -48.5 |
| | | | 55.2 | -8.43 | 13.0 | -117.0 |
| | | | 17.9 | -0.91 | 10.5 | -10.2 |
| | | | -74.5 | -0.85 | 9.3 | -8.4 |
| 42951.97 | Hydrogen | H(53)$\alpha$ | 76.2 | 10.21 | 26.9 | 292.0 |
| 42969.47 | Helium | He(53)$\alpha$ | 75.6 | 1.11 | 25.3 | 29.9 |
| 43026.60 | *t*-CH$_3$CH$_2$OH | $1_{11}$-$0_{00}$ | 56.4 | -0.71 | 9.0 | -6.9 |
| 43303.71 | *t*-HCOOH $^{BC}$ | $2_{12}$-$1_{11}$ | 65.1 | -0.62 | 26.0 | -17.2 |
| 43423.85 | SiO | 1-0 | 73.0 | -13.30 | 19.9 | -272.2 |
| | | | 53.9 | -16.94 | 14.5 | -261.5 |
| | | | 33.5 | -3.74 | 9.2 | -32.4 |
| | | | 18.9 | -7.45 | 12.6 | -100.0 |
| | | | -4.4 | -2.63 | 19.9 | -55.6 |
| | | | -31.6 | -1.17 | 26.3 | -32.8 |
| | | | -75.1 | -4.24 | 11.3 | -51.0 |
| | | | -104.8 | -0.63 | 20.4 | -21.5 |
| 43748.95 | Hydrogen | H(66)$\beta$ | 75.5 | 2.68 | 28.6 | 81.6 |
| 43954.45 | NH$_2$CHO | $2_{11}$-$1_{10}$ | 72.4 | -3.05 | 17.0 | -55.2 |
| | | | 55.7 | -3.31 | 15.3 | -53.9 |
| 44084.17 | H$^{13}$CCCN | 5-4 | 73.5 | -0.80 | 11.6 | -9.9 |
| | | | 57.1 | -1.15 | 9.4 | -11.5 |
| 44100.09 | Hydrogen | H(75)$\gamma$ | 78.0 | 1.26 | 27.0 | 36.3 |
| 44104.78 | *c*-C$_3$H$_2$ $^B$ | $3_{21}$-$3_{12}$ | [10]71.7 | -1.40 | 10.9 | -16.2 |
| | | | 57.2 | -0.84 | 10.1 | -9.1 |

Continued on next page

**Table 10 – Line Identifications and Fit Parameters towards L**

| Line Rest Freq (MHz) | Species | Transition | Fit Velocity ( km s$^{-1}$) | Height (mJy arcsec$^{-2}$) | Width ( km s$^{-1}$) | $\int I_v dv$ (mJy arcsec$^{-2}$ × km s$^{-1}$) |
|---|---|---|---|---|---|---|
| 44430.71 | Hydrogen$^{B}$ | H(82)$\delta$ | [11]74.9 | 0.56 | 50.3 | 30.2 |
| 44497.60 | $CC^{34}S$ | $4_{3}$-$3_{2}$ | 54.9 | -0.75 | 10.4 | -8.3 |
| 44587.40 | $c$-$H_2C_3O^{BC}$ | $3_{12}$-$2_{11}$ | 66.8 | -0.64 | 23.0 | -15.8 |
| 44911.75 | $t$-HCOOH | $2_{02}$-$1_{01}$ | 75.0 | -0.41 | 10.9 | -4.8 |
| | | | 55.7 | -0.46 | 8.8 | -4.3 |
| 45264.72 | $HC_5N$? | 17-16 | 78.1 | -0.40 | 13.0 | -5.5 |
| 45297.35 | $HC^{13}CCN$ | 5-4 | 74.4 | -0.55 | 18.4 | -10.8 |
| | | | [5]50.8 | -0.64 | 17.8 | -12.2 |
| 45301.71 | $HCC^{13}CN$ | 5-4 | 53.3 | -0.40 | 19.4 | -8.2 |
| 45323.48 | U? | | 56.0 | -0.19 | 26.4 | -5.5 |
| 45379.03 | CCS | $4_{3}$-$3_{2}$ | 76.1 | -1.06 | 9.1 | -10.3 |
| | | | 54.7 | -1.26 | 11.7 | -15.6 |
| 45395.79 | $CH_3OCHO$? | $4_{14}$-$3_{13}$E | 74.5 | -0.32 | 10.2 | -3.5 |
| | | | 56.2 | -0.37 | 16.3 | -6.4 |
| 45397.38 | $CH_3OCHO$ | $4_{14}$-$3_{13}$A | 54.4 | -0.22 | 10.3 | -2.4 |
| 45453.72 | Hydrogen | H(52)$\alpha$ | 76.9 | 3.57 | 21.2 | 80.4 |
| 45490.34 | $HC_3N$ | 5-4 | 78.6 | -2.08 | 9.1 | -20.1 |
| | | | 53.3 | -4.88 | 11.3 | -58.7 |
| | | | 16.7 | -0.46 | 16.5 | -8.0 |
| 45768.44 | Hydrogen | H(65)$\beta$ | 77.9 | 0.92 | 22.6 | 22.2 |
| 45843.57 | Contam | —— | [12]62.4 | -0.33 | 12.0 | -4.3 |
| 45909.51 | $CH_3CH_2CN^{BC}$ | $5_{14}$-$4_{13}$ | 62.5 | -0.34 | 28.3 | -10.1 |
| 46123.30 | $NH_3^{BC}$ | (18,18) | 65.0 | -0.31 | 33.8 | -11.0 |
| 46247.56 | $^{13}CS$ | 1-0 | 79.6 | -0.47 | 5.7 | -2.8 |
| | | | 54.9 | -2.66 | 10.7 | -30.2 |
| 46266.93 | $CH_2CHCN$ | $5_{15}$-$4_{14}$ | 76.0 | -0.46 | 9.1 | -4.4 |
| | | | 56.2 | -0.32 | 12.5 | -4.2 |
| 46755.61 | $c$-$C_3H_2$ | $2_{11}$-$2_{02}$ | 76.7 | -0.55 | 9.5 | -5.6 |
| | | | 55.0 | -0.52 | 13.0 | -7.1 |
| 47064.83 | $SiC_2$ | $2_{02}$-$1_{01}$ | 53.7 | -0.33 | 7.6 | -2.7 |
| 47205.21 | $^{13}CH_3OH$ | $1_{01}$-$0_{00}$++ | 51.2 | -0.45 | 9.7 | -4.6 |
| 47354.65 | $CH_2CHCN$ | $5_{05}$-$4_{04}$ | 75.9 | -0.65 | 10.6 | -7.3 |
| | | | 60.3 | -0.51 | 18.2 | -9.8 |
| 47764.35 | Hydrogen | H(80)$\delta$ | 84.7 | 0.19 | 39.0 | 7.7 |
| 47820.62 | $CH_3CHO$ | $1_{10}$-$1_{01}$A | 73.2 | -0.32 | 10.2 | -3.5 |
| | | | 52.7 | -0.31 | 15.3 | -5.1 |
| 47914.18 | Hydrogen | H(64)$\beta$ | 78.0 | 0.86 | 16.9 | 15.5 |
| 48153.60 | Hydrogen | H(51)$\alpha$ | 88.9 | 1.12 | 16.3 | 19.5 |
| | | | 75.0 | 3.25 | 20.1 | 69.5 |
| 48173.22 | Helium | He(51)$\alpha$ | 75.5 | 0.42 | 12.4 | 5.5 |
| 48206.94 | $C^{34}S$ | 1-0 | 79.0 | -0.91 | 6.1 | -5.9 |
| | | | 55.8 | -3.30 | 12.6 | -44.3 |
| | | | 29.8 | -0.20 | 5.3 | -1.1 |
| | | | 2.6 | -0.55 | 16.8 | -9.8 |
| 48372.46 | $CH_3OH$ | $1_{01}$-$0_{00}$++ | 79.7 | -2.01 | 9.9 | -23.6 |
| | | | 50.4 | -4.18 | 12.7 | -58.0 |
| 48376.89 | $CH_3OH$ | $1_{01}$-$0_{00}$ | 56.2 | -1.35 | 17.6 | -25.4 |
| 48990.95 | CS | 1-0 | [13]82.7 | -0.73 | 5.3 | -4.1 |
| | | | [13]67.0 | -2.63 | 8.7 | -28.7 |
| | | | 53.8 | -4.91 | 11.7 | -60.7 |
| | | | 22.6 | -2.16 | 22.6 | -51.9 |
| | | | -2.8 | -3.04 | 18.3 | -59.2 |
| | | | -35.5 | -2.18 | 20.1 | -46.7 |
| | | | -75.8 | -1.90 | 9.8 | -19.8 |
| | | | -106.5 | -0.96 | 8.1 | -8.3 |
| 49671.55 | U? | —— | 56.0 | 0.55 | 10.4 | 6.1 |
| 49726.70 | Hydrogen | H(72)$\gamma$ | 77.5 | 0.49 | 13.0 | 6.7 |
| 49962.84 | $NH_2D$ | $2_{12}$0s-$2_{02}$0a | 73.5 | -0.58 | 8.1 | -4.9 |

[1] Transitions of $CH_3OCH_3$ towards L are more kinematically consistent with being the AA transition than the EE transition, although the EE transition has a higher quantum line strength. Towards K6 and K4, the EE transitions are more kinematically consistent.

[2] Blended with the F=(1-1) transition.

[3] One of only two recombination line fit with two components towards this source. Possible blending.

[4] Blended with $CH_3OCH_3$ $2_{20}$-$3_{13}$EE & AA.

Continued on next page

**Table 10 – Line Identifications and Fit Parameters towards L**

| Line Rest Freq (MHz) | Species | Transition | Fit Velocity ( km s$^{-1}$) | Height (mJy arcsec$^{-2}$) | Width ( km s$^{-1}$) | $\int I_v dv$ (mJy arcsec$^{-2}$ × km s$^{-1}$) |
|---|---|---|---|---|---|---|

[5] The 56 km s$^{-1}$ component of HC$^{13}$CCN is blended with the 76 km s$^{-1}$ component of HCC$^{13}$CN.

[6] Blended with H(80)$\gamma$.

[7] Detected in K6, L, and K4.

[8] Blended with NH$_3$ (16, 16).

[9] Blended with HC$_5$N J=(15-14).

[10] Blended with H(75)$\gamma$.

[11] Blended with H(88)$\epsilon$.

[12] This corresponds to the 9$_{36}$-10$_{2,8}$ line produced by CH$_3$OH in the hot cores. The beam pattern falls near L.

[13] The profile of CS is atypical of line profiles towards L. Instead of absorbing components at 56 and 76 km s$^{-1}$, we observe strong absorption at 56 km s$^{-1}$, fairly strong absorption at 67 km s$^{-1}$, and a weak absorption component at 82 km s$^{-1}$. The 76 km s$^{-1}$ component does not appear in absorption.

Table 11: Line identifications and fit parameters towards K4.

| Line Rest Freq (MHz) | Species | Transition | Fit Velocity ( km s$^{-1}$) | Height (mJy arcsec$^{-2}$) | Width ( km s$^{-1}$) | $\int I_v dv$ (mJy arcsec$^{-2}$ × km s$^{-1}$) |
|---|---|---|---|---|---|---|
| 29901.40 | CH$_3$OCH$_3$ | 1$_{10}$-1$_{01}$EE/AA/EA/AE | 62.4 | -0.24 | 22.7 | -5.8 |
| 29914.49 | NH$_3$ | (11,11) | 82.9 | -1.64 | 15.9 | -27.8 |
| | | | 63.3 | -2.49 | 20.2 | -53.4 |
| | | | 0.1 | -0.54 | 17.5 | -10.1 |
| 29971.48 | Hydrogen | H(75)$\beta$ | 67.9 | 0.87 | 30.2 | 27.8 |
| 29979.38 | *t*-CH$_3$CH$_2$OH | 3$_{12}$-3$_{03}$ | [1]83.0 | 0.24 | 11.9 | 3.0 |
| | | | 4.7 | -0.25 | 12.2 | -3.2 |
| 30001.55 | SO | 1$_0$-0$_1$ | 83.3 | -7.41 | 15.8 | -115.6 |
| | | | 63.7 | -9.84 | 15.6 | -163.9 |
| | | | 3.0 | -0.89 | 17.5 | -16.6 |
| 30500.20 | Hydrogen | H(85)$\gamma$ | 66.2 | 0.28 | 35.4 | 10.4 |
| 30707.38 | Hydrogen | H(93)$\delta$ | 56.3 | 0.31 | 52.9 | 17.3 |
| 31102.23 | U | —— | 62.0 | -0.21 | 16.6 | -3.7 |
| 31106.15 | CH$_3$OCH$_3$ | 2$_{11}$-2$_{02}$EE/AA/EA/AE | 65.6 | -0.44 | 20.9 | -9.8 |
| 31186.68 | Hydrogen | H(74)$\beta$ | 68.3 | 0.78 | 37.0 | 30.7 |
| 31223.31 | Hydrogen | H(59)$\alpha$ | 104.8 | 0.42 | 17.5 | 7.9 |
| | | | 72.9 | 2.95 | 27.6 | 86.9 |
| | | | 54.7 | 1.60 | 16.5 | 28.1 |
| 31236.04 | Helium | He(59)$\alpha$ | 68.6 | 0.21 | 34.3 | 7.5 |
| 31262.33 | NaCN/NaNC$^{BC}$ | 2$_{02}$-1$_{01}$ | 70.1 | -0.23 | 33.0 | -8.0 |
| 31424.94 | NH$_3$ | (12,12) | 82.4 | -2.57 | 16.8 | -45.9 |
| | | | 62.1 | -3.74 | 17.8 | -70.9 |
| | | | 0.6 | -0.80 | 15.5 | -13.2 |
| 31583.40 | Hydrogen | H(84)$\gamma$ | 74.8 | 0.23 | 62.4 | 15.2 |
| 31727.07 | *cis*-CH$_2$OHCHO | 5$_{23}$-5$_{14}$ | [2]57.0 | -0.21 | 13.3 | -3.0 |
| 31833.03 | *cis*-CH$_2$OHCHO | 6$_{24}$-6$_{15}$ | [2]57.0 | -0.27 | 15.5 | -4.4 |
| 31914.62 | H$_2$COH$^+$ | 3$_{03}$-2$_{12}$ | [1]60.0 | 0.25 | 17.9 | 4.7 |
| 31951.78 | HC$_5$N | 12-11 | 83.3 | -0.20 | 11.1 | -2.3 |
| | | | 64.0 | -0.35 | 12.6 | -4.7 |
| 32373.67 | NaCN/NaNC? | 2$_{11}$-1$_{10}$ | 83.3 | -0.21 | 20.0 | -4.5 |
| 32398.56 | $^{13}$CH$_3$OH$^{Maser}$ | 4$_{-1,4}$-3$_{03}$ | 58.0 | 0.82 | 17.9 | 15.6 |
| 32468.48 | Hydrogen | H(73)$\beta$ | 65.6 | 0.62 | 37.5 | 24.9 |
| 32660.65 | *l*-C$_3$H | J=$\frac{3}{2}$-$\frac{1}{2}$ Ω=$\frac{1}{2}$ F=2-1e | 66.9 | -0.22 | 16.4 | -3.8 |

Continued on next page

**Table 11 – Line Identifications and Fit Parameters towards K4**

| Line Rest Freq (MHz) | Species | Transition | Fit Velocity ( $\mathrm{km\,s^{-1}}$) | Height (mJy arcsec$^{-2}$) | Width ( $\mathrm{km\,s^{-1}}$) | $\int I_v dv$ (mJy arcsec$^{-2}$ $\times$ $\mathrm{km\,s^{-1}}$) |
|---|---|---|---|---|---|---|
| 32672.52 | *cis*-$CH_2OHCHO$ | $4_{22}$-$4_{13}$ | 65.9 | -0.19 | 25.5 | -5.1 |
| 32709.18 | $CH_3CHO$ | $4_{04}$-$3_{13}$A | 58.7 | -0.17 | 20.4 | -3.7 |
| 32718.50 | Hydrogen | H(83)$\gamma$ | 66.4 | 0.22 | 28.1 | 6.5 |
| 32742.82 | t-$CH_3CH_2OH$? | $4_{13}$-$4_{04}$ | 2.0 | -0.33 | 11.1 | -3.9 |
| 32852.20 | Hydrogen | H(58)$\alpha$ | 104.5 | 0.39 | 17.7 | 7.3 |
| | | | 70.3 | 2.42 | 33.1 | 85.5 |
| | | | 59.1 | 1.44 | 14.3 | 22.1 |
| 32865.58 | Helium | He(58)$\alpha$ | 66.7 | 0.29 | 25.8 | 7.9 |
| 32978.23 | $CH_3OCH_3$ | $3_{12}$-$3_{03}$EE/AA/AE/EA | 63.6 | -0.42 | 24.3 | -10.8 |
| 33156.85 | $NH_3$ | (13,13) | 82.0 | -1.16 | 15.9 | -19.8 |
| | | | 62.5 | -1.34 | 18.5 | -26.5 |
| | | | 3.3 | -0.22 | 34.5 | -8.2 |
| 33334.34 | U? | —— | [3]62.0 | 0.23 | 8.1 | 1.9 |
| 33704.82 | $CH_2NH$ | $1_{11}$-$2_{02}$ | 79.0 | -1.50 | 16.3 | -26.1 |
| | | | 58.9 | -3.98 | 17.4 | -73.7 |
| 33751.37 | CCS | $3_2$-$2_1$ | 84.3 | -1.09 | 14.8 | -17.2 |
| | | | 65.1 | -1.06 | 14.9 | -16.8 |
| 33821.51 | Hydrogen | H(72)$\beta$ | 66.1 | 0.65 | 25.7 | 17.6 |
| 33908.67 | Hydrogen | H(82)$\gamma$ | 68.5 | 0.26 | 35.8 | 9.7 |
| 34351.45 | $H_2CS$ | $1_{01}$-$0_{00}$ | 82.2 | -0.21 | 21.0 | -4.7 |
| | | | 65.6 | -0.23 | 9.3 | -2.3 |
| 34352.53 | U? | —— | [4]62.0 | 0.23 | 8.7 | 2.1 |
| 34596.38 | Hydrogen$^{Adj}$ | H(57)$\alpha$ | 89.4 | 0.73 | 28.9 | 22.4 |
| | | | 67.6 | 2.04 | 13.3 | 28.9 |
| | | | 55.0 | 1.20 | 28.9 | 36.9 |
| 34614.38 | $HC_5N$ | 13-12 | 62.4 | -0.34 | 13.7 | -5.0 |
| 34684.37 | CCCS$^B$ | 6-5 | [5]71.9 | -0.17 | 30.4 | -5.6 |
| 34824.07 | $CH_3CH_2CN$ | $4_{14}$-$3_{13}$ | 82.5 | -0.31 | 12.1 | -4.0 |
| | | | 65.1 | -0.22 | 14.7 | -3.4 |
| 35065.73 | $CH_2NH$ | $3_{03}$-$2_{12}$ | [2]60.4 | 2.44 | 17.7 | 45.9 |
| 35134.30 | $NH_3$ | (14,14) | 82.2 | -0.88 | 14.3 | -13.3 |
| | | | 63.5 | -0.92 | 18.4 | -18.0 |
| 35157.27 | Hydrogen | H(81)$\gamma$ | 68.2 | 0.19 | 32.5 | 6.7 |
| 35185.80 | U? | —— | 62.0 | 0.22 | 7.9 | 1.8 |
| 35250.77 | Hydrogen | H(71)$\beta$ | 67.1 | 0.56 | 37.9 | 22.5 |
| 35267.41 | $H^{13}CCCN$ | 4-3 | 85.0 | -0.43 | 12.8 | -5.8 |
| | | | 64.5 | -0.47 | 13.2 | -6.6 |
| | | | 2.1 | -0.26 | 9.5 | -2.6 |
| 35360.93 | c-$C_3H_2$ | $4_{40}$-$4_{31}$ | 62.7 | -0.20 | 10.4 | -2.2 |
| 35593.40 | $CH_3OCH_3$ | $4_{13}$-$4_{04}$EE/AA/AE/EA | 63.7 | -0.34 | 25.3 | -9.1 |
| 35722.21 | $CH_3CH_2CN$ | $4_{04}$-$3_{03}$ | 83.5 | -0.55 | 12.8 | -7.5 |
| | | | 63.8 | -0.30 | 12.2 | -4.0 |
| 35733.12 | $^{13}CH_3CN^{BC}$ | $2_0$-$1_0$/$2_1$-$1_1$ | 80.2 | -0.24 | 34.9 | -9.1 |
| 35906.98 | U | —— | 60.4 | -0.23 | 29.6 | -7.3 |
| 36070.55 | U? | —— | 62.0 | 0.24 | 10.9 | 2.8 |
| 36169.29 | $CH_3OH^{Maser}$ | $4_{-1,4}$-$3_{03}$ | 58.1 | 617.11 | 9.2 | 5263.7 |
| | | | 1.0 | 1.66 | 10.9 | 19.2 |
| 36237.95 | $HC^{13}CCN$ | 4-3 | 78.5 | -0.47 | 16.3 | -8.1 |
| | | | [6]57.3 | -0.60 | 15.1 | -9.6 |
| 36241.44 | $HCC^{13}CN$ | 4-3 | 64.3 | -0.54 | 14.5 | -8.3 |
| 36299.95 | $H_2COH^+$ | $1_{11}$-$2_{02}$ | 60.8 | -0.28 | 19.5 | -5.8 |
| 36309.63 | SiS | 2-1 | 62.1 | -0.26 | 12.6 | -3.5 |
| 36392.32 | $HC_3N$ | 4-3 | 83.2 | -6.22 | 12.2 | -81.1 |
| | | | 64.3 | -5.02 | 13.5 | -72.2 |
| | | | 1.1 | -2.33 | 11.7 | -31.9 |
| 36466.26 | Hydrogen | H(56)$\alpha^B$ | [7]101.3 | 0.34 | 30.2 | 11.1 |
| | | | 65.4 | 2.60 | 32.6 | 94.6 |
| 36739.67 | $CH_3CH_2CN$ | $4_{13}$-$3_{12}$ | 80.3 | -0.33 | 17.8 | -6.3 |
| | | | 60.9 | -0.46 | 10.8 | -5.3 |
| 36761.72 | Hydrogen | H(70)$\beta$ | 61.1 | 0.41 | 36.4 | 16.1 |
| 36777.28 | $CH_3^{13}CN$ | $2_0$-$1_0$/$2_1$-$1_1$ | 77.7 | -0.25 | 29.5 | -7.7 |
| | | | 57.6 | -0.17 | 8.0 | -1.4 |
| 36795.47 | $CH_3CN$ | $2_0$-$1_0$/$2_1$-$1_1$ | 84.4 | -4.02 | 22.4 | -95.8 |

Continued on next page

**Table 11 – Line Identifications and Fit Parameters towards K4**

| Line Rest Freq (MHz) | Species | Transition | Fit Velocity ( $\mathrm{km\,s^{-1}}$) | Height (mJy arcsec$^{-2}$) | Width ( $\mathrm{km\,s^{-1}}$) | $\int I_v dv$ (mJy arcsec$^{-2}$ × $\mathrm{km\,s^{-1}}$) |
|---|---|---|---:|---:|---:|---:|
| | | | 64.3 | -3.94 | 14.2 | -59.5 |
| | | | 4.0 | -1.57 | 18.4 | -40.4 |
| 36930.70 | Z-$CH_3$CHNH | $2_{02}$-$1_{01}$E/A | 67.2 | -0.32 | 14.5 | -5.0 |
| 37018.92 | $CH_2$CHCN | $4_{14}$-$3_{13}$ | 80.0 | -0.30 | 14.2 | -4.5 |
| | | | 61.1 | -0.47 | 13.7 | -6.9 |
| 37182.66 | $CH_3C_3N$? | $9_1$-$8_1$/$9_0$-$7_0$ | 72.5 | -0.24 | 10.6 | -2.7 |
| 37276.99 | $HC_5N$ | 14-13 | 62.4 | -0.31 | 10.8 | -3.5 |
| 37350.57 | Hydrogen | H(87)$\delta$ | 69.0 | 0.24 | 11.9 | 3.1 |
| 37385.12 | $NH_3$ | (15, 15) | 82.7 | -1.20 | 16.8 | -21.5 |
| | | | 64.8 | -0.86 | 23.2 | -21.3 |
| | | | -0.1 | -0.34 | 19.9 | -7.3 |
| 37464.17 | $CH_3$CHO | $2_{12}$-$1_{11}$A | 78.7 | -0.75 | 15.3 | -12.2 |
| | | | 60.0 | -1.05 | 14.2 | -15.8 |
| | | | 0.4 | -0.39 | 13.5 | -5.5 |
| 37536.85 | U? | | 62.0 | 0.24 | 15.5 | 4.0 |
| 37686.87 | $CH_3$CHO | $2_{12}$-$1_{11}$E | 80.6 | -0.52 | 12.8 | -7.1 |
| | | | 61.3 | -1.11 | 13.0 | -15.4 |
| 37703.70 | $CH_3$OH | $7_{-2,6}$-$8_{-1,8}$ | 56.8 | -0.70 | 15.3 | -11.4 |
| 37904.85 | $CH_2$CHCN | $4_{04}$-$3_{03}$ F=4-3 | 82.5 | -0.69 | 14.2 | -10.5 |
| | | | 63.0 | -0.67 | 14.0 | -9.9 |
| 38326.81 | U? | —— | 62.0 | -0.28 | 7.5 | -2.2 |
| 38360.27 | Hydrogen | H(69)$\beta$ | 64.7 | 0.51 | 36.4 | 19.9 |
| 38473.36 | Hydrogen$^{Adj}$ | H(55)$\alpha$ | 93.1 | 0.56 | 32.9 | 19.7 |
| | | | 67.8 | 1.54 | 16.4 | 27.0 |
| | | | 53.3 | 1.07 | 27.9 | 31.8 |
| 38506.04 | $CH_3$CHO | $2_{02}$-$1_{01}$E | 83.5 | -1.31 | 13.9 | -19.3 |
| | | | 63.8 | -1.55 | 19.5 | -32.1 |
| 38512.11 | $CH_3$CHO | $2_{02}$-$1_{01}$A | 83.8 | -1.35 | 10.8 | -15.4 |
| | | | [8]61.5 | -1.81 | 24.8 | -47.8 |
| | | | 0.7 | -0.74 | 11.3 | -8.9 |
| 38847.73 | $CH_2$CHCN | $4_{13}$-$3_{12}$ | 83.7 | -0.45 | 15.2 | -7.3 |
| | | | 61.0 | -0.39 | 15.9 | -6.6 |
| 39047.30 | $CH_3OCH_3$ | $5_{14}$-$5_{05}$EE/AA/AE/EA | 63.8 | -0.34 | 24.9 | -9.1 |
| 39362.50 | $CH_3$CHO | $2_{11}$-$1_{10}$E | 80.7 | -0.66 | 13.1 | -9.2 |
| | | | 60.6 | -0.62 | 13.3 | -8.8 |
| 39594.29 | $CH_3$CHO | $2_{11}$-$1_{10}$A | 82.2 | -0.63 | 18.4 | -12.4 |
| | | | 58.7 | -0.52 | 11.7 | -6.5 |
| 39924.77 | $CH_2$CN | $2_{12}$-$1_{11}$ | 82.0 | -0.32 | 21.5 | -7.3 |
| | | | 60.1 | -0.58 | 11.8 | -7.2 |
| 39927.87 | U | —— | [9]61.7 | -0.37 | 9.5 | -3.8 |
| 39941.41 | $NH_3^B$ | (16,16) | [10]79.8 | -0.72 | 29.3 | -22.5 |
| 39956.70 | c-$H_2C_3O$ | $3_{13}$-$2_{12}$ | 82.3 | -0.48 | 9.4 | -4.7 |
| 40039.02 | $H_2$CCO | $2_{12}$-$1_{11}$ | 81.3 | -0.33 | 12.3 | -4.4 |
| 40052.88 | Hydrogen | H(68)$\beta$ | 64.8 | 0.66 | 21.5 | 15.0 |
| 40239.19 | $CH_2CN^B$ | $2_{02}$-$1_{01}$ J=$\frac{5}{2}$-$\frac{3}{2}$<br>F1=$\frac{7}{2}$-$\frac{5}{2}$ F=$\frac{5}{2}$-$\frac{3}{2}$ | [11]84.5 | -0.53 | 7.9 | -4.4 |
| 40239.70 | $CH_2CN^B$ | $2_{02}$-$1_{01}$ J=$\frac{5}{2}$-$\frac{3}{2}$ | [11]81.2 | -1.23 | 6.5 | -8.5 |
| | | F1=$\frac{7}{2}$-$\frac{5}{2}$ F=$\frac{7}{2}$-$\frac{5}{2}$ | [11]59.2 | -1.44 | 28.7 | -43.8 |
| 40247.54 | $CH_2CN^B$ | $2_{02}$-$1_{01}$ J=$\frac{3}{2}$-$\frac{1}{2}$ | [11]82.5 | -0.95 | 16.1 | -16.3 |
| | | F1=$\frac{5}{2}$-$\frac{3}{2}$ F=$\frac{5}{2}$-$\frac{3}{2}$ | [11]58.7 | -0.87 | 15.7 | -14.4 |
| 40256.79 | $CH_2CN^{BC}$ | $2_{02}$-$1_{01}$ J=$\frac{3}{2}$-$\frac{1}{2}$<br>F1=$\frac{3}{2}$-$\frac{3}{2}$ F=$\frac{5}{2}$-$\frac{5}{2}$ | [11]71.5 | -0.30 | 40.2 | -13.0 |
| 40347.34 | U | —— | 62.0 | 0.33 | 10.6 | 3.7 |
| 40352.77 | $Si^{18}O$ | 1-0 | 66.7 | -0.34 | 14.0 | -5.0 |
| 40577.83 | U? | —— | 62.0 | -0.32 | 13.3 | -4.5 |
| 40630.50 | Hydrogen | H(54)$\alpha$ | 103.3 | 0.24 | 37.2 | 9.3 |
| | | | 72.9 | 1.47 | 17.5 | 27.4 |
| | | | 55.7 | 1.74 | 12.9 | 23.8 |
| 40658.60 | $CH_2CN^{BC}$ | $2_{11}$-$1_{10}$ J=$\frac{5}{2}$-$\frac{3}{2}$ | [2]71.5 | -0.44 | 28.1 | -13.2 |
| 40875.44 | $NH_2$CHO | $2_{12}$-$1_{11}$ | [12]76.6 | -1.84 | 27.3 | -53.7 |
| | | | [2]56.0 | -1.68 | 13.4 | -24.0 |
| | | | 2.8 | -0.69 | 15.1 | -11.0 |

Continued on next page

**Table 11 – Line Identifications and Fit Parameters towards K4**

| Line Rest Freq (MHz) | Species | Transition | Fit Velocity ( $km\,s^{-1}$) | Height (mJy $arcsec^{-2}$) | Width ( $km\,s^{-1}$) | $\int I_v dv$ (mJy $arcsec^{-2}$ × $km\,s^{-1}$) |
|---|---|---|---|---|---|---|
| 41124.95 | $t$-$CH_3CH_2OH$? | $6_{15}$-$6_{06}$ | 68.6 | -0.31 | 6.8 | -2.3 |
| 41741.37 | U? | | 62.0 | 0.29 | 8.5 | 2.6 |
| 41846.55 | Hydrogen | H(67)$\beta$ | 65.3 | 0.46 | 27.8 | 13.7 |
| 42373.34 | $^{30}SiO^{Adj}$ | 1-0 | 81.1 | -1.32 | 13.8 | -19.4 |
| | | | 63.2 | -1.87 | 18.8 | -37.6 |
| 42386.06 | $NH_2CHO^{Adj}$ | $2_{02}$-$1_{01}$ | 79.1 | -2.79 | 22.5 | -68.5 |
| | | | [2]55.3 | -2.61 | 14.6 | -40.3 |
| | | | 0.6 | -2.10 | 13.2 | -27.3 |
| 42602.15 | $HC_5N^{Adj}$ | 16-15 | 80.7 | -0.22 | 7.6 | -1.7 |
| | | | 65.7 | -0.33 | 10.0 | -3.5 |
| 42674.19 | $HCS^+$ | 1-0 | 82.5 | -0.53 | 9.4 | -5.3 |
| 42839.92 | $NH_3$ | (17,17) | 78.7 | -0.52 | 17.1 | -9.5 |
| | | | 60.2 | -0.49 | 12.4 | -6.5 |
| 42879.94 | $^{29}SiO$ | 1-0 | 78.1 | -2.62 | 19.6 | -54.6 |
| | | | 59.6 | -2.78 | 10.7 | -31.8 |
| | | | 2.2 | -0.93 | 10.0 | -9.9 |
| 42951.97 | Hydrogen | H(53)$\alpha$ | 70.6 | 1.63 | 15.1 | 26.2 |
| | | | 55.8 | 1.29 | 17.7 | 24.2 |
| 43423.85 | SiO | 1-0 | 82.9 | -6.60 | 19.8 | -139.1 |
| | | | 60.3 | -3.28 | 13.5 | -47.2 |
| | | | 1.5 | -5.46 | 12.8 | -87.0 |
| 43700.42 | U? | —— | 62.0 | 0.39 | 7.7 | 3.2 |
| 43748.95 | Hydrogen | H(66)$\beta$ | 66.4 | 0.47 | 26.7 | 13.3 |
| 43954.45 | $NH_2CHO$ | $2_{11}$-$1_{10}$ | 85.3 | -1.24 | 15.4 | -20.3 |
| | | | 62.2 | -2.26 | 24.8 | -59.6 |
| | | | [13]3.8 | -0.31 | 26.2 | -8.5 |
| 43972.23 | U | | 62.0 | -0.39 | 9.4 | -3.9 |
| 44069.48 | $CH_3OH^{Maser,Adj}$ | $7_{07}$-$6_{16}$++ | 68.4 | 12.90 | 9.7 | 118.7 |
| | | | 56.7 | 50.24 | 9.0 | 462.2 |
| 44084.17 | $H^{13}CCCN^{Adj}$ | 5-4 | 82.5 | -0.54 | 13.9 | -8.0 |
| | | | 64.8 | -0.31 | 11.3 | -3.8 |
| 44104.78 | $c$-$C_3H_2$ $^B$ | $3_{21}$-$3_{12}$ | [14]77.0 | -0.46 | 9.5 | -4.7 |
| | | | 59.4 | -1.34 | 12.9 | -18.4 |
| 44195.58 | U? | —— | 62.0 | 0.42 | 9.5 | 4.3 |
| 44592.31 | U? | —— | 62.0 | -0.36 | 7.6 | -2.9 |
| 44596.99 | $CH_3CH_2CN$ | $5_{05}$-$4_{04}$ | 65.0 | -0.49 | 8.3 | -4.3 |

[1] Weakly masing.
[2] Transition is at an unusual velocity for the source.
[3] A U-line at 33332.3 MHz is reported in the LOVAS catalog.
[4] This may be weak masing by $H_2CS$ at ∼55 $km\,s^{-1}$. This velocity is similar to that at which the methanol masing transitions emit towards this source.
[5] Blended with $CH_3OCH_3$ $2_{20}$-$3_{13}$AA & EE.
[6] The 62 $km\,s^{-1}$ component of $HC^{13}CCN$ is blended with the 82 $km\,s^{-1}$ component of $HCC^{13}CN$.
[7] Blended with H(80)$\gamma$.
[8] Blended with foreground absorption by the E-state transition.
[9] Detected in K6, L, and K4.
[10] Blended with $HC_5N$ J=(15-14).
[11] Multiple hyperfine components are blended.
[12] This contains a bad spectrometer channel that could interfere with the fit.
[13] Possibly blended with HNCO $2_{02}$-$1_{01}$.
[14] Blended with H(75)$\gamma$.